Numerical simulations of katabatic flow in Coats Land, Antarctica

A thesis submitted to the School of Environmental Sciences of the University of East Anglia in partial fulfilment of the requirements for the degree of Doctor of Philosophy

By Hanneke Luijting

December 2009

Abstract

Katabatic winds play a crucial role in the surface wind regime of Antarctica. This thesis presents simulated case studies of katabatic flow using the Met Office's Unified Model, over Coats Land - an area with moderate slopes, typical for much of the Antarctic coast. The model results are verified using observations from Automatic Weather Stations and wind profiles from a Doppler Sodar.

The model is able to simulate the katabatic flow reasonably well, however the katabatic layer is too deep and the wind speed near the surface too low. The sensitivity of the model results to the boundary-layer parameterisation has been examined, focusing on the vertical resolution, the boundary-layer scheme, the stability functions and the roughness length. It was found that the model results are not very sensitive to the vertical resolution or the roughness length. Using a sharper stability function (reducing the mixing at higher stabilities) resulted in higher wind speeds and lower temperatures, but generally the differences were small. The model results were very sensitive to the choice of boundary-layer scheme. The default is a Richardson-number based scheme, but an alternative equilibrium stable boundary-layer scheme was also tried, with this there were some improvements, but the simulations also appeared unrealistic and 'chaotic' at times. None of the experiments resulted in a shallower katabatic layer, or near-surface winds of the correct speed. This suggests that the model formulation of the stable boundary layer needs further improvement especially over sloping terrain.

The downslope momentum budget of the katabatic flow revealed a katabatic jump at the foot of the slope, caused by cold air piling up, which prevents the flow from continuing over the ice shelf. The synoptic forcing and the buoyancy forcing were found to be equally important over most of the slope.

Acknowledgements

First of all I would like to thank my supervisors Ian Renfrew, John King and Phil Anderson. I am grateful for your supervision and input in my thesis. Ian, I am especially grateful for your quick reading and useful comments in these last weeks before submission. I would also like to thank John and Phil for meeting with me more often while Ian was away on sabbatical.

Many people have offered me help in using the Unified Model, for which I would like to thank Chang Wang, Lois Steenman-Clark, Jeffrey Chagnon and Jeff Cole. For the boundary layer parameterisation I had help from Bob Beare, Adrian Lock and William Connolley. A big thank you goes to Gert-Jan Steeneveld who always had time to help me with questions about the stable boundary layer, and who helped me to develop a new stability function. I would also like to thank Gabriel Rooney who helped me with a roughness length issue in the model, and Hendra Adiwidjaja who helped with importing satellite images into Matlab.

At UEA, Guðrún Nína Petersen was always ready to help me with any modelling or Matlab queries. A special thanks goes to Stephen Outten - I am glad we got to share an office for over 3 years and you have been a great help. Not only have we shared many of the high and low points of our PhD, but our friendship also extended outside of academics. I have enjoyed the many game nights with you and Hari, and was honoured to be the photographer at your wedding.

Whenever I tell someone that my thesis is about Antarctica, the first question is whether I have been there. Thanks to Karen Heywood I can answer 'yes' to this question - she very kindly took me along on a research cruise to Antarctica which was an amazing experience.

My PhD was part of the FAASIS project (Fellowships in Antarctic Air Sea Ice Science) by the EU/Marie Cure. I would like to thank Bill Sturges for turning this project into a success and for tirelessly looking for solutions when another administrative 'challenge' came along. Thanks also to the fellow FAASIS students, in particular to Tanja Pangerc, Francis Mani and Nicole Nichols who have become friends for life and who were a great support during my entire PhD.

I have enjoyed my time at UEA in Norwich very much, and made a lot of valuable friendships. A big thanks to Nem, Karla, Patama, Aga, Karel, Alba, Paola, Johannes and Veronika! To Célia, my best friend who has been a massive support for many years now: our friendship means a lot to me, thank you for

being there for me.

I would also like to thank Edmond Hansen and Nalân Koç for very kindly providing me with an office at the Norwegian Polar Institute in Tromsø during the last 6 months of writing up. Thank you to everyone at the institute for being so welcoming and for showing an interest in my work.

Another big thank you goes to my parents who have always been very supportive and enthusiastic about what I am doing. 'Jodokus', met jouw verhaal in mijn achterhoofd kwam ik toch maar mooi door de moeilijke momenten heen! I am very happy that after finishing my thesis I will be able to spend more time with my family.

To Paul... so much more than my Matlab and LaTex guru; thanks for being there for me, for occasionally dragging me away from the computer, and for putting up with a very stressed PhD student. I'm looking forward to our future together, wherever it will bring us :)

Contents

List of tables

List of figures

Chapter 1

Introduction

Antarctica is a continent of extremes. The ice cap holds 70% of the fresh water reserve and 90% of all the ice in the world. The area of the continent more than doubles in size when the surrounding ocean freezes in winter. It holds the record for the lowest temperature ever recorded on Earth (-89 °C at Vostok), and is known to be the highest, driest, coldest and windiest continent. This thesis is about the winds that govern the surface wind regime of Antarctica: katabatic winds.

1.1 Katabatic wind

There are many different definitions of katabatic winds found in the literature, but in general katabatic winds are downslope, density-driven flows. At mid-latitudes, katabatic winds can occur during the night over sloping terrain, when the air near the surface cools down due to longwave radiational cooling. This layer of cold air is denser than the surrounding air, and will accelerate down the slope in response to the buoyancy force. A pressure-gradient force develops, directed down the fall line. This force is also called the 'sloped inversion force', emphasising the importance of topography. The Coriolis force will deflect the flow (to the right in the northern hemisphere and to the left in the southern hemisphere), while surface friction will slow the winds down. Katabatic winds at midlatitudes are considered a mesoscale or boundary-layer phenomenon (King and Turner, 1997).

1.2 Katabatic wind in Antarctica

The ice cap of Antarctica loses heat constantly (most strongly during the winter) and this creates a semi-permanent nocturnal situation (Ball, 1959). Dry snow absorbs only 15-20 % of the incoming shortwave radiation, but it emits longwave radiation nearly as a blackbody, causing a surface radiation deficit (van den

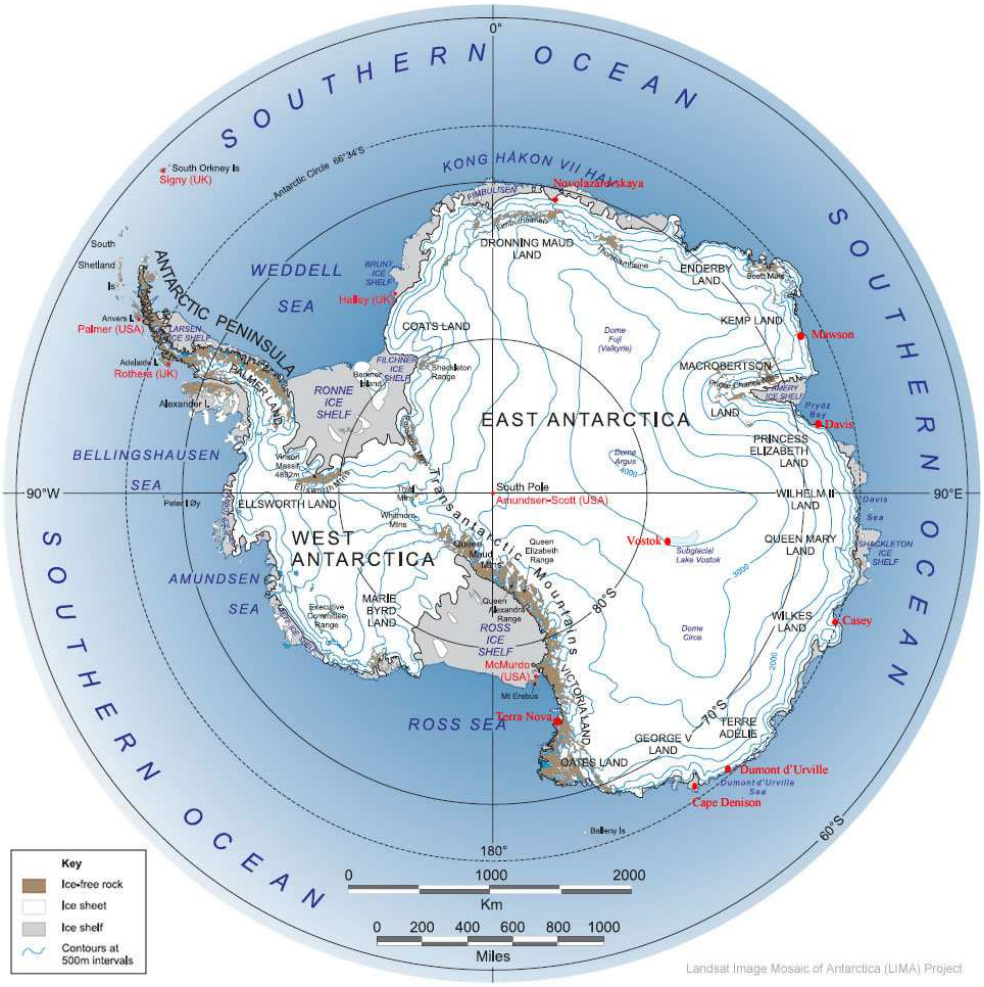

Figure 1.1: Map of Antarctica indicating several regions and research stations.

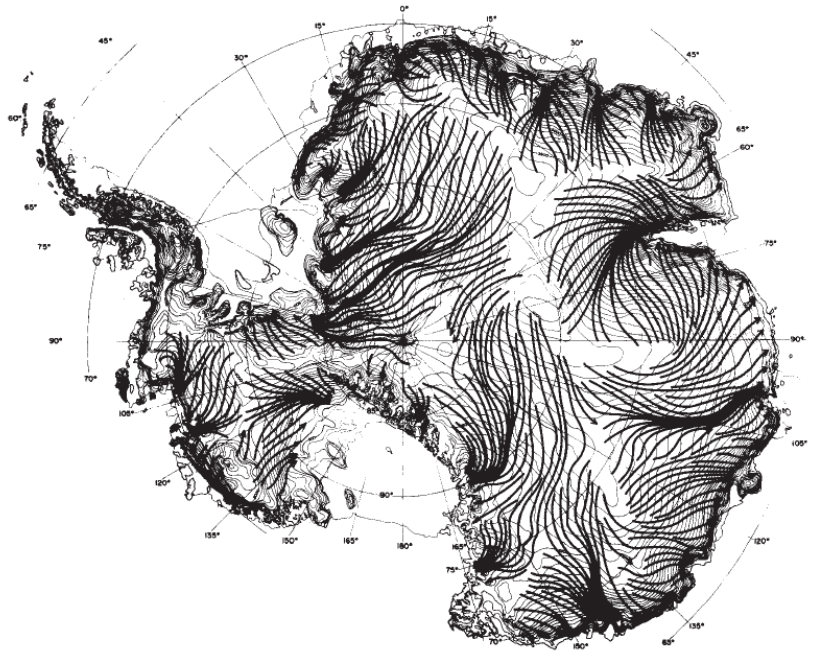

Figure 1.2: Time averaged near-surface wintertime streamlines of cold air drainage over Antarctica, with contoured orography, from Parish and Bromwich (1987)

Broeke *et al.*, 2002). In winter, this results in the strongest and most persistent surface temperature inversion in the world over the interior of Antarctica (Connolley, 1996). Katabatic winds play a key role in the surface wind regime of Antarctica and are essential for the exchange of energy and momentum between the surface and the atmosphere. Because of the size of Antarctica, the katabatic wind regime plays an important role in the global energy and momentum budget (Heinemann, 1997).

The continental ice topography is the most important factor in the katabatic wind regime (Parish, 1988). Antarctica is dome-shaped, with high elevations: 60% of the continent is higher than 2000 m and 30% is higher than 3000 m (see figure 1.1 for a map of Antarctica showing the orography, with the locations of key regions and research stations indicated). This enables katabatic flows originating in the high interior to make their way down all the way to the coast. Figure 1.2 from Parish and Bromwich (1987) illustrates this nicely, showing the average near-surface wintertime streamlines of cold air drainage over Antarctica. The streamlines are obtained from a simple steady-state model by Ball (1959), which uses the balance between the sloped-inversion pressure gradient force, the Coriolis force and friction to describe the winds. It is of course difficult to verify the streamline pattern of figure 1.2 due to the lack of observations over Antarctica, but the pattern does compare well with observations from Automatic

Weather Stations (AWS's) and sastrugi (ridges in the snow created by wind erosion, parallel to the prevailing winds) orientations. The areas where streamlines converge correspond to areas where extreme katabatic winds are observed. van Lipzig *et al.* (2004) also obtained a map of streamlines over Antarctica, from model simulations which include the large-scale pressure gradient which was not included in the study by Parish and Bromwich (1987). The results from van Lipzig *et al.* (2004) were very similar to those from Parish and Bromwich (1987), though with a larger along-coast component in coastal West Antarctica. Twenty years after the study of Parish and Bromwich (1987), the study was repeated using the Polar-optimized Mesoscale Model, Polar MM5. The results are remarkably similar to figure 1.2, showing the same general pattern and the same regions of convergence (Parish and Bromwich, 2007).

1.2.1 Directional constancy

The directional constancy of the surface wind in Antarctica indicates that katabatic winds are among the most persistent on Earth. The directional constancy (D) is defined by the ratio of the resultant wind speed (the vector mean) to the mean wind speed (the scalar mean):

$$D = \left(\frac{\overline{u}^2 + \overline{v}^2}{\overline{u^2 + v^2}} \right)^{1/2} \tag{1.1}$$

(King, 1989). A directional constancy of 1.0 means the wind direction is always the same, while a directional constancy of 0.0 means that there is no preferred wind direction at all. Parish (1982) calculated the directional constancy for historical sites in interior Antarctica, finding annual mean values above 0.8 for most sites. Wendler (1990) calculated the directional constancy for AWS stations in Adélie Land and found annual averages to be between 0.87 and 0.92, except at Dome C (annual average of 0.49) which is located at the top of the slope. According to Parish and Cassano (2003b), the mean monthly directional constancy for Antarctic surface winds typically exceeds 0.9 on all but the most gentle slopes. They find an annual averages of 0.96 for Cape Denison, with values in excess of 0.90 even during the afternoon in summertime. The directional constancy of the wind even during the summer is puzzling. In summer there is enhanced solar heating of the ice surface and thus no significant katabatic forcing. For this reason Parish and Cassano (2003a) state that the role of katabatic winds in Antarctica might be overemphasized, and suggest that the adjustment processes between the continental ice surface and the ambient pressure field are the primary cause of the Antarctic wind field.

1.2.2 Synoptic forcing

In the interior regions of Antarctica, the synoptic forcing is weak, since weather systems rarely develop or penetrate onto the high plateau. As a result, the katabatic winds in these regions are largely determined by local topography. In coastal regions however, cyclones occur, and synoptic forcing associated with these cyclones is likely to modify katabatic winds (King and Turner, 1997). Parish and Cassano (2003b) find that wind direction is a poor indicator of the katabatic nature of winds, as it can be forced either by the horizontal pressure gradient (arising from the general circulation), by blocking phenomena associated with cyclonic circulations, or by radiative cooling of the ice slopes ('pure' katabatic forcing). All these forces result in a terrain following wind, so it is impossible to state whether a flow is katabatically forced just by looking at the wind direction. This indicates the importance of the terrain in shaping the wind field, and also suggests that the term 'synoptic forcing' could be misleading (Parish and Cassano, 2001) since this force is also shaped by the terrain. Similar results were found by van den Broeke *et al.* (2002) and van Lipzig *et al.* (2004) who calculated the momentum budget of the Antarctic atmospheric surface layer. They found that especially over the more gentle inland slopes, the large-scale pressure gradient force can become equally important as the katabatic pressure gradient force. Renfrew and Anderson (2002) analysed surface observations from Coats Land and found the flow is purely katabatic 40-50% of the time, although it appears katabatic about 60-70% of the time. This confirms earlier findings that wind characteristics alone are not enough to determine whether the flow is primarely katabatically forced (by a downslope buoyancy forcing).

Synoptic forcing can influence the katabatic flow. Although strong flows with a katabatic signature commonly occur on the steep slopes in the interior near Casey, they rarely reach the coast, probably due to cold air damming. Adams (2005) found that under the right synoptic conditions, i.e. when a strong southwesterly jet develops over Casey, the synoptics can assist the katabatic wind in reaching the Casey station area. The relative importance of synoptic and katabatic forcing varies considerably from one coastal location to another (King and Turner, 1997).

1.2.3 Extreme katabatic winds

Two of the regions where the streamlines shown in figure 1.2 converge are Adélie Land (named Terre Adélie on the map in figure 1.1) and Terra Nova Bay (on the western coast of the Ross Sea). In East Antarctica, the strongest surface winds on Earth have been measured at coastal sites where katabatic winds persist for nearly 9 months per year (Parish, 1988). During Mawson's Antarctic Expedition in 1912-1913 an annual mean wind speed of 19.3 m s^{-1} was measured at Cape

Denison in Adélie Land, with monthly mean wind speeds never dropping below 12.9 m s^{-1} (Parish, 1981). In Terra Nova Bay, monthly mean wind speeds of 14-18 m s^{-1} have been measured (Bromwich, 1989). The slopes in these two areas are not steeper than in other parts of coastal Antarctica, but the topography causes negatively buoyant air from the high interior to be drawn to this area and then concentrated in a small section of the coastline, causing extremely strong katabatic winds (King and Turner, 1997). These exceptionally strong winds are localised phenomena, if they would occur all over Antarctica, the supply of cold, negatively buoyant air generated in the high interior by radiative cooling would be rapidly exhausted (King and Turner, 1997).

Parish (1982) used a simple diagnostic equation that involves motion, terrain slope and temperature inversion strength to obtain a reasonable picture of the time-averaged winter flow regime over East Antarctica. The streamlines obtained in this way show abnormally large cold air supply pools upslope from Cape Denison-Port Martin (in Adélie Land) and Terra Nova Bay. The same feature was found by Bromwich (1990), who used a three-dimensional primitive equation model to obtain physical insight into the mesoscale confluence feature at Terra Nova Bay. The results suggest a nearly unlimited cold air supply upslope that drains through only two glacier valleys, causing enhancement of the katabatic winds. The horizontal extent of the confluence zone found by Bromwich (1990) is smaller than the one found in Adélie Land, but the dynamical processes are similar: an inland confluence zone generated by local topography channeling an intense katabatic stream towards the coast (King and Turner, 1997). This explains the strongly time-dependent behaviour of katabatic flow along certain regions of coastal Antarctica: the episodic high-intensity katabatic surges correspond to the cyclical period of discharging of the cold air reservoir upslope.

1.2.4 The role of katabatic winds in the Antarctic climate system

Katabatic winds affect the redistribution of snow. In Antarctica, blowing snow plays a role in the overall mass balance of snow surfaces. It is estimated that on a continental scale, about 10% of the total net input of snow is removed by transport of snow into the sea (Giovinetto *et al.*, 1992; van Lipzig *et al.*, 2004). The main factors important for blowing snow are the topography and the surface wind field. Katabatic winds can cause blowing snow, but blowing snow can also play a role in forcing a katabatic flow. Drifting snow can increase the air density, and thus help to maintain the katabatic flow (King and Turner, 1997). Katabatic winds also play a role in the sublimation of blowing snow, which in turn affects the surface mass balance of Antarctica (Bintanja, 2001).

Katabatic winds interact with sea ice, and can form and maintain polynyas (areas of open water). Bromwich and Kurtz (1984) studied the Terra Nova Bay

polynya, a large (about 1000 km^2) polynya which is always present. It is formed by persistent katabatic winds, which advect bay ice eastward and prevent the ice from consolidating, in combination with the Drygalski Ice Tongue that prevents existing sea ice from drifting into Terra Nova Bay from the south. Another polynya, at the edge of the Ross Ice Shelf, is also influenced by katabatic winds. Under the right synoptic conditions, strong katabatic winds can cross the entire Ross Ice Shelf and play an important role in keeping the polynya open (Bromwich *et al.*, 1992, 1993). Polynyas influence the atmosphere, since the surface water temperature is much higher than the continent, and this temperature difference can cause a thermal wind that adds to the katabatic wind. This wind in turn helps keeping the polynya open (Adolphs and Wendler, 1995). The presence of open water has a large impact on the three-dimensional structure of the wind field near the coast (Heinemann, 1997). Polynyas contribute to the production of sea ice and the atmospheric energy balance, but also influence the oceanic circulation beneath ice shelves and thus the melting rate of the ice shelf.

On a larger scale, katabatic winds play a role in the general circulation over Antarctica. As the continental-scale katabatic flows transport consideral amounts of cold air northward, they modify the horizontal pressure field over the high southern latitudes and are a major feature of the mean meridional circulation (Parish *et al.*, 1994, 1997). The Antarctic orography and associated katabatic drainage play a primary role in two climatological features of Antarctica: the semi-annual oscillation of surface pressure over the interior and the circumpolar band of easterlies about the periphery (Parish *et al.*, 1994, 1997). The surface pressure over Antarctica shows seasonal changes of up to 20 hPa during the autumn and springtime transition periods. The mass transport by the drainage flow is likely the mechanism behind the pressure falls in autumn (Parish *et al.*, 1997). Parish and Bromwich (1998) analysed a case study where a pressure decrease of up to 20 hPa occurred over much of the Antarctic continent during a 4-day period in late June (midwinter) 1988. They found that this change accompanied intense cyclonic activity north of the ice sheet, with the equatorward mass transport redistributing the atmospheric pressure as far north as the subtropics of the Southern Hemisphere. This mass transport occurs mostly through the katabatic wind regime (Parish and Bromwich, 1998). Parish and Bromwich (1998) speculate that the katabatic wind pattern over Antarctica results in climatologically favoured positions for cyclones about the continent, which are fed by the cold, negatively buoyant air.

Katabatic winds can have far-reaching consequences, since changes in frequency or intensity of the katabatic surge over the ice shelf affects the mass balance of Antarctic ice sheets. This is rare for a mesoscale phenomenon (King and Turner, 1997).

Figure 1.3: The two wind turbines at the Australian Antarctic station Mawson. Photo courtesy of F. Olivier.

1.2.5 Katabatic winds as a power generator

The Australian Antarctic research base Mawson is the first station to use katabatic winds to generate power. In February 2003, two wind turbines were installed. Wind modelling indicated that 80% of the time over a full year, and 100% of the time over winter, conditions are suitable for running Mawson station without diesel fuel (Paterson, 2001). In the 2003 winter, the two turbines were generating up to 90% of Mawson's instantaneous electrical power. This results in fuel savings and lower greenhouse gas emissions (Paterson, 2003). Figure 1.3 shows the two wind turbines at Mawson.

1.3 Observations of katabatic wind in Polar regions

There is a general lack of observations at both Polar regions, because of the harsh environment. The earliest studies of katabatic flow used sastrugi patterns to derive climatological surface winds (Mather, 1969), or relied on manned observing stations. Instrumented observations can be problematic in Polar regions. Hoar and rime ice accumulation on instruments is often a problem. Rime ice is most common close to the coast where it forms through the freezing of supercooled water droplets from fog or low-level clouds (Anderson *et al.*, 2005). In a thick fog it can rapidly build up to a 10 cm depth. Hoar frost occurs when water freezes directly from the vapour phase when a structure (radiatively) cools down to below the local frost-point temperature (Anderson *et al.*, 2005). To avoid this, sensors should be heated and ventilated and this makes observations away from manned

stations very difficult. Equipment failure can also occur due to blowing snow or electrostatic discharges in blizzards (Anderson *et al.*, 2005). Erecting observation masts or towers on the ice of Antarctica is expensive and logistically challenging, and limited to low heights (typically 10-50 m) by construction considerations (Anderson *et al.*, 2005).

Most observational studies therefore use surface measurements and often take place during summer when access to remote locations is easier. Measurements of the vertical profile of katabatic winds are rare.

1.3.1 Automatic Weather Stations

Observational studies are often carried out using Automatic Weather Stations (AWS), as these are relatively easy to install even away from manned stations, and can provide observations of temperature, wind, pressure, and sometimes also snow accumulation or radiation. In Dronning Maud Land, 4 AWSs are placed along a traverse line from the Riiser-Larsen ice shelf up to the interior plateau, providing data averaged over 2 hours, and used in studies by van den Broeke *et al.* (2004, 2005). Bromwich (1989) describes the katabatic wind regime at Terra Nova Bay based on three years of AWS observations in that region. In Coats Land, a network of AWSs was installed from 1996 to 2003, providing hourly observations over the slope and ice shelf, from which Renfrew and Anderson (2002) derived the surface climatology of Coats Land.

The advantage of these kind of studies is that data is collected continuously, often over many years, and a climatology can be derived from the observations. AWSs only measure at the surface though, so no information about the vertical structure of katabatic winds can be derived.

1.3.2 Vertical profiles from kites and balloons

Sorbjan *et al.* (1986) used kites and balloons to obtain vertical profiles of the wind and temperatures in Adélie Land in January 1983 (summer). Profiles were taken every 6 hours. This resulted in vertical profiles of the wind vector and temperature, showing the development of a shallow but strong temperature inversion during the night which was destroyed during the day. However, only 22 profiles were obtained.

During the Austral summer of 1985, the IAGO (Interaction-Atmosphère-Glace-Océan) experiment collected vertical soundings (using kites, balloons and instrumented drones) in Adélie Land, to obtain a better description and understanding of the katabatic winds, and specifically to collect a dataset against which parameterised models of katabatic winds could be developed. Three teams took simultaneous measurements at three sites to monitor the time development of the katabatic flow as well as the stratification and the flow velocity (Pettré

and André, 1991). This large experiment resulted in a wealth of data, described by Wendler (1990) and Pettré and André (1991), and used as verification against model results by Pettré *et al.* (1990) (among others). The measurements were limited to summertime.

1.3.3 Instrumented aircraft

Some observational studies used instrumented aircraft, for example Parish and Bromwich (1989) and Gosink (1982), both in the area of the Ross Ice Shelf. These studies did not give any information on the vertical structure of the katabatic flow, as the aircraft flew at a constant level relative to the terrain.

The KABEG'97 (Katabatic wind and boundary-layer front experiment around Greenland) took place during April and May 1997 in Greenland, with surface stations at 5 positions on the ice shelf and in the tundra. Nine katabatic wind flights were carried out, with flight legs at different heights to obtain the three-dimensional structure of the katabatic flow (Heinemann, 1999, 2002; Heinemann and Klein, 2002; Heinemann, 2004). Even though there are a lot of similarities between Greenland and Antarctica, there are also important differences. Melting occurs at the ice surface of the Greenland ice sheet in summer, and the katabatic wind system in the melting zone is therefore not driven by radiational cooling of the snow surface, but instead by the daytime warming of the boundary layer over the tundra (Heinemann, 1999).

1.3.4 Vertical profiles from acoustic profilers

Sodar systems can measure data with high spatial and temporal resolution on a routine basis, are able to reach far above the region that meteorological towers can access and can operate unattended for long periods of time, making them very suitable for Antarctic studies.

In July 1991, a Doppler sodar and a RASS (Radio Acoustic Sounding System, measuring temperature profiles) were combined with a 30 m mast to measure profiles of wind and temperature over the Greenland ice sheet (Meesters *et al.*, 1997). This is in summer, when the surface is usually at the melting point.

In the Spring of 1992, a field program was carried out during one month at Siple Coast, a confluence area (see figure 1.2) on the Ross Ice Shelf. Apart from surface observations, remote sensing profilers, sodar and RASS were used to obtain a cross-sectional structure of the confluence zone (Bromwich and Liu, 1996; Liu and Bromwich, 1997).

In 1993, a three-axis Doppler sodar was installed at Dumont d'Urville, running continuously for two years (Pettré and Argentini, 2001). Reliable measurements were taken up to 900 m high all year long, except in summer when the noise ratio was increased due to the arrival of a large group of Adélie penguins

(Argentini *et al.*, 1996).

A Doppler Sodar was installed at the Russian Antarctic station Novolazarevskaya in Queen Maud Land during December 2006 and January 2007 over a deglaciated (rocky) area (oasis). This enabled Kouznetsov (2009) to analyse the vertical structure of nocturnal katabatic flow. However, this Doppler Sodar was a one-component version which only provides profiles of the vertical wind component, and measured during the summer in a rocky terrain which is not representative of most of Antarctica. This is the same area where a monostatic acoustic sounder was installed, at the Indian Antarctic base Maitri, together with a 28 m tower (Naithani and Dutta, 1995), to study the structure of the planetary boundary layer.

During 2002 and 2003, an autonomous Doppler sodar wind profiler was installed on the steepest part of the sloping ice shelf south of Halley in Coats Land, which resulted in over 2600 vertical profiles over a 2-year period, both in winter and in summer (Anderson *et al.*, 2005; Renfrew and Anderson, 2006). These measurements and the measurements from the Coats Land AWS network mentioned earlier will be used in this study and discussed in more detail later.

1.4 Modelling of katabatic wind in Polar regions

Due to the lack of observations of katabatic flow over Antarctica (and the Arctic), most of our understanding relies on numerical simulations. The first modelling studies were based on Ball (1956, 1957, 1959)'s work on Antarctic surface winds, for example the streamlines in figure 1.2 (from Parish and Bromwich (1987)) are obtained using the Ball model. This model describes the wind as a balance between the sloped-inversion pressure gradient force, the Coriolis force and friction.

Many model studies used idealised models to perform katabatic wind simulations. Gallée and Schayes (1992) used a hydrostatical model to study katabatic flow along idealised slopes representative of the Antarctic coast. Renfrew (2004) carried out idealised simulations of 'pure' katabatic flow using a high resolution mesoscale model, over an idealised slope representing Coats Land. The same setup was used by Yu *et al.* (2005) and Yu and Cai (2006) to study katabatic jumps in Coats Land. Parish and Cassano (2003b) used idealised numerical simulations so that they could prescribe a different pressure-gradient force over an idealised slope. Heinemann (1997) performed idealised simulations for similar reasons; to carry out sensitivity analyses on the effect of the presence of sea ice on the katabatic flow.

Other studies have focused on real case studies forced by realistic atmospheric flow. Bromwich *et al.* (2001) used the Polar version of MM5 to simulate katabatic winds over Greenland, just like Klein *et al.* (2001) who used the Norwegian

Limited Area Model over the same area and for the same period. Both studies used data collected during the KABEG'97 field study for verification. Davolio and Buzzi (2002) used a hydrostatic limited area model to study a summer katabatic event in Terra Nova Bay. Adams (2005) used the Australian Bureau of Meteorology's Antarctic Limited-Area Prediction System (ALAPS) to study events of strong southerly wind at Casey Station in East Antarctica.

1.5 This study

It is clear that katabatic winds play a crucial role in the surface wind regime of Antarctica. Due to the lack of observations over Antarctica, especially during the harsh winter, many katabatic studies rely on numerical modelling, often without observations to verify the model results. Numerical models are known to have difficulties simulating the meteorological processes in Antarctica because of problems in model physics, as described in for example Cullather *et al.* (1997), Hines *et al.* (1999) and Cassano *et al.* (2001). It is therefore important to verify the model results with observations other than global analyses. Due to logistical restriction, most observational studies take place during the Antarctic summer. Moreover, both observational and modelling studies tend to focus on the confluence regions (figure 1.2) with extreme katabatic flow, while most of coastal Antarctica is outside of these regions and receives more moderate katabatic flow.

In this study we will use high resolution numerical modelling to simulate case studies of katabatic flow over Coats Land, Antarctica. Coats Land has moderate slopes of about 5%, with moderate katabatic winds of 7.5 m/s on average (Renfrew and Anderson, 2002), which is typical for much of the Antarctic coast (outside of the confluence regions). As real case studies are used, the model results can be verified with observations. The available observations are from the AWS network over the slope of Coats Land, combined with rare profiles of katabatic flow observed by the Doppler Sodar located at the steepest part of the slope. The Doppler Sodar measured high resolution (both in time and space) three-dimensional wind profiles during both the summer and the winter season, which is very rare for Antarctica. The combination of this rare data with real case studies using a high resolution numerical model over a very typical area of coastal Antarctica is what makes this study unique. Having data to verify the model results also enables a thorough examination of the Atmospheric Boundary Layer (ABL) parameterisation scheme of the model, something which has not been presented before even though numerical models are known to have shortcomings in simulating meteorological processes over Antarctica. Finally, the dynamics of the katabatic flow are examined using the downslope momentum budget, which will give insight into the forcing of the katabatic flow.

Chapter 2 describes Coats Land and the available observations in more detail,

as well as the model simulations. Chapter 3 discusses the results of the model simulations compared to the observations for three different case studies: two winter cases and one summer case. Chapter 4 discusses the boundary layer parameterisation of the model including several sensitivity analyses for different boundary layer settings. Chapter 5 analyses the dynamics of katabatic flow in more detail using the momentum budget of the katabatic flow, and chapter 6 will summarize and discuss the conclusions from the previous chapters.

Chapter 2

Method

2.1 Method outline

This study uses a mesoscale model to study katabatic winds in Antarctica. First a study area was selected, see section 2.2. The model chosen to perform the simulations is discussed in section 2.3. Available observations (see section 2.4) were used to validate the model output for three selected case studies (see section 2.5). Sensitivity studies were also carried out on those case studies. After successful model validation, the model is then used to study certain aspects of the katabatic flow in greater detail.

2.2 Site selection

The area chosen for this study is Coats Land, Antarctica. Coats Land is a region on the eastern shore of the Weddell Sea, consisting of the Brunt Ice Shelf and the adjoining continent to the south. Figure 2.1 shows a map of the Coats Land region. The continental ice sheet flows towards the coast at about a few hundred metres per year. The topography of Coats Land is relatively two-dimensional, with moderate slopes, about 5% at most - typical for much of the Antarctic coast. This makes it a good region for studying moderate katabatic flow. Another reason for choosing this region is the location of Halley, a research station run year-round by the British Antarctic Survey. This research station provides observations which can be used to verify model results. Halley is located on the Brunt Ice Shelf, about 10 km from the coast (see figure 2.1). During 2002 and 2003, a Doppler Sodar was installed on the steepest part of the slope near Halley, to measure three-dimensional wind profiles. The available observations are discussed in more detail in section 2.4.

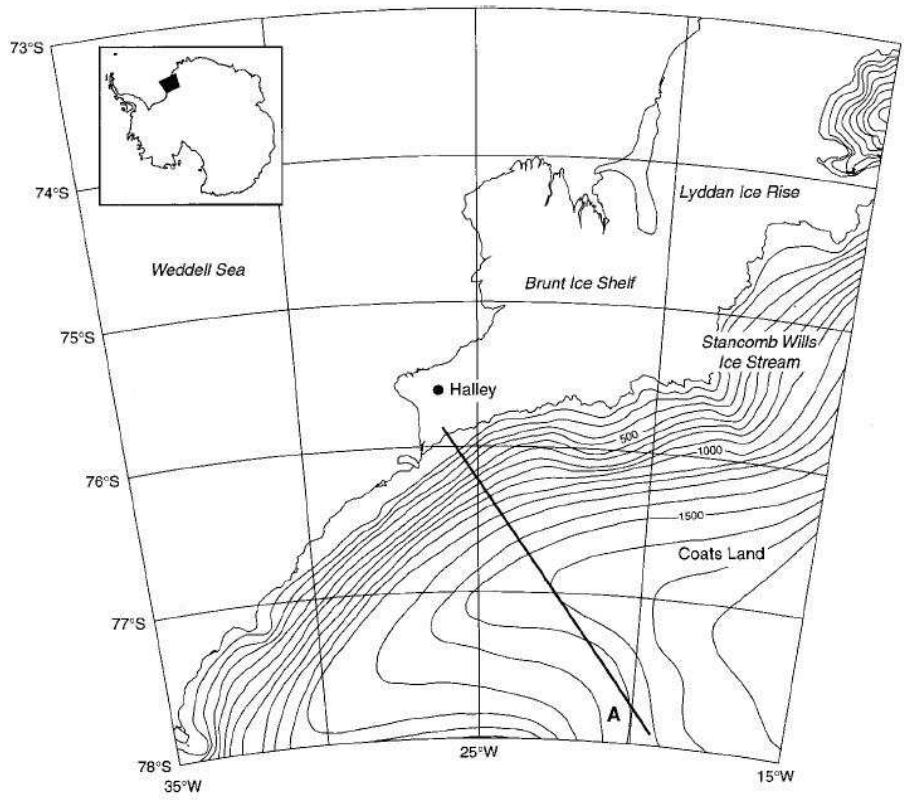

Figure 2.1: A map of the Coats Land region in Antarctica. The traverse marked as 'A' is the one by Peel (1976). Figure from King *et al.* (1998).

2.3 The Unified Model

2.3.1 Model description

Case studies are carried out using the U.K. Met. Office (UKMO) Unified Model (UM) version 6.1 (Cullen, 1993; Davies *et al.*, 2005). This model is used for operational forecasts (both globally and at higher resolution limited area configurations), climate modelling and for various environmental research applications. It can be used in atmosphere-only mode, ocean-only mode or coupled ocean-atmosphere mode. In this study, a limited area configuration of the atmosphere-only mesoscale model is used. The dynamical core of the UM uses a semi-implicit, semi-Lagrangian, predictor-corrector scheme to solve the non-hydrostatic, deep-atmosphere equations. The predictor step includes all the processes (including the physics) but approximates some of the (non-linear) terms. The corrector step then updates the approximate terms to achieve a more accurate solution. This allows the model to run at very high resolutions. Arakawa C-grid staggering is used in the horizontal. This means that the U component is east-west, staggered from temperatures and the V component is north-south staggered. In the vertical, the Charney-Phillips grid is used: potential temperature is on the same level as vertical velocity. This grid is terrain-following near the surface but evolving to constant height surfaces higher up.

Lateral boundary conditions are taken from larger scale model runs (starting from a global run). Figure 2.2 illustrates this schematically. The model uses a global start dump based either on UKMO or ECMWF operational data. The global dump can be reconfigured into a limited area start dump and higher resolution ancillary files can be incorporated into this limited area start dump. Ancillary files contain input data to replace or add to the start dump. Ancillary data can also be incorporated while the run progresses. This can be useful for the periodic updating of fields such as ozone concentration to allow for the effects of seasonal variations. In this way it is also possible to use higher resolution orography for example, or add missing fields to the start dump (monthly mean soil temperatures for example). Limited area domains use a rotated pole to ensure grid lengths over the domain are quasi-uniform.

The land surface scheme used is the UK Meteorological Office Surface Exchange Scheme (MOSES) version 2.2 (Essery *et al.*, 2001). This scheme calculates the surface energy balance at each point for up to nine different land surface types, which include five vegetation types. In Coats Land, the land surface type is permanent land ice. Snow masses and snow melt rates are calculated for each surface type in a grid box. The cold deep snow albedo over ice is set to a constant value of 0.8, but this is reduced to account for when the surface temperature exceeds -2 °C to represent snow aging (Essery *et al.*, 2001). The cloud scheme used is described in Smith (1990). It uses a statistical parameterisation method. The

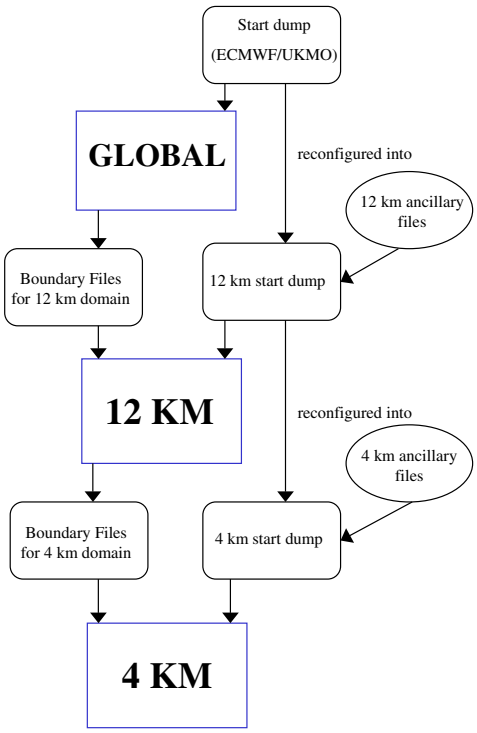

Figure 2.2: Diagram showing the sequence of model runs from global to 4 km, including the input and output of each run.

precipitation scheme by Wilson and Ballard (1999) contains a full microphysical calculation of the cloud phase and generation of precipitation with water vapour, cloud liquid water and ice particle content as prognostic variables. Microphysical processes are treated as transfer terms between water vapour, liquid, ice, and rain. 'Ice' is used to describe all frozen water in large-scale clouds, including aggregated snow, pristine ice crystals and rimed particles. Ice is advected around the model domain using the model's positive semi-definite advection scheme. It is also mixed within the boundary layer by a tracer-mixing scheme. No direct coupling occurs between the large-scale cloud and precipitation schemes and the convection scheme (Wilson and Ballard, 1999). There are some differences in the choice of precipitation scheme for each domain in the setup used in this thesis. The global domain uses the originally recommended mixed-phase precipitation scheme described above (by Wilson and Ballard (1999)), while the 12 km domain uses a scheme based on the one used in the global domain but containing improvements in the specification of the microphysics and the subgrid-scale parameterization. This scheme diagnostically determines the fraction of cloud ice content that is pristine ice crystals and snow aggregate particles and treats the two categories separately in the microphysical transfer terms. The 4km domain uses a scheme which contains the same physics as the scheme used in the 12

km domain but this scheme has adjusted numerics and includes cloud fraction changes. This scheme also includes prognostic rain, which allows the model to advect rain with the 3-dimensional wind field, rather than rely on the assumption of equilibrium within a model grid column (diagnostic representation). The liquid cloud mixing ratio is passed on to nested domains through the lateral boundary files. The radiation scheme treats both long wave and short wave spectral regions within a common flexible framework, as far as possible. Convective and stratiform clouds, and water droplets and ice crystals within clouds are all treated separately. More details can be found in Ingram *et al.* (2004). An earlier version of the convection scheme is described in Gregory and Rowntree (1999). This scheme is used for both precipitating and non-precipitating convection. The triggering of convection in this scheme is determined by the diagnosis scheme used to classify boundary-layer types. Where the cumulus-capped boundary layer is diagnosed, cumulus convection is classified as precipitating or non-precipitating according to the diagnosed depth. The boundary layer parameterisation and the boundary layer types will be discussed in more detail in the next section.

2.3.2 Boundary layer parameterisation

The parameterisation of the boundary layer in the UM is split in two parts based on the stability of the boundary layer (Lock *et al.*, 2000). In the unstable boundary layer, a K-profile closure with explicit entrainment parameterisation at the boundary layer top is used. In the case of a stable boundary layer, a local scheme is used that depends on stability via the Richardson number (Brown *et al.*, 2008). In this study, we focus on the parameterisation for the stable boundary layer as the boundary layer over Coats Land is hardly ever unstable.

The default boundary layer scheme in the UM is the Richardson number based scheme. It is based on the scheme described by Holtslag and Boville (1993), a non-local diffusion scheme that determines an eddy-diffusivity profile based on a diagnosed boundary-layer height and a turbulent velocity scale while incorporating non-local (vertical) transport effects for heat and moisture. This scheme was extended by van Meijgaard and van Ulden (1998) to allow for mixing driven by radiative cooling at the top of a stratocumulus cloud top. It combines non-locally determined eddy-diffusivity profiles with an explicit parameterisation for entrainment. It uses moist conserved thermodynamic variables, which enables the scheme to treat both dry and cloudy boundary layers in the same way (Lock *et al.*, 2000).

The basis of the scheme is the identification of unstable layers based on the buoyancy of parcels lifted from the surface and lowered from the top of clouds. The six different boundary layer types distinguished by the model are shown in figure 2.3. The model also distinguishes between well-mixed unstable layers and those in which cumulus convection is present. This is done so that different

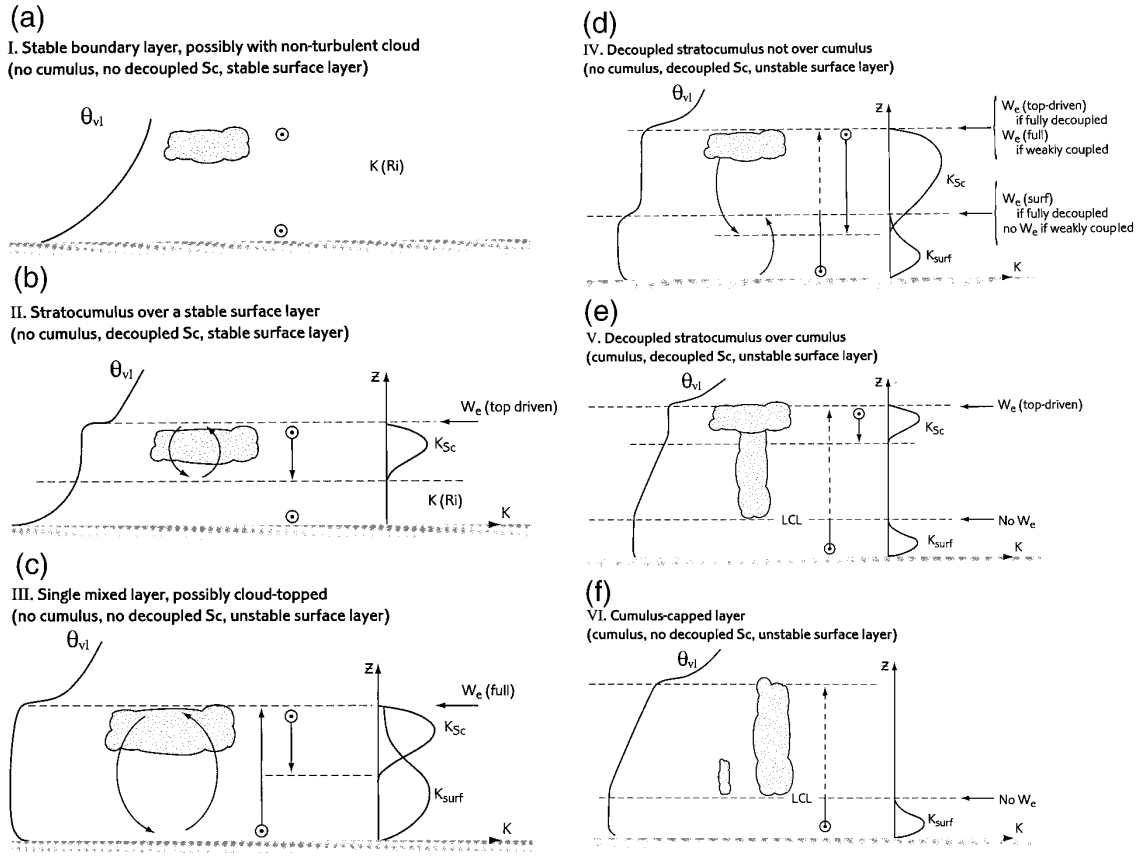

Figure 2.3: Schematic representation of the six boundary layer types, from Lock *et al.* (2000).

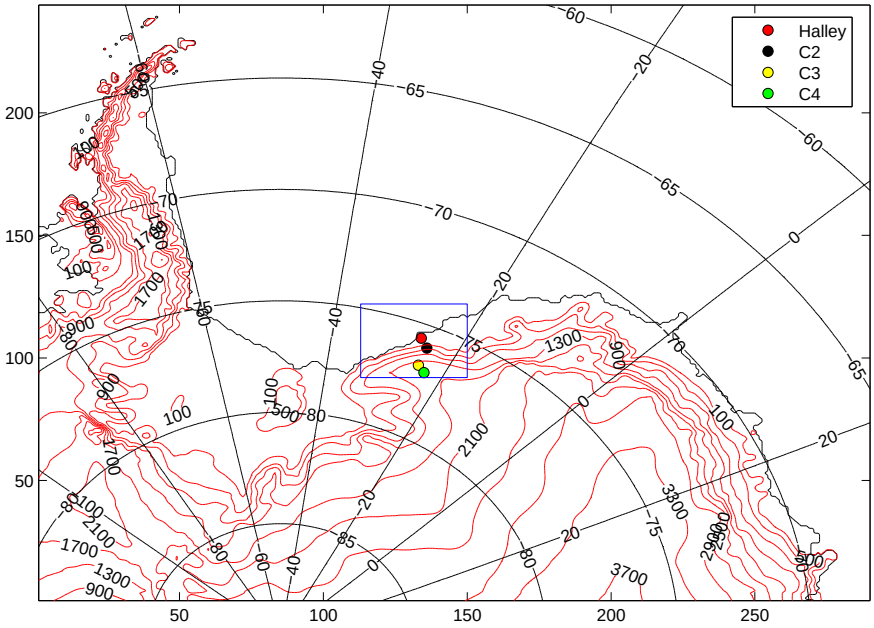

Figure 2.4: The outer domain, with a resolution of 0.11°(approximately 12 km), with outlined in blue the inner one-way nested domain with a resolution of 0.036°(approximately 4 km). The x and y axis shows the number of grid points of the outer domain, and the locations of Halley and C2-C4 are indicated. Orography is contoured (in red) every 400 m (starting at 100 m).

mixing schemes can be used in different types of unstable layers. For well-mixed layers, the flux parameterisation scheme used is based on the one described in Holtslag and Boville (1993) but extended to allow for the effects of turbulence driven from the cloud top as well as from the surface (Lock *et al.*, 2000). In cumulus layers, a mass convection scheme by Gregory and Rowntree (1990) is used.

The default stability function is the 'long-tailed' form. Several alternative options for the stability functions, as well as an alternative boundary layer scheme are available in the UM. The alternative options are discussed in more detail in chapter 4, on the parameterisation of the boundary layer.

2.3.3 Model setup

Two model domains are used via one-way nesting. The outer domain has a resolution of 0.11°(approximately 12 km), 244 x 290 grid points and 38 vertical levels, and covers a large part of the Antarctic continent including the peninsula (figure 2.4). A second (one-way nested) domain with a resolution of 0.036°(approximately 4 km), 114 x 92 grid points and 76 vertical levels covers Coats Land. Figure 2.4 shows the location of both domains. The 12 km domain will be used for analysing the synoptic situation, while the 4 km domain will be

used for analysing the smaller scale and for comparison with observations.

The orography in the Unified Model comes from the Global Land One-km Base Elevation (GLOBE) data set. Within this data set, the Antarctic Digital Database (ADD) dataset from 1993 is used over Antarctica. The ADD from 1993 has since been superceded by much improved high resolution elevation data, with much more satellite-derived data included. As the slope is an important factor in katabatic wind studies, a good representation of the orography is essential. Therefore the default UM orography was replaced by the high-resolution Radarsat Antarctic Mapping Project (RAMP) Digital Elevation Model (DEM) dataset that has a nominal resolution of 1 km. Figure 2.5 shows the orography over the 4 km domain from both the new dataset and the default UM orography. The DEM dataset shows a steeper part of the Coats Land slope around the location of C2, while the orography from the UM shows a homogeneous gradient. Figure 2.6 shows a cross-section along the slope over the traverse measured by Peel (1976), as compared to the default orography from the UM and the improved orography based on the DEM dataset. The elevations of the original traverse are accurate to about $\pm$ 20 m, and were measured using several altimeters with distance tracked by a revolution counter fitted to the vehicles, corrected to fit astronomically fixed control points (Peel, 1976). The default UM orography again shows a very homogeneous slope. The orography from the DEM dataset shows a much improved profile, with steeper slopes around C2. It is important to have a good representation especially in this area as C2 is the location of the Doppler Sodar. Higher up the slope, both UM profiles do not match the Peel traverse very well. Both UM profiles are up to 200 m lower than the Peel traverse and also show a less steep slope. This shows how difficult it is to obtain a good representation of orography in Antarctica. The elevations from Peel (1976) are obtained using barometric levelling which is not particularly accurate, but elevation measurement by satellites (used in the DEM dataset) also have problems, especially in regions with steep slopes.

2.4 Observations

2.4.1 Halley Research Station

Halley Research Station is operated year-round by the British Antarctic Survey. The meteorological observing station gives hourly observations of pressure, wind (measured by a cup-vane anemometer at a height of 4m, checked daily for rime build up), temperature and humidity (both measured by Vaisala HMP35A sensors in a R. M. Young force-ventilated radiation shield, at a height of 2 and 4m) (Renfrew and Anderson, 2002). Synoptic observations (like cloud cover) are gathered every three hours, and a radiosonde is launched once a day. A 32 m high mast measures temperature, wind and humidity at six different heights (1, 2, 4,

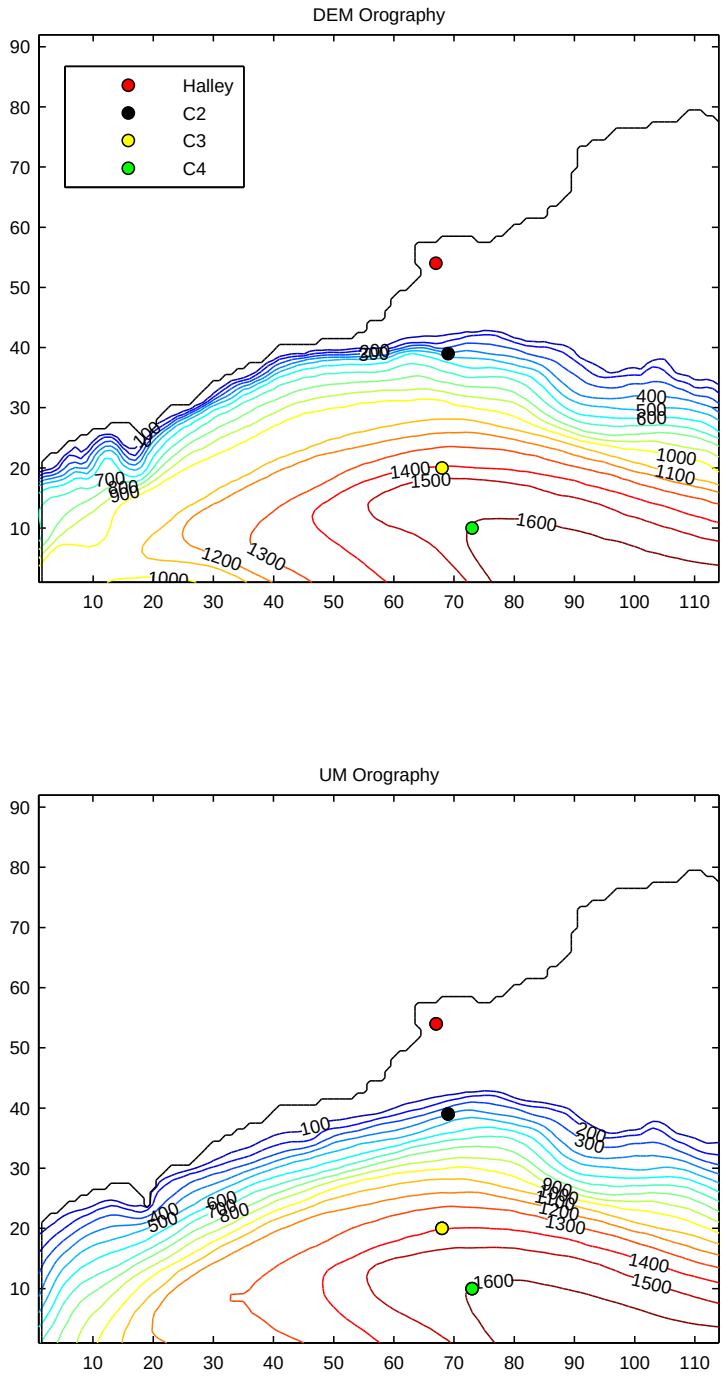

Figure 2.5: The orography from the Digital Elevation Model (top, shown here at 4km resolution) and the default orography used in the UM (bottom) over the 4km domain. The locations of Halley and the Automatic Weather Stations C2-C4 (see section 2.4) are indicated.

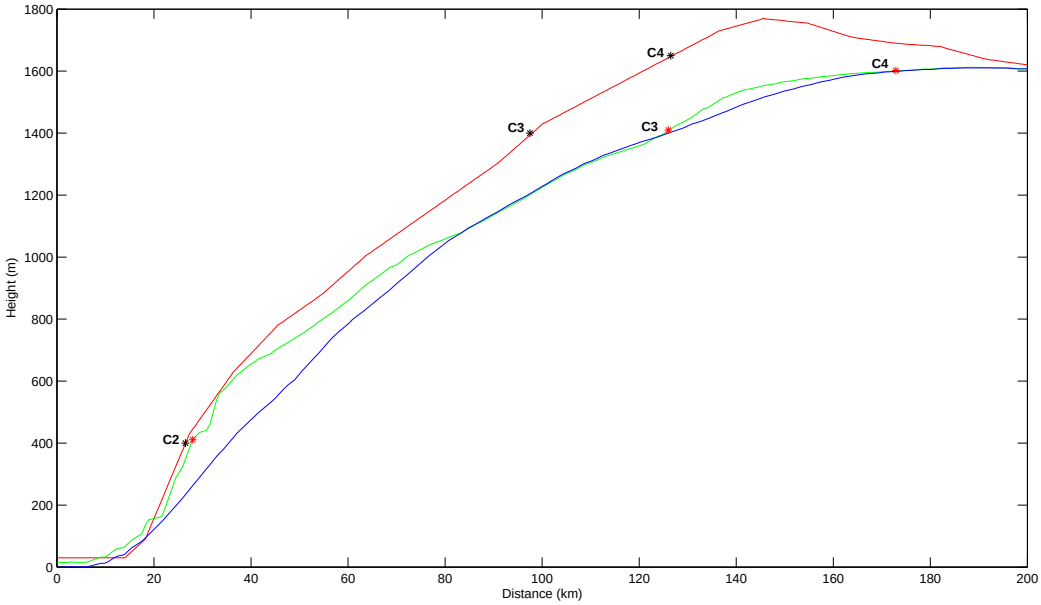

Figure 2.6: A topographic section along the traverse by Peel (1976) (in red), compared to the default UM orography (in blue) and the improved UM orography (in green). See figure 2.1 for the location of this traverse. The locations of C2, C3 and C4 are indicated by a black asterisk on Peel's traverse while their chosen locations on the improved UM orography are indicated by a red asterisk.

8, 16 and 32m) from 2003 onwards, available as 10-minute averages. Radiation data (short wave and long wave) are also available as 10-minute averages, from 2003 onwards. More details on observations at Halley can be found in King and Anderson (1994).

2.4.2 Automatic Weather Stations

From 1996 to 2003 a network of Automatic Weather Stations (AWS's) recorded hourly observations in Coats Land, on the slope near Halley research station: C1 - C4. C1 was located at the bottom of the slope (37 km from Halley research station), the so-called hinge zone: the area where the ice sheet leaves the land

Station	Latitude	Longitude	Height (m)	Slope (%)	Fall line	Distance from Halley (km)
Halley	-75.60	-26.20	37	0.07	155	0
C1	-75.88	-25.49	43	0.7	160	37
C2	-75.96	-25.41	400	5.5	165	46
C3	-76.70	-24.53	1400	1	150	132
C4	-76.81	-23.50	1650	0.8	145	155

Table 2.1: Geographical data for Halley and the Coats Land Automatic Weather Stations C1-C4, from Renfrew and Anderson (2002)

and starts to float on the ocean. This area is heavily crevassed though at C1 itself it is relatively flat and undisturbed. C2 was located at the steepest part of the slope, 10 km from C1. C3 and C4 were located further up the slope. C1 was only employed until 1997 and will not be used in this study. Table 2.1 summarizes the details of the Coats Land AWS's and Halley research station. Note that locations are approximate, as the ice sheet moves towards the coast.

The AWS's measured air temperatures and humidity at two heights: 1 m and 2.5 m, using Vaisala HMP35D sensors (using 1/30 DIN platinum resistance thermometers and solid state capacitive humidity sensors) housed in a modified R. M. Young naturally ventilated shield. Ventilation is assisted by an internal solar-powered fan during periods of strong insolation (Renfrew and Anderson, 2002). The temperature data are calibrated each year, for each AWS separately, see Renfrew and Anderson (2002) for full details. Post-calibration of the relative humidity measurements is carried out for each year of data and for each sensor using the method of Anderson (1994). Wind speed and direction are measured at a height of 3m, by a R. M. Young propeller-vane anemometer. This design was found to have fewer problems with becoming frozen into position (Renfrew and Anderson, 2002). The pressure sensor is calibrated each year against a Vaisala PA11 digital barometer (calibrated annually by the UK Met Office calibration laboratory) (Renfrew and Anderson, 2002).

In order to compare the observations from the AWS's with the model results, their location needs to be found within the model domain. Simply matching their latitude/longitude location does not give the correct heights, a problem illustrated in figure 2.6. For the katabatic wind simulations, the location (in height and steepness) on the slope is more important than the exact latitude/longitude location, therefore the locations of the AWS's were chosen by finding their height on the slope. This is demonstrated in figure 2.6. The black asterisks on the traverse measured by Peel (1976) (the red line) are believed to be the 'true' locations of the AWS's. The red asterisks on the improved UM orography (the green line) are their locations in the UM as used in this thesis. This is most problematic for C4, as the orography used in the UM does not reach up to its height of 1650 m. C4 had to be placed near the top of the UM slope, which is not ideal as the slope is not as steep there. The location of C4 in the model is also quite close to the edge of the model domain. Unfortunately it was not possible to enlarge the domain as it can be difficult to select a stable domain in the UM, especially when the edges of the domain are over orography.

2.4.3 Doppler Sodar Wind Profiling System

During 2002 and 2003, an autonomous Doppler Sodar wind profiling system was deployed at the site of C2. The soundings obtained from this profiler are the first remote wintertime wind profiles of katabatic flow in Antarctica. It is very

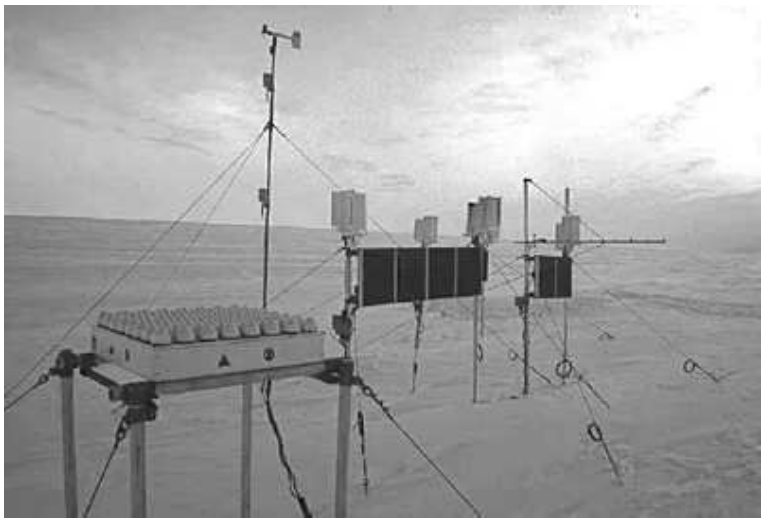

Figure 2.7: Photograph of the Doppler sodar wind profiler. The actual profiler is visible in the foreground (on the left), in the background the solar panels, wind generators, radio antenna and AWS mast are visible. Photo courtesy Ian Renfrew.

challenging to obtain such profiles in Antarctica, due to its remoteness (difficult access, high costs for logistical support), difficult environment (ice sheets), low temperatures, low humidity, high wind speeds, and problems like blowing snow, hoar and rime ice accumulation and electrostatic discharges in blizzards (Anderson *et al.*, 2005). Doppler radar profilers do not have high enough resolution for studying the shallow katabatic flow, and systems based on automatic launching of weather balloons do not give continuous profiles and are difficult to maintain (Anderson *et al.*, 2005). A Doppler Sodar wind profiler does have high enough resolution and can remotely obtain continuous wind profiles. The main disadvantage is the amount of power this system needs.

The Doppler Sodar wind profiler used a Scintec flat-array sodar (FAS64). This sodar works by transmitting acoustic pulses into the atmosphere and detecting the Doppler shift in the backscatter signal. It is then possible to calculate the wind profile in three dimensions. The system was powered by (heated) batteries charged by solar panels and (vertical axis) wind generators. For full details on design, build, testing and deployment of this system see Anderson *et al.* (2005). Figure 2.7 shows a photo of the Doppler Sodar. For a description and analysis of the collected data see Renfrew and Anderson (2006).

The system was switched on remotely, from Halley research station, by radio link. This radio link also transmitted data from the AWS, to help decide whether to switch on the system based on meteorological conditions. Most sounding periods lasted about 12-48 hrs. The height range of the three-dimensional wind profiles was typically 100-300 m (after quality control). This range is less than

the expected 500 m, a limitation caused by the strongly stable boundary layer at this site, which leads to a highly stratified flow with very little turbulence (King and Turner, 1997). This will reduce the acoustic backscatter of the system and thus the height range of the wind profiles (Anderson *et al.*, 2005). During the 2 years of operation, about 30 generally high quality sounding periods were obtained.

2.4.4 Satellite images

Satellite images are available several times a day, and will be used for analysing the cloud fields during the model simulation. These satellite images are obtained from a satellite receiver (ARIES: Antarctic Reception of Imagery for Environmental Studies) for the NOAA High Resolution Picture Transmission (HRPT) data stream from the NOAA series of Polar orbiting weather satellites. The receiver is based at Rothera Station, a British Antarctic Survey base on the Antarctic peninsula.

2.5 Case studies

The case studies have been selected based on the availability of high quality Doppler Sodar data. Three case studies were selected: two Antarctic winter cases and one Antarctic summer case. These case studies will be used for a comparison with observations, sensitivity experiments (mostly focused on the boundary layer parameterisation) and for studying the dynamics of the katabatic flow. The three case studies and the results of the model simulations will be discussed in the next chapter.

Chapter 3

Model Results

3.1 Introduction

This chapter describes the model results for three case studies: two winter cases (August 2003 and September 2002) and a summer case (February 2002). The model results are compared to the available observations. For the large scale comparison, results from the 12km simulation are used. This domain has 38 vertical levels, and uses the default Richardson-number based boundary-layer scheme with the SHARPEST stability function. For all other comparisons, results from the 4km domain are used. This domain has 76 levels, uses the default Richardson number based boundary-layer scheme and the default long-tailed stability function (see chapter 2 for a detailed description of the model settings). Sensitivity experiments with different model settings will be discussed in the next chapter. A short description of each case study will be given now, while the remainder of this chapter will discuss the results of the three case studies as compared to observations.

3.1.1 Winter case study 1: August 2003

This case study focuses on 14 August 2003, when Doppler profiles are available every 15 minutes between 10:30 and 16:00. The observed katabatic flow is clear but weak. It is cloudy over the Brunt Ice Shelf most of the time. A low pressure area to the north influences the katabatic flow especially higher up the slope. This case study is also discussed in Renfrew and Anderson (2006).

The model runs from an UKMO start dump of the 13th of August 09 UTC (derived from a model run started at 06 UTC, so three hours into the simulation). The 12 km domain runs for 48 hours, and the 4 km domain for 36 hours.

3.1.2 Winter case study 2: September 2002

This case study focuses on 4 September 2002. Doppler profiles are available for five hours, between 14:30 and 19:30, with a typical height range of 150 m and

showing southerly katabatic winds during the last two hours. It is cloudy for the first part of the day and then it clears up.

The model is run from an UKMO start dump of the 3rd of September at 09 UTC (derived from a model simulation that started at 06 UTC, so three hours into the simulation). The 12 km domain simulation is run for 48 hours, while the 4 km domain is run for 36 hours.

3.1.3 Summer case study: February 2002

This case study spans four days: 21-24 February 2002. This is in the Antarctic summertime, when the diurnal cycle of solar radiation will influence the katabatic flow (see for example Parish *et al.* (1993b) and Renfrew and Anderson (2006)). The background synoptic flow is weak during these four days, and hardly influences the katabatic flow (Renfrew and Anderson, 2006). The skies are mostly clear, so the diurnal signal is strong. Doppler profiles are available every 15 minutes starting at the 21st of February 21:45, with a height range of about 200 m. The availability of good quality profiles and the fact that there are hardly any synoptic influences make it an ideal summertime case study. This case study has also been described briefly in Renfrew and Anderson (2006).

Model runs are carried out for 48 hours from an ECMWF start dump from the 21st of February 00 UTC, followed by another 48 hours simulation from an ECMWF start dump of the 23rd of February. This is done because after about 48-72 hours the model results start to significantly drift away from the observed situation.

3.2 Winter case 1: August 2003

3.2.1 Large scale

Figures 3.1 and 3.2 show the geopotential height at 500 mb over the 12km domain at 12 UTC for 13 and 14 August 2003, for both the model results and from ECMWF operational reanalysis data. Coats Land is in between two areas of low geopotential height, one to the north and one to the south. The geopotential height from the model is in good agreement with the reanalysis, though the model slightly overestimates the geopotential height. The overall pattern is well represented by the model. The absolute domain-averaged error for the geopotential height at 500 mb ranges from 12.3 m at the beginning of the model run to 24.5 m at the end of the model run.

Figures 3.3 and 3.4 are similar to figures 3.1 and 3.2 but show the mean sea level pressure. A low pressure area moves towards the east over the sea north of Coats Land. Over land, the differences in mean sea level pressure between the model and the ECMWF Reanalysis are larger. Over orography, the pressure at

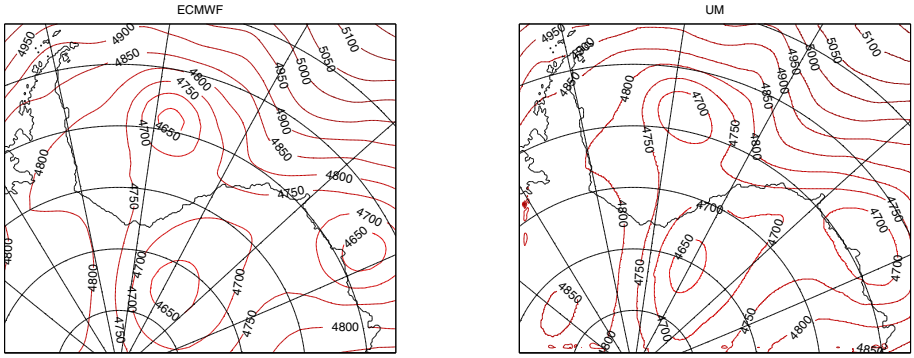

Figure 3.1: Geopotential height at 500 mb (in metres) at 12 UTC 13 August 2003 (T+3), from the ECMWF Reanalysis (left panel) and from the model run (right panel).

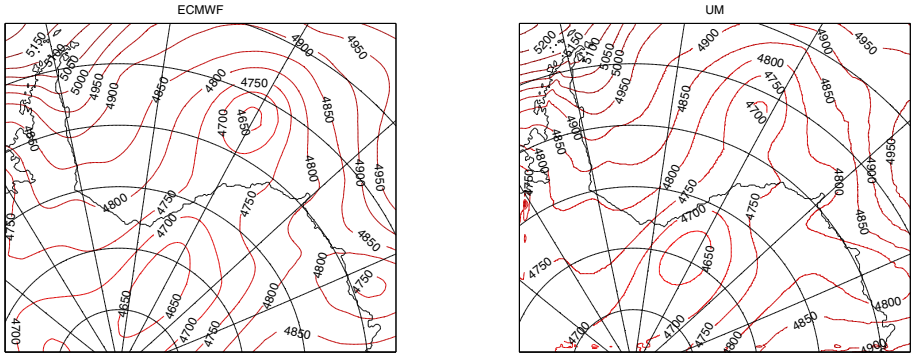

Figure 3.2: Geopotential height at 500 mb (in metres) at 12 UTC 14 August 2003 (T+27), from the ECMWF Reanalysis (left panel) and from the model run (right panel).

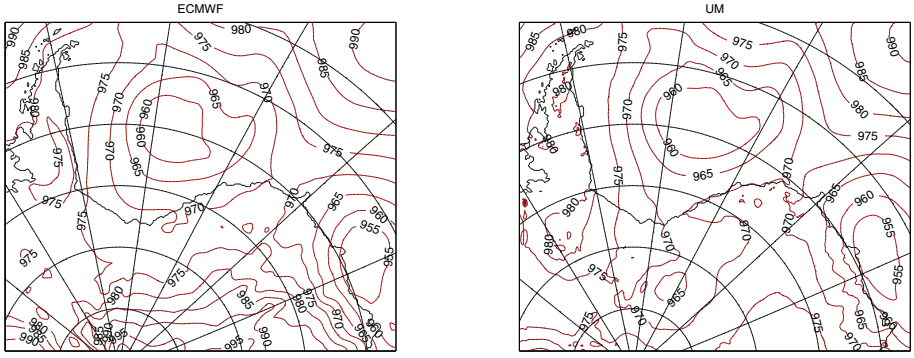

Figure 3.3: Mean Sea Level Pressure (in mb) at 12 UTC 13 August 2003 (T+3), from the ECMWF Reanalysis (left panel) and from the model run (right panel).

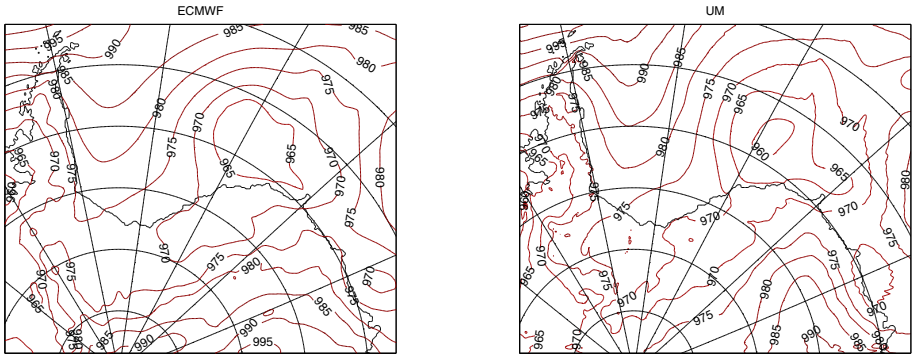

Figure 3.4: Mean Sea Level Pressure (in mb) at 12 UTC 14 August 2003 (T+27), from the ECMWF Reanalysis (left panel) and from the model run (right panel).

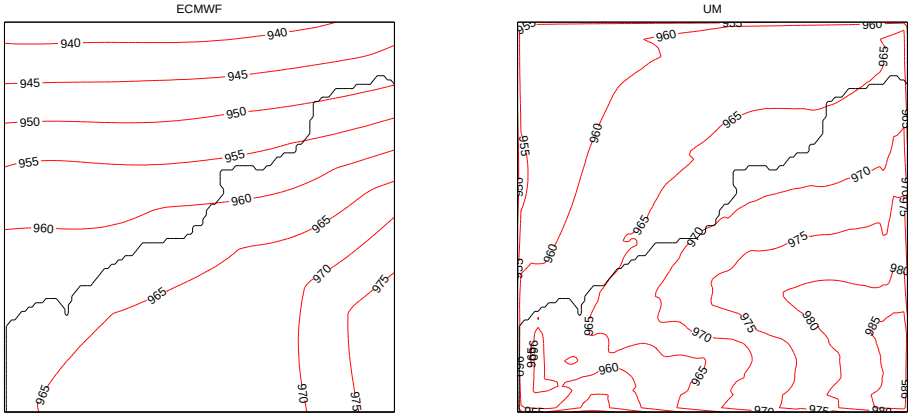

Figure 3.5: Geopotential height at 850 mb (in metres) at 12 UTC 13 August 2003 (T+3), from the ECMWF Reanalysis (left panel) and from the model 4 km run (right panel).

sea level is calculated by reducing the surface pressure to mean sea level using the temperature at the surface and assuming a constant lapse rate. As this calculation requires several variables which could have different values in both models, the differences over orography will naturally be larger than over sea. The orography will also differ between both models, and the ECMWF has a much coarser resolution (1 degree) compared to the UM (0.11 degree), so the orography in the ECMWF Reanalysis will be smoother. Over sea, the mean sea level pressure is represented well by the model. At 12 UTC on 14 August (T+27h) the model starts to differ more from the ECMWF Reanalysis, but the overall pattern is still reasonably well represented. The absolute domain-averaged error for the mean sea level pressure over sea ranges from 0.97 mb at the beginning of the run to 2.0 mb at the end of the run.

The large scale synoptic situation looks reasonably well represented by the model (in the 12 km domain), but it is important that the synoptic situation on

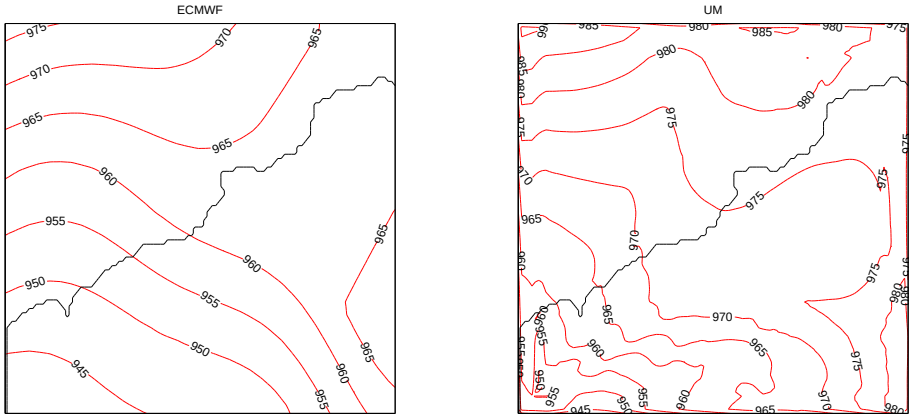

Figure 3.6: Geopotential height at 850 mb (in metres) at 12 UTC 14 August 2003 (T+27), from the ECMWF Reanalysis (left panel) and from the model 4 km run (right panel).

the smaller scale is also well represented. The 4 km domain will be used for all further comparisons with observations. Figures 3.5 and 3.6 show the geopotential height at 850 mb over the 4km domain at 12 UTC for 13 and 14 August, for both the model results (from the 4 km model run) and from ECMWF operational reanalysis data. It is important to realise that the ECMWF data has been interpolated onto the 4 km grid, from its original resolution of 1 degree (about 110 km). The 4 km domain is thus only covered by about 3 x 4 gridpoints from the ECMWF reanalysis. Figures 3.5 and 3.6 shows more clearly that the model overestimates the geopotential height as compared to the ECMWF reanalysis. At 12 UTC on 13 August (figure 3.5), the ECMWF reanalysis shows the largest gradient in geopotential height over sea and the smallest over land, while this is opposite in the UM. A day later (figure 3.6), the model and the ECMWF reanalysis show a more similar patter.

3.2.2 AWS comparison

Figure 3.7 shows the perturbation from the time-mean surface pressure (p') from the model and from AWS observations. It is not possible to compare the surface pressure from the model and from AWS observations directly, as the exact heights of the AWS's are not known precisely as they were not well surveyed. Using the perturbation from the mean pressure is a way to get around this problem as this reflects the trend in surface pressure regardless of the actual height. The model shows the same general trend as the observations: a slight decrease of the pressure for the first 24 hours followed by an increase in pressure. The extent of the decrease and increase is smaller in the model as compared to observations. In addition the rate of change of pressure is lower towards the end of the simulation period. In other words, the model appears less sensitive to pressure changes than

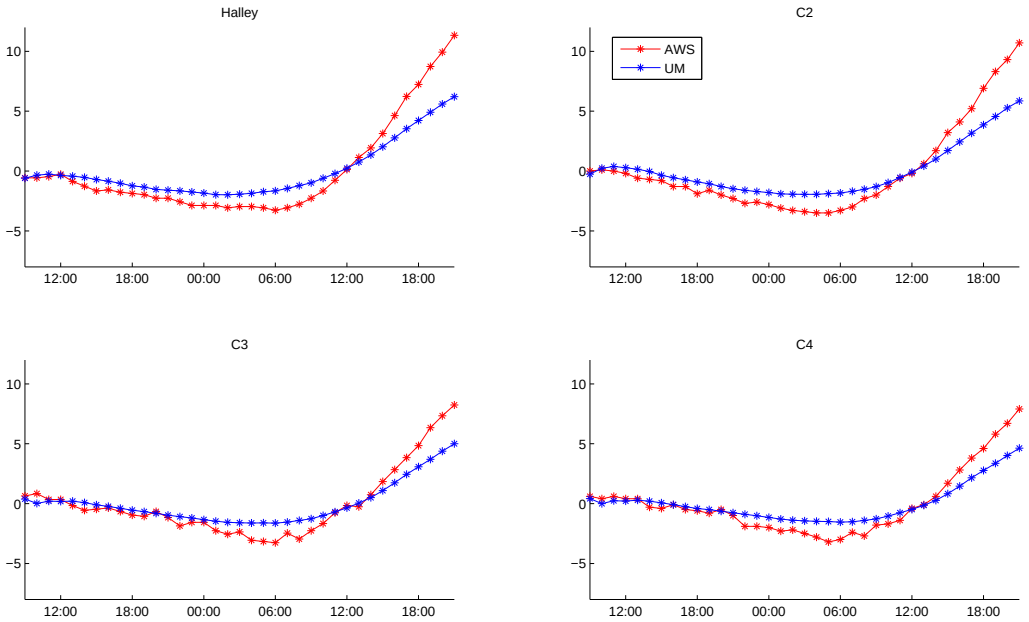

Figure 3.7: Perturbation from the mean (over 36 hours) surface pressure (mb) for 13 and 14 of August 2003, from the model (in blue) and from AWS observations (in red).

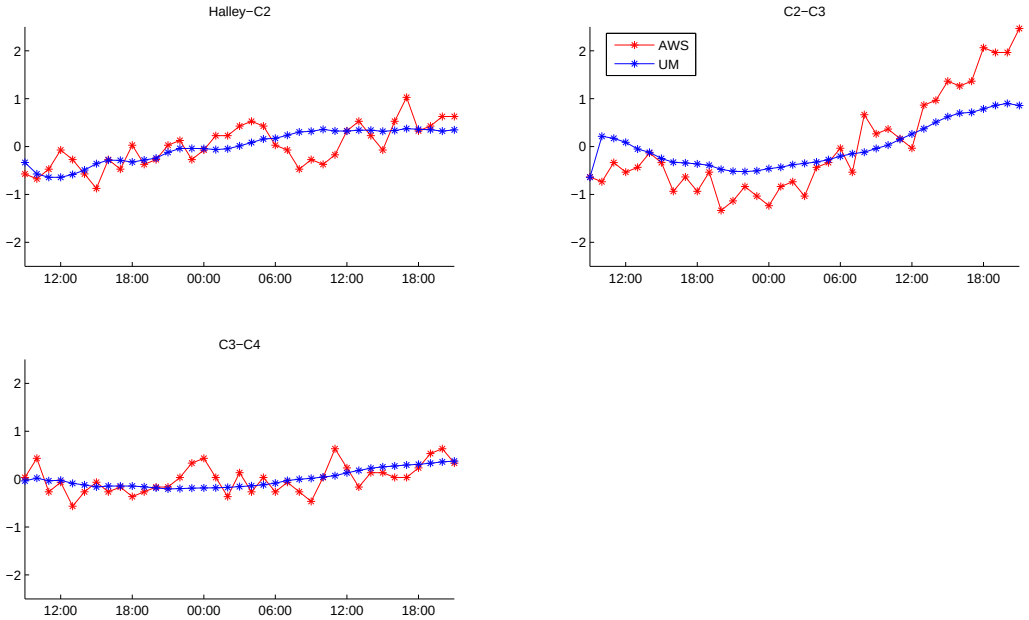

Figure 3.8: Perturbation from the mean (over 36 hours) difference in surface pressure (mb) between Halley and C2 (top left), C2 and C3 (top right) and C3 and C4 (bottom left), from the model (in blue) and from observations (in red), for 13 and 14 August 2003.

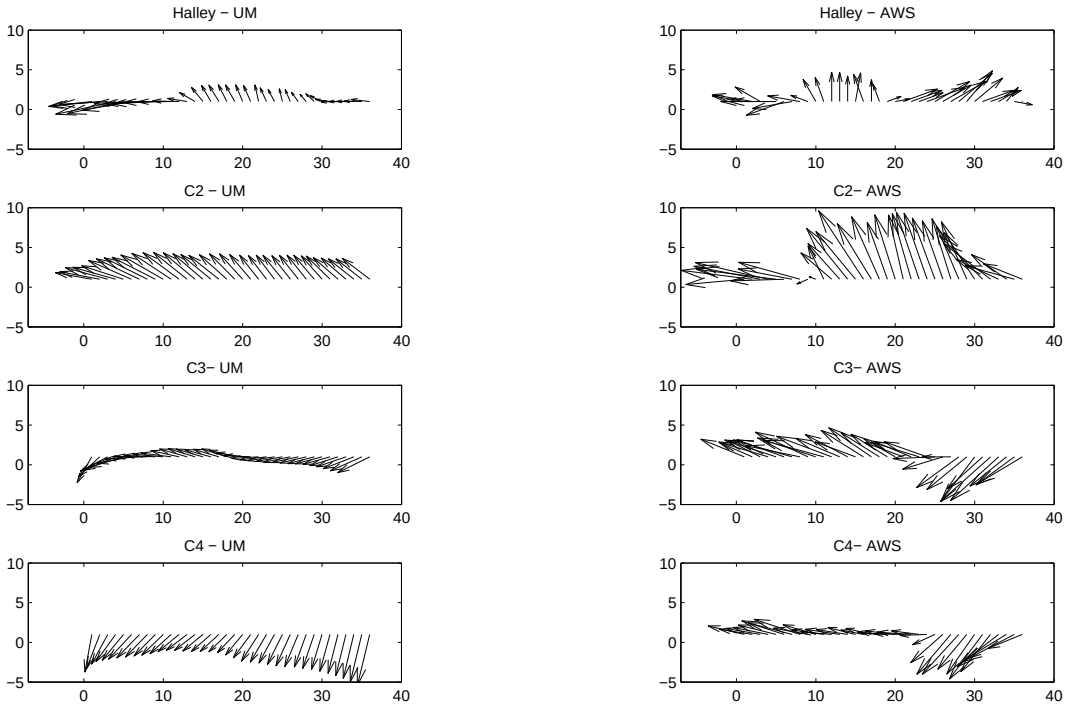

Figure 3.9: Wind vectors from the model (on the left) and from AWS observations (on the right). The x-axis shows hours from the 09 UTC 13 of August 2003. The y-axis points North.

the observations suggest it should be. Figure 3.8 shows the perturbation from the mean differences in surface pressure between two observation locations, i.e. the gradient in p'. For the Halley-C2 and the C3-C4 pairs, the model compares quite well to the observations. For the C2-C3 pair the model predicts a much lower mean difference then is observed. This means that the model underestimates the perturbation pressure gradient between these two locations. From figures 3.3 and 3.4 it is hard to tell if this is also the case in the mean sea level pressure field over the 12km domain due to the lower resolution used. Calculating the perturbation from the mean differences between the observation pairs in a similar way but over the 12 km domain (not shown) reveals the same pattern however: the model compares very well to the ECMWF Reanalysis for the Halley-C2 and C4-C3 pair, but for the C2-C3 pair the model mostly underestimates the mean pressure difference, and thus the pressure gradient between C2 and C3.

Figure 3.9 shows wind vectors for both the model and observations. In general, wind directions are reasonable well represented but the model does not show sudden changes in wind direction like the observations do (for example at 25 hours into the model run at C3 and C4). Wind speeds are mostly underestimated by the model, especially at C2 and C3. A possible explanation for this underestimation is the fact that the model underestimates the pressure difference

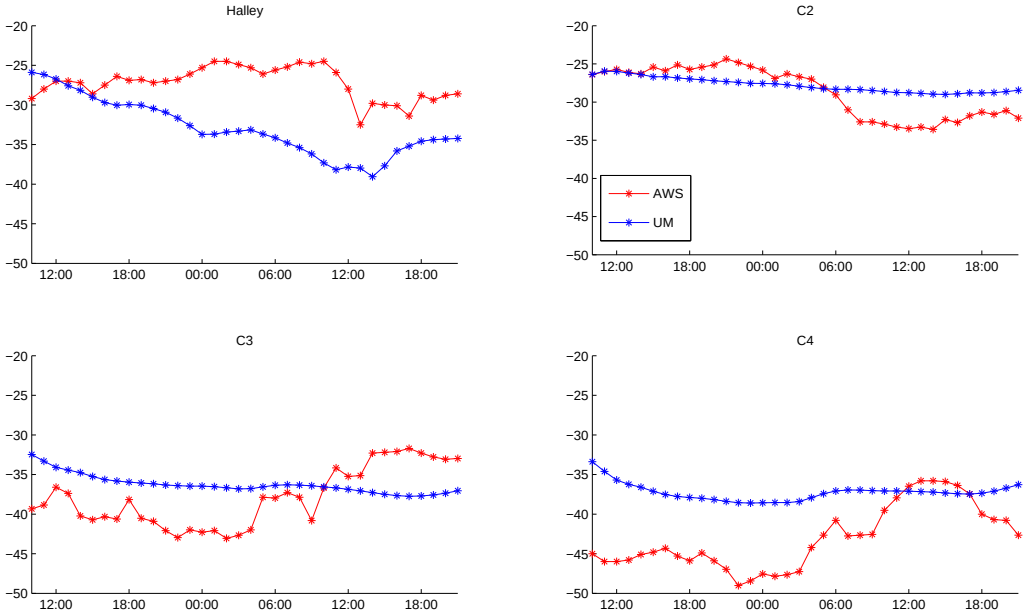

Figure 3.10: Air temperature (degrees Celsius) for 13 and 14 August 2003, from the model (in blue) and from AWS observations (in red).

between C2 and C3, as discussed earlier and as shown in figure 3.8, resulting in lower wind speeds. The model shows (relatively strong) upslope winds at C4 during the entire simulation. This could be a result of the representation of the synoptic situation in the model. Figures 3.5 and 3.6 show a strong gradient in the geopotential height at 850 mb over the highest part of the slope, where C4 is located, which would result in an upslope wind. In the ECMWF reanalysis this gradient is much weaker, especially early in the model run (figure 3.5).

Figure 3.10 shows the surface air temperatures from the model and from observations. The model results do not compare very well to observations. At Halley, the model underestimates the temperature by up to 12 degrees Celsius. At C3 and C4, the model overestimates the temperatures by about 5-7 degrees Celsius. The model performs best at C2. The observed temperatures at Halley and C2 are very similar, while the model even shows higher temperatures at Halley compared to C2, despite the higher location of C2 at 400 m on the slope. Renfrew and Anderson (2002) showed that this phenomenon often occurs in Coats Land during the winter months. They suggest that C2 is located within the so-called 'thermal belt', a band of high brightness temperatures. This belt has been observed in remote-sensing studies, for example by Nakagawa and Shimoodori (1994) and King *et al.* (1998) (the latter specifically over the Coats Land region). Nakagawa and Shimoodori (1994) attributed this thermal belt to the

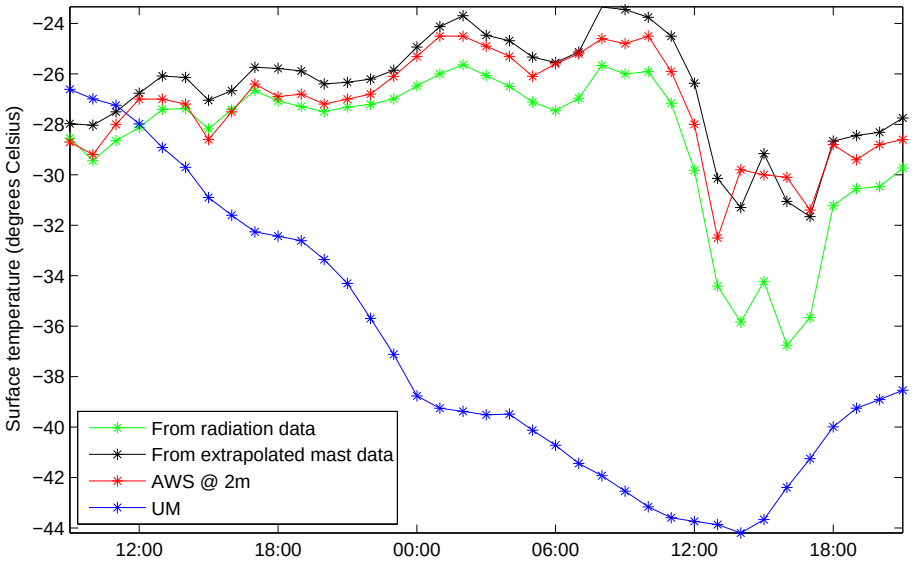

Figure 3.11: Surface temperature (in degrees Celsius) at Halley from the model (in blue), from the AWS (at 2 m, in red), from extrapolated mast data (in black) and derived from radiation data (in green) for 13-14 August 2003.

greater degree of turbulent mixing over the slope (creating higher surface temperatures), while over the ice shelf a surface-layer inversion can develop during periods of very low wind speeds.

To study the problem of the underestimation of the surface temperature at Halley, a comparison was made with different ways of determining the surface temperature from observations. Figure 3.11 shows the surface temperature from the model (in blue) and the temperature at 2 m height from the AWS (in red). The green line shows the snow temperature (surface temperature, T_s) estimated from radiation data using:

$$LW^{\uparrow} = \sigma T_s^4 \tag{3.1}$$

in which $LW^{\uparrow}$ is the outgoing longwave radiation (in W/m^2) and σ the Stefan - Boltzmann constant ($5.67 \cdot 10^{-8}$ W m^{-2} K^{-4}). This equation uses the Stefan - Boltzmann law and assumes an emissivity of 1, i.e. the snow surface is a black body. Figure 3.11 shows that the resulting temperature is highly correlated with the AWS temperature. The black line in figure 3.11 is obtained by linear extrapolation of the mast data. The mast measures temperature at 1, 2, 4, 8, 16 and 32 m, and by linear extrapolation we obtained the temperature at the surface (0 m). The three ways of estimating the surface temperature show very similar results and agree within a range of two degrees, except from 12 to 18 UTC on 14 August when the snow temperature derived from longwave radiation shows much colder temperatures. This corresponds with a period of clearer skies at Halley, which decreases the incoming longwave radiation and therefore also the surface

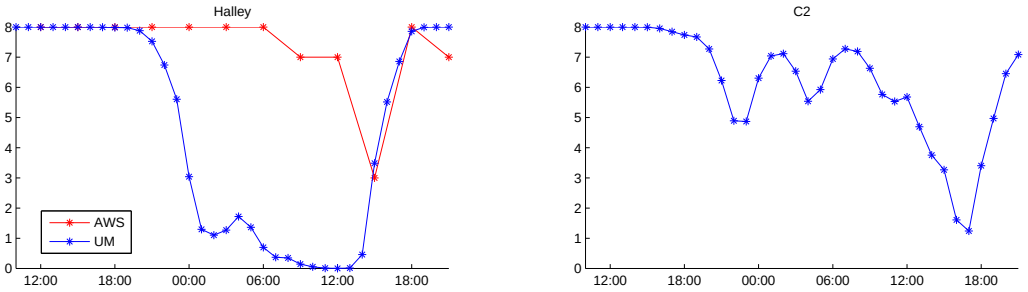

Figure 3.12: Cloud cover (in eighths) for 13 and 14 August 2003, from the model (in blue) and from synoptic observations at Halley (in red).

temperature. The model strongly underestimates the surface temperature as compared to the observed surface temperature regardless of which method is used to calculate the observed surface temperature, as can be seen in figure 3.11. The reasons for this are possibly related to the model's estimation of cloud cover.

Figure 3.12 shows the cloud cover for Halley and C2 from the model and from manually-observed cloud observations (only at Halley). At C3 and C4 the model shows full cloud cover for nearly the entire run (not shown). At Halley, the model predicts nearly clear skies for a large part of the run, while in reality it was mostly very cloudy except for a few hours in the afternoon of 14 August. This is probably the main reason for the underestimated temperatures at Halley in the model (see figures 3.10 and 3.11). The satellite image in figure 3.13 shows low cloud cover over the ice shelf around Halley, while further towards the slope it is clearer. Over the slope there appears to be thinner cloud cover. This is consistent with model results. Earlier satellite images (not shown) show cloud cover over the ice shelf and the lower part of the slope, with clearer skies higher up the slope. Later satellite images (not shown) show cloud cover over the ice shelf and higher up the slope, with a clearer patch around the bottom of the slope. This means that C3 and C4 (high on the slope) are not always covered by cloud, while the model shows full cloud cover at all times during the model run for both these locations (not shown). This could explain why the model overestimates the temperature at C4 for the entire run and at C3 during the first part of the run (see figure 3.10). C2 shows more cloud cover on 13 August with more clear patches during 14 August. This is well represented by the model, see figure 3.12. This also explains why the modeled air temperature is closer to the observed values for C2 as compared to the other locations (see figure 3.10).

Figure 3.14 shows the longwave radiation budget for Halley. The model shows a lot less incoming and outgoing longwave radiation than observed. This links back to the model predicting mostly clear skies while in reality it is much more cloudy. The net longwave radiation from the model is negative for most of the run while in reality the net longwave radiation is slightly positive except for the period when clearer skies were observed. The negative net longwave radiation from the

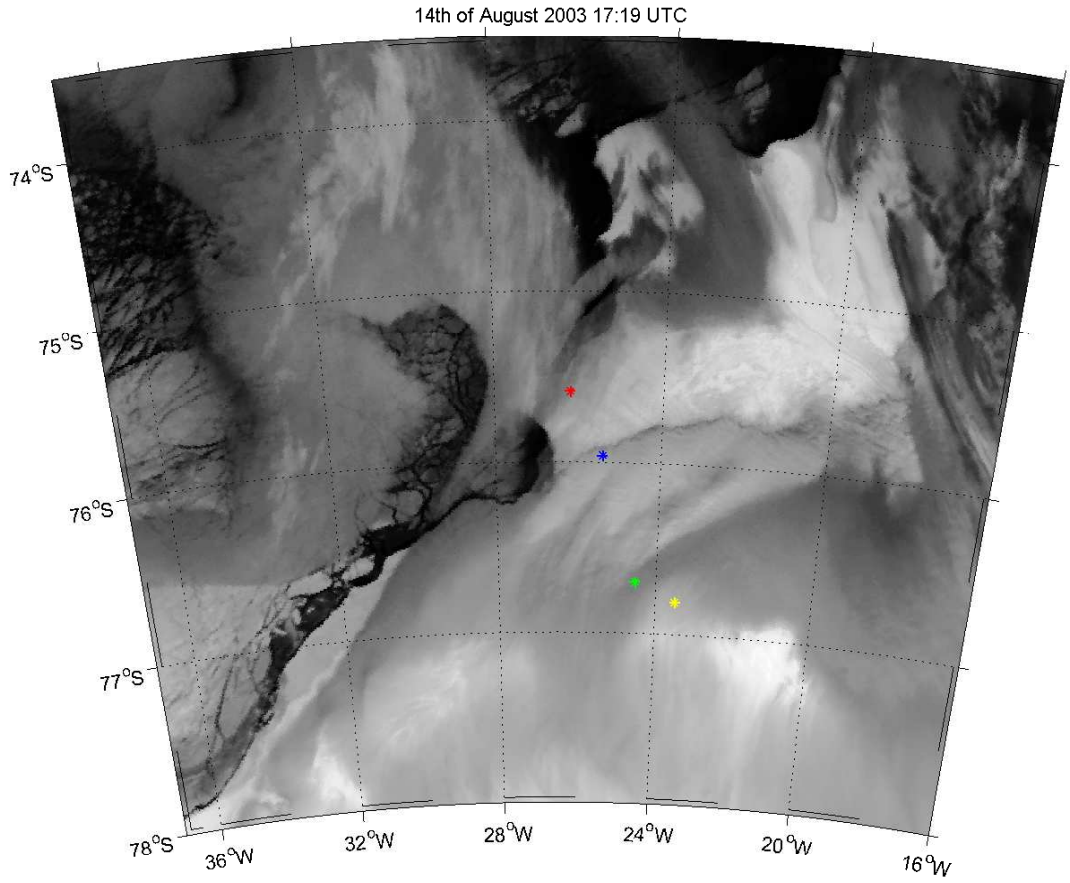

Figure 3.13: Infrared satellite image of 17:19 UTC 14 August 2003. The locations of Halley (in red), C2 (in blue), C3 (in green) and C4 (in yellow) are indicated.

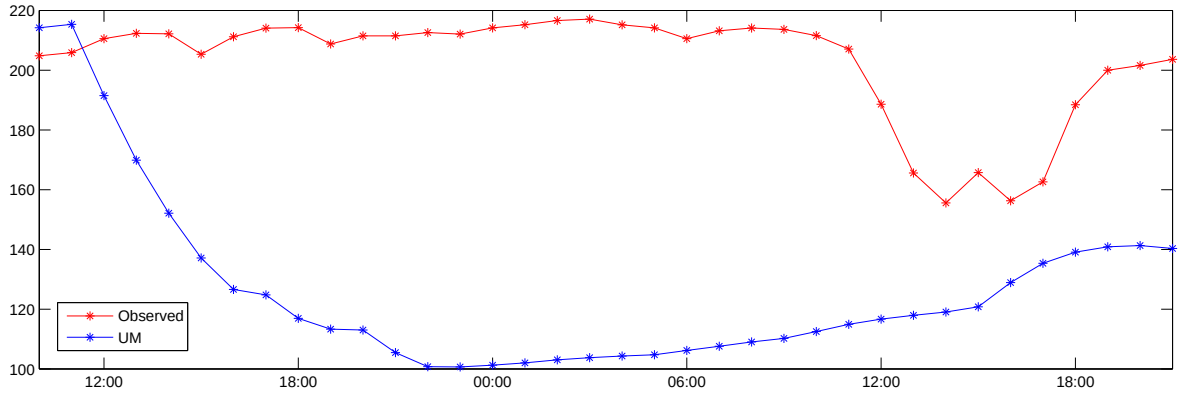

(a) Incoming Longwave Radiation (W/m^2)

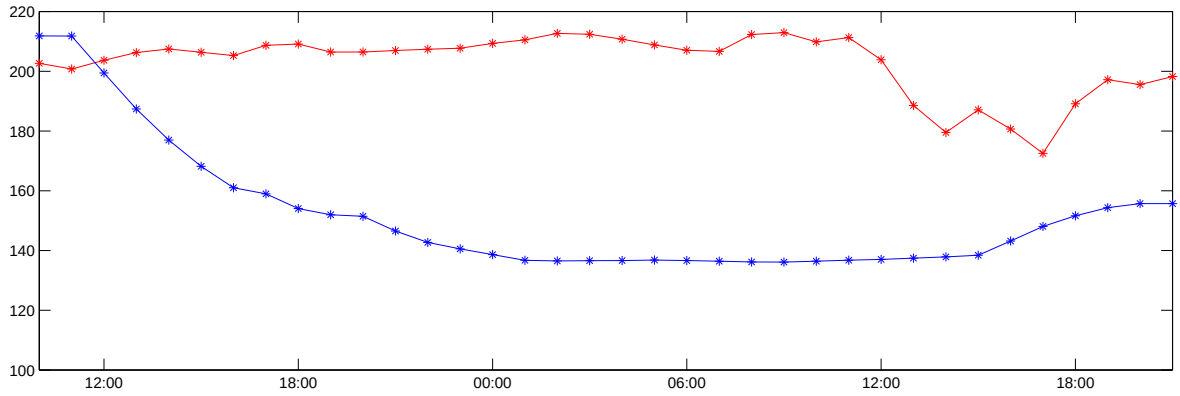

(b) Outgoing Longwave Radiation (W/m^2)

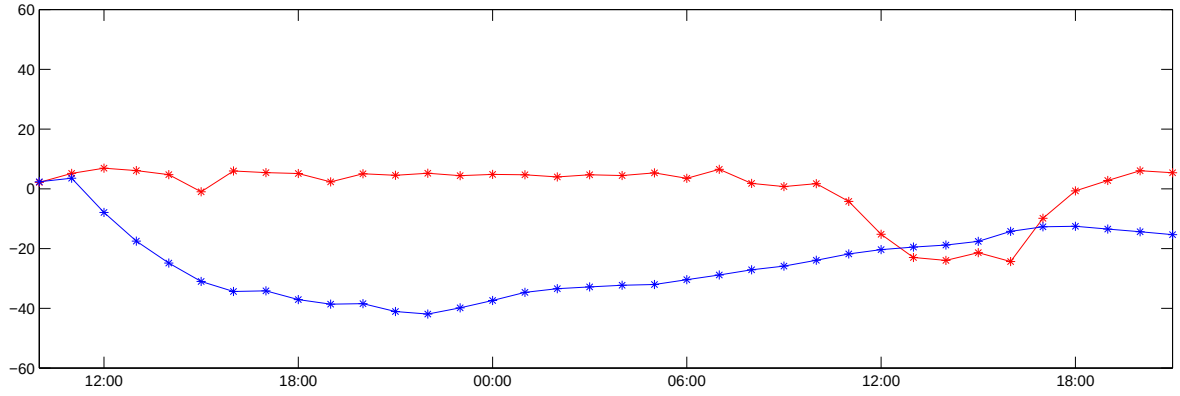

(c) Net Longwave Radiation (W/m^2)

Figure 3.14: Longwave radiation (W/m^2) at Halley for 13 and 14 August 2003, from the model (in blue) and from observations (in red).

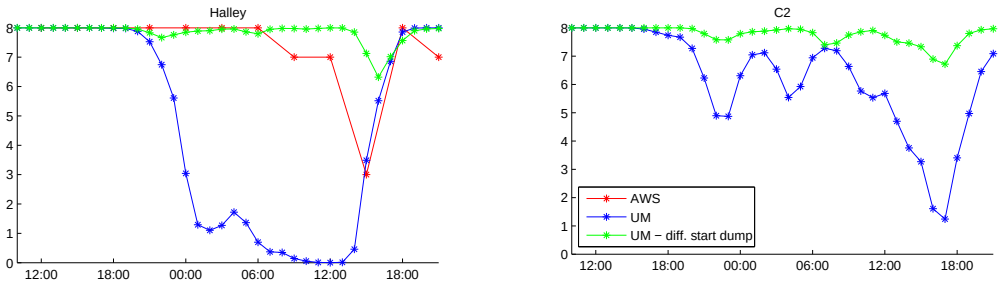

Figure 3.15: Cloud cover (in eighths) for 13 and 14 August 2003 from synoptic observations at Halley (in red) and for the model using the default start dump (in blue) and using an earlier start dump (in green).

model means that the surface loses heat due to radiational cooling (typical for clear sky conditions) and this explains the strong cooling and underestimation of the surface temperature in figure 3.11. The longwave radiation observations showing slightly positive net longwave radiation means that in reality, the surface is warming up due to outgoing longwave radiation being re-emitted by the clouds. From about 10 UTC on 14 August, the net longwave radiation from observations becomes negative, caused by the clear skies during this period (see figure 3.12). This means that the surface will start to cool. This pattern of initial warming followed by stronger cooling when the skies clear up can clearly be seen from all observations in figure 3.11. Obviously the underestimation of the surface temperature at Halley by the model is mainly caused by the model predicting clear skies while in reality it was cloudy during most of the model run. It is not clear why the model is not predicting the cloud cover very well, as the model does have a good representation of the general synoptic situation (see figures 3.1 to 3.4).

To find out whether the cloud cover is an issue resulting from the initial conditions (the start dump), this case study was also run with a start dump from a day earlier (12 August 09 UTC, derived from a model run which started at 06 UTC). Figure 3.15 is similar to figure 3.12 but also shows the results from the model simulation using the earlier start dump. The cloud cover over Halley is much improved by using a different start dump; the model does not show the clear skies anymore. Figure 3.16 shows that the improved cloud cover at Halley results in much improved air temperatures. This model simulation does not show the large underestimation of the air temperature and compares much better to observations. For C2-C4 the air temperatures from the simulation with an earlier start dump do not compare better to observations though. The air temperatures are warmer as a result of the higher cloud cover, but this is not an improvement in this case. Figure 3.17 is similar to figure 3.9 but showing the model results for the simulation with an earlier start dump. The model shows stronger wind speeds at all locations, which is a slight improvement at C2, but not at other

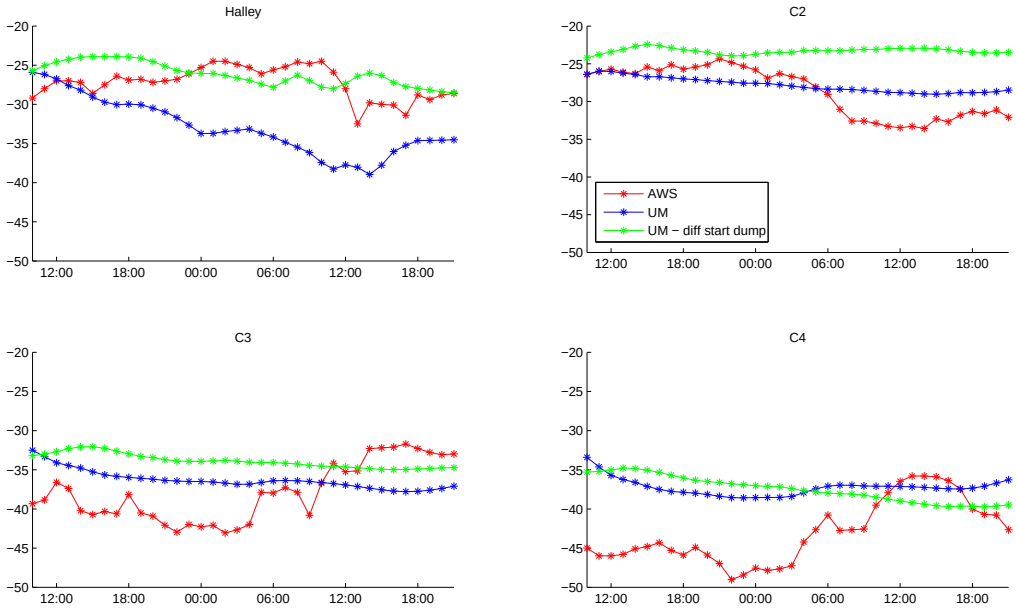

Figure 3.16: Air temperature (degrees Celsius) for 13 and 14 August 2003, from AWS observations (in red) and for the model using the default start dump (in blue) and using an earlier start dump (in green).

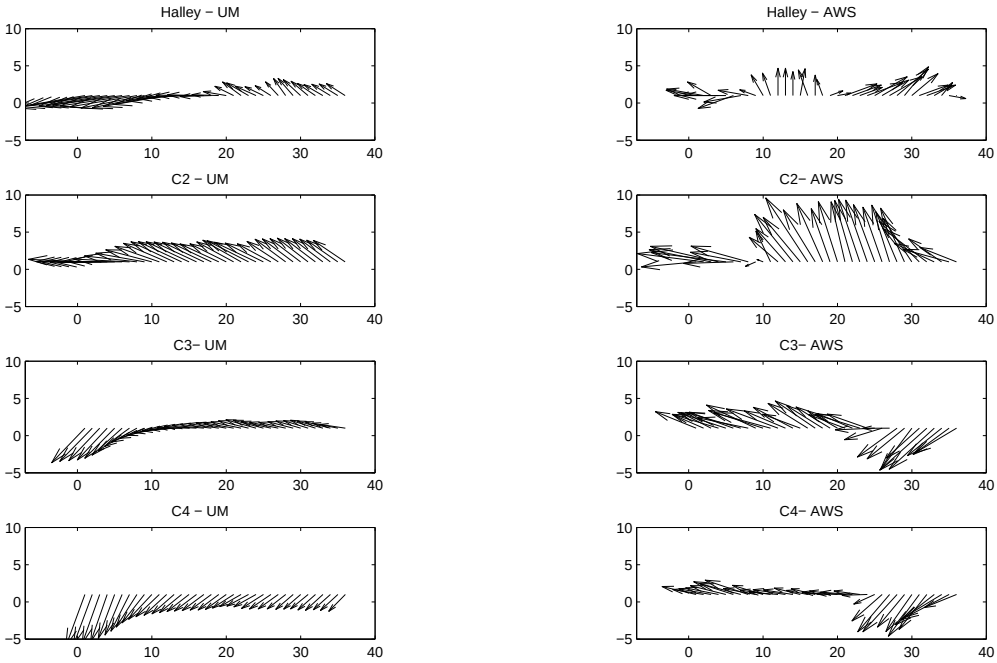

Figure 3.17: Wind vectors from the model using a different start dump (on the left) and from AWS observations (on the right). The x-axis shows hours from the 09 UTC 13 of August 2003. The y-axis points North.

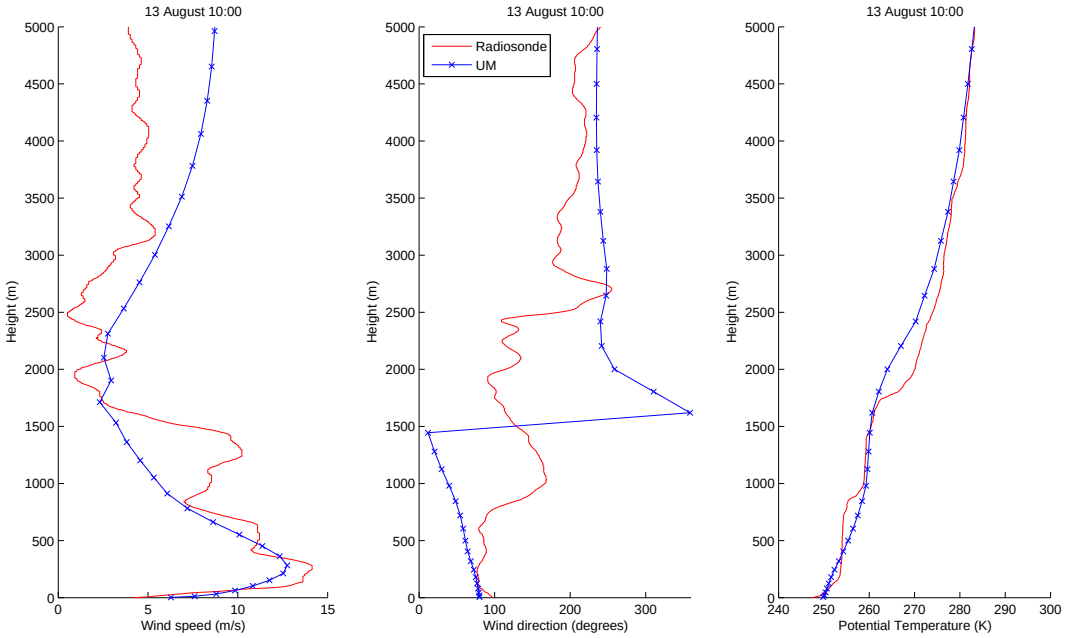

Figure 3.18: Profiles of wind speed (left), wind direction (middle) and potential temperature (right) from the model (in blue) and from radiosonde data (in red) at Halley for 10 UTC 13 August 2003.

locations. At C3, the wind directions are not very well represented. So even though the earlier start dump improved the cloud cover and air temperature at Halley, it does not show an improvement at other locations or for other variables. Therefore it was decided not to use this model simulation in the remainder of this thesis.

3.2.3 Radiosonde comparison

Figure 3.18 shows the wind speed and wind direction profiles (on the left and in the middle, respectively) for Halley for 10 UTC 13 August. For the wind speed, the model profile compares quite well to the radiosonde profile. The low level wind jet is well captured, though slightly underestimated by the model. In the radiosonde profile, an elevated jet is present at a height of 1000-1500 m. The model does not capture this jet and strongly underestimates the wind speed at these heights. Above 2000 m, the model starts to overestimate the wind speed. This is only one hour into the model run, so it is likely that the model is still spinning up. The profile from the model an hour later (at 11 UTC, not shown) is very similar however (both for the wind speed and the wind direction), though the low level jet has become stronger and compares better to the radiosonde profile. The wind direction is not very well represented by the model. Figure 3.19 shows the same but for 10 UTC 14 August. Here, both the wind speed and the wind direction are better represented by the model. The model performs poorly for the lowest 500 m of the wind speed profile though: the profile shows a

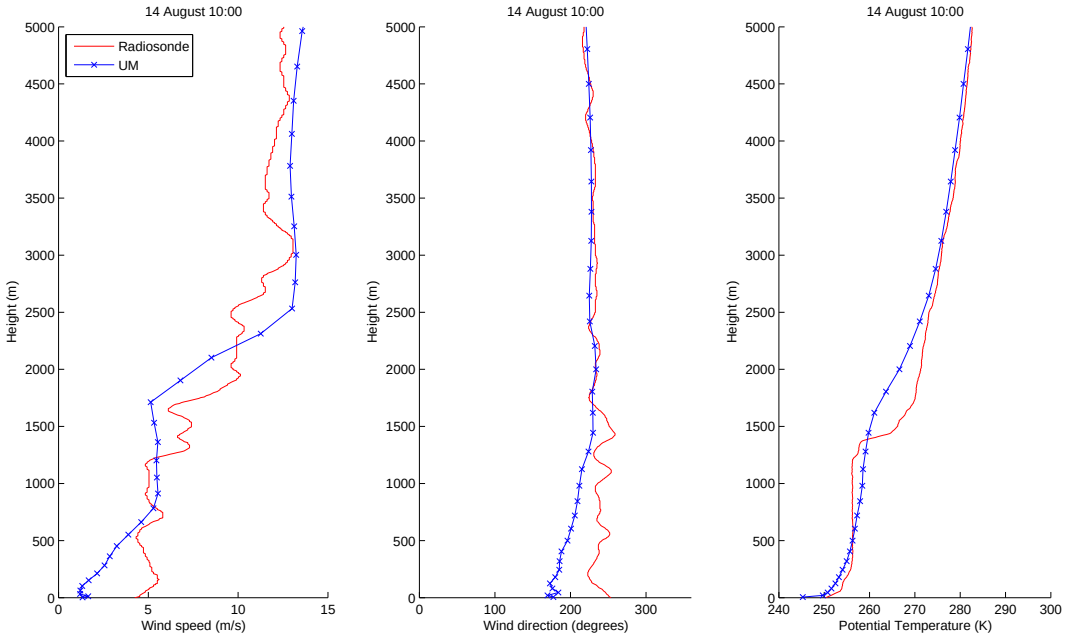

Figure 3.19: Profiles of wind speed (left), wind direction (middle) and potential temperature (right) from the model (in blue) and from radiosonde data (in red) at Halley for 10 UTC 14 August 2003.

different shape and wind speeds are underestimated. The wind direction profile is very well represented above 1500 m, but not in the lowest part of the atmosphere. Comparing figures 3.18 and 3.19, the model does capture the general change in the shape of the wind profile quite well though.

Figure 3.18 shows the profiles of potential temperatures (on the right) for 10 UTC on 13 August 2003, for both the model and data from the radiosonde launch. The model matches the radiosonde profile reasonably well, though it does not pick up smaller features in the radiosonde profile, like the inversion at 800-900 m and another (much weaker) inversion at 850-900 m (indicating the bottom of the elevated jet). Higher up the model matches the radiosonde profile very well. Figure 3.19 shows the potential temperature profile 24 hours later, for 10 UTC 14 August 2003. The model does performs slightly worse in this case, poorly representing the inversion at 1400 m and underestimating the potential temperature at the surface by about 5 K. At the same time the wind speed is also strongly underestimated, indicating that the boundary-layer in the model is too stable at this point.

3.2.4 Doppler Sodar comparison

Figure 3.20 shows downslope wind speeds from the model and from the Doppler Sodar at location C2 as 15 min averages. The model wind profiles show very little temporal variability, except for a gradual small increase in wind speed over time at all heights. The standard deviation from the mean profile is very small:

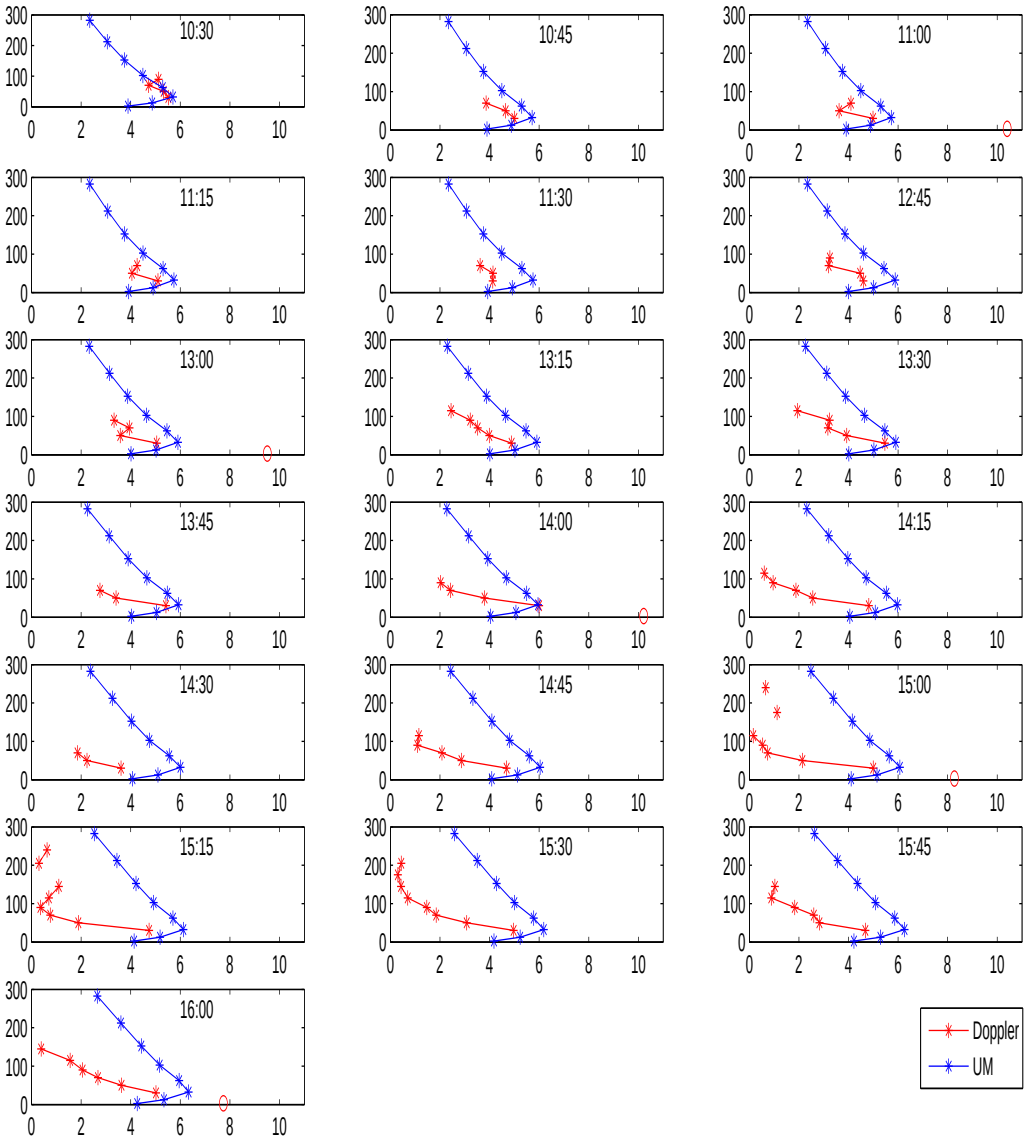

Figure 3.20: Downslope wind speed at the C2 station from the model (in blue) and from the Doppler sodar (in red), for 14 August 2003. At every whole hour, the 3m wind speed as measured by the AWS is indicated by a red circle. Note that the AWS observations are 10s averages while the Doppler measurements and model data are 15min averages.

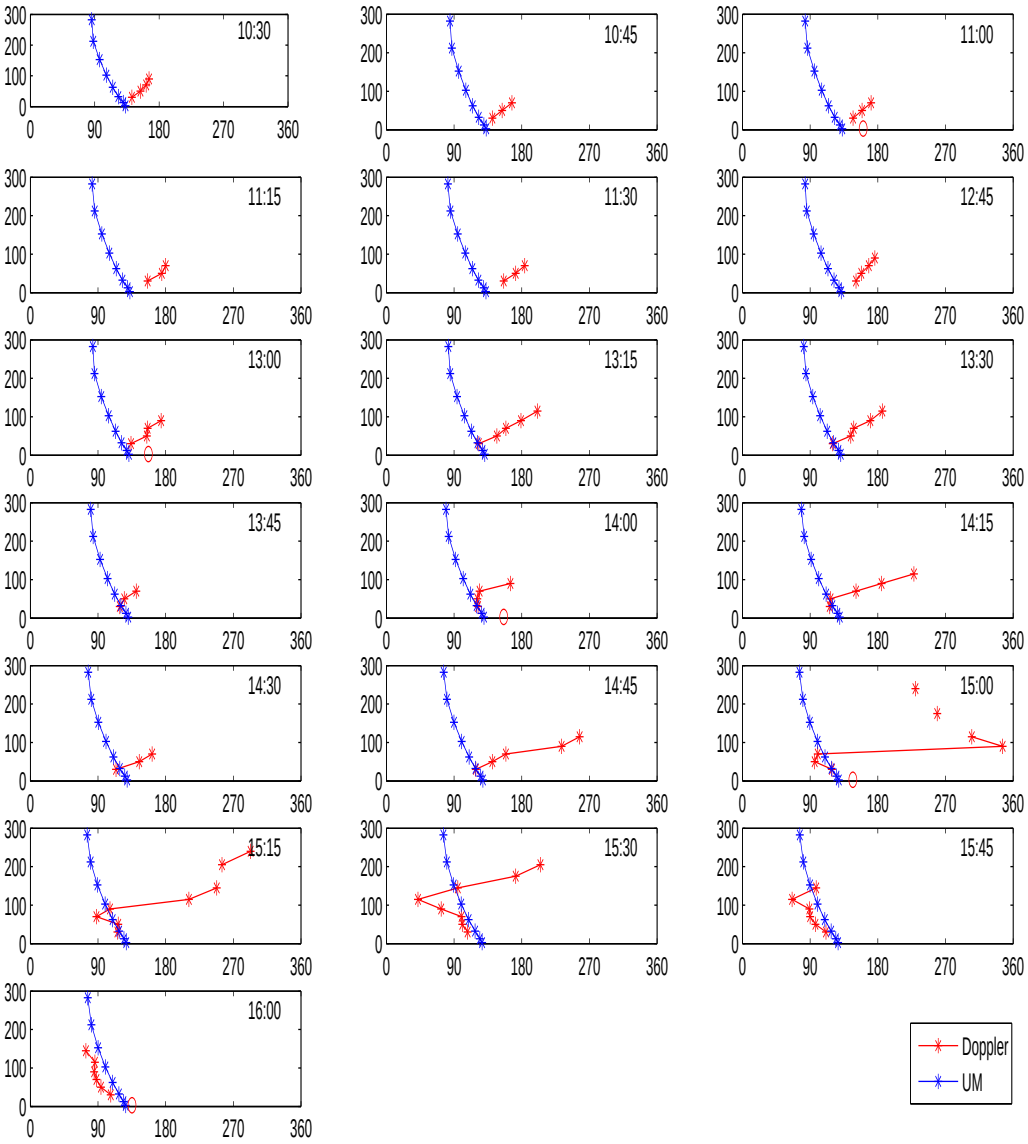

Figure 3.21: Wind direction at the C2 station from the model (in blue) and from the Doppler sodar (in red), for 14 August 2003. At every whole hour, the wind direction at a height of 3m as measured by the AWS is indicated by a red circle. Note that the AWS observations are 10s averages while the Doppler measurements and model data are 15min averages.

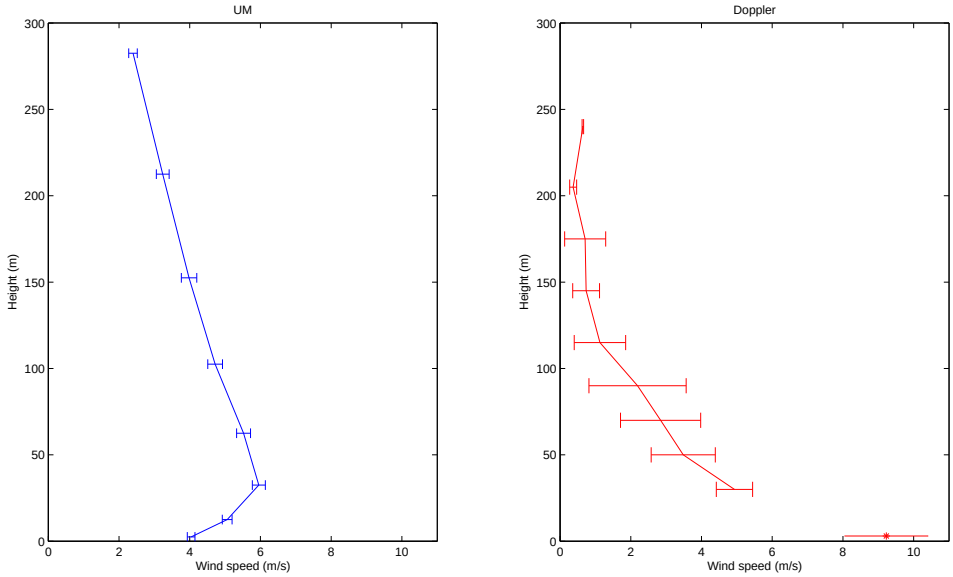

Figure 3.22: Average profiles of wind speed (m/s) taken from 15 minute averaged profiles between 1030 UTC and 1600 UTC for 14 August 2003, on the right from Doppler Sodar observations and on the left from model output. The errorbars indicate the standard deviation. The lowest data point in the Doppler Sodar plot comes from the AWS hourly measurements.

0.1 - 0.2 m/s. The Doppler wind speed profiles show significantly more variation. Initially, the model compares reasonably well to observations, but later on the model generally overestimates the wind speeds at every height except at the surface. The high wind speeds at the surface (from the C2 AWS) indicate that the height of the maximum wind speed is probably located between the height of the AWS and the bottom of the lowest volume that the Doppler Sodar measures, e.g. between 3 and 20 m above the surface. The model shows the maximum wind speed at a height of 32 m (i.e. at model level 3 for this simulation), hence the model overestimates the height of the katabatic jet maximum. Figure 3.21 shows the wind directions from the model and from Doppler Sodar observations. Again, the model shows less variability in wind directions over time as compared to the Doppler Sodar measurements. The model compares reasonably well to the AWS surface observations, but not to the Doppler wind directions higher up. The model shows a backing of the wind direction with height over the entire profile, while the observations only show a backing over the lowest part of the profile (sometimes only visible between the AWS wind direction and the first Doppler level wind direction). This backing of the wind is consistent with the decrease of frictional forcing with height (Renfrew and Anderson, 2006).

To get around the differences between the highly variable Doppler observations and the more constant model results, figure 3.22 shows the average over all profiles shown in figure 3.20, both for the model and for the Doppler observations.

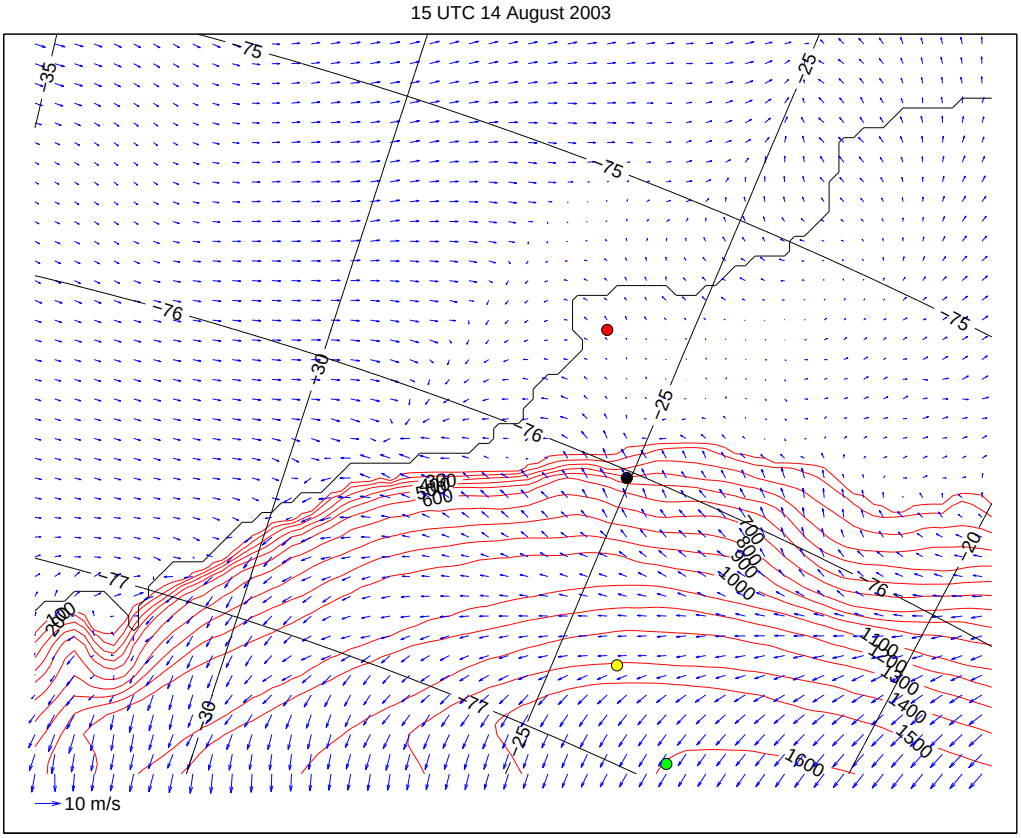

Figure 3.23: Wind arrows for the horizontal wind field at the first model level (2.5 m above the surface), for the 15 UTC 14 August 2003. Orography is contoured every 100 m, and the locations of Halley and C2-C4 are indicated. A scaling arrow is given in the lower left corner and applies to both directions.

The very small standard deviation shows just how constant the model wind speed profiles are during this period. The shape of the model profile matches the observations above 30 m (a decrease of the wind speed with height), but the wind speeds are overestimated by the model. On the other hand, the model underestimates the average near-surface wind speed, compared to the AWS average.

3.2.5 Horizontal and vertical cross-sections

Figure 3.23 shows the horizontal wind field at the first model level (at 2.5 m) for 15 UTC 14 August 2003. The wind is downslope for a large part of the lower part of the slope in the vicinity of C2 and further east. Higher up the slope, the wind directions go from parallel to the height lines to upslope wind directions at the top of the slope. This corresponds with observations, see figure 3.9. Over the sea, a line with abrupt changes in wind direction corresponds to the sea ice edge. Overall, this figure clearly shows that the wind direction changes

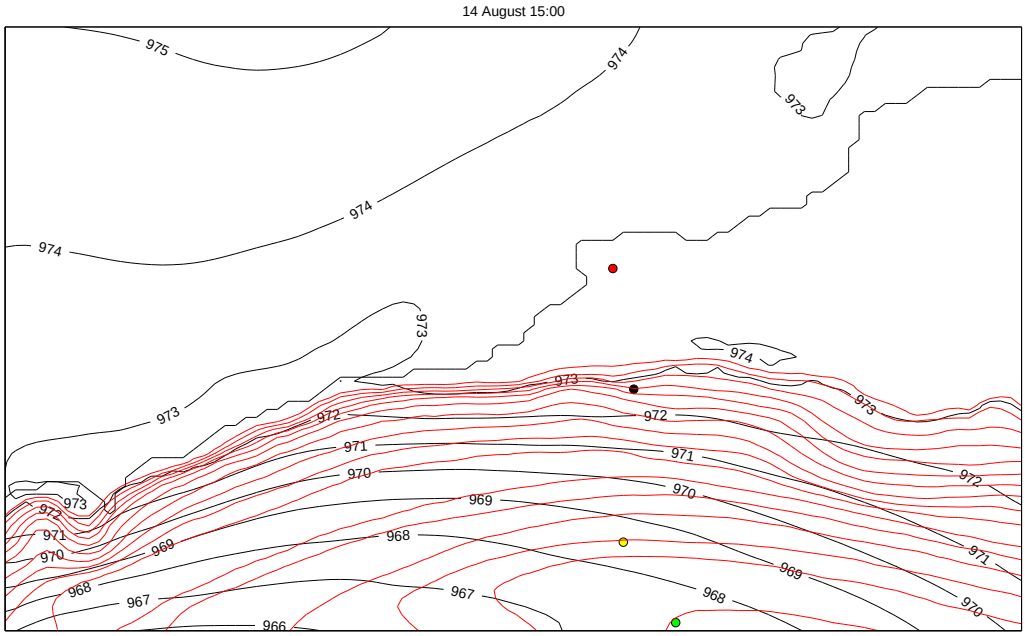

Figure 3.24: Mean sea level pressure over the 4km domain for 15 UTC 14 August 2003. Orography is contoured every 100 m, and the locations of Halley and C2-C4 are indicated.

with topography. The katabatic flow is strongest (converges) on the left side (looking downslope) of topographic depressions, something also shown by Parish and Cassano (2003a). Figure 3.24 shows the mean sea level pressure over the 4 km domain at 15 UTC 14 August 2003, the same time as the wind field in figure 3.23. The pressure field roughly follows the orography, especially on the lower part of the slope, and is opposed to the katabatic forcing.

Figure 3.25 shows cross-sections of the horizontal wind speed along the slope, in a line along the y-direction of the model grid roughly from C4 to Halley. A shallow katabatic flow develops close to the surface, with wind speeds of up to 6 m/s at the steepest part of the slope. Higher wind speeds are seen at the top of the slope, but these are upslope winds (see figure 3.23). The wind speeds show a minimum at a few hundred metres above the surface. Over time, the katabatic flow starts to retreat up the slope and then starts to flow over the ice shelf at a height of a few hundred metres instead of at the surface. Figure 3.26 shows the potential temperatures for the same cross-section. The area at the bottom of the slope shows cooling, and the cold pool that forms blocks the katabatic flow and causes it to override the cold pool, as seen in figure 3.25 at 15 and 18 UTC. Gallée *et al.* (1996) explains that this cold pool forms when the cold air piles up when the wind slows down in front of the katabatic flow (in our case at the bottom of the slope, where the buoyancy force will disappear and thus slow down the katabatic

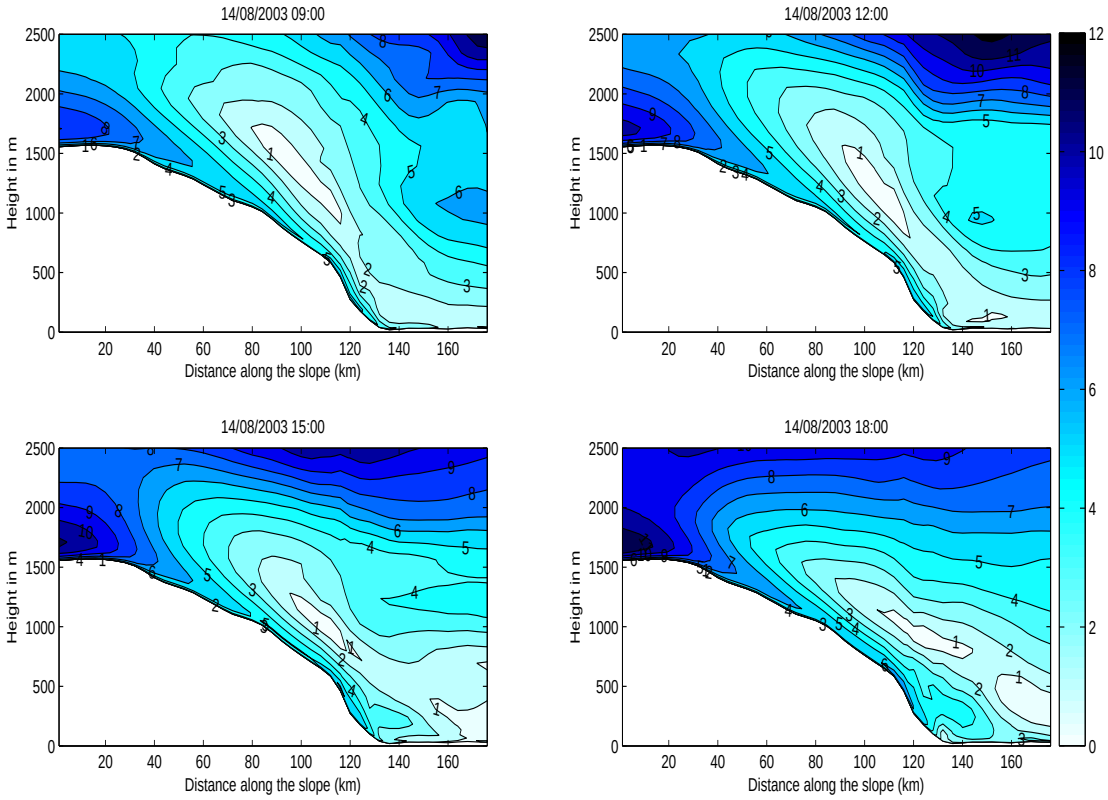

Figure 3.25: Horizontal wind speed (m/s) along the slope for 09, 12, 15 and 18 UTC 14 August 2003, along the model y direction roughly from C4 on the left to Halley on the right.

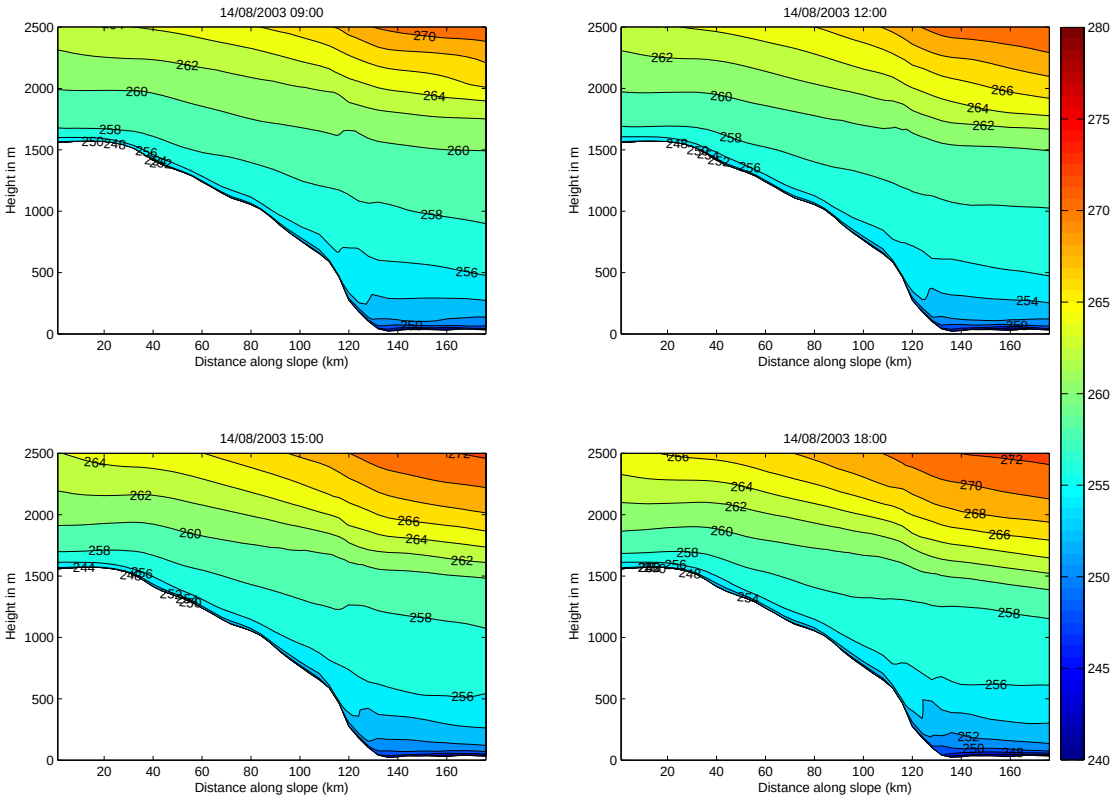

Figure 3.26: Potential temperature (K) along the slope for 09, 12, 15 and 18 UTC 14 August 2003, along the model y direction roughly from C4 on the left to Halley on the right.

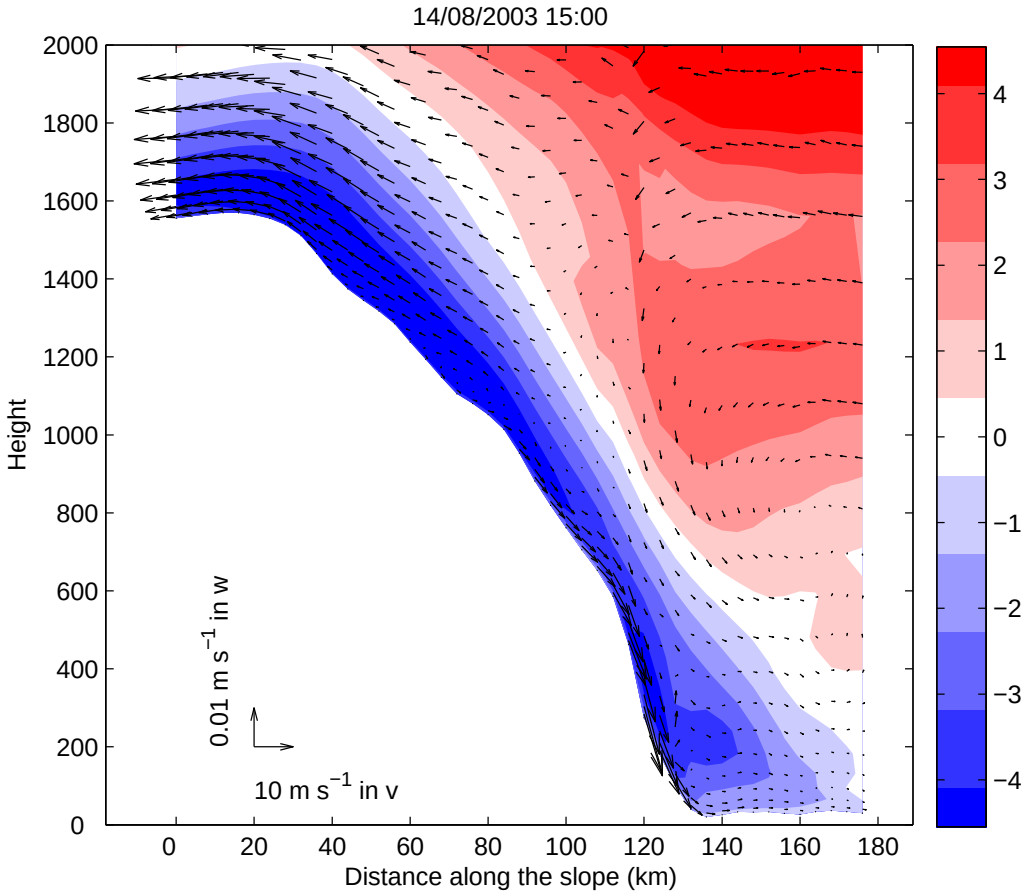

Figure 3.27: Wind vectors from the model's grid relative v (roughly downslope) and w components, for 15 UTC 14 August 2003. The u component (roughly cross-slope) is shaded. A scaling arrow is given in the lower left corner. The cross-section is taken along the model's y direction, roughly from C4 on the left to Halley on the right.

flow). This then strengthens the temperature contrast, which in turn causes a pressure contrast which will further slow down the katabatic flow (Gallée *et al.*, 1996). This phenomenon is also discussed in Renfrew and Anderson (2002) and Renfrew (2004). The wind profiles from radiosonde measurements (figures 3.18 and 3.19) do show a jet at a height of 200-300 m above the surface. In the idealised modelling study over Coats Land by Renfrew (2004), this weak elevated jet at a height between 70 and 200 m was found to be a common feature of the model simulations. Renfrew (2004) suggests that this is the tail end of the katabatic flow that overrides the cold pool. Yu *et al.* (2005) (using idealised numerical simulations) found that the sudden cessation of the katabatic flow at the foot of the slope in Coats Land is associated with a katabatic jump, the formation of which is facilitated by the upslope pressure gradient associated with a pool of cold air over the ice shelf.

Figure 3.27 shows the same cross-section as in figures 3.25 and 3.26 but with the vertical axis exaggerated. It shows grid relative wind arrows from the v (roughly downslope) and w component, with the u component (roughly cross-slope) shaded. Again we observe downslope winds over the lowest half of the slope, and upslope winds higher up. When the flow reaches the cold pool at the bottom of the slope, upward motions are observed. Figures 3.26 and 3.27 show similarities to results by Davolio and Buzzi (2002), who studied katabatic winds near Terra Nova Bay using a three-dimensional hydrostatic limited area model. Their figures also show a wave present over the steepest part of the slope (Davolio and Buzzi, 2002), showing both as waves in the potential temperature fields and upwards vertical wind motions. Renfrew (2004) suggests that a train of internal gravity waves is triggered at the bottom of the slope (propagating energy upwards) where the katabatic flow changes from shooting to tranquil.

3.2.6 Summary

The large scale synoptic situation is reasonably well represented by the model. The main problem on the smaller scale is the cloud cover: the model shows clear skies over Halley for a large part of the run, while in reality it was mostly cloudy, and this causes the surface temperatures at Halley to be underestimated by the model by up to 12 degrees. A different (earlier) start dump improved this issue, but did not improve the model results in other areas. The model is not capable of reproducing the highly variable Doppler Sodar observations. It underestimates the wind speeds at the surface, while overestimating wind speeds higher up. The katabatic layer in the model appears too deep, though this is impossible to prove as the peak of the katabatic jet seems to fall in the observation gap between the AWS and the lowest level of the Doppler Sodar. The model does show the downslope winds at the bottom of the slope, while showing upslope winds higher up, as seen in the observations. The model also shows the development of a cold pool at the bottom of the slope.

The problem with the cloud cover appears to be a problem in the initial conditions. This was tested by using a different start dump, of 12 August 2003 instead of 13 August 2003. The cloud cover over Halley is now better represented, and the surface temperature is not underestimated by the model. Many other aspects of the model run are not improved by using this earlier start dump though, so the results of this experiment are not shown or discussed any further in this chapter.

In conclusion, the model performs reasonably well but there is definitely room for improvement. We will investigate the sensitivity of the model results to changing the boundary layer parameterisation . The results of this sensitivity experiment will be discussed in the next chapter.

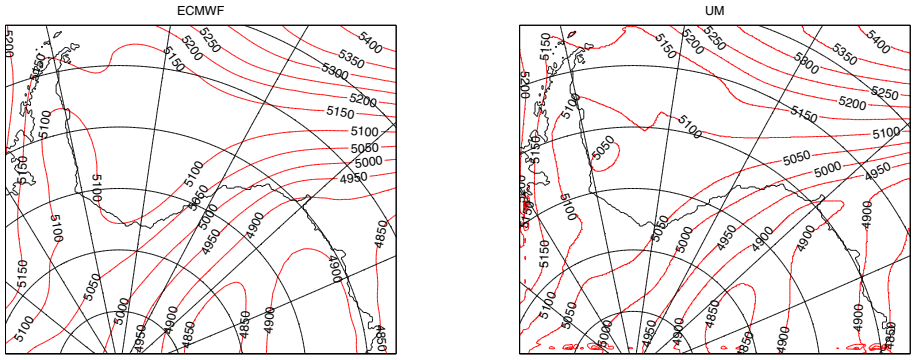

Figure 3.28: Geopotential height at 500 mb (in metres) at 12 UTC 3 September 2002 (T+3), from the ECMWF Operational Analysis (left panel) and from the model run (right panel).

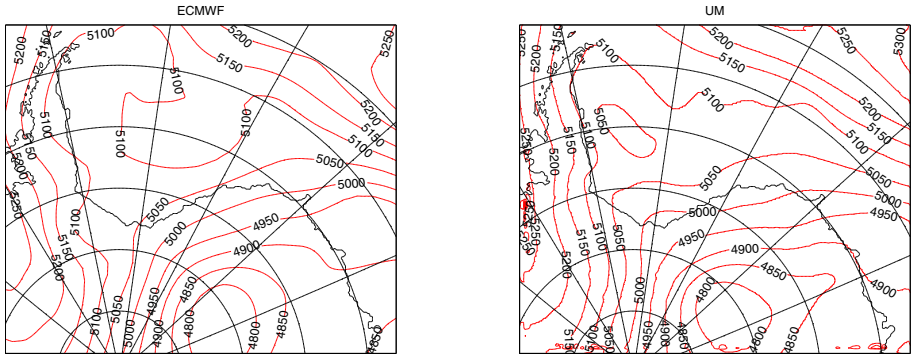

Figure 3.29: Geopotential height at 500 mb (in metres) at 12 UTC 4 September 2002 (T+27), from the ECMWF Operational Analysis (left panel) and from the model run (right panel).

3.3 Winter case study 2: September 2002

3.3.1 Large scale

Figures 3.28 and 3.29 show the geopotential height at 500 mb over the 12km domain at 12 UTC for respectively 3 and 4 September 2002, for both the model results and from ECMWF Operational Analysis data. The general shape of the geopotential height field is well represented by the model though it tends to underestimate the geopotential height as compared to the ECMWF Operational Analysis. The absolute domain averaged error for the geopotential height at 500 mb ranges from 12.0 m at the beginning of the run to 31.5 m later in the run.

Figures 3.30 and 3.31 show the mean sea level pressure at 500 mb over the 12km domain at 12 UTC for respectively 3 and 4 September 2002, for both the model results and from ECMWF Operational Analysis data. A low pressure area is present north of Coats Land. In the ECMWF Operational Analysis, this low

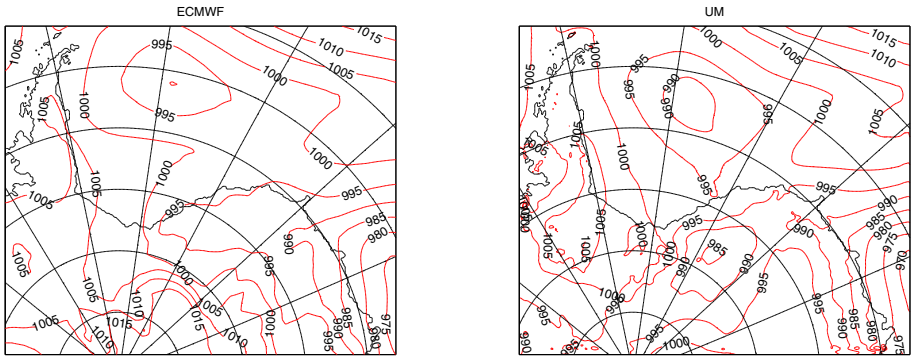

Figure 3.30: Mean Sea Level Pressure (in mb) at 12 UTC 3 September 2002 (T+3), from the ECMWF Operational Analysis (left panel) and from the model run (right panel).

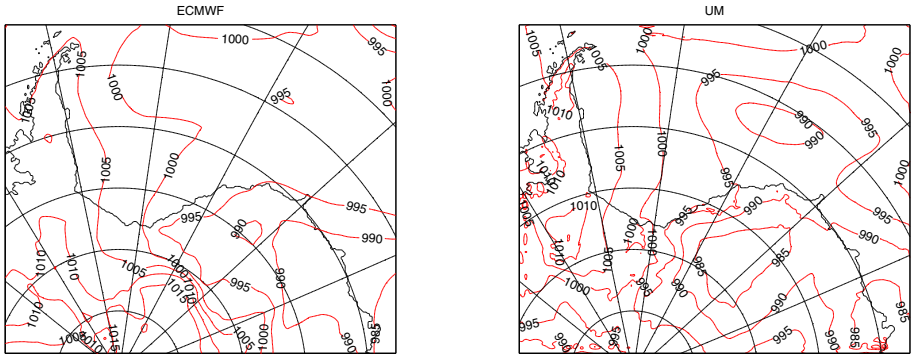

Figure 3.31: Mean Sea Level Pressure (in mb) at 12 UTC 4 September 2002 (T+27), from the ECMWF Operational Analysis (left panel) and from the model run (right panel).

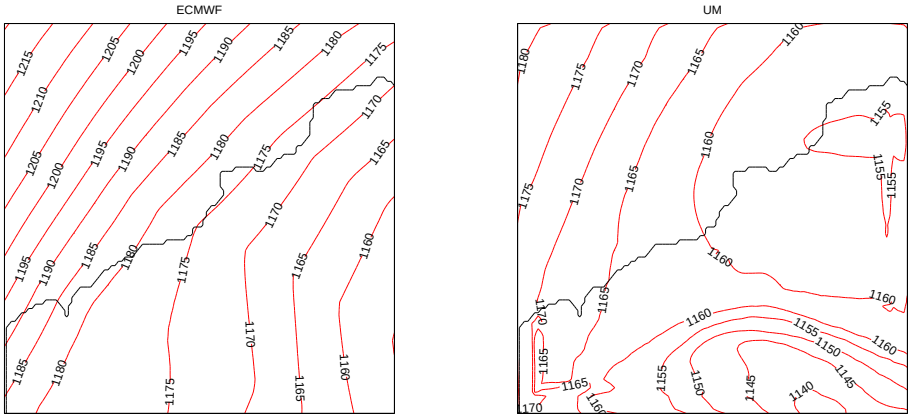

Figure 3.32: Geopotential height at 850 mb (in metres) at 12 UTC 3 September 2002 (T+3), from the ECMWF Operational Analysis (left panel) and from the 4 km model run (right panel).

pressure area moves eastward while filling up until it has nearly disappeared. Over Coats Land the synoptic situation is quiet. The UM shows a deeper low pressure area which is still present on 4 September (see figure 3.31). The UM also shows a low pressure area to the south of Coats Land. Over Coats Land, the UM shows a stronger pressure gradient as compared to the ECMWF Operational Analysis. The absolute domain averaged error for the mean sea level pressure (over sea only) ranges from 0.94 mb at the beginning of the run to 1.34 mb later in the run.

To investigate the synoptic situation on a smaller scale, figures 3.32 and 3.33 show the geopotential height at 850 mb over the 4 km domain at 12 UTC for 3 and 4 September, for both the model results (from the 4 km model run) and from ECMWF operational reanalysis data. Contrary to the August 2003 case, the model now underestimates the geopotential height at 850 mb. The model also shows a stronger gradient over the highest part of the slope and a much weaker gradient over the lower part of the slope and over the sea, as compared to the the ECMWF reanalysis.

3.3.2 AWS comparison

Figure 3.34 shows the perturbation from the mean surface pressure from the model and from AWS observations. The model does very well for C3 and C4, but less so for Halley and C2. The general pattern is captured (an increase in pressure followed by a decrease), but the model starts the pressure decrease about 12 hours too early for Halley and C2. The model shows a stronger pressure gradient compared to observations, corroborating the comparison against ECMWF operational analyses of figures 3.30 and 3.31. Figure 3.35 shows the perturbation from the mean differences in surface pressure between two observation locations.

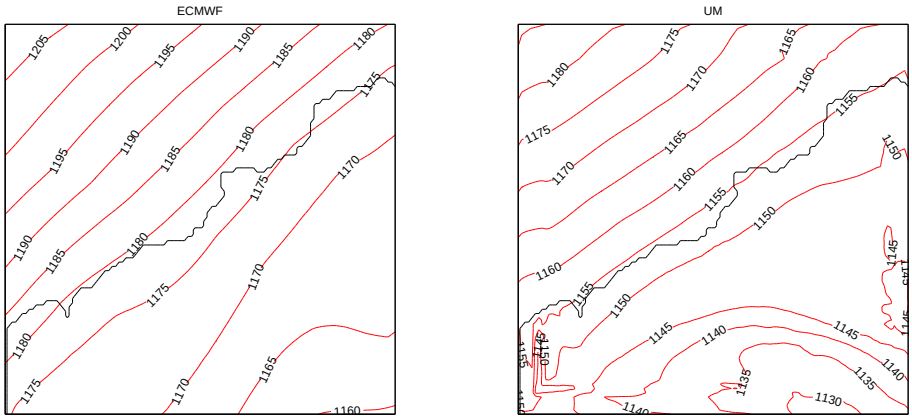

Figure 3.33: Geopotential height at 850 mb (in metres) at 12 UTC 4 September 2002 (T+27), from the ECMWF Operational Analysis (left panel) and from the 4 km model run (right panel).

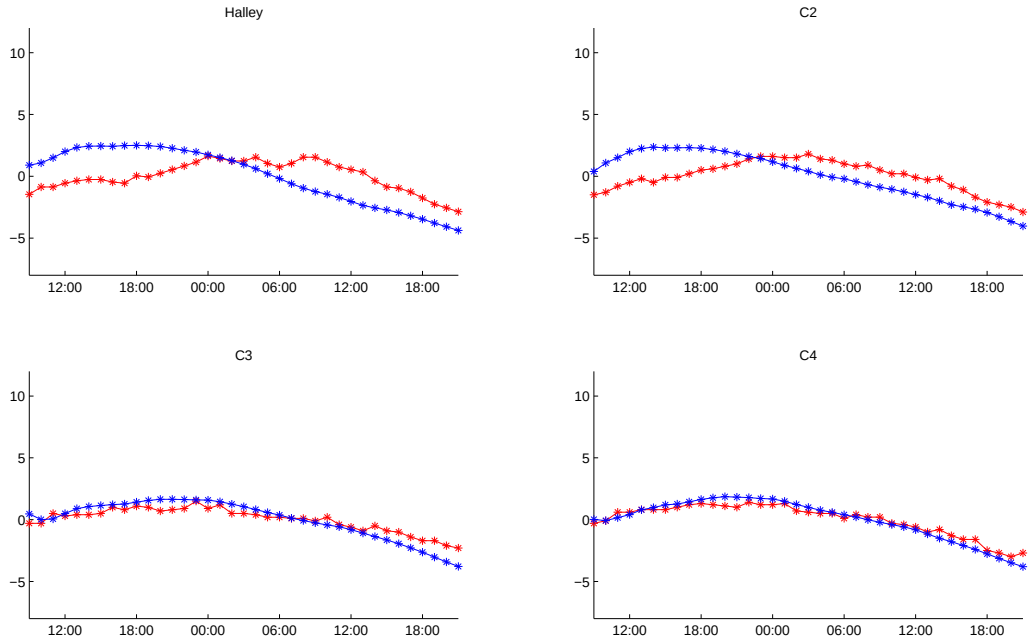

Figure 3.34: Perturbation from the mean (over 36 hours) surface pressure (mb) for 3-4 September 2002, from the model (in blue) and from AWS observations (in red).

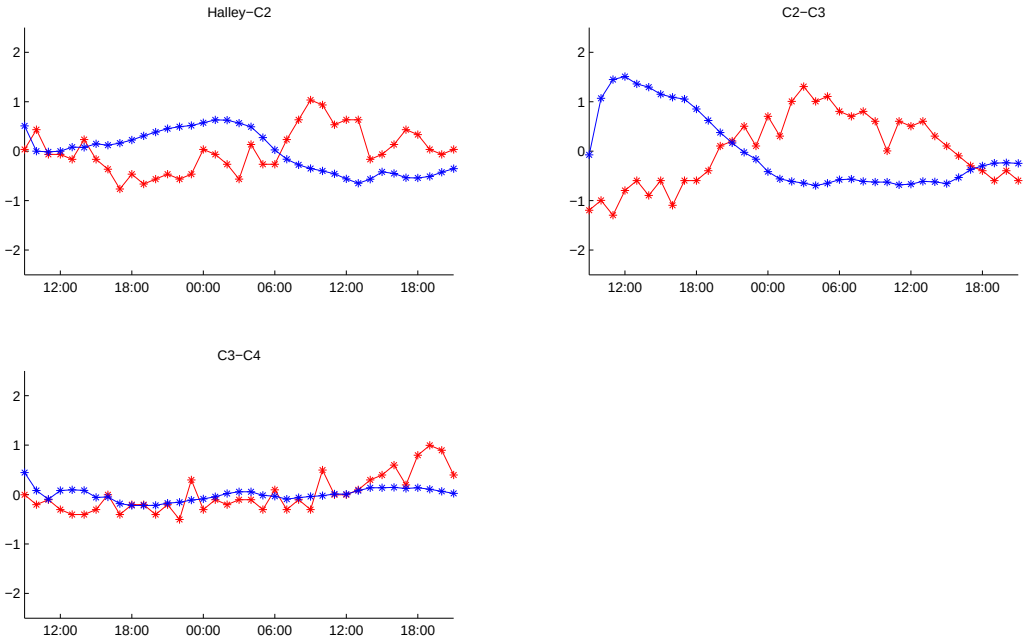

Figure 3.35: Perturbation from the mean (over 36 hours) difference in surface pressure (mb) between Halley and C2 (top left), C2 and C3 (top right) and C3 and C4 (bottom left), from the model (in blue) and from observations (in red), for 3 and 4 September 2002.

The model does very well for the C3-C4 pair, which is not surprising since the perturbation from the mean surface pressure was well captured by the model (see figure 3.34). Because the model starts decreasing too late in the model at Halley and C2 as compared to observations, the perturbation from the mean difference in surface pressure for the Halley-C2 and C2-C3 case is not captured well by the model either.

Figure 3.36 shows wind vectors for both the model and observations. The model underestimates the wind speed at all sites, except for Halley. The wind directions are reasonably well represented by the model, except for a few hours between 14-23 hours into the model run where the model shows northerly (upslope) winds at Halley and C4, something not found in the observations. The wind directions at C2 are not very well represented by the model. The observations show relatively strong downslope winds at C2, C3 and C4 for the entire simulation. The geopotential height at 850 mb from the ECMWF reanalysis (see figures 3.32 and 3.33) shows that the geopotential wind is directed downslope as well. In the model however, the geopotential height at 850 mb indicates a more cross-slope wind, and the gradient of the geopotential height at 850 mb is very small at the bottom part of the slope. This might partly explain why the model does not show such a clear and relatively strong downslope flow.

Figure 3.37 shows the temperatures for the model and from AWS observations. Again we can see the effect of the thermal belt in the AWS observations, with much higher temperatures at C2 compared to Halley. The model shows

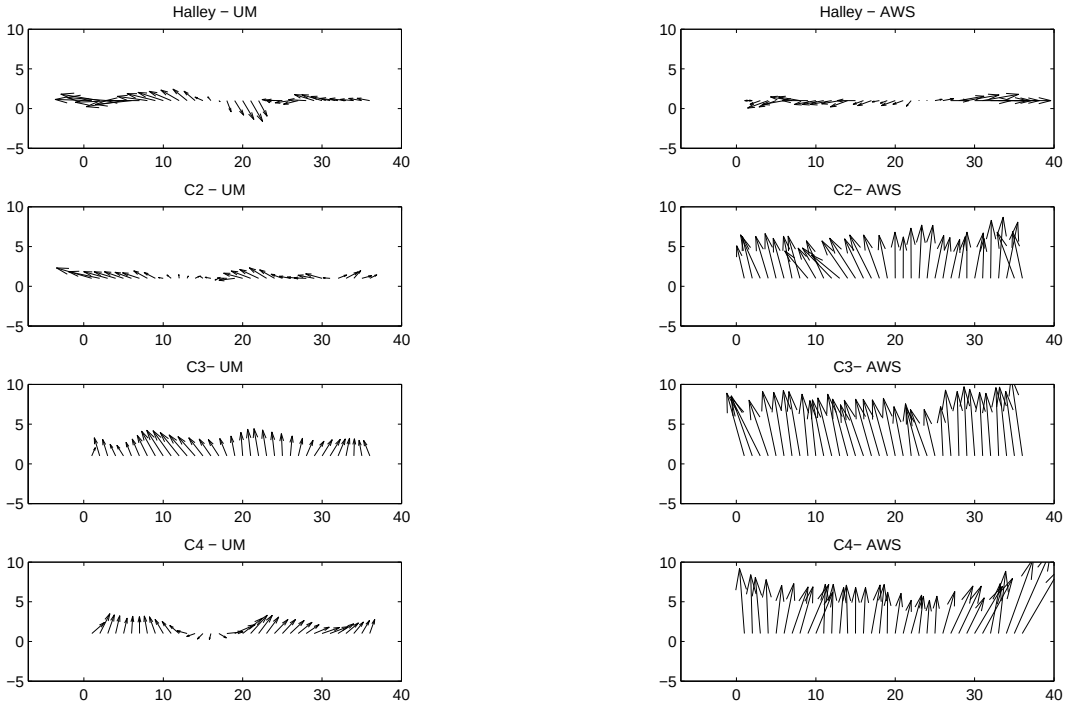

Figure 3.36: Wind vectors from the model (on the left) and from AWS observations (on the right). The x-axis shows hours from 09 UTC 3 September 2002. The y-axis points North.

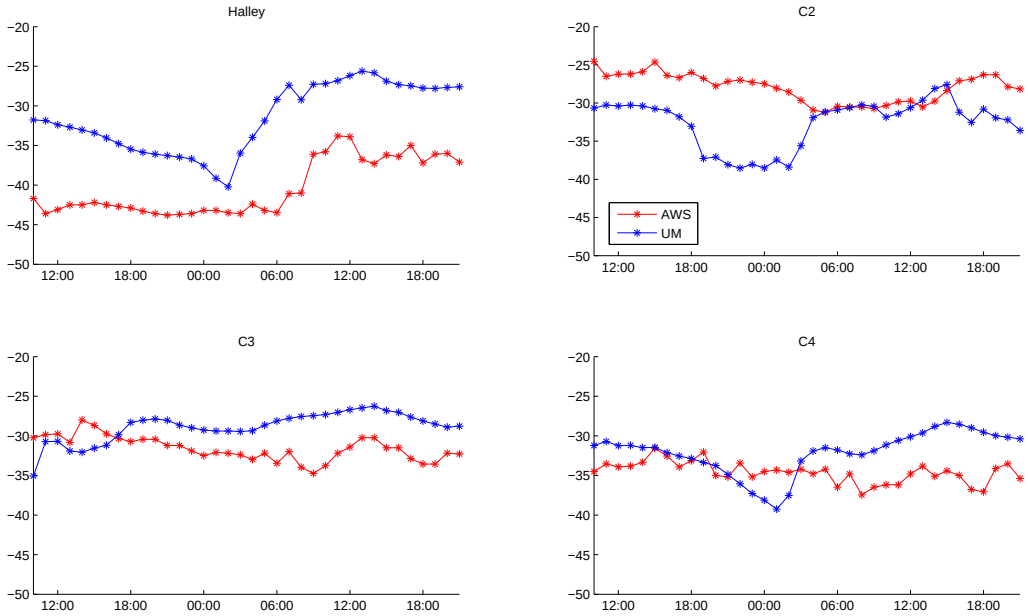

Figure 3.37: Air temperature (degrees Celsius) for 3 and 4 September 2002, from the model (in blue) and from AWS observations (in red).

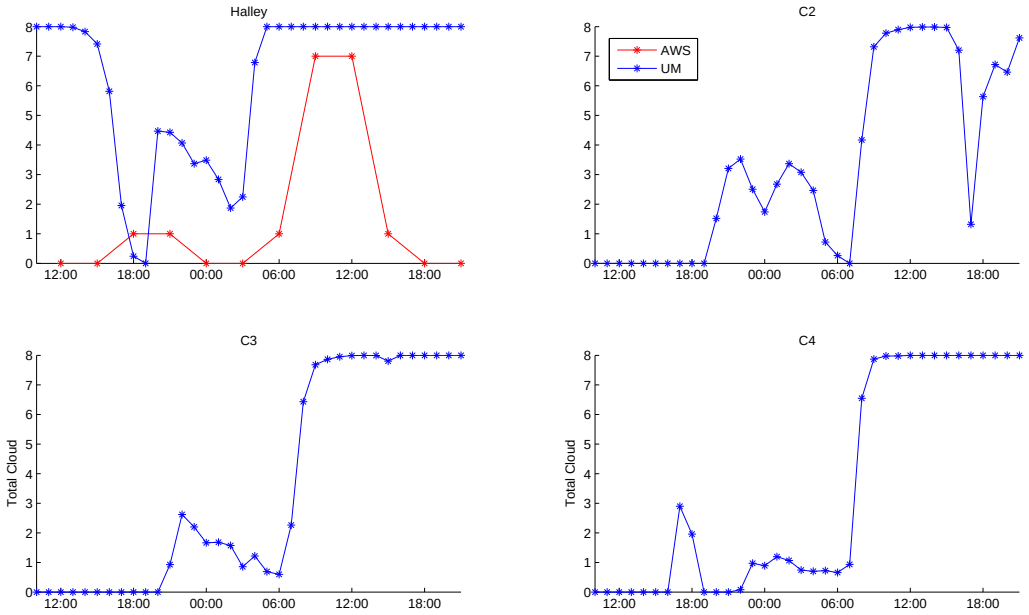

Figure 3.38: Cloud cover (in eighths) for 3 and 4 September 2002, from the model (in blue) and from synoptic observations at Halley (in red).

this too, but to a lesser extent. The model produces good results for C3 and C4, though temperatures during the second part of the run are overestimated by about 5 degrees by the model. At Halley, the model overestimates the temperature by about 9 degrees for the entire run. The rise in temperature that starts at 06 UTC in the AWS observations is simulated by the model, but about 4 hours too early. At C2, the model underestimates the temperature for the first half of the run, but during the second half of the run, the model captures the observed temperatures quite well. Figure 3.38 shows the total cloud cover from the model for all locations, and from synoptic observations at Halley. The model overestimates the cloud cover at Halley at nearly all times. This is likely the reason for the large overestimation of the temperature at Halley as seen in figure 3.37. For the other locations, the model shows clearer skies during the first half of the run, with cloud cover quickly increasing from about 6 UTC on 4 September. The satellite image in figure 3.39 shows clear skies just before 18 UTC, while the model shows full cloud cover for Halley, C3 and C4 at that time (see figure 3.38). This shows that for C3 and C4, the cloud cover is also overestimated by the model, resulting in overestimated temperatures (see figure 3.37). At C2, the model does show a period of clearer skies around 18 UTC. Earlier satellite images do show cloud cover for part of 4 September 2002 (not shown), as can be seen from the observations in figure 3.38 as well, but later satellite images (not shown) show clear skies again towards the end of 4 September, confirming that the model overestimates cloud cover at all locations during the last part of the run.

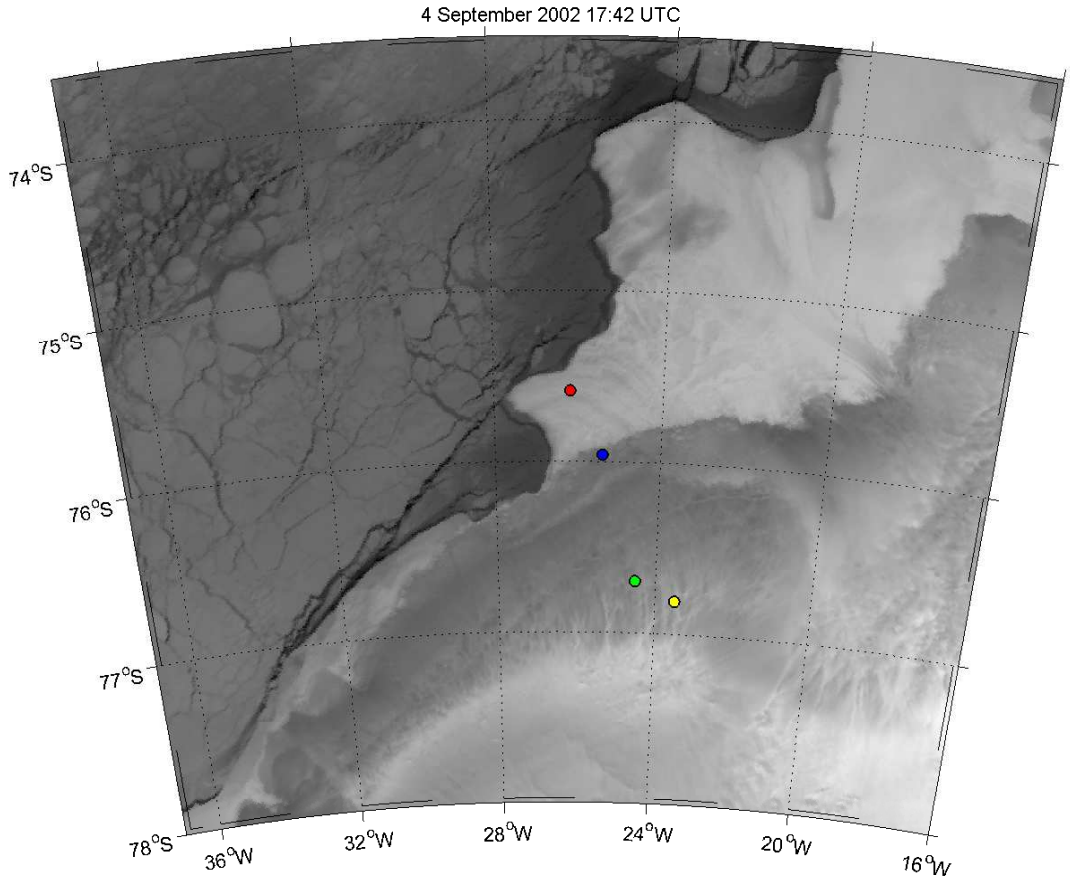

Figure 3.39: Infrared satellite image of 17:42 UTC 04 September 2002. The locations of Halley (in red), C2 (in blue), C3 (in green) and C4 (in yellow) are indicated.

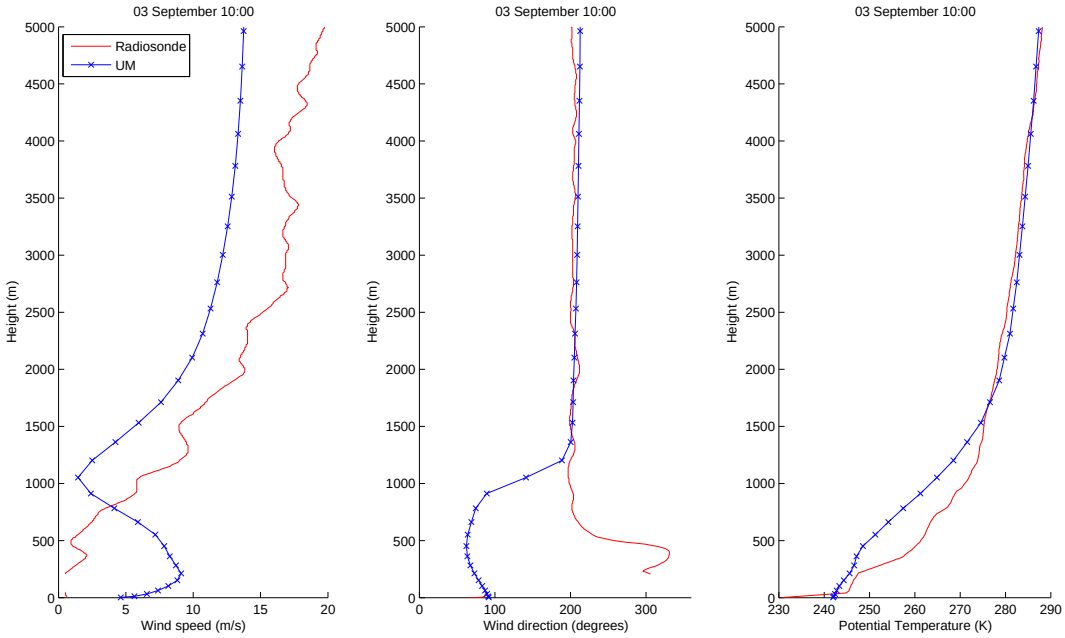

Figure 3.40: Profiles of wind speed (left), wind direction (middle) and potential temperature (right) from the model (in blue) and from radiosonde data (in red) at Halley for 10 UTC 3 September 2002.

3.3.3 Radiosonde comparison

Figure 3.40 shows the wind speed and wind direction profiles (on the left and in the middle respectively) for Halley for 10 UTC 03 September 2002. The profiles from the model do not match the radiosonde profiles very well. Wind speeds are overestimated by the model in the lowest part of the profile (below 800 m), and highly underestimated higher up. The wind direction in the lowest 1000 m of the profile is off by more than 100 degrees, higher up the shape of the profile is very well matched. Figure 3.41 shows the same profiles but for 10 UTC 04 September 2002. The model does a better job now. Wind speeds are overestimated by the model in the lowest 1000 m, but well represented higher up. The model does not represent the wind direction at the surface very well, but above 1 km the shape of the profile is very well represented.

Figure 3.40 shows the potential temperature profiles (on the right) from the model and from radiosonde data for 10 UTC 03 September 2002. The potential temperature at the surface is highly overestimated by the model, which fails to capture a very strong surface temperature inversion. The potential temperature is underestimated up to 1500 m, above that height the model matches the radiosonde profile very well. This situation has improved on 04 September, as shown in figure 3.41, where the model matches the radiosonde profile a lot better. Potential temperatures in the lowest 400 m are underestimated by the model by about 3 degrees, but above 800 m the model does a very good job.

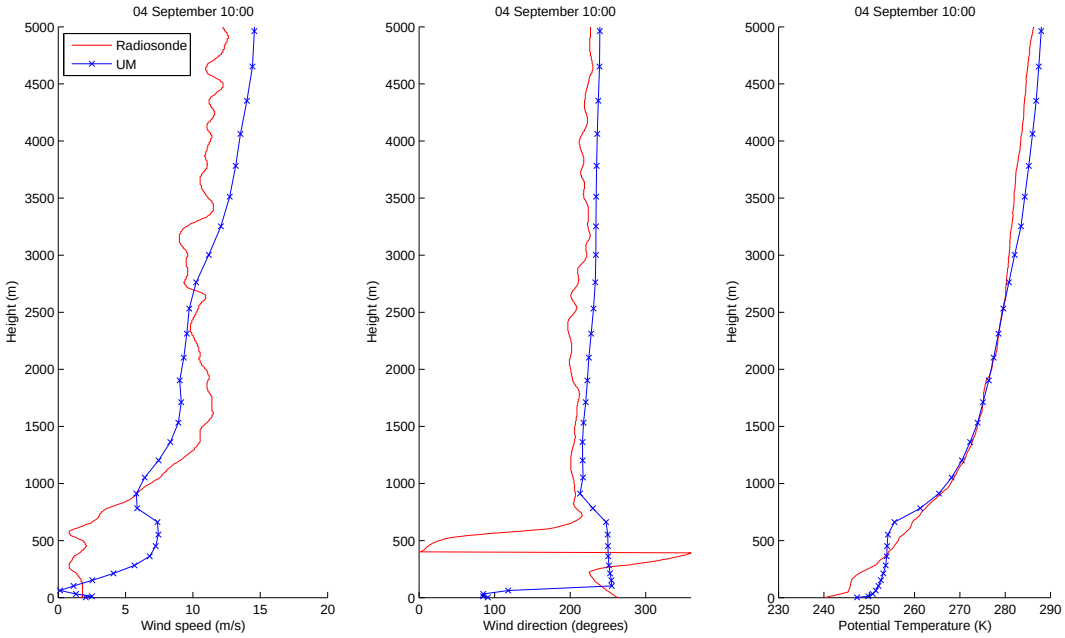

Figure 3.41: Profiles of wind speed (left), wind direction (middle) and potential temperature (right) from the model (in blue) and from radiosonde data (in red) at Halley for 10 UTC 4 September 2002.

3.3.4 Doppler Sodar comparison

Figure 3.42 shows downslope wind speeds from the model and from the Doppler Sodar as 15 min averages. The model shows more variability now as compared to the August 2003 case (see figure 3.20). Figure 3.36 showed that the surface wind speed at C2 is largely underestimated by the model. In the vertical profiles of figure 3.42 the model shows very low wind speeds, never exceeding 3 m/s. The Doppler observations initially show even lower wind speeds, but later on the lowest Doppler level reaches about 6 m/s, and thus the model strongly underestimates the wind speed. The model shows a mostly constant wind speed over height, while the observations often show up to 2 peaks in the wind speed profile. Figure 3.43 shows the wind directions from the model and from Doppler Sodar observations. The model shows a sudden change in wind speed happening around 17:30, when wind directions change from roughly 70-90 degrees over the whole profile to about 250 degrees, a change of 180 degrees. This can also be seen in figure 3.36. At certain times, the shape of the wind direction profile is well matched, for example at 16:45 the model does pick up the change in wind direction between a height of 50 and 100 m, but generally the model does not match the Doppler profiles very well when comparing individual soundings, neither for the wind speed or the wind direction. The model initially shows a backing of the wind direction with height over the lowest 100 m, but after the change in wind direction, the model shows a veering of the wind direction in the lowest 100 m. The observations mostly (but not always) show a backing of the wind with

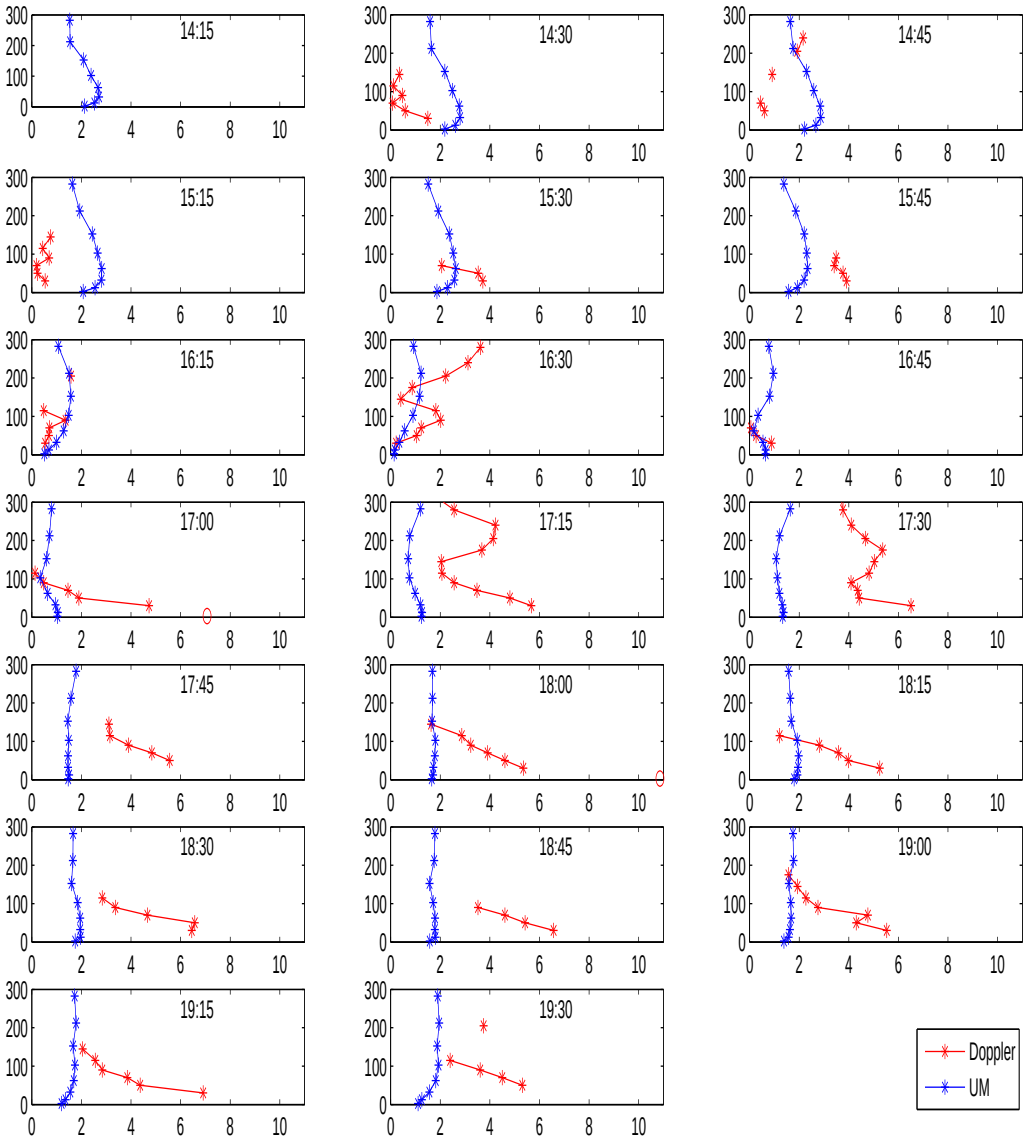

Figure 3.42: Downslope wind speed at the C2 station from the model (in blue) and from the Doppler sodar (in red), for 04 September 2002. At every whole hour, the 3m wind speed as measured by the AWS is indicated by a red circle. Note that the AWS observations are 10s averages while the Doppler measurements are 15min averages.

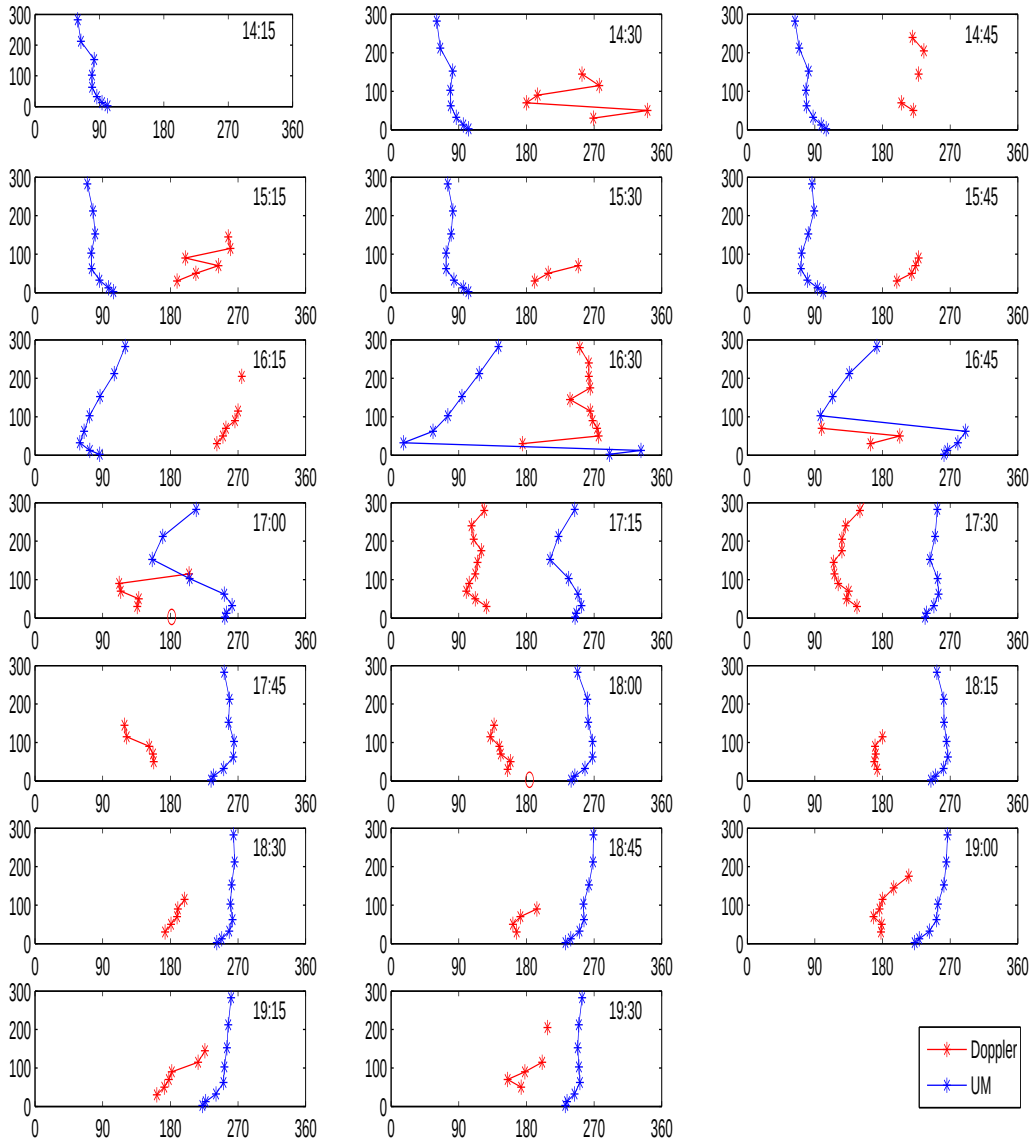

Figure 3.43: Wind direction at the C2 station from the model (in blue) and from the Doppler sodar (in red), for 4 September 2002. At every whole hour, the wind direction at a height of 3m as measured by the AWS is indicated by a red circle. Note that the AWS observations are 10s averages while the Doppler measurements are 15min averages.

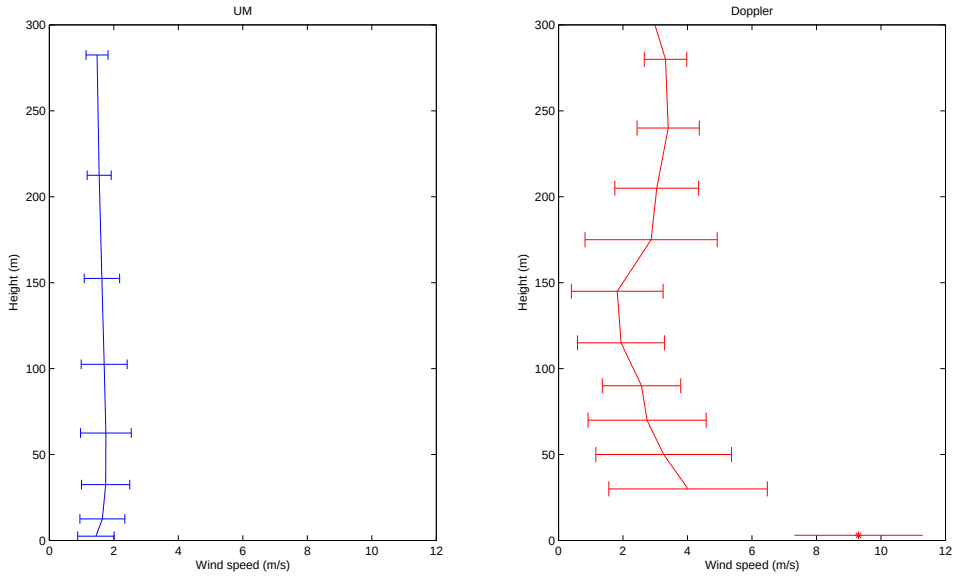

Figure 3.44: Average profiles of wind speed (m/s) taken from 15 minute averaged profiles between 1415 UTC and 1930 UTC for 4 September 2002, on the right from Doppler Sodar observations and on the left from model output. The errorbars indicate the standard deviation. The lowest data point in the Doppler Sodar plot comes from the AWS hourly measurements.

height, which, as discussed previously, is due to the decrease of frictional forcing with height.

Figure 3.44 shows the average over all profiles shown in figure 3.42, both for the model and for the Doppler observations. The model shows very low wind speed and underestimates the wind speeds over the entire profile when compared to the Doppler observations.

3.3.5 Summary

The large scale synoptic situation is reasonably well represented by the model, though on the smaller scale the perturbation pressure is not very well captured at the lower part of the slope. The model underestimates the wind speed at all sites except Halley. The wind direction is well represented most of the time. At Halley, the cloud cover is overestimated for a large part of the run, which results in overestimated temperatures. The model does not represent the Doppler Sodar profiles very well, neither in wind speed or in wind direction. The wind speed is underestimated over the entire profile.

In conclusion, the model does not perform very well for this case study. We have decided to focus on the August 2003 case for the sensitivity experiments, so this case study will not be discussed any further in this thesis.

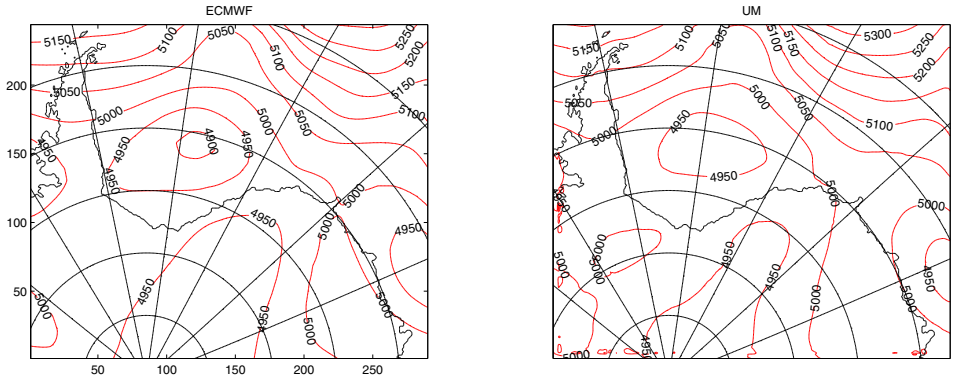

Figure 3.45: Geopotential height at 500 mb (in metres) at 12 UTC 21 February 2002 (T+12), from the ECMWF Operational Analysis (left panel) and from the model run (right panel).

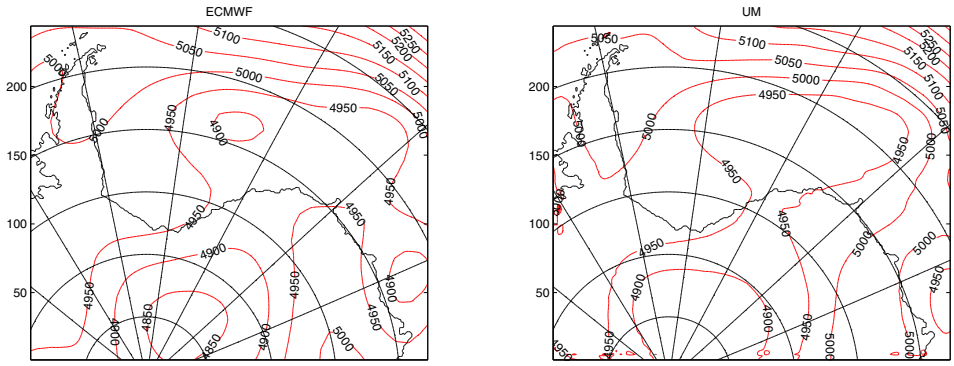

Figure 3.46: Geopotential height at 500 mb (in metres) at 12 UTC 22 February 2002 (T+36), from the ECMWF Operational Analysis (left panel) and from the model run (right panel).

3.4 Summer case study: February 2002

3.4.1 Large scale

Figures 3.45, 3.46, 3.47 and 3.48 show the geopotential height at 500 mb over the 12km domain for 12 UTC on 21, 22, 23 and 24 February 2002 respectively, from the model as well as from the ECMWF Operational Analysis. An area of low geopotential height is present to the north of Coats Land, moving eastward on 23 February. On 24 February, a weak trough in geopotential height has formed north of Coats Land, with areas of high geopotential height present outside of the domain. The model performs reasonably well compared to the ECMWF Operational Analysis, though it slightly overestimates the geopotential height especially in the first model run (figures 3.45 and 3.46). The second model run (figures 3.47 and 3.48) compares very well to the Operational Analysis. The

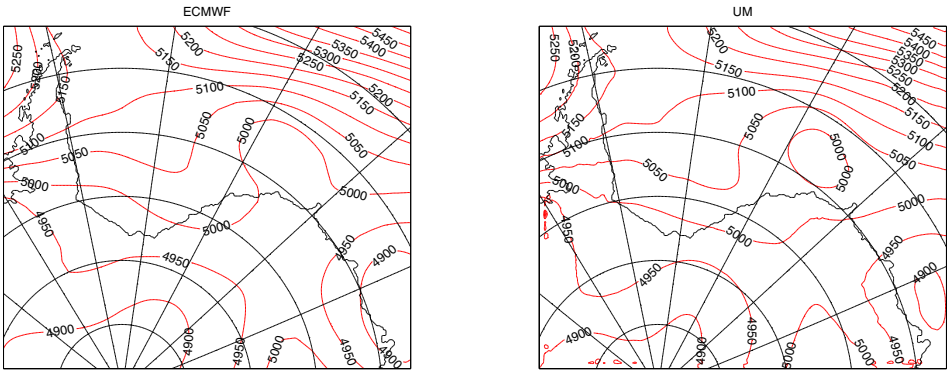

Figure 3.47: Geopotential height at 500 mb (in metres) at 12 UTC 23 February 2002 (T+12), from the ECMWF Operational Analysis (left panel) and from the model run (right panel).

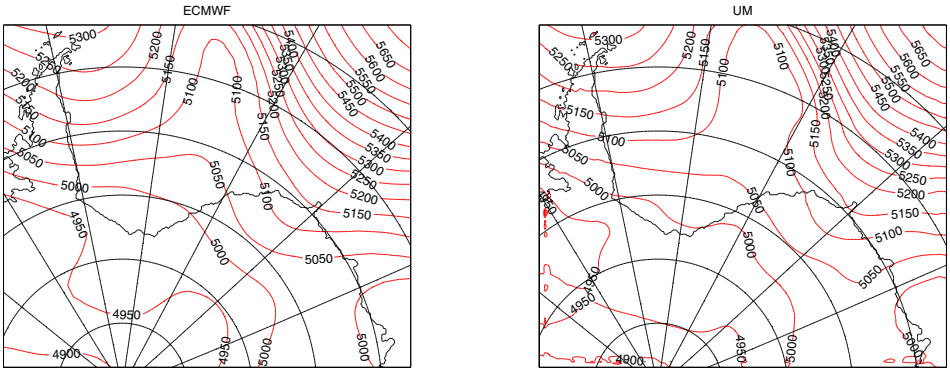

Figure 3.48: Geopotential height at 500 mb (in metres) at 12 UTC 24 February 2002 (T+36), from the ECMWF Operational Analysis (left panel) and from the model run (right panel).

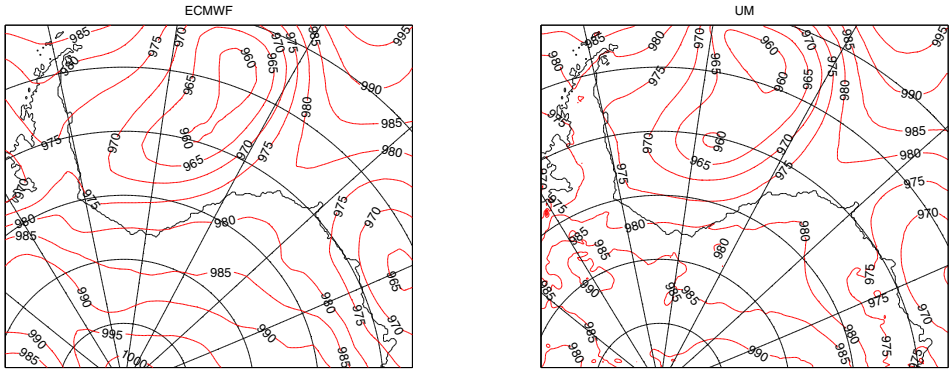

Figure 3.49: Mean Sea Level Pressure (in mb) at 12 UTC 21 February 2002 (T+12), from the ECMWF Operational Analysis (left panel) and from the model run (right panel).

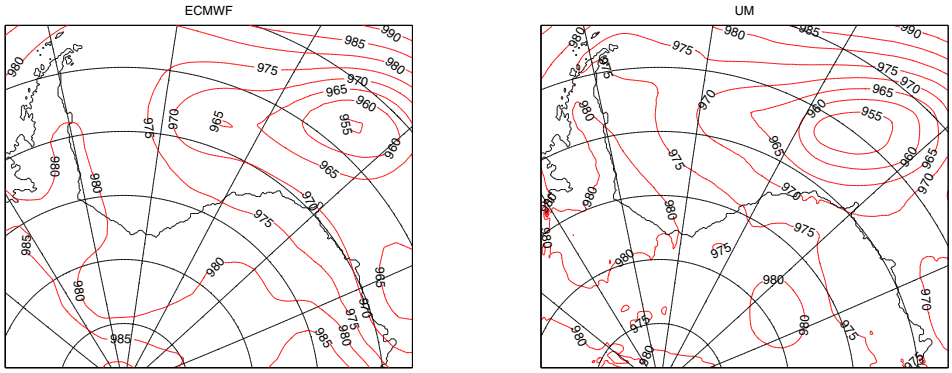

Figure 3.50: Mean Sea Level Pressure (in mb) at 12 UTC 22 February 2002 (T+36), from the Operational Analysis (left panel) and from the model run (right panel).

absolute domain-averaged error for the geopotential height at 500 mb ranges from 16.5 to 35.8 m over both runs.

Figures 3.49, 3.50, 3.51 and 3.52 show the mean sea level pressure over the 12km domain for 12 UTC on 21, 22, 23 and 24 February 2002 respectively, from the model as well as from the ECMWF Operational Analysis. A low pressure area moves eastwards during the first two days, and has moved outside the domain by 23 February. Another low pressure area is present on 24 February. These low pressure areas are far from Coats Land, the area of interest, and will not influence the synoptic situation in this area. A smaller and much weaker low pressure area starts to form over the continent east of Coats Land on 24 February. The model compares very well to the ECMWF Operational Analysis, also at T+36 (figures 3.50 and 3.52). The model tends to slightly underestimate the mean

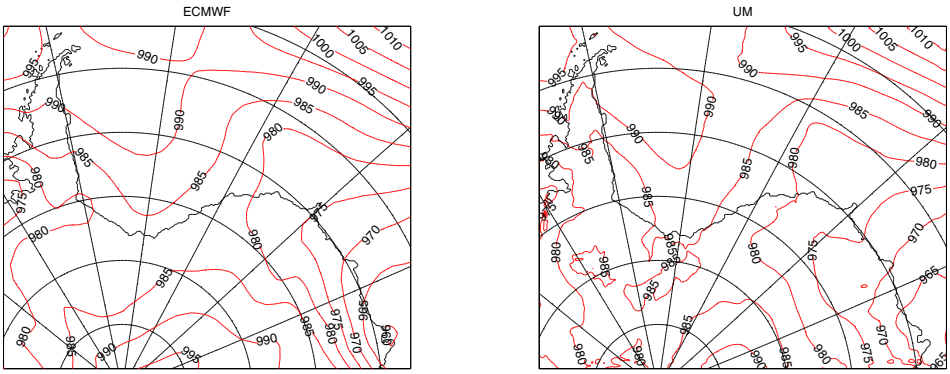

Figure 3.51: Mean Sea Level Pressure (in mb) at 12 UTC 23 February 2002 (T+12), from the ECMWF Operational Analysis (left panel) and from the model run (right panel).

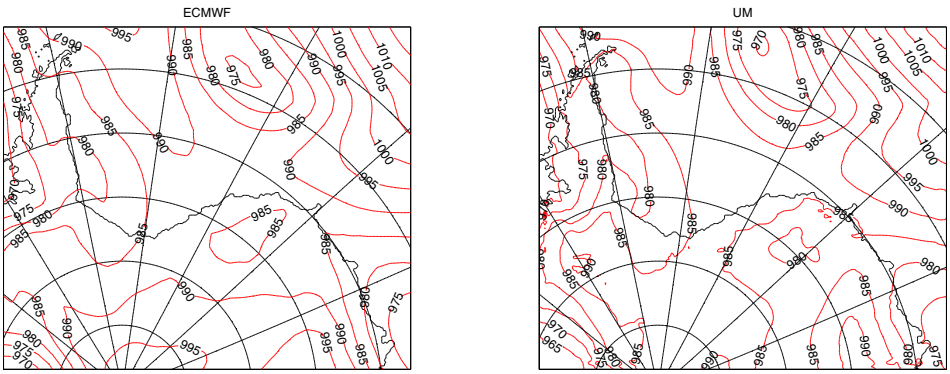

Figure 3.52: Mean Sea Level Pressure (in mb) at 12 UTC 24 February 2002 (T+36), from the ECMWF Operational Analysis (left panel) and from the model run (right panel).

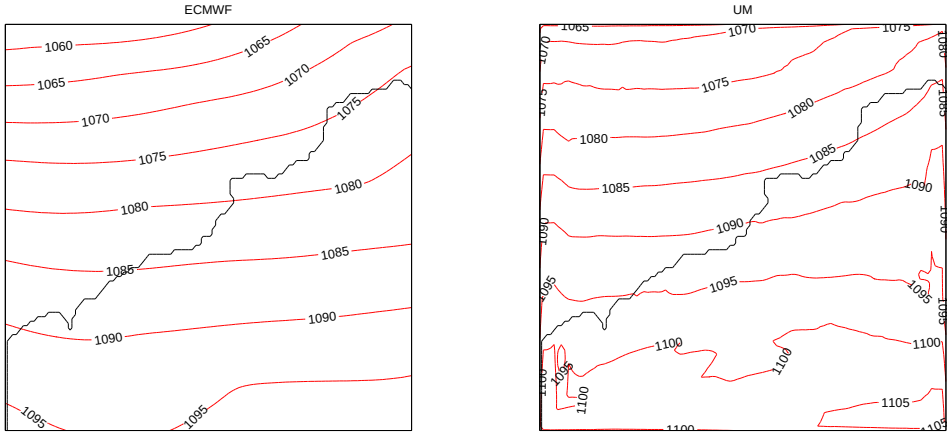

Figure 3.53: Geopotential height at 850 mb (in metres) at 12 UTC 21 February 2002 (T+12), from the ECMWF Operational Analysis (left panel) and from the model 4 km run (right panel).

sea level pressure, especially later on in the model runs. The absolute domain-averaged error for mean sea level pressure (only over sea) ranges from 1.5 to 2.4 mb over both runs.

To investigate the synoptic situation on a smaller scale, figures 3.53 to 3.56 show the geopotential height at 850 mb over the 4 km domain at 12 UTC for 21-24 February, for both the model results (from the 4 km model run) and from ECMWF operational reanalysis data. The model results are much more similar to the ECMWF reanalysis than in either of the winter cases, though the model overestimates the geopotential height at 850 mb. The general pattern is well represented, though at the end of the model simulation (figure 3.56, the model shows a stronger gradient in geopotential height compared to the ECMWF reanalysis.

3.4.2 AWS comparison

Figure 3.57 shows the perturbation from the mean surface pressure from the model and from AWS observations. All locations show a decrease in surface pressure over the first 24 hours, followed by an increase in surface pressure during the remainder of the model runs. The model performs very well compared to the observations, except towards the end of the second model run where a rapid increase in surface pressure is underestimated by the model at all locations. Figure 3.58 shows the perturbation from the mean differences in surface pressure between two observation locations. For the C3-C4 pair the perturbations are very small and the model performs very well compared to the observations. For the Halley-C2 and C2-C3 pairs, the model predicts the general trend very well, but especially towards the end of the first model run (late on 22 February) the

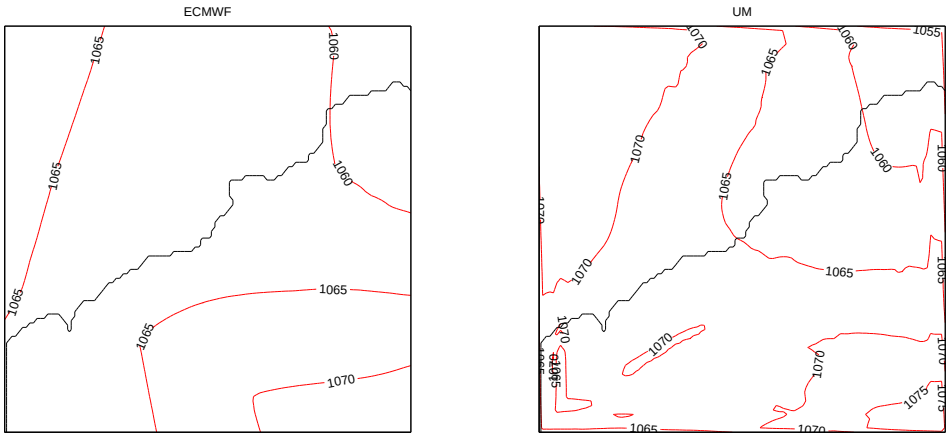

Figure 3.54: Geopotential height at 850 mb (in metres) at 12 UTC 22 February 2002 (T+36), from the ECMWF Operational Analysis (left panel) and from the model 4 km run (right panel).

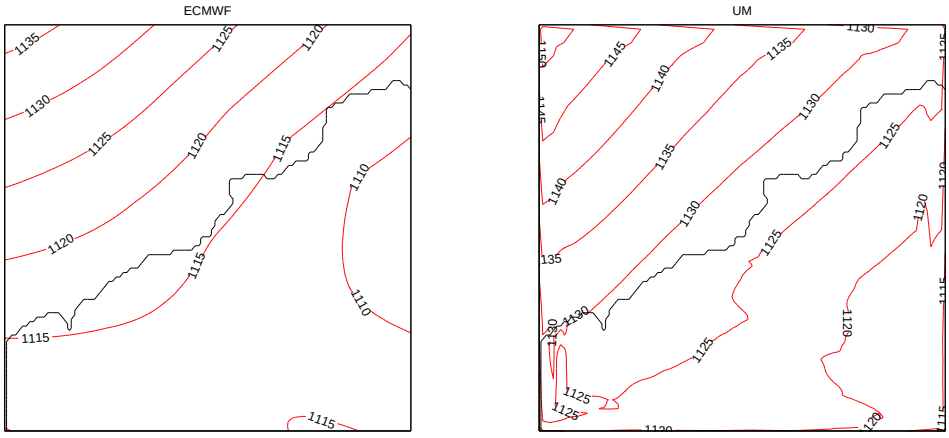

Figure 3.55: Geopotential height at 850 mb (in metres) at 12 UTC 23 February 2002 (T+12), from the ECMWF Operational Analysis (left panel) and from the model 4 km run (right panel).

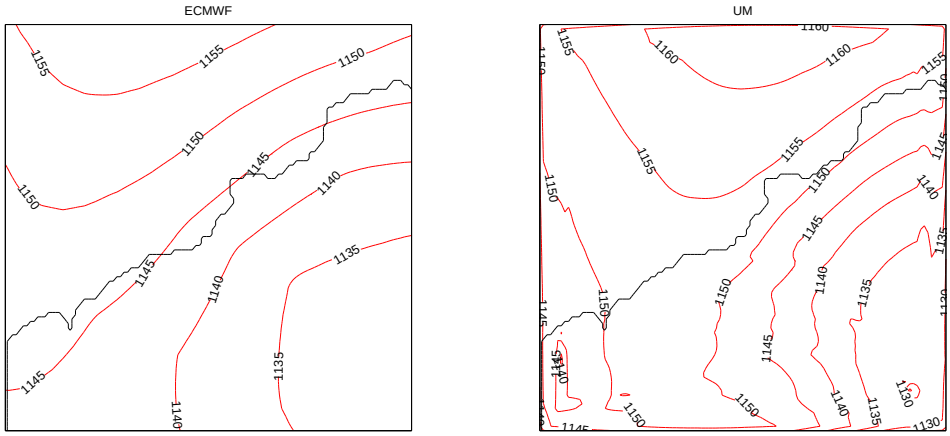

Figure 3.56: Geopotential height at 850 mb (in metres) at 12 UTC 24 February 2002 (T+36), from the ECMWF Operational Analysis (left panel) and from the model 4 km run (right panel).

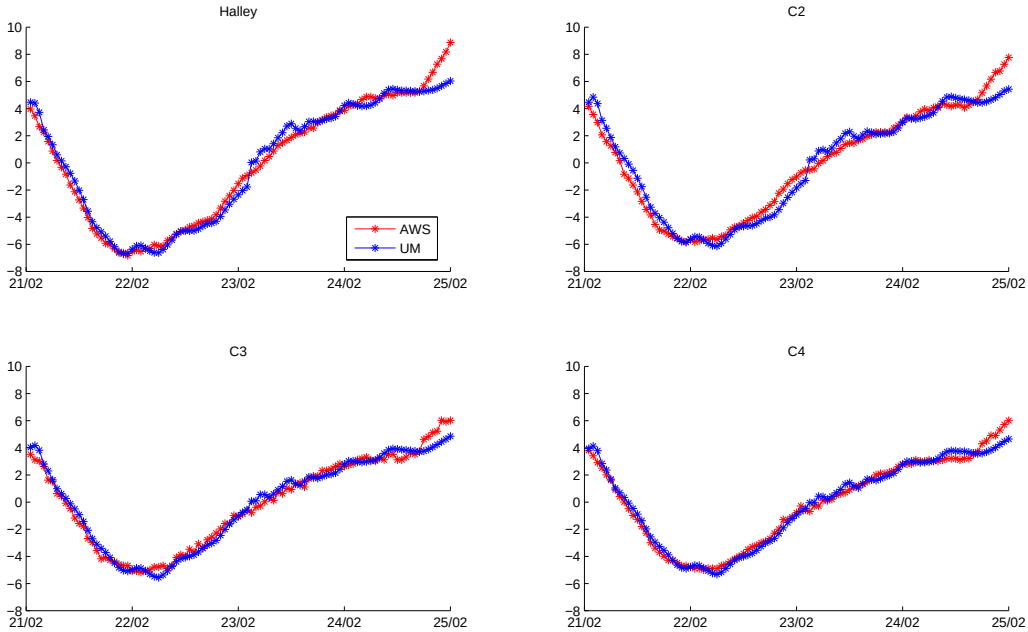

Figure 3.57: Perturbation from the mean (over 96 hours) surface pressure (mb), from the model (in blue) and from AWS observations (in red), for 21-25 February 2002.

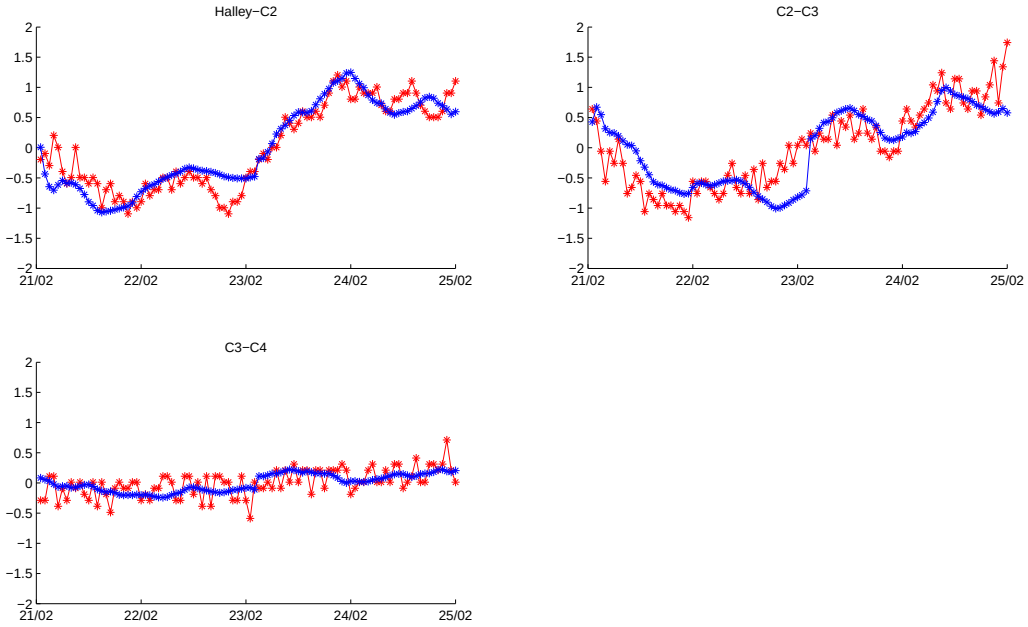

Figure 3.58: Perturbation from the mean (over 96 hours) difference in surface pressure (mb) between Halley and C2 (top left), C2 and C3 (top right) and C3 and C4 (bottom left), from the model (in blue) and from observations (in red), for 21-25 February 2002.

model starts to move away from the observations. This is then corrected in the second model run. During the first part of the first model run, the model slightly underestimates the perturbation of the mean difference between Halley and C2 while overestimating the perturbation between C2 and C3. Overall the performance for this case, in terms of p', is a little better than the winter cases.

Figure 3.59 shows wind vectors for both the model and observations. Both the model and the observations show a diurnal variation in the wind speed, though this is clearer in the model. The wind direction at all locations is southerly (downslope). The model shows this only at C2, at other locations the wind also has northerly (upslope) components. The model underestimates the wind speed at C2, especially later into the run. At Halley, the AWS observations show very variable winds, something not picked up by the model. The diurnal cycle in wind speed has been shown in previous studies, for example by Heinemann (1999) over the Greenland ice sheet, and Heinemann (1997) and Gallée and Pettre (1998) over Antarctica. Previous studies have also shown that although katabatic winds have a clear diurnal cycle in the wind speed, the wind directions are often remarkably constant, something which we find for this case study as well at C2, both in the model and in the observations. For example, Parish *et al.* (1993b) studied the diurnal cycle of katabatic wind at Adelie Land in late February (using a two-dimensional numerical model, and setting a solar declination angle of -10 °) and found that the wind speed is reduced by more than half of the strongest wind speed during one diurnal cycle, which is similar to the results of this study

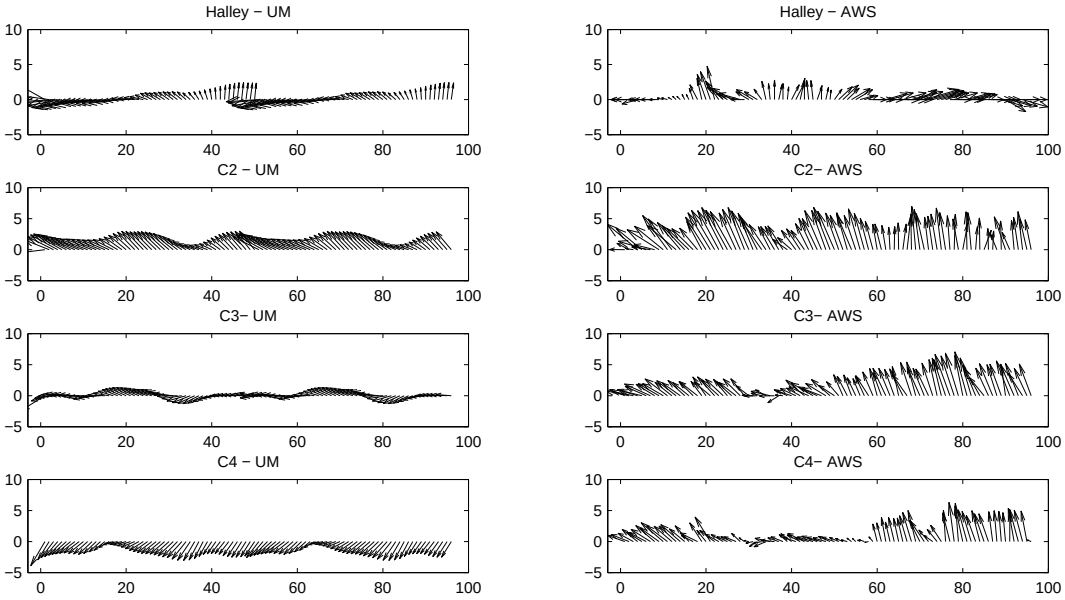

Figure 3.59: Wind vectors from the model (on the left) and from AWS observations (on the right). The x-axis shows hours from 01 UTC 21 February 2002. The y-axis points North.

(both from the model and from AWS observations). The wind directions however vary by only about 20 degrees during each cycle in the study by Parish *et al.* (1993b), which again compares very well to both our model results and the AWS observations at C2. However, at C3, the wind direction also shows a diurnal cycle, showing roughly a downslope wind during the night changing to a cross-slope wind during the day. This interesting result is not supported by the AWS observations at C3, which show a constant downslope wind except for a few hours during the second day (30-35 hours into the run) where the winds become slightly more cross-slope (see figure 3.59). At C4, the model shows a slight diurnal cycle, with weaker winds during the night, though the wind is directed upslope. There is no diurnal cycle present at the AWS observations at C4 however, and wind directions are mostly downslope to cross-slope. It is unclear why the model shows upslope winds at C4. In the August 2003 case this could be explained by the synoptic situation, but in this case the synoptic situation would result in downslope winds.

Figure 3.60 shows the air temperature from the model and from AWS observations. Here we can clearly see the diurnal variation of the temperature at all locations. The model is able to represent the diurnal variation, but underestimates the amplitude of this diurnal variation at all locations. At C3 and C4 the model also shows a delay in the diurnal cycle of about 1-2 hours compared to the observations. At Halley, and to a lesser extent at C2, the model overestimates

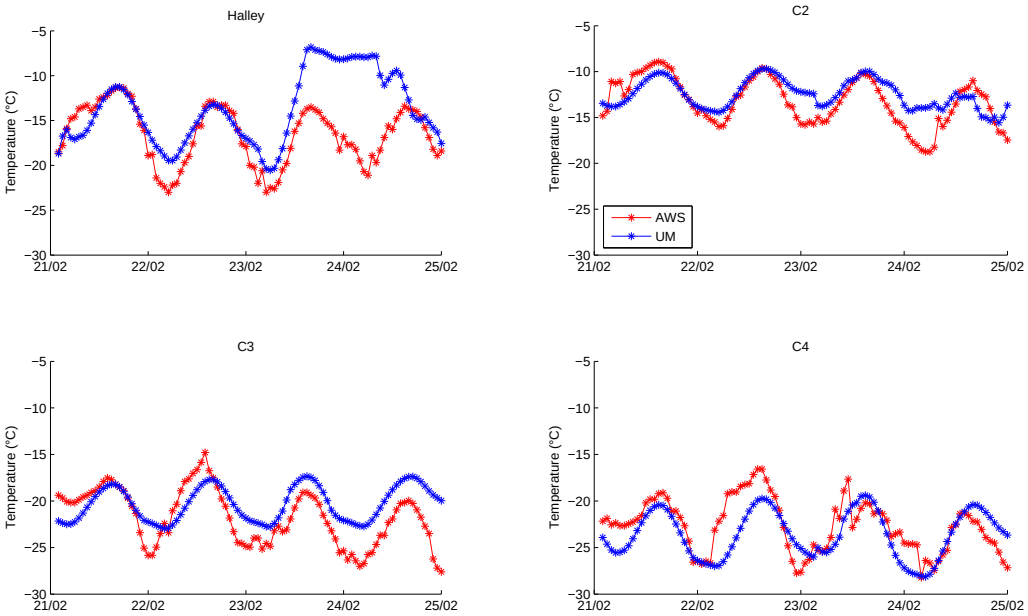

Figure 3.60: Air temperature (degrees Celsius) for 21-25 February 2002, from the model (in blue) and from AWS observations (in red).

the surface temperature during the last two days of the run as well as hardly showing a diurnal cycle during this period. It is unclear why the model shows such constant surface temperatures at Halley during 23 and 24 February. Long periods of constant temperatures during the Antarctic summer are not found in the observations. Despite Renfrew and Anderson (2002) showing that during the summer the temperature generally decreases with elevation, the temperature at C2 is still higher than at Halley.

Parish *et al.* (1993b) found an idealised diurnal cycle for temperature at Adelie Land with an amplitude of 12 degrees Celsius. The amplitude of the diurnal cycle in temperature at Halley is comparable but slightly weaker, about 10 degrees Celsius. Ishikawa *et al.* (1990) also studied the variation of meteorological features in Adelie Land during the summer season, but using only observations. They find similar diurnal variation in the temperature and wind speed, and also very small variations in wind direction. In addition, they note that the maximum in the wind speed occurs about 2 hours after the minimum in surface temperature, while the lowest wind speeds were observed 5 hours after the maximum surface temperature (Ishikawa *et al.*, 1990). This delay can be explained by the fact that cooling of the air near the surface is one of the driving forces behind the katabatic wind, and it takes some time for the wind speeds to adjust to the cooling temperatures. The model results for C2 show roughly the same pattern; the wind extremes occur a few hours later than the temperature extremes, and

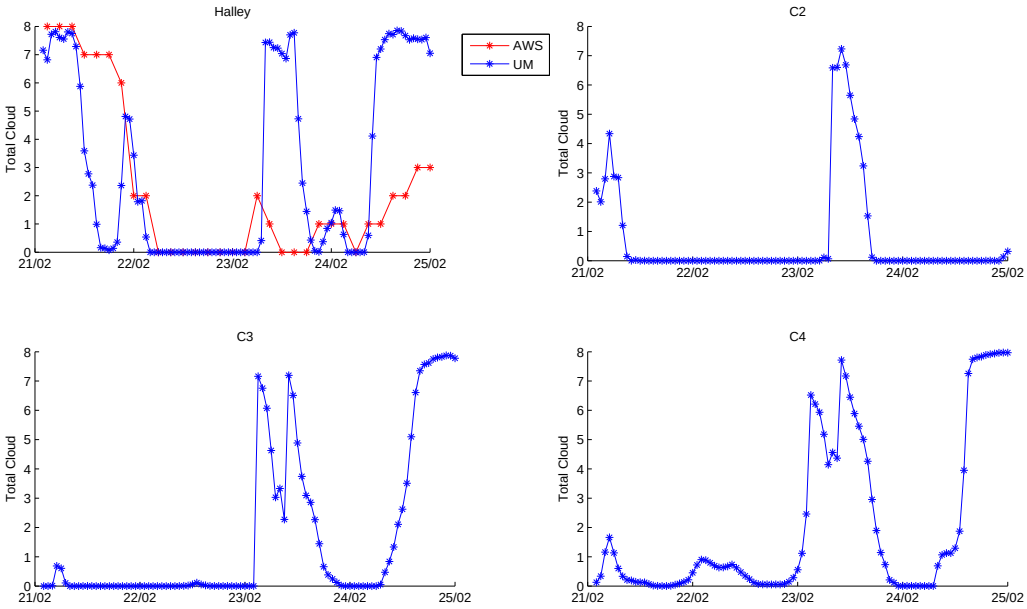

Figure 3.61: Cloud cover (in eighths) for 21-25 February 2002, from the model (in blue) and from synoptic observations at Halley (in red).

this difference is greater during the day. The AWS observations do not show this so clearly however. This is partly because the wind speed is quite variable and it is hard to determine the exact time of the maximum or minimum in the wind speed. During the day, the minimum wind speed occurs either at the same time or about an hour later than the temperature maximum. During the night, the maximum wind speed sometimes appears to occur a few hours before the minimum temperature is reached. We are using the temperature at a height of 3 m instead of the surface temperature, which means the minimum and maximum will occur slightly later than at the surface. This might explain why the wind speed maximum sometimes occurs after the minimum temperature is reached.

Figure 3.61 shows the cloud cover from the model, and for Halley also from synoptic observations. The observations show a very cloudy start of 21 February, slowly clearing up to clear skies on 22 February. On 23 February there are partly cloudy periods with clear skies in between. From 24 February the cloud cover starts to increase. The model does show this general trend, but often shows fast changes from clear sky to fully cloudy skies. For 23 and 24 February the model overestimates the cloud cover. The overestimated cloud cover at Halley during 23 and 24 February explains the overestimation of surface temperature at that time, though there is no visible effect on the surface temperature when the cloud cover goes down a lot during the late hours of 23 February and early hours of 24 February. In general, changes in cloud cover do not seem to affect the surface temperatures in the model very much. This could indicate that the model underestimates the optical thickness of the clouds, as clouds with a low optical thickness have less influence on the surface temperatures than clouds with

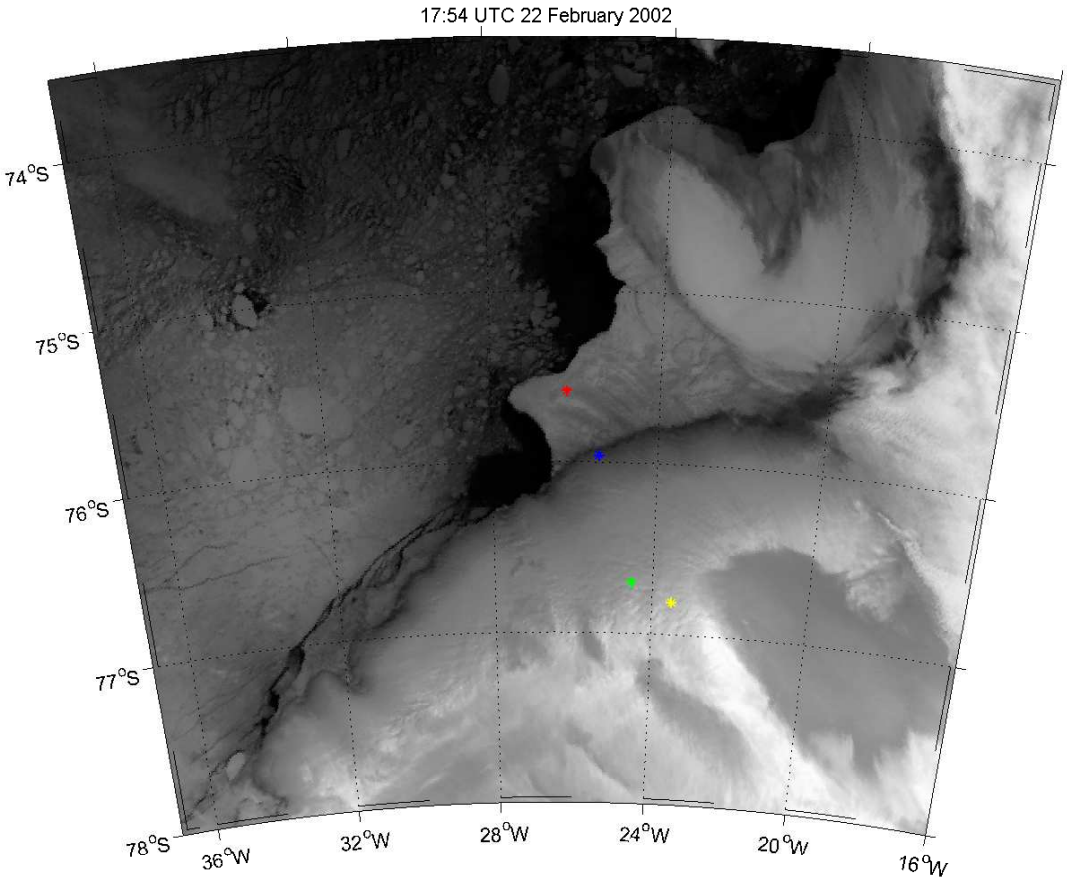

Figure 3.62: Infrared satellite image of 17:54 UTC 22 February 2002. The locations of Halley (in red), C2 (in blue), C3 (in green) and C4 (in yellow) are indicated.

a high optical thickness. For C2, C3 and C4 there are no cloud cover observations available. The model predicts mostly clear skies for 21 and 22 February, while 23 February is mostly cloudy. On 24 February, the model shows fast increasing cloud cover except at C2 where the model shows clear skies. This could explain why the model overestimates the temperature (see figure 3.60) for C3 and C4 at 24 February.

Figure 3.62 shows an infrared satellite image for 17:54 UTC 22 February 2002. At this time, there are clear skies at all AWS locations (see figure 3.60). The satellite image shows clear skies over a large area. There is some cloud cover over the Brunt Ice Shelf, but far to the east of Halley. The satellite image shows warm flow stripes over the ice shelf towards Halley, a phenomenon discussed in Anderson (2005). These warm flow stripes are lines of thicker ice shelf, but the mechanism behind the strength of the thermal infrared signature (which do not always show the same strength under similar circumstances) is still uncertain (Anderson, 2005). Earlier satellite images (not shown) do show some cloud cover

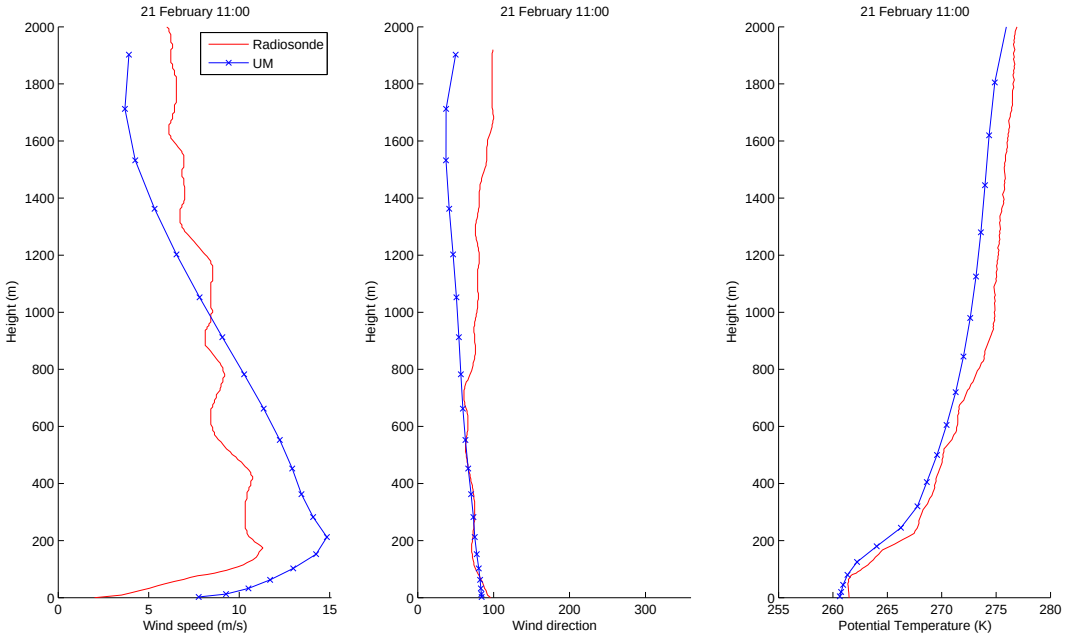

Figure 3.63: Profiles of wind speed (left), wind direction (middle) and potential temperature (right) from the model (in blue) and from radiosonde data (in red) at Halley for 11 UTC 21 February 2002.

towards the end of 21 February over the ice shelf and lowest part of the slope (captured by the model only for Halley), which has completely cleared by the early hours of 22 February though some cloud cover is present on the top of the slope (captured very well by the model). The high cloud cover shows in figure 3.61 for 23 February can not be confirmed by satellite images, and the model overestimates the cloud cover for this day.

3.4.3 Radiosonde comparison

Figures 3.63, 3.64, 3.65 and 3.66 show the wind speed and wind direction profiles (on the left and in the middle, respectively) for Halley for 11 UTC 21, 22, 23 and 24 February respectively, from radiosonde data and from the model. On 21 February (figure 3.63) the model overestimates the wind speed by up to 4 m/s for the lowest km of the profile. Higher up, the model underestimates the wind speed by up to 3 m/s. The general shape of the profile matches the observations, and the peak of the jet is also located at about the right height. The wind direction from the model matches the observations very well, especially in the lower 800 m. On 22 February (figure 3.64) the model slightly underestimates the wind speed for most of the profile, although overall it does a good job. The wind direction at the surface is well represented by the model, but higher up the model shows an increasing bias. On 23 February (figure 3.65) the wind speed is represented quite well by the model, though the model underestimates the wind speed in the lowest 100 m. The wind directions in the lowest 500 m are not very

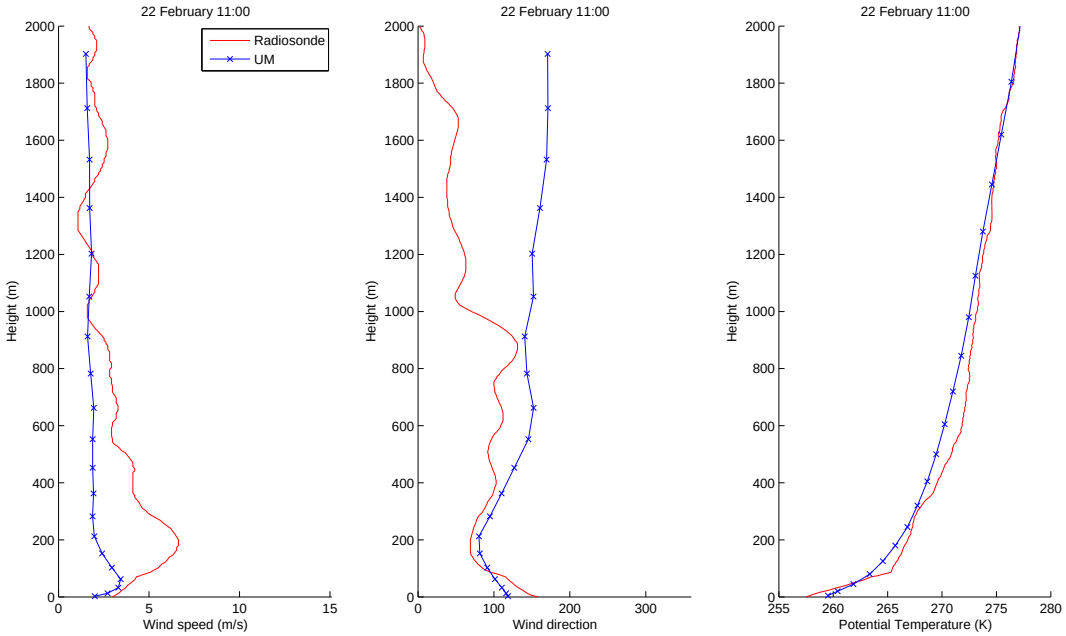

Figure 3.64: Profiles of wind speed (left), wind direction (middle) and potential temperature (right) from the model (in blue) and from radiosonde data (in red) at Halley for 11 UTC 22 February 2002.

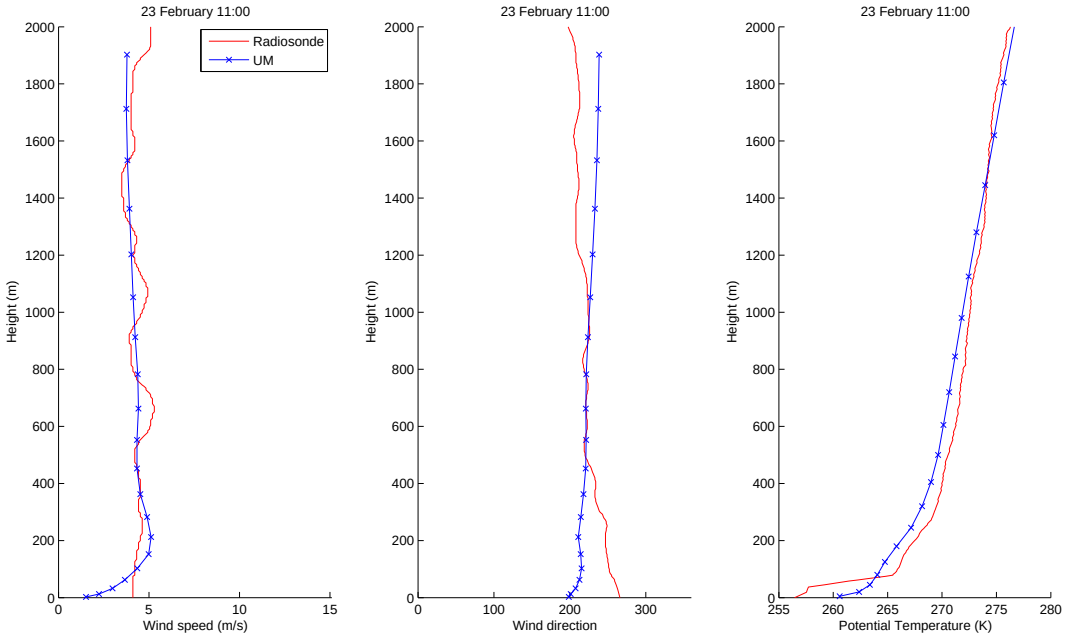

Figure 3.65: Profiles of wind speed (left), wind direction (middle) and potential temperature (right) from the model (in blue) and from radiosonde data (in red) at Halley for 11 UTC 23 February 2002.

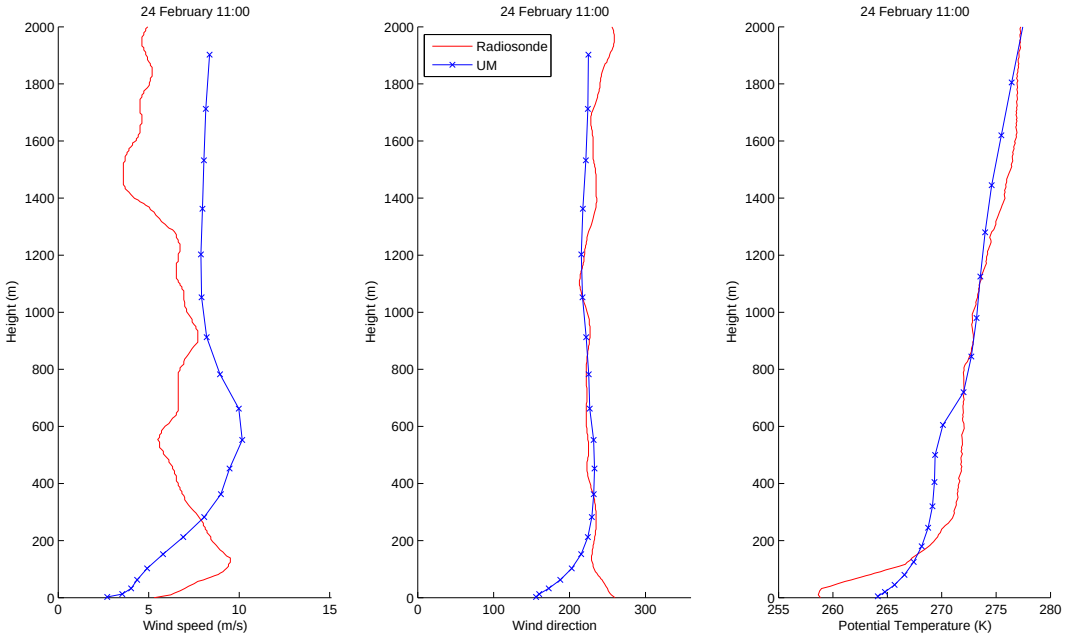

Figure 3.66: Profiles of wind speed (left), wind direction (middle) and potential temperature (right) from the model (in blue) and from radiosonde data (in red) at Halley for 11 UTC 24 February 2002.

well represented by the model. On 24 February (figure 3.66) the wind profiles from the model do not match the radiosonde data very well. In the first 200 m of the profile, the wind speed is underestimated by the model by about 4 m/s and the peak of the wind jet is located much too high in the model. The wind directions are not very well captured by the model in the lowest 150 m, while higher up the model profile matches the radiosonde profile very well.

Figure 3.63 shows profiles of potential temperature (on the right) for 1100 UTC 21 February 2002, from radiosonde data and from the model. The model profiles matches the observations quite well. The model underestimates the potential temperature by about 1 K in the lowest 700 m of the profile and by about 2-3 K higher up, but the shape of the profile matches the observations very well. On 22 February (figure 3.64) the model overestimates the potential temperature at the surface, while showing an underestimation of 1-2 K higher up. Again, the shape of the profile matches the radiosonde profile very well. On 23 February (figure 3.65), the model overestimates the surface temperature by 4 K, and the general shape of the profile does not match the observations below 200 m. Higher up, the model compares very well to the observations. On 24 February (figure 3.66), again the model overestimates the potential temperature at the surface by 5 K and here the model profile does not compare well with the observed profile over the total height of the profile.

In general, looking at figures 3.63 to 3.66, we can conclude that the model does a better job for the first part of the model run (21 and 22 February) compared to

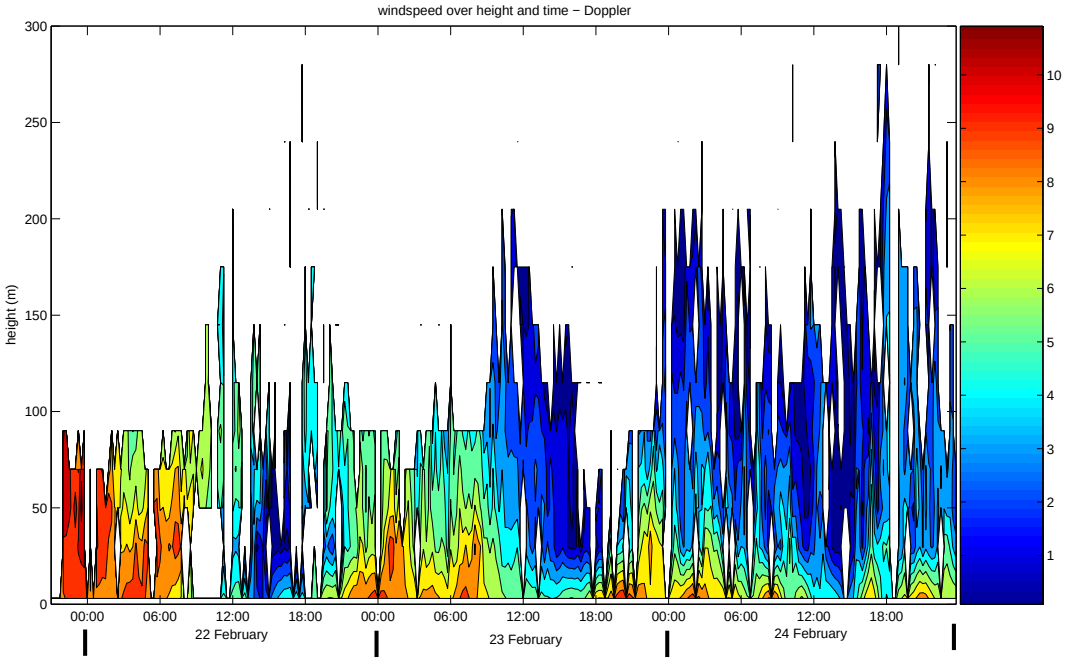

Figure 3.67: Wind speed over height and time from the Doppler Sodar (15 minute averages every 15 minutes), for 21-24 February 2002. The lowest level is provided by the AWS at the same location. Note that the AWS observations are taken at a height of 3 m, while the lowest Doppler level is at 30 m. This causes the gradients in the lowest levels.

the second part of the model run (23 and 24 February). Also, the performance of the model in representing the shape of the profile is very similar for all three profiles (wind speed, wind direction and potential temperature); either the model represents all three profiles well, or it does poorly for all three.

3.4.4 Doppler Sodar comparison

Figure 3.67 shows the wind speed over height and time from the Doppler Sodar for 21-24 February 2002. The measurements show a clear diurnal cycle, with maximum wind speeds during the night (between 18:00 and 08:00 UTC) and much lower wind speeds during the day (between 06:00 and 18:00). This diurnal signal extends to a height of at least 100 m. Unfortunately the core of the katabatic jet seems to fall in the gap between the AWS measurements at a height of 3 m and the lowest Doppler level at 30 m. Figure 3.68 is similar to figure 3.67 but showing the model results. The model also shows a clear diurnal cycle, with maximum wind speeds during the night and minimum wind speeds during the day. The diurnal signal is visible up to a height of 300 m, not just at the surface. The core of the katabatic jet is located at a height of about 60-70 m in the model. This is too high compared to the Doppler observations (figure 3.67). During the

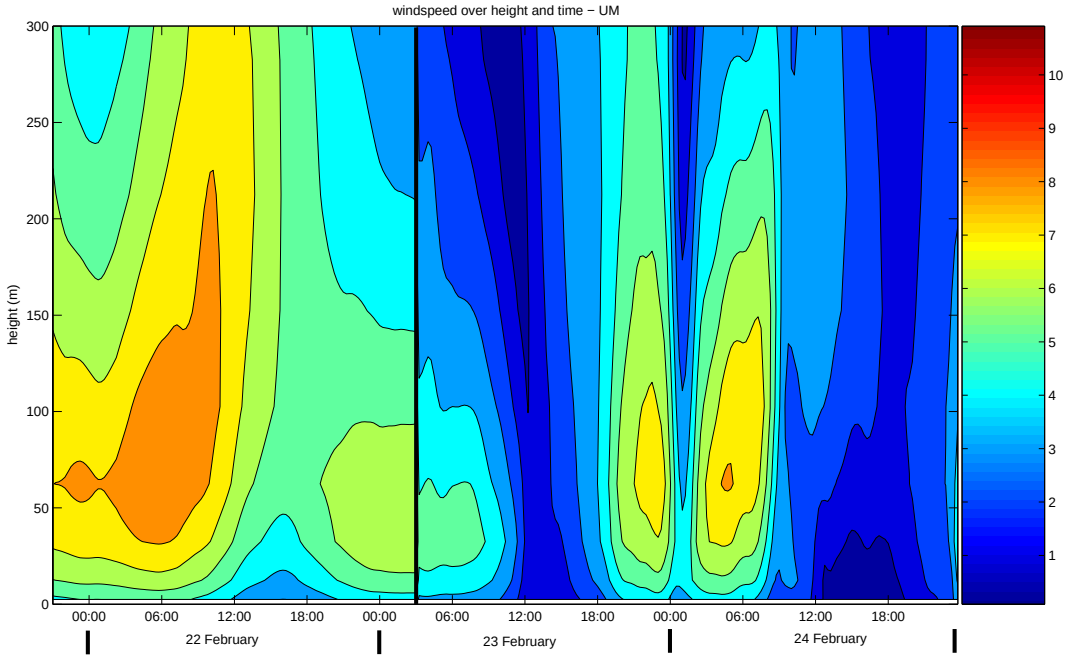

Figure 3.68: Wind speed over height and time from the UM (15 minute averages every 15 minutes), for 21-24 February 2002.

early hours of 23 February, the model shows lower wind speeds than during the other nights, and strongly underestimates the wind speed as compared to the Doppler observations. During the third night, it simulates the dual maxima also seen in the observations.

Figure 3.69 shows averaged nighttime wind speed profiles both from the model and from Doppler Sodar observations, obtained by averaging the 15 minute-averages profiles between 20 UTC and 09 UTC (when katabatic winds are strongest) for 21-24 February. The shape of the profile from the model compares quite well to the Doppler profile, though the wind speed at the surface is underestimated and the maximum wind speed is located too high up in the model. Figure 3.70 shows daytime average wind speed profiles, taken between 14 and 18 UTC for 21-24 February (when katabatic winds are weakest). The daytime profiles are quite different from the nighttime profiles, both for the model and for the observed profiles. Wind speeds are much weaker over the entire height of the profile. The model compares quite well to the Doppler observations, except the model again underestimates the wind speed at the surface.

3.4.5 Summary

The large scale synoptic situation is well represented by the model. The model is capable of capturing the diurnal variation in temperature, wind speed and

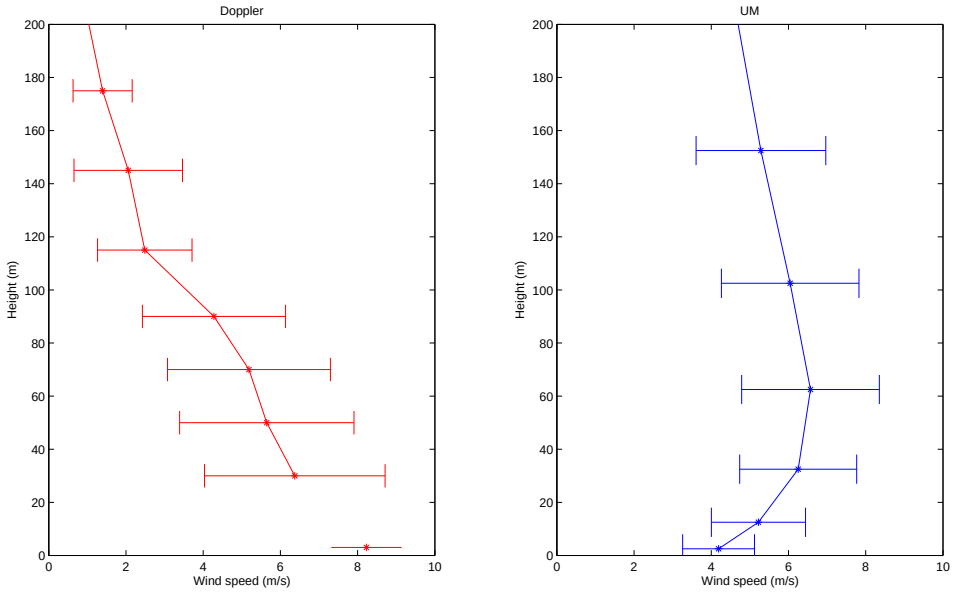

Figure 3.69: Nighttime average profiles of wind speed (m/s) taken from 15 minute averaged profiles between 20 UTC and 09 UTC for 21 to 24 February 2002, on the left from Doppler Sodar observations and on the right from model output. The errorbars indicate the standard deviation. The lowest data point in the Doppler Sodar plot comes from the AWS hourly measurements.

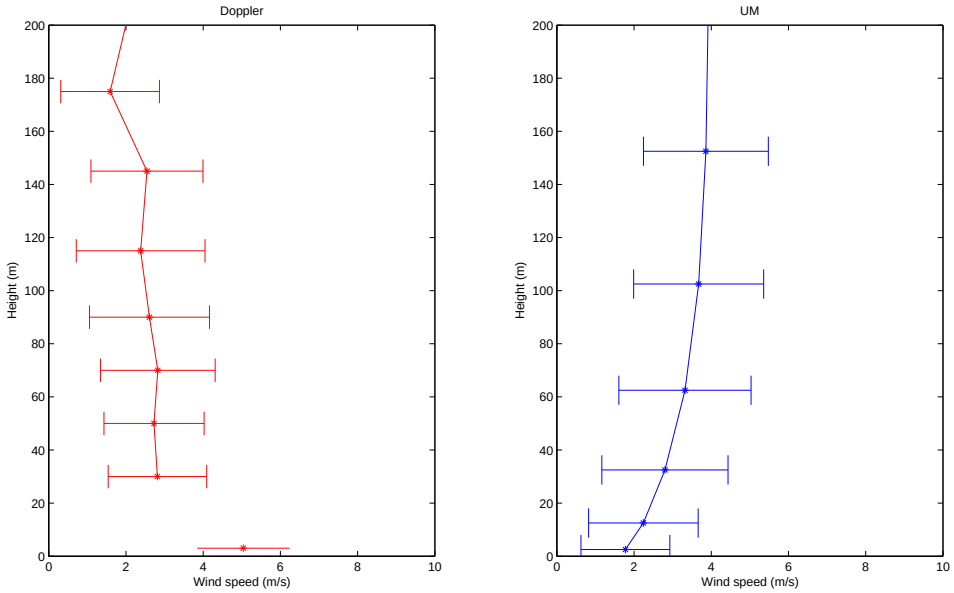

Figure 3.70: Daytime average profiles of wind speed (m/s) taken from 15 minute averaged profiles between 14 UTC and 18 UTC for 21 to 24 February 2002, on the left from Doppler Sodar observations and on the right from model output. The errorbars indicate the standard deviation. The lowest data point in the Doppler Sodar plot comes from the AWS hourly measurements.

direction during this Antarctic summer case study. Skies are clear for most of the four days of this case study, and the diurnal cycle in temperature is very clear. During the last two days of the model run, the model overestimates the cloud cover at Halley, which disrupts the diurnal cycle and causes an overestimation of the temperature. The model captures the diurnal variation in wind speed and direction at C2, though wind speeds are underestimated. The model also shows a clear diurnal cycle in the wind speed and direction at C3, while AWS observations do not confirm this. Both the Doppler Sodar observations and the model results show significantly different wind profiles during the day and during the night. The model shows a katabatic layer that is too deep, while underestimating the wind speed at the surface.

In conclusion, the model performs reasonably well for this case study - better than for both winter cases. There is still room for improvement though. The sensitivity of the model results to changing the boundary layer parameterisation will be discussed in the next chapter.

3.5 Conclusions

In all three case studies, the large scale synoptic situation is reasonably well represented by the model. The main problem on the smaller scale is the cloud cover: often the cloud cover especially over Halley is too high or too low in the model, causing a significant bias in the model temperatures at Halley. This problem appears to originate in the initial conditions. For the August 2003 case, using an different start dump improved the cloud cover and solved the temperature issue at Halley. However, many other aspects of the model run were not improved by using this start dump, so it was decided not to use the results of this model simulation.

The model shows little variation over time, and does not reproduce the highly variable observations from the Doppler Sodar that were seen in the two winter case studies. In general, the model underestimates wind speeds at the surface (a problem also found in Renfrew (2004) and Renfrew and Anderson (2006)). The katabatic layer in the model appears too deep, though this is impossible to prove as the peak of the katabatic jet often seems to fall in the observation gap between the AWS and the lowest level of the Doppler Sodar, a problem also discussed in Renfrew and Anderson (2006). The model shows the development of a cold pool at the bottom of the slope, something also found in modelling studies by Renfrew (2004). It is difficult to show this phenomenon in observations, as the only observed profiles of temperature and wind speed available are at Halley, about 50 km from the bottom of the slope.

The model performs better for the summer case than it did for either of the winter cases. The diurnal cycle is well captured, though the magnitude of the

diurnal variation is underestimated by the model.

In conclusion, the model performs reasonably but there is definitely room for improvement. We will investigate the sensitivity of the model results to changing the boundary-layer parameterisation for the August 2003 and the February 2002 case. The results of these sensitivity experiments will be discussed in the next chapter.

Chapter 4

Boundary Layer Parameterisation

4.1 Introduction

4.1.1 Atmospheric Boundary Layer

The Atmospheric Boundary Layer (ABL) is that part of the atmosphere directly influenced by the surface of the Earth. This layer responds to surface forcing in an hour or less. One of the main characteristics of the ABL is the presence of diurnal variation. Solar radiation warms the ground during the day, which forces transport of heat, moisture and momentum in the boundary layer. One of the important transport processes in the boundary layer is turbulence in the shape of eddies (irregular swirls of motion). The ABL over land will generally be deep during the day and shallow during the night.

4.1.2 Stable Boundary Layer

Whenever the surface of the Earth is cooler than the air above, the boundary layer can become stably stratified. This often happens at night time at mid-latitudes and the resulting boundary layer is called a Nocturnal Boundary Layer (NBL). In polar regions, where the surface mostly consists of snow and ice, a Stable Boundary Layer (SBL) is present most of the time.

4.1.3 Representation of the Stable Boundary Layer in atmospheric models

The Stable Boundary Layer is very complex. The balance that exists between the mechanical creation of turbulence and damping by stability varies from case to case (Stull, 1988). The structure of the stable boundary layer is more complicated and more variable than the structure of the daytime boundary layer (Mahrt *et al.*, 1998; Steeneveld *et al.*, 2008b). This makes the SBL difficult to describe and to

model. The representation of the SBL in models is rather poor at the moment, and progress is slow (Viterbo *et al.*, 1999; Holtslag and Boville, 1993; Cuxart *et al.*, 2006). One of the reasons is that the stable boundary layer is driven by two distinct physical processes: turbulence and radiative cooling (Steeneveld *et al.*, 2008b). Another problem is that SBL parameterisations are generally tuned to perform reasonably at mid-latitudes (Viterbo *et al.*, 1999). The highly stable conditions that often occur in the polar regions are rarely encountered at mid-latitudes. This means the SBL parameterisations commonly used in atmospheric models are unlikely to be accurate over the polar regions (King *et al.*, 2001).

Unfortunately, model results are very sensitive to the model formulation of mixing in stratified conditions (Holtslag, 2006). King *et al.* (2001) demonstrated the sensitivity of Antarctic climate model simulations to changes in surface and boundary fluxes parameterisations under stable conditions. Viterbo *et al.* (1999) used the ECMWF model with two slightly different stability functions (to parameterize the effect of changing atmospheric stability on the surface) in the mixing scheme and found differences in the mean winter temperatures as large as 10 K over continental areas. Besides the degree of turbulent mixing, stable boundary layer modelling is also sensitive to the coupling between the atmosphere and the land surface (Steeneveld *et al.*, 2006) and to the radiation parameterisation (Ha and Mahrt, 2003).

4.1.4 Vertical resolution

To model the stable boundary layer it is important to have sufficient vertical resolution in the model, as this layer is often very shallow. This study focuses on the area of Coats Land in Antarctica. At Halley the SBL is often as shallow as 50 m (King, 1990), which means that in many atmospheric models, this layer will be represented by only one model level. Cassano *et al.* (2001) performed katabatic wind sensitivity simulations over Halley. They found that model results are very sensitive to the depth of the SBL (mostly determined by the height of the lowest model level). They found significant differences in the simulated cooling, the depth of the katabatic flow and the (katabatic layer) mass transport (Cassano *et al.*, 2001).

4.1.5 Roughness length

Stable boundary layers often occur over snow and ice, which often (but not always) means that the surface is relatively smooth. Wind across a smooth surface will cause less turbulence, and therefore a stabler boundary layer. Therefore it is important that a model uses an accurate roughness length.

4.2 Boundary Layer settings in the Unified Model

For the boundary layer scheme of the Met Office Unified Model version 6.1 there are two options: the Richardson number based scheme (default option) and the Equilibrium Stable Boundary Layer Scheme. In addition to this, the stability functions can be changed. The default Richardson number based scheme was discussed in more detail in chapter 2. Here we will describe the alternative options.

4.2.1 Equilibrium stable boundary layer scheme

The equilibrium stable boundary layer scheme (EqSBL) is a first order closure scheme for mixing under stably stratified conditions. It is an alternative to the default Richardson number based scheme implemented only for stable conditions. The EqSBL scheme was developed because of the limited ability of the Richardson number based scheme to control the mixing behaviour of the boundary layer as a whole. In this scheme, there is fundamentally no connection between the height of the boundary layer and the vertical extent of turbulent mixing, as the boundary layer height is rather arbitrarily defined as the level above which the Richardson number is larger than one. The equilibrium stable boundary layer scheme is based on second moment budget equations with a quasi-equilibrium assumption and attempts to retain the local character of turbulent mixing in stable conditions, while introducing a high level of external control on the gross mixing characteristics of the layer (Williams, 2003). Note that in a newer version of the UM (version 6.3), it is not possible to use the EqSBL scheme anymore. It was decided that the increased complexity of the EqSBL scheme when compared to the much simpler Richardson number based scheme did not give enough benefit. Despite this gloomy prognosis, it is worth examining its performance for our persistent SBL situations.

The basis of the EqSBL scheme is the same as the Richardson number based scheme: it distinguishes between six different boundary layer types. For an overview of the boundary layer types, see figure 2.3. The mixing scheme changes only when boundary layer type I (stable boundary layer) or II (stratocumulus over a stable surface layer) is detected. The EqSBL scheme uses a 1D theoretical model of an equilibrium SBL, formulated in terms of dimensionless ratios of local similarity theory. The equations in this model are solved by a simple iterative technique. It is assumed that the boundary layer tends to relax towards a quasi-equilibrium state so that transport terms in the governing equations remain small (Williams, 2003). The scheme uses the surface buoyancy flux, the temperature and the friction velocity to calculate the surface Monin-Obukhov length (L_0). From L_0 and the current wind and temperature profiles, the SBL height is estimated using a variable bulk gradient Richardson number, predicted

by the theoretical analysis. If the profile of the local Monin Obukhov length ($L(z/h)$) is known, the theoretical analysis of the equilibrium model will give a 1D approximate solution for the eddy diffusivities ($K_\chi^{eq}(z/L)$, in which the 'eq' superscript indicates the prediction from the equilibrium model). To combine the external conditions with the 'internal' equilibrium model, an approximate profile for $L(z/h)$ must be specified. This is done by prescribing 'equilibrium' profiles for the stress and buoyancy flux, based on observational and modelling studies. The actual model fluxes should tend to relax towards these equilibrium profiles if external forces are held constant. An idealised Monin Obukhov length (L^{eq}) can be constructed from the equilibrium profiles, and the assumption $L \cong L^{eq}$ is made. The eddy diffusivities from the equilibrium model can be used with the actual UM profiles of wind and temperature, using the quasi-equilibrium assumption, to estimate fluxes in the UM:

$$\overline{w\chi} \cong -K_\chi^{eq}\frac{\partial \chi}{\partial z} \tag{4.1}$$

(Williams, 2003). It is expected that the UM profiles tend to relax towards corresponding equilibrium profiles (obtained if external conditions were held constant). These equilibrium profiles can be calculated by dividing the prescribed equilibrium flux profiles by $-K_\chi^{eq}$ and then integrating upwards from surface values (Williams, 2003).

4.2.2 Stability functions

When a stable boundary layer has been identified by the boundary layer scheme in the UM, the local scheme is used to calculate turbulent diffusivities (for unstable conditions, the non-local scheme is used). In a local scheme, the turbulent flux of a quantity is proportional to the local vertical gradient of that quantity. The eddy diffusivity depends on local gradients of mean wind and mean virtual temperature. These are reasonable assumptions when the length scale of the largest turbulent eddies is smaller than the boundary-layer height over which the turbulence extends, which is typically true for neutral and stable conditions. In unstable and convective conditions, the largest transporting eddies may have a size similar to the boundary-layer height itself. In such conditions a local diffusion approach is no longer appropriate, and it is better to use a non-local scheme that uses turbulent properties characteristic of the boundary layer to calculate turbulent diffusivities.

The Richardson number (Ri) is the dimensionless ratio of buoyant production (or consumption) of turbulence and the shear production of turbulence. It is used

as a measure of stability and given by (Williams, 2003):

$$Ri = \left(\frac{g}{\Theta}\frac{\partial\Theta}{\partial z}\right) / \left(\frac{\partial U}{\partial z}\right)^2 \tag{4.2}$$

To parameterise the effect of changing atmospheric stability on surface fluxes, a stability correction function f_m is used. The 'neutral' value of the diffusivities is multiplied by this function to take account of stability effects. When Ri >0 (the stable regime), the 'long-tailed' form of the boundary-layer stability function is used in the boundary layer:

$$f_m = \frac{1}{1 + g_0 Ri} \tag{4.3}$$

in which the constant $g_0 = 10$. This function decays very slowly with increasing Ri, giving significantly more mixing at higher stabilities than observations or large-eddy simulation (LES) indicate (Beare *et al.*, 2006). This excessive mixing can lead to boundary layers that are too deep which leads to further errors, see for example Brown *et al.* (2005).

There are alternative stability functions available. These functions decrease more rapidly (e.g. $1/\mathrm{Ri}^2$ instead of $1/\mathrm{Ri}$) with increasing stability. It is possible to use these different stability functions in the UM. One option is to replace equation 4.3 with the 'SHARPEST' functions (Derbyshire, 1997):

$$f_m = \begin{cases} (1 - 0.5 g_0 Ri)^2 & 0 < Ri < 0.1 \\ (2 g_0 Ri)^{-2} & Ri > 0.1 \end{cases} \tag{4.4}$$

Another option is to use the Louis stability function (Louis, 1979) given by:

$$f_m = \frac{1}{(1 + 5Ri)^2} \tag{4.5}$$

Figure 4.1 shows the three different stability functions mentioned above. The three stability functions are described in Lock (2007). The Unified Model also has an option to blend linearly from Louis at the surface to SHARPEST from a height of 200 m. None of the above stability functions distinguish between stability functions for heat and for momentum, and thus use $f_m = f_h$.

The above stability functions are used only in the boundary layer. The Monin-Obukhov similarity theory is used to describe the surface layer, using stability functions from Beljaars and Holtslag (1991). The Monin-Obukhov similarity theory is based on the approximation that the surface layer is a constant flux layer in which the mean flow and turbulence characteristics depend only on four independent variables: the height above the surface, the surface drag, the surface kinematic heat flux and the buoyancy variable (Arya, 1988). These four variables contain three fundamental dimensions: length, time and temperature. The independent dimensionless combination traditionally used is z/L, in which

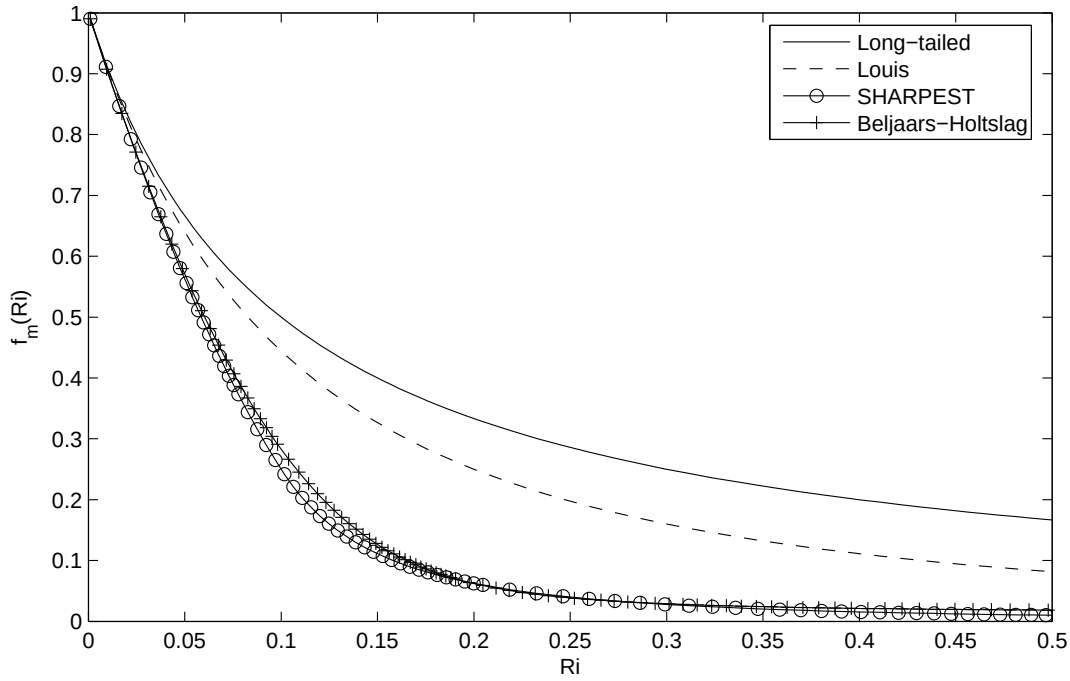

Figure 4.1: The different stability functions: long-tailed (solid line), Louis (dashed line), SHARPEST (solid line with circles) and the Beljaars and Holtslag (1991) stability function for momentum (solid line with plusses).

L is the Obukhov length defined by:

$$L = \frac{-v_*^3}{kF_{B0}/\rho_0} \tag{4.6}$$

where k is the von Karman constant, F_{B0} is the surface buoyancy flux, and the subscripts 0 represent a surface value while subscript * represents a surface layer scaling quantity (Lock, 2007). The Monin-Obukhov length scale L describes the height above the ground where mechanically produced turbulence is in balance with the dissipative effect of negative buoyancy (thus where the Richardson number equals one). The non-dimensional wind and temperature profiles in the surface layer can be expressed as:

$$\phi_m(\frac{z}{L}) = \frac{kz}{u_*}\frac{\partial u}{\partial z} \tag{4.7}$$

and

$$\phi_h(\frac{z}{L}) = \frac{kz}{\theta_*}\frac{\partial \theta}{\partial z} \tag{4.8}$$

The functions $\phi_m(\frac{z}{L})$ and $\phi_h(\frac{z}{L})$ must be determined theoretically or empirically. Ψ_M and Ψ_H are integrated versions of these dimensionless stability functions of height (z) divided by the Obukhov length (L). Beljaars and Holtslag (1991) define

Ψ_M and Ψ_H by:

$$-\Psi_M = a\frac{z}{L} + b\left(\frac{z}{L} - \frac{c}{d}\right)e^{-d\frac{z}{L}} + \frac{bc}{d} \tag{4.9}$$

and

$$-\Psi_H = \left(1 + \frac{2}{3}\frac{az}{L}\right)^{3/2} + b\left(\frac{z}{L} - \frac{c}{d}\right)e^{-d\frac{z}{L}} + \frac{bc}{d} - 1 \tag{4.10}$$

where a = 1, b = 2/3, c = 5 and d = 0.35.

Equation 4.9 was originally proposed by Holtslag and De Bruin (1988), using slightly different values for a and b, and using $\Psi_M = \Psi_H$. The changes proposed by Beljaars and Holtslag (1991) account for the fact that the exchange of heat is far less efficient than the exchange of momentum when turbulence is intermittent (in extreme stable cases).

The long-tailed, SHARPEST and the Louis stability functions used in the boundary layer are functions of the Richardson number, while the Beljaars and Holtslag (1991) functions used at the surface are functions of z/L. This makes it difficult to compare them directly. However, it is possible to derive the Beljaars and Holtslag (1991) functions as a function of the Richardson number, as described below.

The Ψ-functions are integrated ϕ-functions as defined by:

$$\Psi = \int \frac{1-\phi}{\zeta} d\zeta \tag{4.11}$$

where $\zeta = \frac{z}{L}$ (de Bruin, 2005). This leads to:

$$\phi = 1 + \zeta\Psi'(\zeta) \tag{4.12}$$

Below we will show the derivation of ϕ_m and ϕ_h using this method.

We start with the the equation for momentum (equation 4.9), which can also be written as:

$$-\Psi_m = a\zeta + b\zeta e^{-d\zeta} - b\frac{c}{d}e^{-d\zeta} + \frac{bc}{d} \tag{4.13}$$

The derivation of equation 4.13, using the product rule, gives:

$$\Psi'_m(\zeta) = a + be^{-d\zeta} - db\zeta e^{-d\zeta} + bce^{-d\zeta} = a - \left(db(\zeta - \frac{c}{d}) + b\right)e^{-d\zeta} \tag{4.14}$$

Doing the same for the equation for heat (equation 4.10), the derivation using the product rule results in:

$$\Psi'_h(\zeta) = a\left(1 + \frac{2}{3}a\zeta\right)^{1/2} - \left(db(\zeta - \frac{c}{d}) + b\right)e^{-d\zeta} \tag{4.15}$$

After multiplying equations 4.14 and 4.15 by ζ and adding one (following equation 4.12), the resulting functions for ϕ_m and ϕ_h are:

$$\phi_m = 1 + a\zeta + \zeta\left(-db(\zeta - \frac{c}{d}) + b\right)e^{-d\zeta} \tag{4.16}$$

and

$$\phi_h = 1 + a\zeta\left(1 + \frac{2a\zeta}{3}\right)^{1/2} + \zeta\left(-db(\zeta - \frac{c}{d}) + b\right)e^{-d\zeta} \tag{4.17}$$

Duynkerke (1990) derived the following equation, which can be used to calculate the Richardson number:

$$Ri = (\frac{\phi_h}{\phi_m^2})\frac{z}{L} \tag{4.18}$$

Using the flux profile relationships and the definition of K, Duynkerke (1990) derived the following equations for the turbulent eddy diffusivities K_m and K_h:

$$K_m = \frac{(kz)^2}{\phi_m^2}\left|\frac{\partial v}{\partial z}\right| \tag{4.19}$$

$$K_h = \frac{(kz)^2}{\phi_m\phi_h}\left|\frac{\partial v}{\partial z}\right| \tag{4.20}$$

in which $\frac{\partial v}{\partial z}$ is the wind shear. These equations are also described in Holtslag (1998).

The turbulent eddy diffusivity can also be written as (see for example Cuxart *et al.* (2006) and Steeneveld *et al.* (2008a), or Holtslag (1998) for a detailed derivation):

$$K = (kz)^2\left|\frac{\partial v}{\partial z}\right| f(Ri) \tag{4.21}$$

By combining equations 4.19 and 4.20 with their equivalent version of equation 4.21 we can derive equations for f_m and f_h:

$$f_m = \frac{1}{\phi_m^2} \tag{4.22}$$

and

$$f_h = \frac{1}{\phi_m\phi_h} \tag{4.23}$$

With these results it is possible to plot f_m and f_h against the Richardson number, and compare this to the stability functions used in the boundary layer. The result is shown in figure 4.1 as the Beljaars and Holtslag (1991) stability function, for momentum only. The stability function for heat is not shown as it is very similar to the stability function for momentum. The Beljaars and Holtslag (1991) stability function is very similar to the SHARPEST function. By default, the UM uses the long-tailed stability function in the boundary layer and the Beljaars and Holtslag (1991) function at the surface. Brown *et al.* (2005) show that when modelled stable boundary layers are too deep, switching to the stable boundary layer parameterisation based on Monin-Obukhov similarity theory by Beljaars

Name of run	BL Scheme	Stability Function	Vertical levels	Base Roughness Length (m)
Base	Ri nr based	Long-tailed	38	3.0×10^{-4}
Base76	Ri nr based	Long-tailed	76	3.0×10^{-4}
Base76HR	Ri nr based	Long-tailed	76	3.0×10^{-4}
eqSBL	EqSBL	Long-tailed	76	3.0×10^{-4}
Louis/SHARPEST	Ri nr based	Louis/SHARPEST	76	3.0×10^{-4}
SHARPEST	Ri nr based	SHARPEST	76	3.0×10^{-4}
BHrev	Ri nr based	Revised Beljaars and Holtslag	76	3.0×10^{-4}
Z0ice	Ri nr based	Long-tailed	76	1.0×10^{-4}
Z0half	Ri nr based	Long-tailed	76	5.0×10^{-5}

Table 4.1: Boundary layer scheme, stability functions, vertical levels and roughness length (over land) settings for each model run.

and Holtslag (1991) (in the surface layer as well as in the boundary layer) gives more realistic results.

King *et al.* (2001) have implemented both the Louis and the SHARPEST scheme in the Hadley Centre climate model version HadAM2 (i.e., UM version 4.5). In this version of the UM the surface scheme used the same stability functions as the boundary layer scheme, and the changes were implemented in both schemes. They suggest that using either of those stability functions will improve the simulation of surface fluxes over Antarctica and other regions with stable stratification. Brown *et al.* (2008) found that reducing turbulent mixing in stable conditions over sea by using SHARPEST combined with more efficient turbulent mixing in convective conditions significantly reduced long-standing model errors in the Unified Model. They use SHARPEST only over sea, to avoid the heterogeneity argument: it is thought that the traditional long-tailed functions effectively parameterise the effect of heterogeneity leading to mixing within a grid box even when the mean grid box is stable (Mahrt, 1987). This would explain why using functions with less mixing have often given disappointing results showing excessive cooling at the surface and less skill in predicting the synoptic situation (Viterbo *et al.*, 1999). This problem is still not well understood. However, over Antarctica and especially over the Coats Land domain used in this study, the terrain is very homogeneous and therefore using the SHARPEST function over land and over sea should not give any problems.

4.3 Method

To find out which boundary layer settings work best for the katabatic case studies, a comparison study is set up. A 4 km run has been repeated with different

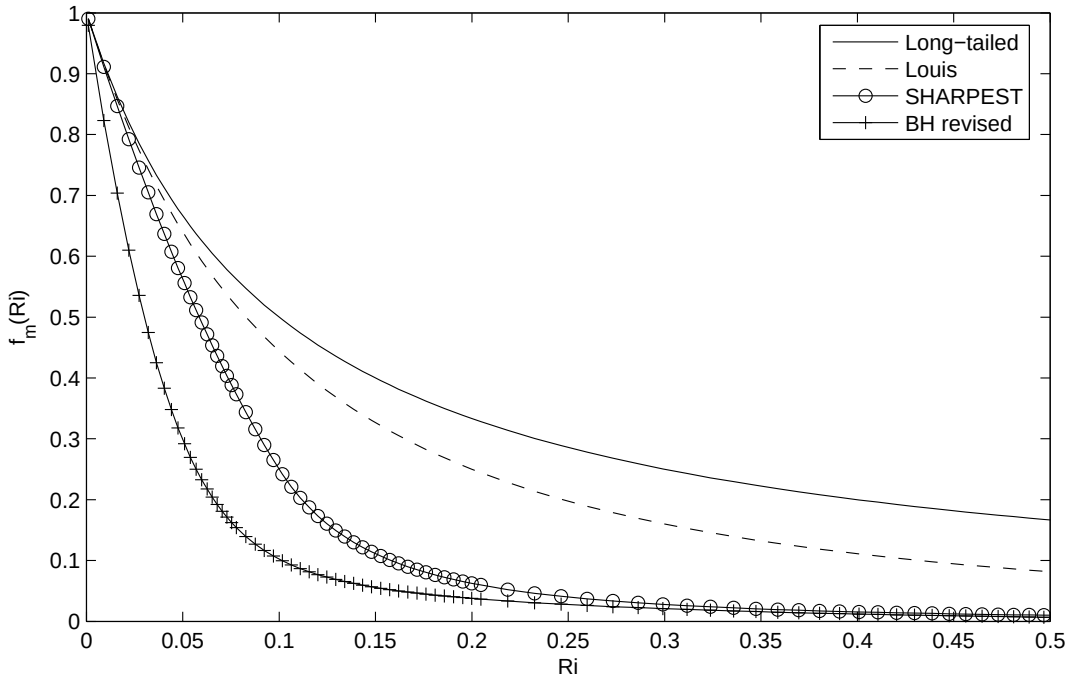

Figure 4.2: The different stability functions: long-tailed (solid line), Louis (dashed line), SHARPEST (solid line with circles), and the revised version of the Beljaars and Holtslag stability function for momentum (solid line with plusses).

settings for the boundary layer scheme, the stability functions, the vertical resolution and the roughness length over land. This is done for both the August 2003 (winter) case and the February 2002 (summer) case. The details of those runs are given in table 4.1, and further discussed below.

Comparing the Base run with the Base76 enables us to study how sensitive the model results are to the number of vertical levels. We expect that a higher vertical resolution will give better results, so for the remainder of the runs we will use 76 vertical levels. However, even with 76 levels the resolution in the (shallow) boundary layer is not very high. We are mostly interested in the lowest 250-300 m, which means the lowest 7 model levels when using 76 vertical levels. For one of the experiments in this chapter (Base76HR), we have doubled the number of vertical levels in the lowest 500 m, while reducing the resolution higher up in the atmosphere. The total number of vertical levels is still 76. This will give us higher resolution results in the boundary layer, but it will also show us whether the default resolution near the surface is high enough.

The differences between the default Richardson number based scheme and the equilibrium stable boundary layer scheme will be analysed by comparing the BASE76 run to the eqSBL run (see table 4.1).

Comparing BASE76 to Louis/SHARPEST and SHARPEST should give us more insight into the available stability functions. The model results described in

chapter 3 show a boundary layer that in many cases is too deep, suggesting that there is too much mixing going on. Using a sharper stability function means less mixing with increasing stability, and this could improve the simulations. However, in our model simulations, we find Richardson numbers in the range of 0.02 to 0.04. In this range, there is not much difference between the stability functions, as can be seen in figure 4.1. Because of this, we decided to create an even sharper stability function than SHARPEST, both in the boundary layer and at the surface. By tuning the constants in equations 4.9 and 4.10 we found a stability function where the mixing decreases very rapidly with increasing stability. From a Richardson number of about 0.3 and higher, this new function is similar to the SHARPEST function. This revised version of the Beljaars and Holtslag function is shown in figure 4.2, together with the SHARPEST, Louis and long-tailed stability functions for comparison. This was obtained by using a = 5, b = 2/3, c = 7 and d = 2. There is no literature on changing these constants, and so these values have been determined purely by means of tuning until the desired result was found. It is believed that it is better to use the same stability functions at the surface and in the boundary layer, therefore we have also tuned the SHARPEST function to match the revised Beljaars and Holtslag function. The new function used is:

$$f_m = \begin{cases} (1 - 0.9 g_0 Ri)^2 & 0 < Ri < 0.057 \\ (3.5 g_0 Ri)^{-2} & Ri > 0.057 \end{cases} \tag{4.24}$$

The experiment with these values for the constants a-d in the surface layer and equation 4.24 for the boundary layer is referred to as BHrev (see table 4.1).

A somewhat separate experiment is carried out to study how sensitive the model is to changing the roughness length over land. One of the main problems found in the previous chapter was that the wind speed at the surface is underestimated by the model. This could indicate that the roughness length in the model is too large. A too high roughness length can also lead to a too deep boundary layer (see for example Kara *et al.* (1998)), as the increased roughness allows for increased turbulence. A too deep boundary layer is another problem found in the previous chapter. The surface over the slope is very smooth, so the roughness length should be very small. In the BASE76 run, the roughness length over land has a base value of 3.0×10^{-4} m (over sea the roughness length depends on the wind speed). To calculate the roughness length, the model uses the base roughness length but orographic enhancement is also included, as well as a stability dependence that linearly reduces when the surface bulk Richardson number approaches the critical Richardson number (taken as 0.5). In the BASE76 run, the average roughness length is 3.0×10^{-4} m at Halley, 6.8×10^{-4} m at C2, 3.5×10^{-4} m at C3 and 3.4×10^{-4} m at C4. King and Anderson (1994) found a roughness length of 5.6×10^{-5} m for Halley, with a range of uncertainty

from 5.0×10^{-5} to 6.1×10^{-5} m. Earlier, King (1990) measured a mean roughness length of 1.1×10^{-4} m at the same site. Renfrew (2004) used a roughness length of 1.0×10^{-4} m in his idealised model simulations of katabatic flow in Coats Land. Compared to these values, the roughness length in the BASE76 run is relatively high and this could explain both the overestimated wind speeds at the surface and the too deep boundary layer. It is possible to change the base roughness length that the model uses. In the Z0ice run (see table 4.1), we changed the base roughness length to 1.0×10^{-4} m. This results in an average roughness length of 1.0×10^{-4} m at Halley, 2.9×10^{-4} m at C2 and 1.2×10^{-4} m at C3 and C4. To study how sensitive the model is to changing the roughness length over land, we have carried out another experiment in which we halved the roughness length to 5.0×10^{-5} m. This results in an average roughness length of 5.0×10^{-5} m at Halley, 1.7×10^{-4} m at C2, 6.5×10^{-5} m at C3 and 6.1×10^{-4} m at C4. Comparing these two runs with the BASE76 run will enable us to study the effect of changing the roughness length over land on the model results.

4.4 Results

For the locations discussed in this section (Halley and C2-C4), a stable boundary layer was present nearly all the time (type I from figure 2.3). On rare occasions, a type II boundary layer (stratocumulus over a stable boundary layer) was detected.

4.4.1 Vertical resolution

This section discusses the results of three runs: the BASE run, using 38 vertical levels, the BASE76 run with 76 vertical levels and the BASE76HR run which uses 76 levels that are distributed in a different way to give higher resolution near the surface and lower resolution in the upper atmosphere. Even though it has been decided to use 76 levels for the model runs in this thesis, we still discuss the results of using 38 levels, to study how sensitive the model is to the vertical resolution. For the BASE run, we show results only from the August 2003 case study. For the BASE76 and BASE76HR runs, results are shown both from the August 2003 and the February 2002 case. We will first discuss the BASE run as compared to the BASE76 run, followed by the results from the BASE76HR run.

Figure 4.3 shows the bulk Richardson number for the BASE run and the BASE76 run. A critical Richardson number (R_c) of about 0.25 is often used, where turbulence is present when the Richardson number is below the critical number. When the Richardson number is greater than R_c, the probability of turbulence decreases. Calculating the Richardson number is only possible when local gradients are known. The bulk Richardson number can be calculated from discrete measurement heights. The depth of the layer over which the bulk

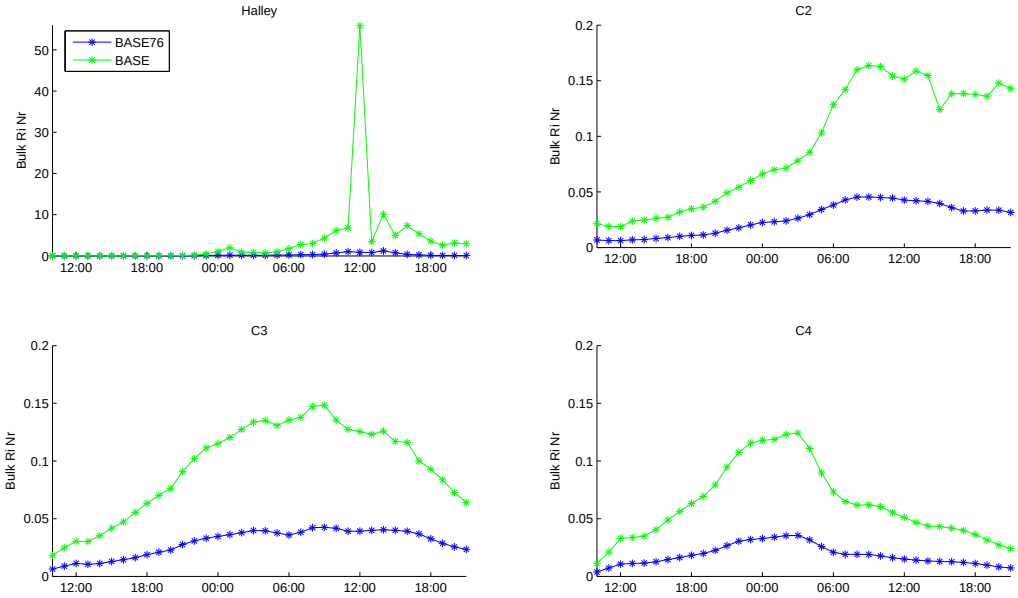

Figure 4.3: The bulk Richardson number for Halley and Automatic Weather Stations C2-C4, for the BASE run (in green) and the BASE76 run (in blue), for the August 2003 case. Note that for Halley, the y axis uses a different scale than C2, C3 and C4.

Richardson number is calculated, influences the critical Richardson number. The thinner the layer, the closer the critical Richardson number will likely be to 0.25 (Stull, 1988). In the UM, the bulk Richardson number is calculated over the lowest layer of the atmosphere. In the BASE run, the lowest model level is at a height of about 10 m, while for the BASE76 run this is about 5.0 m. Figure 4.3 shows that the bulk Richardson numbers for C2, C3 and C4 are below 0.25 for both the base and the BASE76 run, so some turbulence will be present. In the BASE76 run, bulk Richardson numbers are lower than in the base run by a factor 3-4, but this is partly caused by the fact that they are calculated over layers with different depths. For Halley, the bulk Richardson number becomes unrealistically high in the BASE run. Values in the BASE76 run for Halley are much lower, though still exceeding the R_c for the second half of the run, indicating a stable boundary layer with very little turbulence present. Unlike C2-C4, Halley is located on the flat ice shelf so these values are expected. The high values in the BASE76 run show that there is very little turbulence and an extremely stable boundary layer will be present.

Figure 4.4 shows the temperatures from the BASE and BASE76 run, compared to observations. For Halley, the BASE run shows very low temperatures in the second half of the run, in the same period as the unrealistically high bulk Richardson numbers. This shows that the boundary layer has probably become

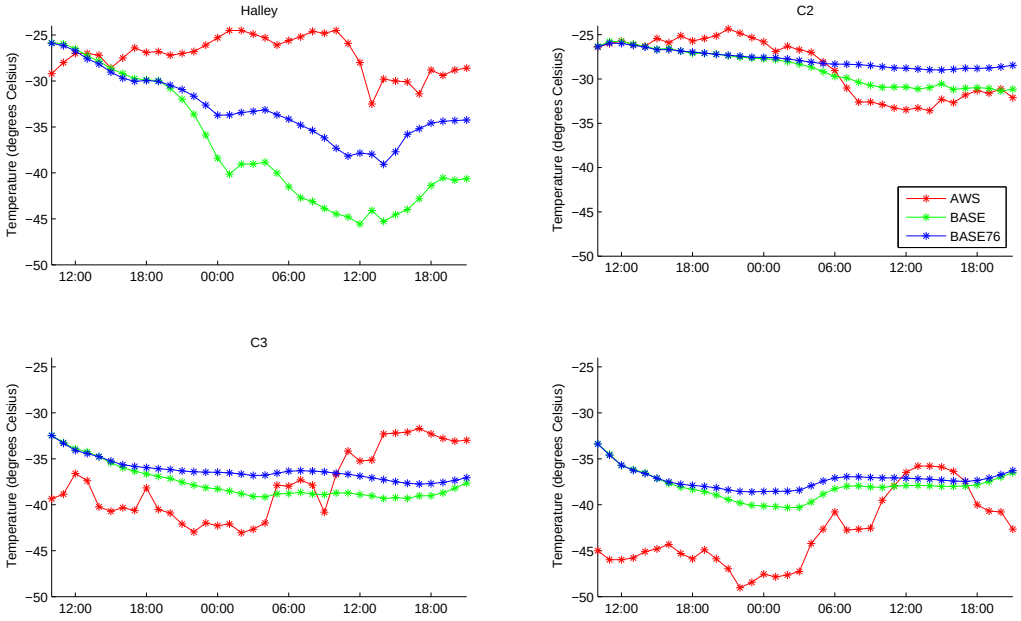

Figure 4.4: Surface temperatures for the BASE run (in green) and the BASE76 run (in blue), compared to the AWS observations (in red), for 13 and 14 August 2003.

decoupled at Halley during this run, resulting in very low surface air temperatures. The BASE76 run still has surface air temperatures that are too low, but much improved compared to the BASE run. The BASE76 run is up to 8 °C warmer than the BASE run. For C2-C4, temperatures from the BASE76 run are also higher than those from the BASE run, which is not an improvement. The BASE run shows very low wind speeds at Halley (probably also related to the decoupled boundary layer), and this is also improved in the BASE76 run. At all locations, the BASE76 run shows stronger wind speeds compared to the BASE run, but the differences are largest at Halley.

We will now discuss the differences between the BASE76 and the BASE76HR run. For the air temperature, the differences between BASE76 and BASE76HR are very small. For the August 2003 case (not shown), the air temperature at C3 and C4 are nearly identical in both runs. At C2, the BASE76HR run is about 1-2 degrees colder than the BASE76 run. At Halley the BASE76HR is initially slightly colder, but on 14 August around 14:00 (when the BASE76 run reaches a minimum in temperature) the BASE76HR is up to 2 degrees warmer compared to the BASE76 run. Figure 4.5 shows the air temperatures from the BASE76 and the BASE76HR run for February 2002. The BASE76HR run shows slightly warmer temperatures at C3 and C4 (and Halley, though not for the entire run) as compared to the BASE76 run. At C2, the BASE76HR run shows colder temperatures when compared to the BASE76 run, with larger differences during

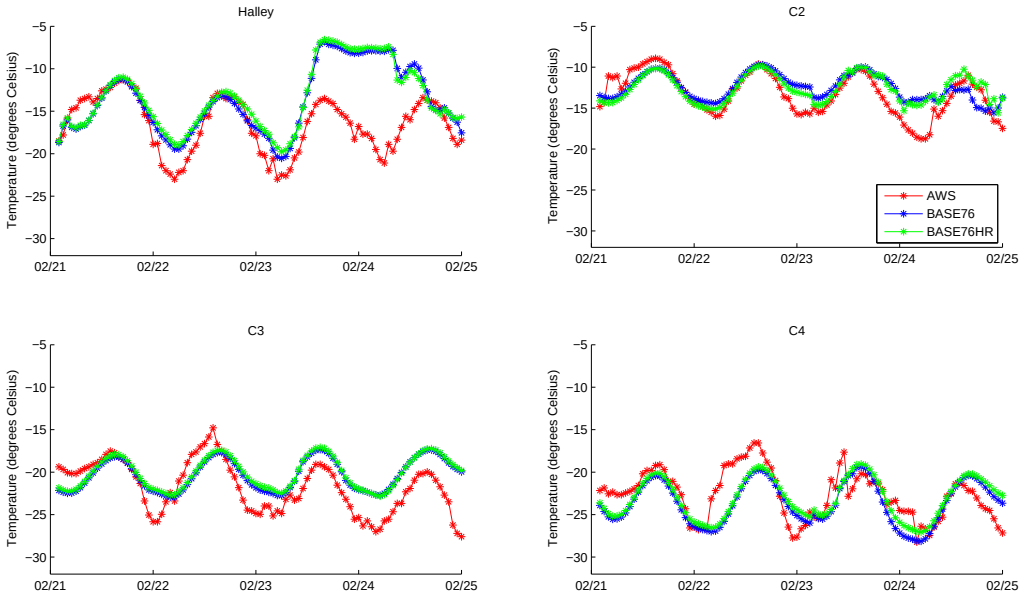

Figure 4.5: Surface temperatures for the BASE76 run (in blue) and the BASE76HR run (in green), compared to the AWS observations (in red), for 21-25 February 2002.

the night. The BASE76HR run performs significantly better when compared to the BASE76 run for the last part of 24 February.

Figure 4.6 shows the average wind profile with standard deviation, for the BASE76 and the BASE76HR runs and for the Doppler Sodar observations. The BASE76HR run shows higher wind speeds in the lowest 50 m, above 50 m the BASE76 and BASE76HR profiles are nearly identical. The maximum wind speed is located slightly higher up in the BASE76HR run as compared to the BASE76 run, which is not an improvement. Figure 4.7 shows average day time and night time profiles for both runs, from the February 2002 case. During the night, the BASE76HR run is not very different from the BASE76 run. During the day, the differences are larger; the BASE76HR run shows stronger wind speeds in the lowest 30 m and weaker wind speeds above 30 m, as compared to the BASE76 run. The observations (see figures 3.69 and 3.70) show an almost constant profile of 2.5-3.0 m/s above 30 m during daytime, so the BASE76HR compares better to observations in this case.

Discussion on vertical resolution

The model is sensitive to the vertical resolution; improving the vertical resolution from 38 to 76 model levels improved the model simulation significantly. The decoupling that takes place over Halley in the BASE run (resulting in very low surface temperatures and wind speeds falling down to nearly zero m/s) is much

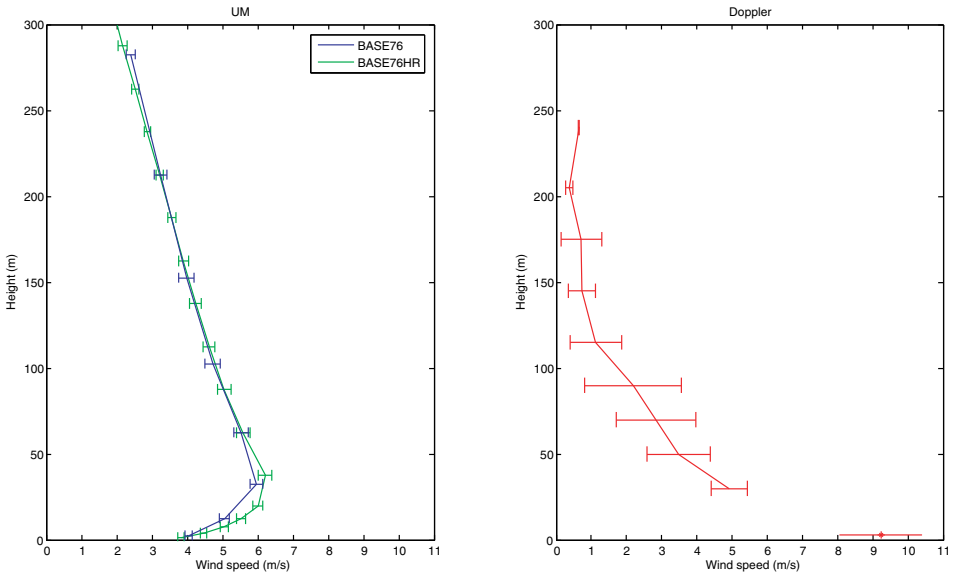

Figure 4.6: Average profiles of wind speed (m/s) taken from 15 minute averaged profiles between 1030 UTC and 1600 UTC for 14 August 2003, on the right from Doppler Sodar observations and on the left from model run BASE76 (in blue) and BASE76HR (in green). The errorbars indicate the standard deviation. The lowest data point in the Doppler Sodar plot comes from the AWS hourly measurements.

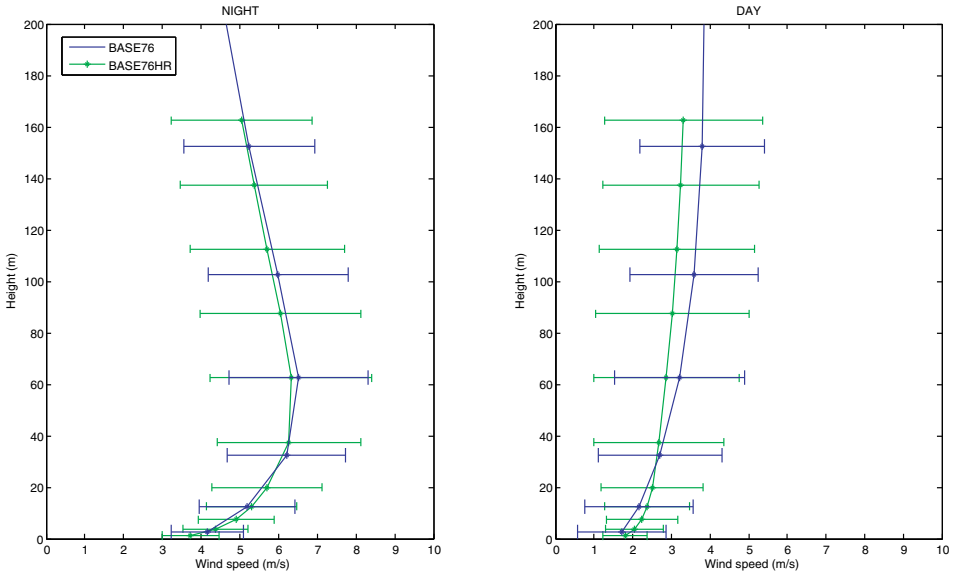

Figure 4.7: Average profiles of wind speed (m/s) taken from 15 minute averaged profiles, on the left the night time profiles, averaged between 20 UTC and 09 UTC for 21 to 24 February 2002 and on the right the day time profile, averaged between 14 UTC and 18 UTC for 21 to 24 February 2002, from model run BASE76 (in blue) and BASE76HR (in green). The errorbars indicate the standard deviation.

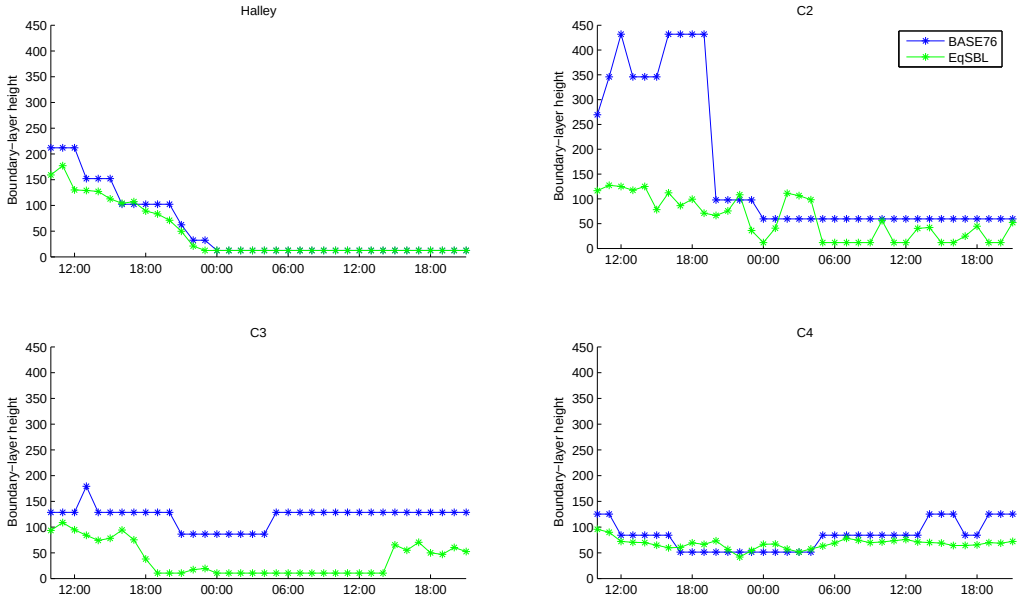

Figure 4.8: The boundary layer height for Halley and Automatic Weather Stations C2-C4, for the BASE76 run (blue line) and the EqSBL run (green line), for 13 and 14 August 2003.

less of a problem in the BASE76 run and this is an important improvement. The bulk Richardson number is also more realistic in the BASE76 run. Overall, the greater resolution of the BASE76 run is an improvement to the model simulation. However the BASE76HR run does not differ significantly from the BASE76 run. From this we can conclude that the problems that we experience in the BASE76 run (a too deep katabatic layer, and wind speeds at the surface underestimated when compared to observations, see chapter 3 for details) are not caused by a lack of vertical resolution. The BASE76HR run doubles the number of vertical levels in the boundary layer (and thus in the katabatic layer), but the results remain similar.

4.4.2 Boundary layer scheme

In this section we will discuss the differences between the BASE76 run (using the default Richardson number based boundary layer scheme) and the eqSBL run (using the equilibrium stable boundary layer scheme). Figure 4.8 shows the boundary-layer height for Halley and C2-C4 for the August 2003 run, for the BASE76 and the EqSBL run. For Halley and C4, the differences in boundary-layer height are insignificant. For C2 and C3 the SBL run shows shallower boundary layers, at times as shallow as the boundary layer at Halley (about 12m). This seems unrealistic as those stations are located on the slope, where katabatic wind should allow vertical mixing resulting in a thicker boundary layer.

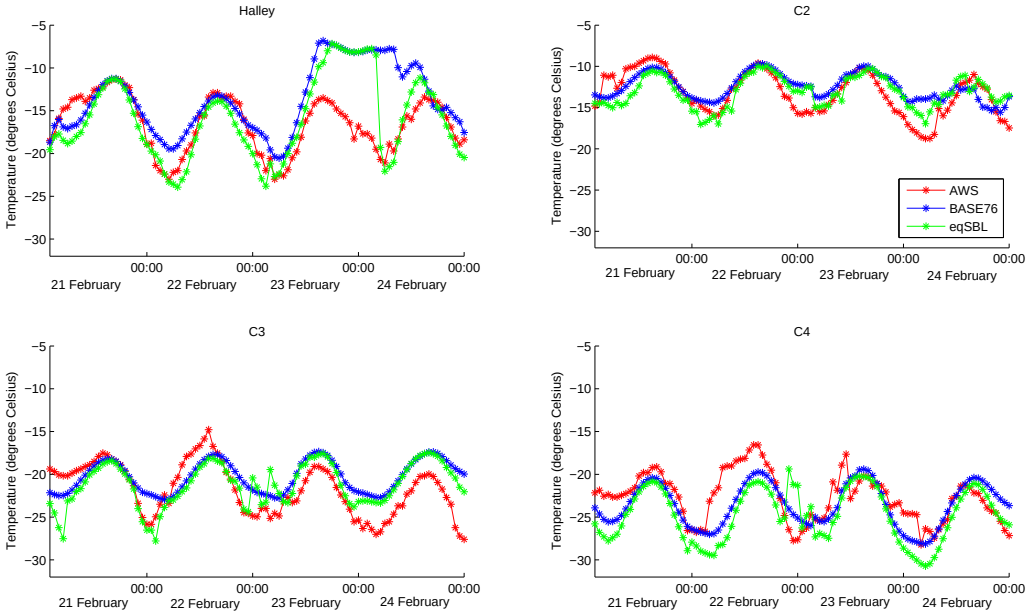

Figure 4.9: Air temperature (degrees Celsius) for 21-25 February 2002, from the BASE76 run (in blue), the eqSBL run (in green) and from AWS observations (in red).

Results from the February 2002 model runs (not shown) show the same pattern: the EqSBL run shows lower boundary-layer heights, sometimes as low as 12 m at all locations. The differences are largest at C2, where the BASE76 shows a boundary-layer height of 750 m at the beginning of the run, while the EqSBL run shows boundary-layer heights of about 100 m at the same time.

Figure 4.9 shows the temperatures from the BASE76 and eqSBL run compared to the AWS observations, for the February 2002 case. The EqSBL run shows a stronger diurnal cycle, mainly because of lower temperatures during the night. This is an improvement over the BASE76 run. At Halley, the eqSBL run compares much better to observations during the last 24 hours of the run. The BASE76 run overestimates the temperatures and does not show much cooling during the 23-24 February night. For the August 2003 case, the eqSBL run shows temperatures that are a few degrees lower than those from the BASE76 run, and the EqSBL run shows greater hourly variability (not shown). The greater hourly variability reflects the variability of the observations better, but in general the temperatures from the eqSBL run do not compare better to observations.

This increased variability of the EqSBL run as compared to the BASE76 clearly shows in figure 4.10, which shows profiles of wind speed from both model runs as compared to the Doppler Sodar profiles, for August 2003. The BASE76 run profiles are remarkably constant, they hardly change during the 5 hours

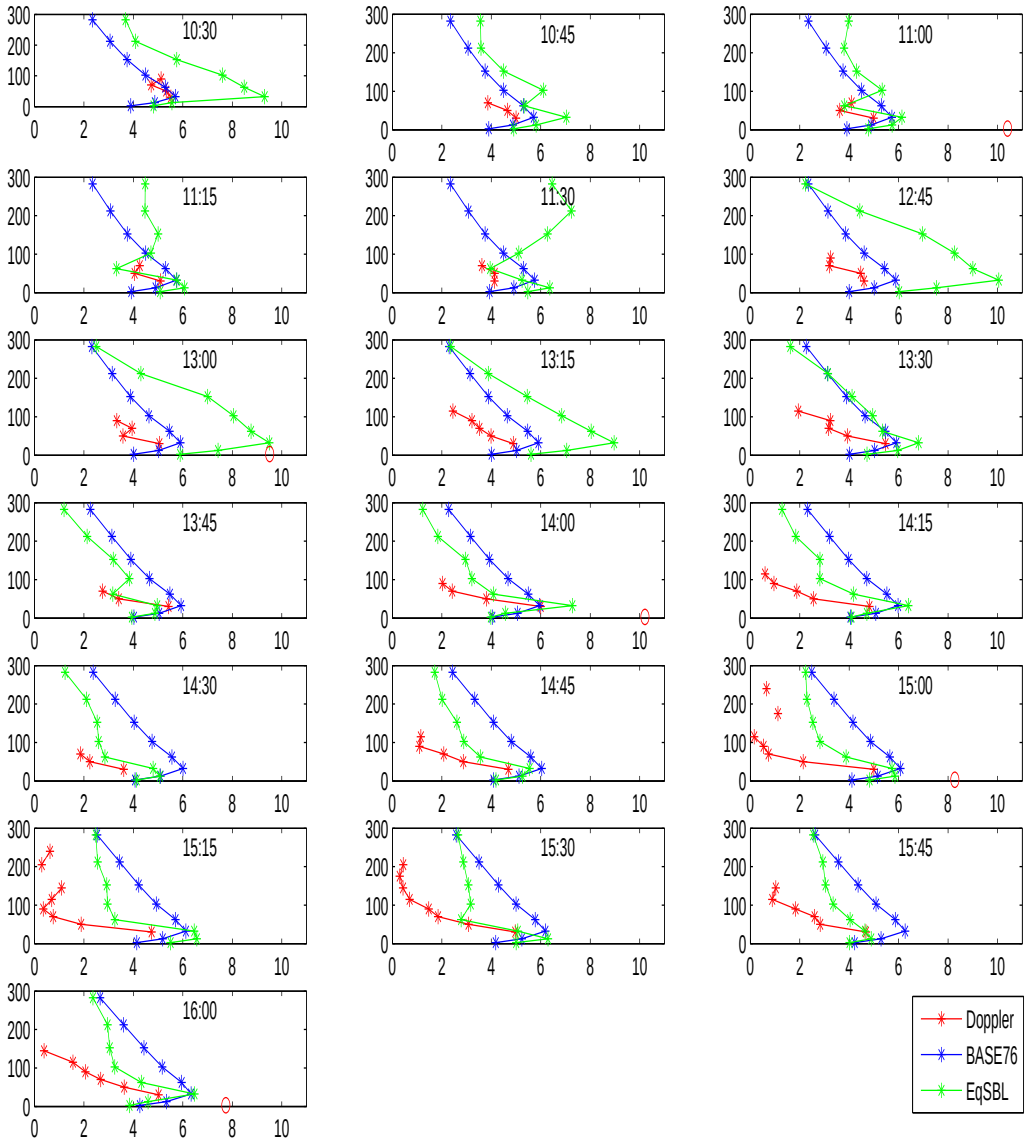

Figure 4.10: Downslope wind speed at the C2 station from the BASE76 run (in blue), the EqSBL run (in green) and from the Doppler sodar (in red), for 14 August 2003. At every whole hour, the 3m wind speed as measured by the AWS is indicated by a red circle. Note that the AWS observations are 10s averages while the Doppler measurements and model data are 15min averages.

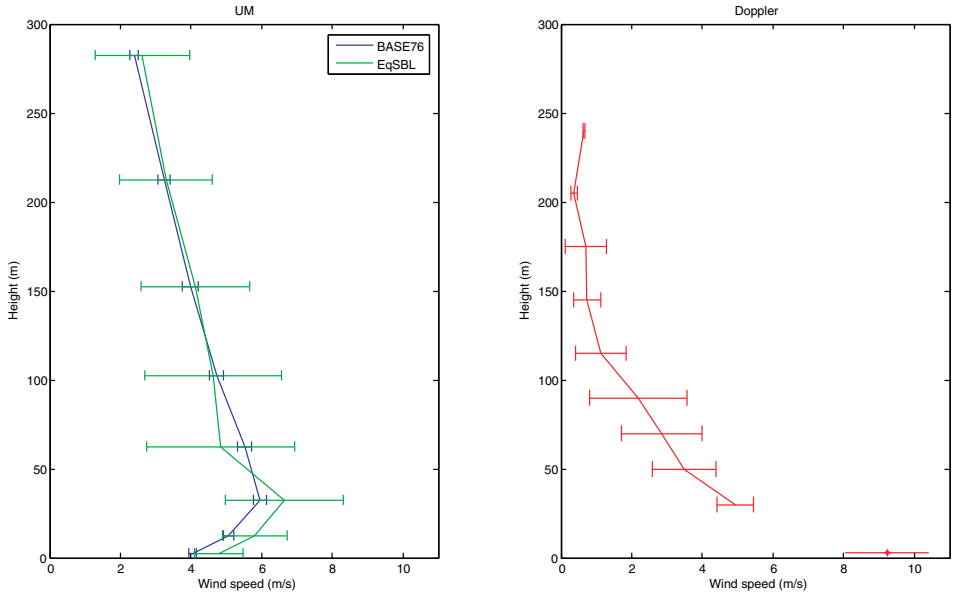

Figure 4.11: Average profiles of wind speed (m/s) taken from 15 minute averaged profiles between 1030 UTC and 1600 UTC for 14 August 2003, on the right from Doppler Sodar observations and on the left from model run BASE76 (in blue) and EqSBL (in green). The errorbars indicate the standard deviation. The lowest data point in the Doppler Sodar plot comes from the AWS hourly measurements.

shown. The EqSBL profiles show large temporal variability, which often compares favourably to the Doppler Sodar profiles. The shape of the EqSBL profiles often matches the Doppler Sodar profiles much better than the BASE76 run, for example at 11:00 and 13:45 (see figure 4.10). However, at some timesteps the EqSBL run overestimates the wind speed over the entire profile to a much larger extent than the BASE76 run, especially between 12:45 and 13:15. The wind speed at the surface is still underestimated in both model runs. The EqSBL run in general shows a 'sharper' profile, with a stronger maximum, though this maximum is often at the same height as in the BASE76 run (hence too high as compared to the observations). Figure 4.11 shows the average profile with standard deviation, for both model runs and for the Doppler Sodar observations. Above 100 m, both model profiles are very similar though the EqSBL run shows a larger standard deviation. Below 100 m, the EqSBL run shows a sharper katabatic jet with stronger wind speeds as compared to the BASE76 run. The general problems discussed in the previous chapter remain in the EqSBL run: the maximum wind speed is located too high up and the wind speed at the surface is underestimated.

Figure 4.12 shows grid relative wind arrows from the v (roughly downslope) and w component, with the u component (roughly cross-slope) shaded, from the EqSBL run. Refer to figure 3.27 in the previous chapter for a similar plot for

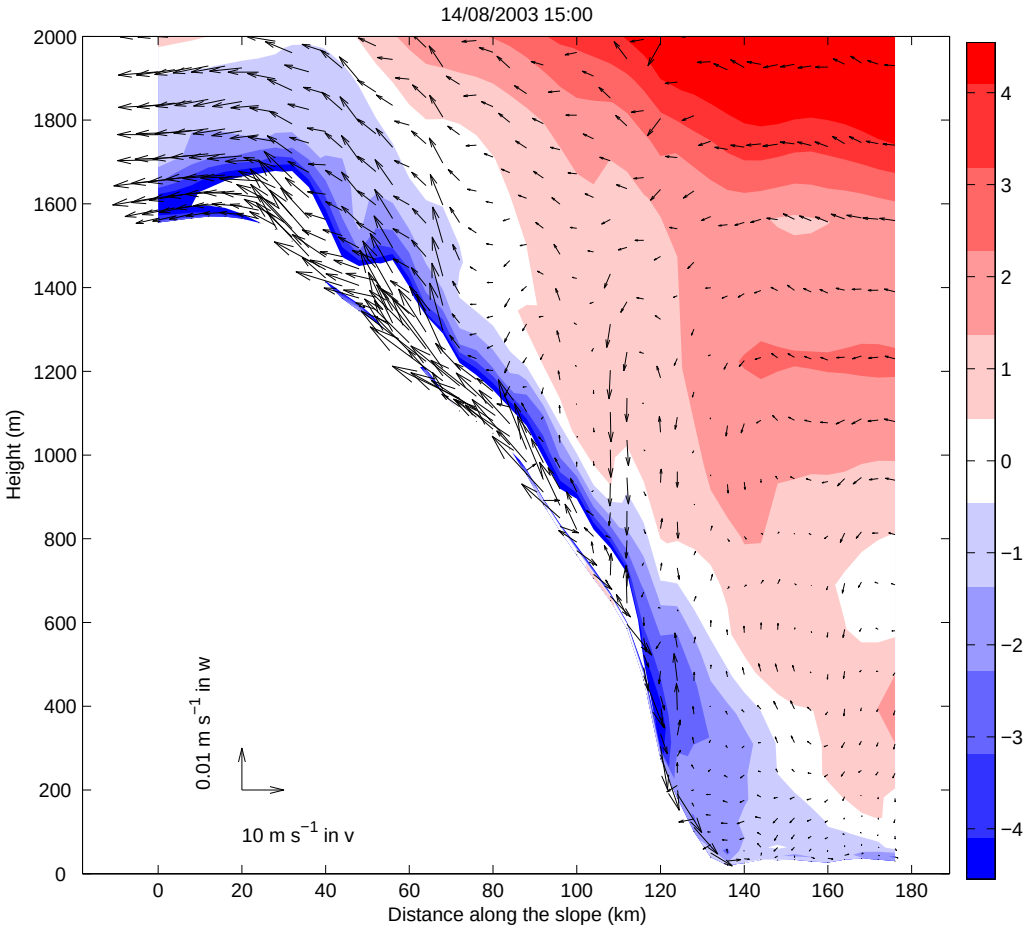

Figure 4.12: Wind vectors from the model's grid relative v (roughly downslope) and w components, from the EqSBL run, for 15 UTC 14 August 2003. The u component (roughly cross-slope) is shaded. A scaling arrow is given in the lower left corner. The cross-section is taken along the model's y direction, roughly from C4 on the left to Halley on the right.

the BASE76 run. Figure 4.12 clearly demonstrates the variable character of the EqSBL run (in all aspects). For example, wind directions sometimes change by 180 degrees in two bordering grid points. The vertical motions are strong, and the upward motions at the bottom of the slope are compensated by strong downward motions a little higher up the slope. It is hard to say whether this behaviour is desirable. It could be the case that this boundary layer scheme actually reflects the natural variability better than the other model simulations, but it could also be undesirable random behaviour of the boundary layer scheme.

Discussion on the boundary layer scheme

The model is quite sensitive to the choice of boundary layer scheme. For C2 and C3 the boundary-layer height was significantly lower in the SBL run, often as low as the boundary-layer height at Halley (about 12 m). This is too low for stations based on the slope (see for example Renfrew and Anderson (2006)). Surface temperatures are slightly lower in the EqSBL run, which is an improvement in most cases (except at Halley), and for February 2002 the extent of the diurnal cycle in temperature is better represented by the EqSBL run. All variables show more variability in the EqSBL run as compared to the BASE76 run. At times the results from the EqSBL run match the observations remarkably well, but at other times the chaotic behaviour of this boundary layer scheme does not match the observations at all. It is hard to judge whether the EqSBL scheme shows 'random' chaotic behaviour that happens to match the observations at certain times (by coincidence), or whether the EqSBL scheme actually improves the behaviour of the model and is capable of simulating certain quick changes seen in the observations. Figure 4.10 illustrates this most clearly: at times the EqSBL wind profiles match the Doppler profiles remarkably well (for example at 11:00, 13:45, 14:00), but at other times there are very large differences between the EqSBL profiles and the Doppler profiles (most notable between 12:45 and 13:15). The BASE76 run shows a wind profile that hardly changes during those 5.5 hours, and which does not match the much more variable Doppler observations very well, but the EqSBL run at times shows much larger overestimation when compared to the Doppler profiles. It is difficult to determine which results are more desirable.

4.4.3 Stability functions

This section discusses the results of using four different stability functions: the long-tailed stability function (BASE76 run, equation 4.3), the Louis/SHARPEST stability function (combining equation 4.5 and equation 4.4), the SHARPEST stability function (equation 4.4) and finally the BHrev run which uses a revised

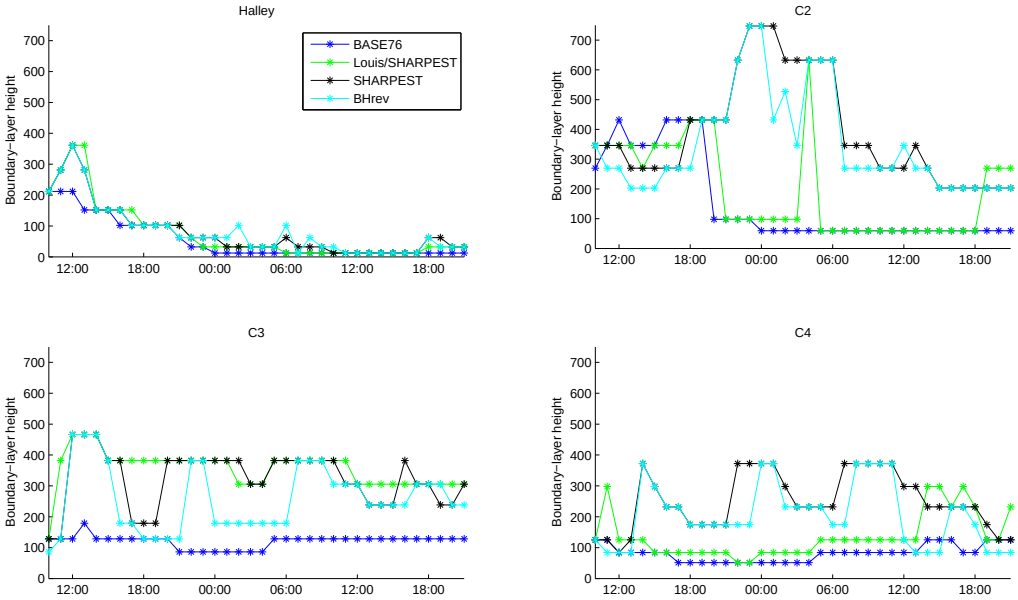

Figure 4.13: The boundary-layer height for Halley and Automatic Weather Stations C2-C4 for the BASE76 run (in blue), the Louis/SHARPEST run (in green),the SHARPEST run (in black) and the BHrev run (in cyan), for 13 and 14 August 2003.

version of the Beljaars and Holtslag (1991) stability functions both in the boundary layer (equation 4.24) and at the surface (using a = 5, b = 2/3, c = 7 and d = 2 in equations 4.9 and 4.10). The first three stability functions (long-tailed, Louis/SHARPEST and SHARPEST) are only used in the boundary layer while the stability functions at the surface are those described by the original Beljaars and Holtslag (1991) equations.

Figure 4.13 shows the boundary-layer heights for these four runs. At Halley, the differences between the runs are very small, except for a peak in the first few hours where all runs except the BASE76 run show an increased boundary-layer height. At C3 and C4, the boundary-layer heights range from about 50 to 450 m, with the BASE76 constantly showing the lowest boundary-layer heights. C2 shows the largest differences between the runs, and the boundary-layer heights range from 50 to 750 m. The SHARPEST and the BHrev run show the largest boundary-layer heights, while the Louis/SHARPEST run stays closer to the BASE76 run. It is surprising that those stability functions that allow for less mixing with increasing stability (SHARPEST and BHrev) show higher boundary-layer heights when compared to the stability functions that allow more mixing with increasing stability. For the February 2002 runs (not shown) the differences are smaller, but the BASE76 run still generally shows the lowest boundary-layer heights.

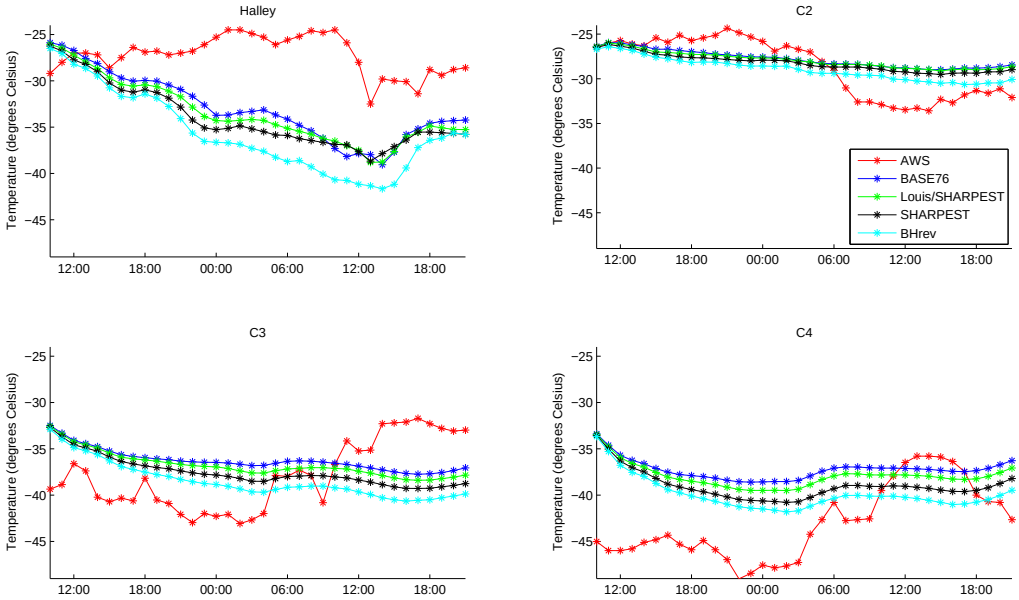

Figure 4.14: Surface temperatures for the BASE76 run (in blue), the Louis/SHARPEST run (in green), the SHARPEST run (in black) and the BHrev run (in cyan), compared to the AWS observations (in red) for 13 and 14 August 2003.

Figure 4.14 shows the temperatures for the BASE76, Louis/SHARPEST, SHARPEST and BHrev runs compared to observations, for the August 2003 case. There are no major differences between the three runs. The BHrev run shows the lowest temperatures, while the BASE76 shows the highest temperatures. The differences are never larger than about 2 °C though (except at Halley where the BHrev run is almost 6 degrees colder than the BASE76 run), and the surface air temperatures follow the same pattern in all four runs.

Figure 4.15 shows the temperatures from the BASE76 and BHrev run compared to the AWS observations, for the February 2002 case. The BHrev run simulates the range in the diurnal cycle much better than the BASE76 run, mainly because of lower temperatures during the night. We saw a similar improvement with the EqSBL run in figure 4.9, but the BHrev run shows a much smoother diurnal cycle and even colder temperatures during the night, both of which are improvements compared to the observations. Only at C4, the BHrev results are not an improvement compared to the BASE76 results. The results of the Louis/SHARPEST and SHARPEST run are not shown in this plot, but in general they follow the same pattern and fall in between the BASE76 run and the BHrev (similar to the results of the August 2003 case, see figure 4.14).

These results (shown both in figure 4.14 and 4.15) show that the sharper the stability function, the colder the air temperature near the surface. A sharper

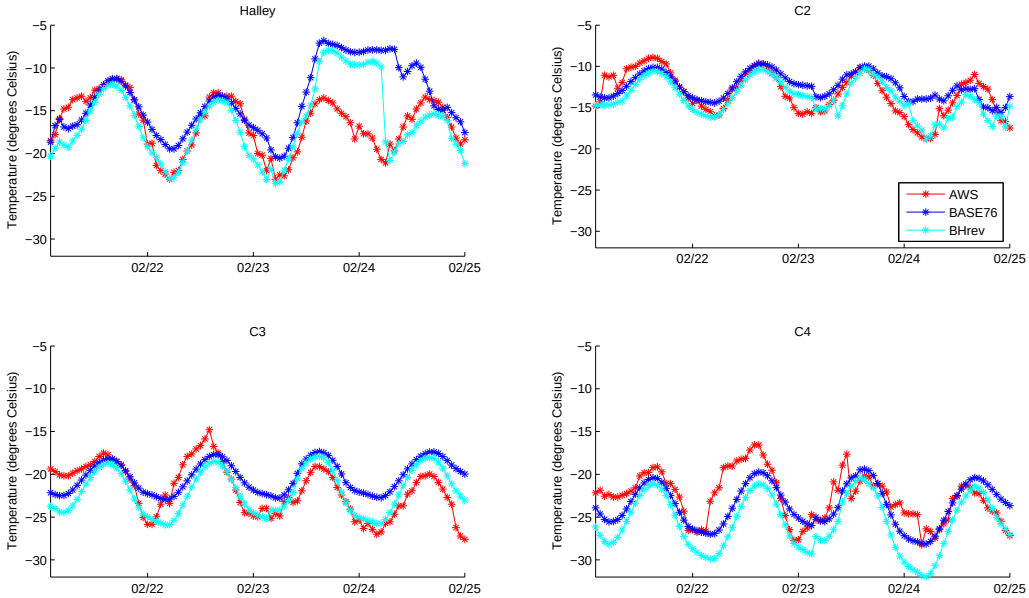

Figure 4.15: Air temperature (degrees Celsius) for 21-25 February 2002, from the BASE76 run (in blue), the BHrev run (in cyan) and from AWS observations (in red).

stability function allows for less mixing at a given stability, which results in a stronger temperature inversion near the surface, allowing the surface temperatures to cool down stronger than with a less sharp stability function.

The same goes for other variables (not shown). For example for the wind speeds, the Louis/SHARPEST run shows lower wind speeds compared to the BASE76 run, and the SHARPEST one has lower wind speeds than both the other runs. The differences are never exceeding 0.5 m/s so these are not major differences. It seems that even though the boundary-layer heights show large differences, this does not influence other variables much. The Doppler profiles for the August 2003 cases are very similar for the four runs, the differences are never exceeding 1 m/s. The largest differences occur at the peak of the katabatic jet. The BASE76 shows the weakest maximum, the other three runs (Louis/SHARPEST, SHARPEST and BHrev) show maxima of about 1 m/s stronger than BASE76. The maximum wind speed still occurs at the same height though, and all runs underestimate the wind speed at the surface. Figure 4.16 shows the wind speed over time and height for the BHrev run for the February 2002 case, similar to figure 3.68 for the BASE76 run and figure 3.67 from observations. This figure shows that although the maximum wind speed is stronger, it is still located at the same height as in the BASE76 run, and the wind speeds at the surface are even lower than those in the BASE76 run.

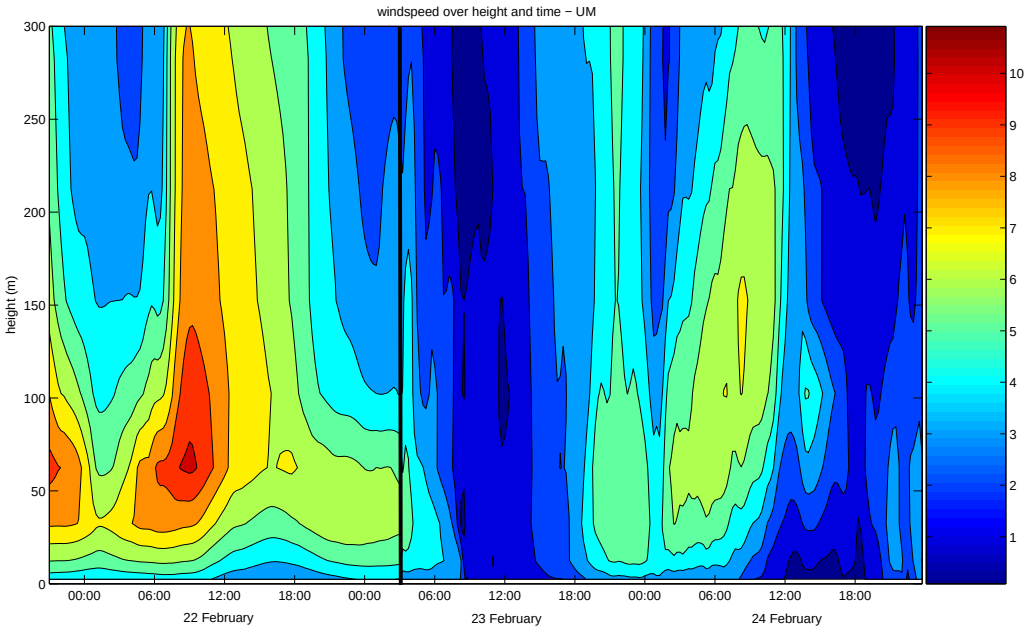

Figure 4.16: Wind speed over height and time from the Doppler Sodar (15 minute averages every 15 minutes), for 21-24 February 2002, for the BHrev run. The lowest level is provided by the AWS at the same location. Note that the AWS observations are taken at a height of 3 m, while the lowest Doppler level is at 30 m. This causes the gradients in the lowest levels.

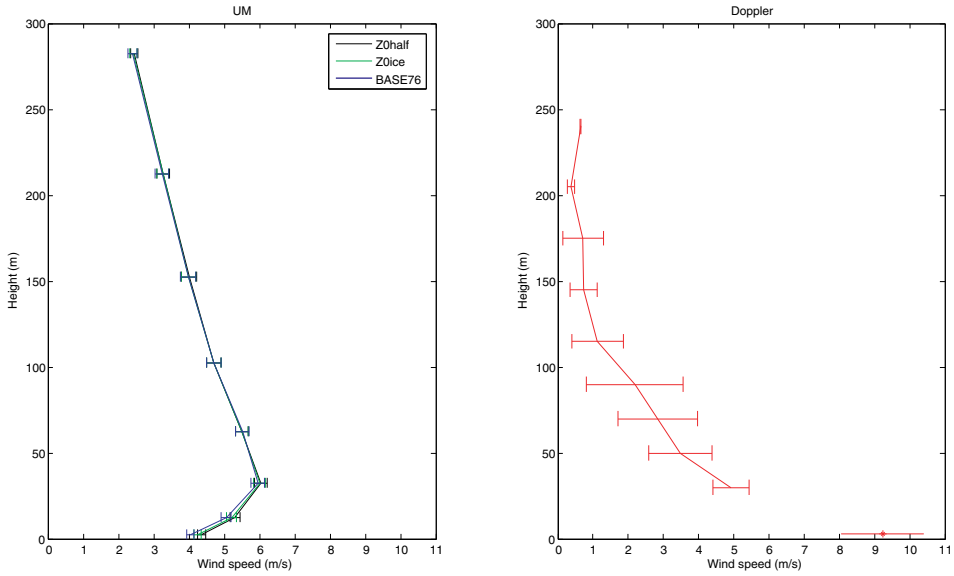

Figure 4.17: Average profiles of wind speed (m/s) taken from 15 minute averaged profiles between 1030 UTC and 1600 UTC for 14 August 2003, on the right from Doppler Sodar observations and on the left from model run BASE76 (in blue), Z0ice (in green) and Z0half (in black). The errorbars indicate the standard deviation. The lowest data point in the Doppler Sodar plot comes from the AWS hourly measurements.

Discussion on stability functions

Changing the stability functions made a significant difference on the boundary-layer height (see figure 4.13), but it did not seem to make much difference for other variables. Especially in the August 2003 case the differences are very small. For the February 2002 summer case, the difference are slightly larger. In this case the results concerning the surface temperatures are improved with each sharper stability function as the temperatures decrease during the night which results in a better represented diurnal cycle. In both case studies, the sharper the stability function, the stronger the wind speed maxima. However, the height of this maximum does not change; it is still too high compared to the Doppler Sodar observations. The wind speed at the surface remains underestimated by all model runs.

4.4.4 Roughness length

This section discusses the results of the experiment in which we change the base roughness length over land from the default 3.0×10^{-4} m in the BASE76 run, to a value of 1.0×10^{-4} m in Z0ice and a value of 5.0×10^{-5} m in Z0half.

Figure 4.17 shows the average wind profile for the August 2003 case with standard deviation, for the BASE76, the Z0ice and the Z0half runs and for the

Doppler Sodar observations. The profiles from all three model runs are very similar and differ only for the lowest three model levels. The Z0half run shows the strongest wind speeds, followed by the Z0ice run and finally the BASE76 run shows the lowest wind speeds. These results are not surprising; decreasing the roughness length will increase the wind speeds near the surface as the winds are slowed down less by surface friction. However, the differences between the three runs are very small. At the lowest model level, the difference between the BASE76 run (with the highest roughness length) and the Z0half run (with the lowest roughness length) is only 0.35 m/s.

Further results show that the boundary layer height decreases with decreasing roughness length (not shown), but here too, the differences are very small. Over the slope, decreasing the roughness length results in slightly increased air temperatures (about 0.1 degrees maximum, not shown). At Halley, decreasing roughness lengths result in decreased temperatures with a maximum difference of 1 degree between BASE76 and Z0half. This does not improve the comparison to the observations though, as the model largely underestimates the air temperatures at Halley in BASE76.

Discussion on the roughness length

Even though the roughness length is decreased by a factor 6 in the Z0half run as compared to the BASE76 run, the model results do not change very much. As expected, the wind speeds near the surface increase when the roughness length is decreased, but the changes are relatively small. This shows that the model results are not very sensitive to changing the roughness length, and that the underestimated wind speeds and too deep boundary layer are not simply caused by a too high roughness length.

4.5 Summary and conclusions

Increasing the vertical resolution significantly improved the model results, especially over the ice shelf (Halley). The BASE76 run still shows too low surface temperatures at Halley, but to a much lesser extent than the 38-level BASE run did. The BASE76HR, which also has 76 vertical levels but with a higher (doubled) resolution in the lowest 500 m (and a lower resolution higher up in the atmosphere), does not significantly improve the results as compared to the BASE76 run. This shows that the problems with the overly deep katabatic layer and the underestimation of wind speeds at the surface are not related to the vertical resolution. Higher resolution near the surface will enable us to study certain aspects of the model results in greater detail though.

The model is sensitive to the choice of boundary-layer scheme. The EqSBL run shows increased variability in all variables, which does compare better to

observations. It also represents the range of the diurnal cycle in the February 2002 case better than the BASE76 run. However, the EqSBL run shows 'chaotic' random behaviour which at times does not match the observations at all, and it is hard to decide whether this behaviour is desirable.

The model is less sensitive to the choice of stability function than to the choice of boundary-layer scheme. In most cases, the BASE76, Louis/SHARPEST, SHARPEST and BHrev runs show broadly the same pattern, though the temperatures decrease and the wind speed increases with the sharpness of the stability functions, i.e. when less mixing is allowed. The diurnal cycle in temperature in the February 2002 case is best represented by the BHrev run, which shows the lowest temperatures during the night.

Decreasing the roughness length did not make a significant impact on the model results. As expected, the wind speeds near the surface increase when the roughness length is decreased but the changes are very small, showing that the model results are not very sensitive to the chosen roughness length.

Unfortunately, none of the different model runs discussed above makes a significant impact on the height of the katabatic layer which is still too deep; nor the height of the katabatic jet maximum which is too high; nor the wind speed at the surface which is still underestimated in all the model runs.

Chapter 5

Dynamics of the katabatic flow

5.1 Introduction

This chapter will discuss the general dynamics of the katabatic flow by means of two different ways of calculating the momentum budget. The momentum budget is a useful tool for interpreting the model simulations of katabatic flow, as it shows which forces dominate the katabatic flow. It can also provide more insight into what happens at the foot of the slope, where the katabatic flow meets the flat Brunt ice shelf.

King (1993) observes that the wind regime at Halley is very similar to the wind regime at the hinge zone at the bottom of the slope, indicating that the transition between katabatic flow over the slope and the wind regime over the ice shelf takes place more rapidly than expected from simple inertial adjustment. He suggests that this could be explained by a hydraulic jump, something also supported by the fact that from Halley, a band of clouds running parallel to the hinge slope is often observed, possibly generated by the strong vertical motions associated with such a hydraulic jump (King, 1993). Renfrew and Anderson (2002) analysed 5 years of the Coats Land AWS data and observed that the Brunt Ice Shelf is generally unaffected by katabatic winds. When the surface flow is katabatic over the slope, the Brunt ice shelf often shows low to moderate wind with no preferred direction. They also suggest that a hydraulic jump would explain this situation.

Hydraulic jumps have been observed in katabatic flows, see for example Pettré and André (1991) who described observations of 'Loewe's Phenomenon' (Valtat, 1959) during a field program that took place in 1985 in Adélie land. This phenomenon (generally observed on the steep ice slopes near the coast (King and Turner, 1997)) consists of a sudden transition from 'shooting' to 'tranquil' flow and is therefore also known as a 'katabatic jump' (by analogy to the hydraulic jump). In terms of hydraulic theory (see Ball (1956); Mahrt (1982)), a flow is shooting (or rapid) when the Froude number (a dimensionless number using

the ratio between the inertia force and the gravitational force) is greater than one, and tranquil when the Froude number is less than one (Renfrew, 2004). In shooting flow, the inertia of the flow dominates over gravity and vice versa for tranquil flow (Ball, 1956). The local Froude number will be defined later in this chapter.

Idealised model simulations by Renfrew (2004) shows how a pool of cold air at the bottom of the slope causes a combination of upslope forces that balance the buoyancy force, and forces the katabatic flow to retreat upslope. These upslope forces are probably related to a katabatic jump. Figures 3.25 and 3.26 indicate that our model simulation also shows a cold pool blocking the flow at the bottom of the slope. This pool of cold air is also found in model simulations over the East Antarctic ice sheet by van den Broeke *et al.* (2002), who found that cold air piling up over the sea ice and ice shelves at the coast causes a considerable opposing force to the katabatic force, with rising motions indicating the deceleration of the flow in this area. Gallée and Schayes (1992) and Gallée and Pettre (1998) also found that the piling up of cold air is a possible mechanism that can lead to the sudden cessation of katabatic flow near the coast by producing an upslope pressure-gradient force. Yu *et al.* (2005) and Yu and Cai (2006) performed idealised numerical simulations (using the non-hydrostatic model RAMS) over Coats Land to study katabatic jumps. It will be interesting to compare the results of our real case studies with the results of these idealised studies.

5.2 Momentum budget - two-layer framework

The two-layer downslope momentum budget is the one used in Renfrew (2004), which is based on the framework set out in Mahrt (1982). This framework is developed to work over sloping terrain. In this method, we assume two layers: an active lower layer and a quiescent upper layer. The lower level is the katabatic layer. The downslope momentum budget is defined by:

$$\frac{Du_{kls}}{Dt} = \frac{g\Delta\theta}{\theta_0} sin\alpha - cos\alpha \frac{g}{\theta_0} \frac{\partial(\Delta\theta h_{inv})}{\partial x} + f v_{kls} - \frac{\partial\overline{(u'w')}}{\partial z} \qquad (5.1)$$

Renfrew (2004). The subscript *kls* indicates that the variable has been averaged over the katabatic layer and oriented into downslope direction. θ_0 is a reference potential temperature, taken as the potential temperature in the upper layer. $\Delta\theta$ is the potential-temperature deficit between the upper and the lower level, so that $\Delta\theta = \theta_0 - \theta_{kl}$. f is the Coriolis parameter, g is the gravitational acceleration and α is the positive slope angle. h_{inv} is the height of the katabatic layer, which in this case is defined as the height of the temperature inversion. Following Renfrew (2004), we use a threshold value of 0.025 K/m for the winter case study, i.e. the katabatic flow (lower layer) has $\partial\theta/\partial z > 0.025$ K/m. For the summer

case study, we used a slightly higher value of 0.027 K/m. Sensitivity tests showed that the results are quite robust and do not change much when the temperature threshold is changed. Heinemann (1999) and Heinemann and Klein (2002) used a similar method to study the dynamics of katabatic flow over Greenland. The $\partial\theta/\partial z$ threshold used by Heinemann and Klein (2002) is 0.02 K/m, which is similar to ours.

We use a cross-slope, downslope and perpendicular to the slope coordinate system for (x, y, z), with velocity components (u_{kls}, v_{kls} and w_{kls}). In the original framework, the downslope component is in the x direction and the cross-slope component in the y direction. For our case, where the downslope direction is in the model's y-direction, this means that the x-direction from the model needs to be reversed, i.e. we use: $u = v_{um}$ and $v = -u_{um}$, where the subscript um indicates the model's grid relative wind coordinates. We assume that the downslope direction is the same over the entire domain, even though in reality the slope does change direction. However, the results shown in this chapter are for the AWS locations which are roughly on one line down the slope. The topography over our domain has moderate slopes and therefore $\sin\alpha \approx \alpha$ and $\cos\alpha \approx 1$. After integrating over the katabatic layer and expanding the Lagrangian derivatives we get the following equation for the downslope momentum budget:

$$\begin{aligned}\frac{\partial v_{kls}}{\partial t} &= -\left(v_{kls}\frac{\partial v_{kls}}{\partial y} + w_{kls}\frac{\Delta v_{kls}}{h_{inv}}\right) + \frac{g\Delta\theta}{\theta_0}\alpha - \frac{gh_{inv}}{\theta_0}\frac{\partial\Delta\theta}{\partial y} - \frac{g\Delta\theta}{\theta_0}\frac{\partial h_{inv}}{\partial y} + fu_{kls} \\ &\quad - \frac{\overline{v'w'}_{inv} - \overline{v'w'}_{sfc}}{h_{inv}} \\ &= F_{adv} + F_b + F_{\Delta\theta} + F_h + F_{Cor} + F_{div}\end{aligned} \tag{5.2}$$

(Renfrew, 2004). In this equation, v_{kls} is derived from v_{um} and u_{kls} from $-u_{um}$, as discussed before. Δv_{kls} is the difference between the upper and the lower velocity. The upper velocity is taken as the velocity at a height of 250 m above h_{inv}, as the quiescent layer in our real simulations does not start right above h_{inv} as was the case in for example the idealised simulations by Renfrew (2004). Δv_{kls} is mostly negative, especially over the areas with a clear katabatic flow. The inversion-height variables (indicated with the subscript inv) are found by interpolating to the height of the $\partial\theta/\partial z$ threshold. The subscript sfc indicates variables at the surface, taken as the first model level. F_{adv} is the total advection (inertial force); F_b the buoyancy or katabatic force; $F_{\Delta\theta}$ the force due to the downslope gradient in the potential-temperature deficit; F_h the force due to the downslope gradient in the katabatic-layer height; F_{Cor} the Coriolis force; and F_{div} the momentum flux divergence force. F_{in} is the inertial term (the storage of mean momentum, or time tendency, the term on the left side of the equation ($\frac{\partial u_{kls}}{\partial t}$)). The residual term ($F_{res}$) is the sum of all terms. This two-layer framework

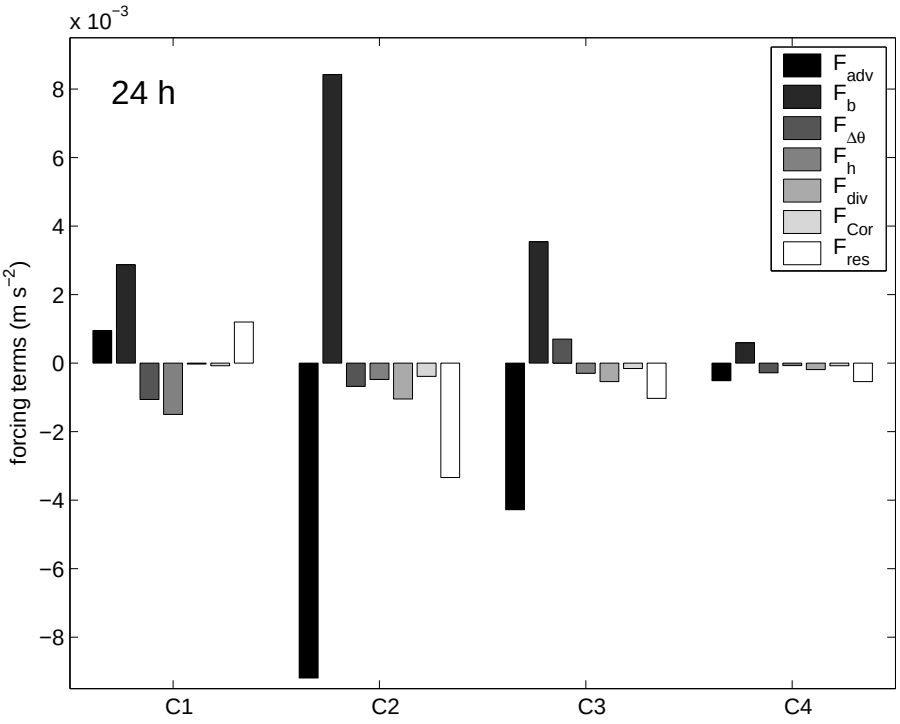

Figure 5.1: Forcing terms in the downslope momentum equation after 24 hours of idealized model simulation using the RAMS model: F_{adv} is the advection term, F_b is the buoyancy force, $F_{\Delta\theta}$ is the force due to the gradient in the potential-temperature deficit, F_h is the force due to the gradient in the katabatic-layer height, F_{div} is the momentum flux divergence force, F_{Cor} is the Coriolis force and F_{res} is the residual. From Renfrew (2004).

assumes no synoptic forcing, which is a valid assumption in ideal simulations like in Renfrew (2004), but for our real case studies this could mean that any synoptic forcing ends up in the residual force. All heights are taken as the height above the ground level. The terms of the downslope momentum budget are calculated using model variables averaged over 3 hours. The momentum flux divergence term is calculated using the wind stress term (τ) from the model using:

$$\overline{(v'w')} = -\frac{1}{\rho}\tau_y \tag{5.3}$$

(Stull, 1988)

5.2.1 Results for the winter case study

Renfrew (2004) used equation 5.2 to analyse the downslope momentum budget of an idealized katabatic flow simulation over Coats Land. Figure 5.1 shows the forcing terms of the downslope momentum budget as found by Renfrew (2004), after 24 hours of simulation time and using data averaged over 3 hours. Figure 5.1

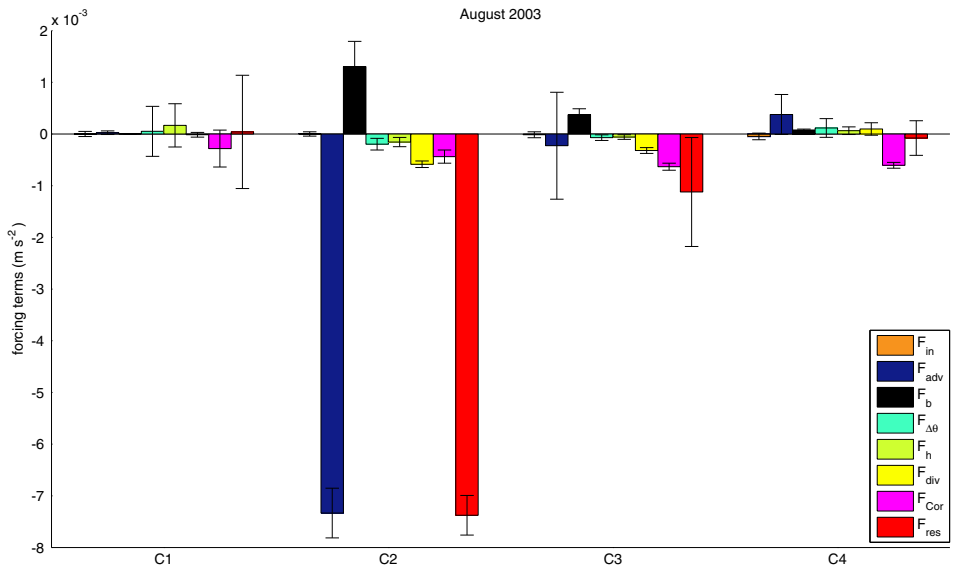

Figure 5.2: Average forcing terms (with error bars indicating the standard deviation) in the downslope momentum equation for the August 2003 case: F_{int} is the inertia term (storage of mean momentum), F_{adv} is the advection term, F_b is the buoyancy force, $F_{\Delta\theta}$ is the force due to the gradient in the potential-temperature deficit, F_h is the force due to the gradient in the katabatic-layer height, F_{div} is the momentum flux divergence force, F_{Cor} is the Coriolis force and F_{res} is the residual.

shows a balance between the advection term and the buoyancy forcing at C2, C3 and C4. These locations are all higher on the continental slope, while C1 is located at the foot of the slope. Here, the balance is different: the buoyancy force is balanced by F_h, $F_{\Delta\theta}$ and F_{div}. As previously discussed, this combination of upslope fores that together balance the buoyancy force are primarily caused by a pool of cold air that forms over the ice shelf and dams the downslope flow, leading to a deceleration at C1 (Renfrew, 2004). We will discuss this phenomenon in more detail later on.

Figure 5.2 is similar to figure 5.1, but from the UM model simulation for August 2003. Since this is not an idealized case study, the budget is more variable throughout the model simulation. To illustrate the variability of the momentum budget, figure 5.2 shows the average forcing terms (averaged over 12 3-hour periods) with the standard deviation. It is interesting to compare figures 5.1 and 5.2 to investigate how the budget from an idealized case differs from that of a real case study. Overall, the terms of the momentum budget in figure 5.2 are smaller than those in the idealised case study. Renfrew (2004) did not calculate the inertial term, but this term is found to be negligibly small at all locations in our case. At C2, the advection term is only partly balanced by the buoyancy force. The buoyancy force is about 5-6 times smaller than the buoyancy force

found in the idealised budget by Renfrew (2004). The buoyancy term is the only positive term, and this creates a very large residual term, slightly larger even than the advection force. At C3, the buoyancy force is almost balanced by the advection term, but both forces are rather small compared to those in the idealized case study. At C4, the advection force is balanced by the Coriolis force, but here we do not have a katabatic wind situation, as the winds are upslope at C4 (see figure 3.9). These upslope winds appear to be forced by the Coriolis force. At C1, all forces are rather weak, and quite variable - all terms show both positive and negative values. At C2, the sign of each term is the same throughout the simulation. C2 shows downslope flow through the entire simulation (see figure 3.9), which according to figure 5.2 can not be explained by the buoyancy force alone. At C3, the advection term shows a high standard deviation. This is because the advection force decreases at first (to negative values), before increasing to positive values. This is probably related to the changes taking place at C3, for example during the run the wind direction changes from downslope to upslope. All other terms show a relatively small standard deviation. In our budget, the buoyancy force is very small when compared to the buoyancy force from Renfrew (2004) (see figure 5.1). This could be due to a smaller potential-temperature deficit in our case, caused by the fact that the layer above the katabatic layer is not as quiescent as in an idealised simulation. The potential temperature inversion is stronger in the idealised simulations, and for our model simulations $\partial\theta/\partial z$ is around 0.01-0.02 K/m in the quiescent layer, while this value is closer to zero in the idealised simulations. Underestimating the buoyancy force could also explain the large residual force. The very large (negative) residual force (especially at C2 but also at C3) includes uncertainties in calculating the other terms of the momentum budget, as well as synoptic forcing influencing the katabatic flow. Many studies have shown that the synoptic or large-scale pressure-gradient force influences the katabatic flow considerably (see for example Parish *et al.* (1993a); Parish and Cassano (2001, 2003b); Heinemann and Klein (2002); van den Broeke *et al.* (2002); van den Broeke and van Lipzig (2003); Bintanja (2000)) and is hard to distinguish from 'pure' katabatic forcing as this synoptic forcing is also strongly shaped by the terrain and acts in the downslope direction (Parish and Cassano, 2001). However, this synoptic force is not included in the momentum budget framework used here. Some authors suggest that this momentum equation should include a horizontal pressure gradient, but according to Haiden (2003) this is incorrect and leads to errors unless the vertical pressure gradient is also included, furthermore, if the temperature perturbation is constant along the slope, alongslope accelerations due to the horizontal and vertical perturbation pressure gradients would cancel each other exactly.

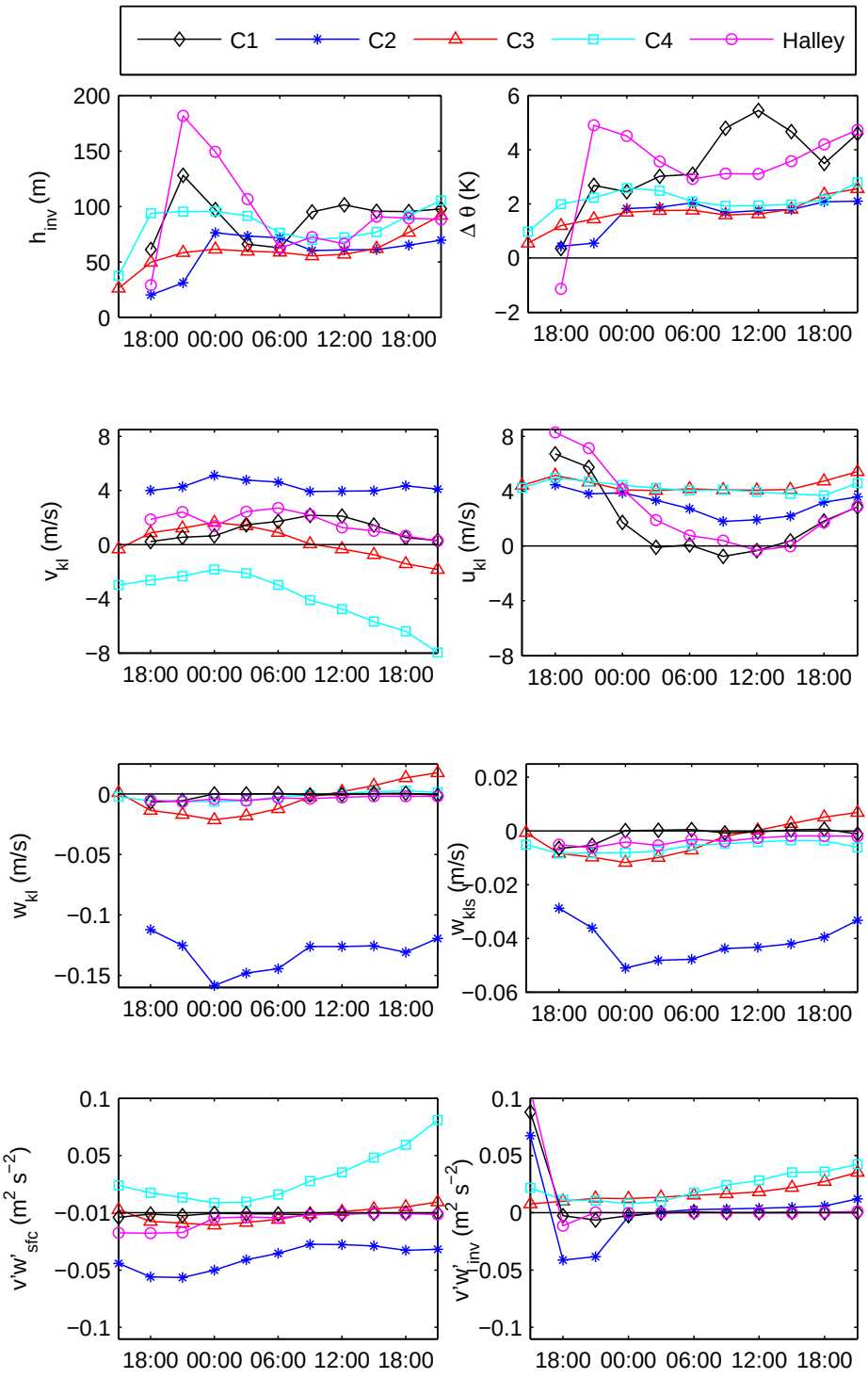

Figure 5.3: Variables used in the calculation of the winter case (August 2003) downslope momentum budget: the katabatic layer height (h_{inv}), the potential temperature difference between the katabatic layer and the upper layer ($\Delta\theta$), katabatic-layer means of v (v_{kl}: downslope velocity), u (u_{kl}: cross-slope velocity), w (w_{kl}: vertical velocity and w_{kls}: slope-relative vertical velocity), and surface and inversion height fluxes ($v'w'_{sfc}$ and $v'w'_{inv}$) for C1-C4 and Halley. These are all 3-hour means ending at the plotted time.

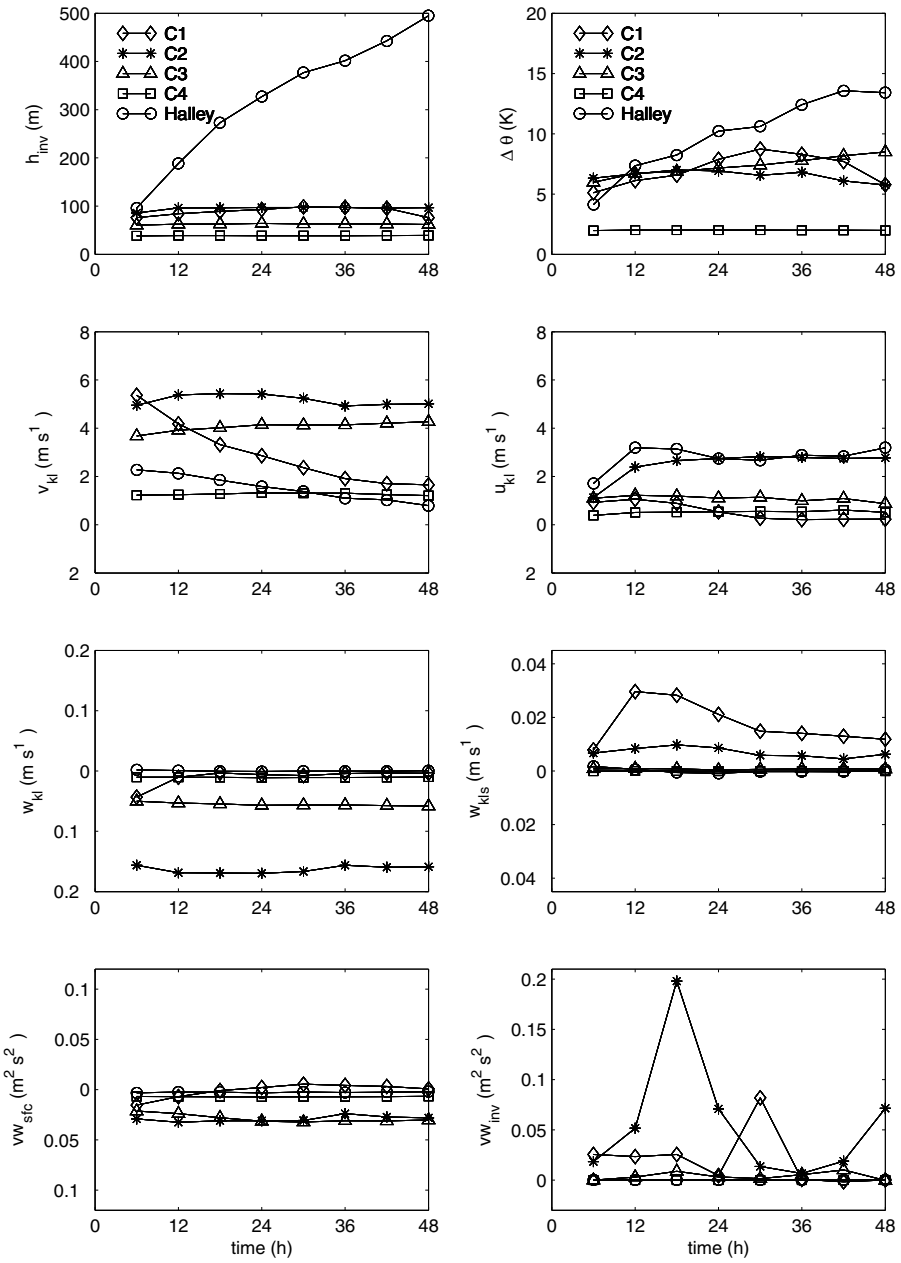

Figure 5.4: Variables used in the calculation of the downslope momentum equation from an idealized model simulation using the RAMS model: the katabatic layer height (h_{inv}), the potential temperature difference between the katabatic layer and the upper layer ($\Delta\theta$), and katabatic-layer means of v (v_{kl}, downslope velocity), u (u_{kl}, cross-slope velocity), w (w_{kl}, vertical velocity), w (w_{kls}, slope-relative vertical velocity), and surface and inversion height fluxes (vw_{sfc} and vw_{inv}) for C1-C4 and Halley. These are all 3-hour means ending at the plotted time. Figure from Renfrew (2004).

Figure 5.3 shows a timeseries for some variables that were used in the calculation of the downslope momentum budget. The katabatic layer height is between 50 and 100 m at nearly all locations, and is quite stable during the model run. The potential temperature difference between the katabatic layer and the upper layer ($\Delta\theta$) is mostly between 1-3 K. C2 actually shows the smallest value of around 2 K, while C1 is the most variable ranging from nearly 0 to nearly 6 K. At Halley, the potential temperature difference is initially negative, but this quickly changes to values between 3 and 6 K. The down-slope wind component averaged over the katabatic layer v_{kl} is largest (and positive) at C2, while showing negative values at C3 and C4, corresponding to the upslope winds at these locations. The cross-slope wind component u_{kl}, averaged over the katabatic layer, is positive at nearly all times and at all locations. The vertical wind speed averaged over the katabatic layer (w_{kl}) is close to 0 m/s at all locations except at C2, where it shows values between -0.1 and -0.15 m/s. These sinking motions seen in figure indicate an acceleration of the flow at this part of the slope. The slope-relative vertical velocity (w_{kls}) is similar to w_{kl} though much smaller. We can compare figure 5.3 to figure 5.4 from Renfrew (2004). This figure shows the same variables as figure 5.3 but calculated for an idealised model simulation. Except for at C1, the katabatic layer height in his simulation is similar to ours, while the potential temperature difference was larger (around 7 K). v_{kl} at C2 is about the same for both model simulations, but there are some differences for other locations (especially C4) due to the fact that our simulation is a real case study, with a synoptic situation that causes upslope winds at C3 and C4. w_{kls} in the idealised simulation shows positive values at all locations, while these are negative in our model simulation. The values of $v'w'_{sfc}$ are quite similar in the idealised simulation (as compared to our simulation), but $v'w'_{inv}$ does not show the large peak seen in the idealised simulation.

Figure 5.2 shows that there is a large difference between the budget at C2 and at C1, which are about 32 km apart. The katabatic flow reaches the foot of the slope just 20 km downslope from C2, and this changes the momentum budget. At C1, the budget is quite variable, with the standard deviation ranging from positive to negative values. Renfrew (2004) shows how a pool of cold air at the bottom of the slope causes a combination of upslope forces that balance the buoyancy force. van den Broeke *et al.* (2002) found that cold air piling up over the sea ice and ice shelves at the coast causes a considerable opposing force to the katabatic force, with rising motions indicating the deceleration of the flow in this area. Figure 5.3 does not show rising motions for C1, but further analysis (not shown) reveals that these rising motions are present about 20 km before the flow reaches C1. It is interesting to investigate how the downslope momentum budget changes along the slope. Figure 5.5 shows the average forcing terms in a cross-section over the slope ranging roughly from C4 on the left to Halley on

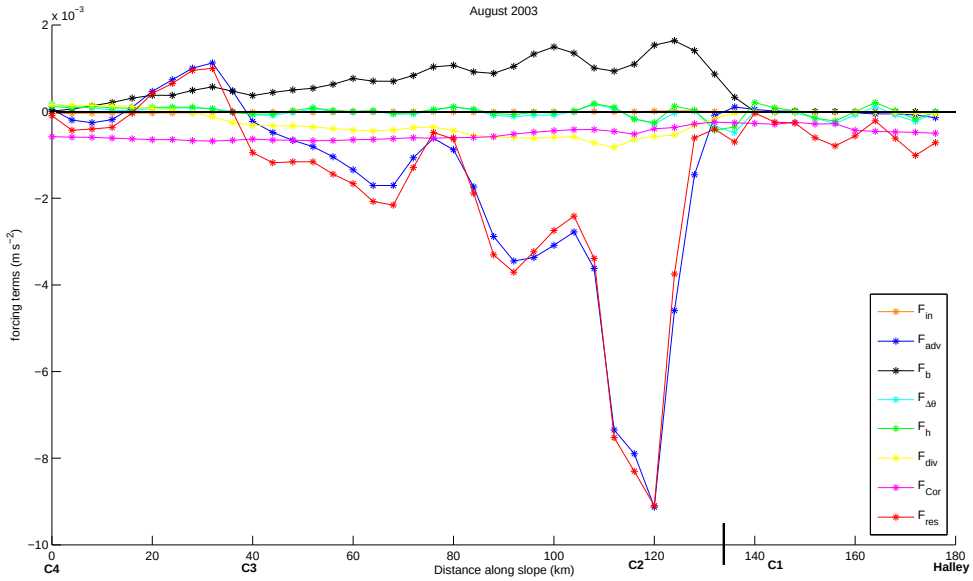

Figure 5.5: Average forcing terms along the slope for the August 2003 (winter) case study: F_{int} is the inertia term (storage of mean momentum), F_{adv} is the advection term, F_b is the buoyancy force, $F_{\Delta\theta}$ is the force due to the gradient in the potential-temperature deficit, F_h is the force due to the gradient in the katabatic-layer height, F_{div} is the momentum flux divergence force, F_{Cor} is the Coriolis force and F_{res} is the residual. The locations of Halley and C1-C4 are indicated, and the vertical line on the x-axis indicates the bottom of the slope.

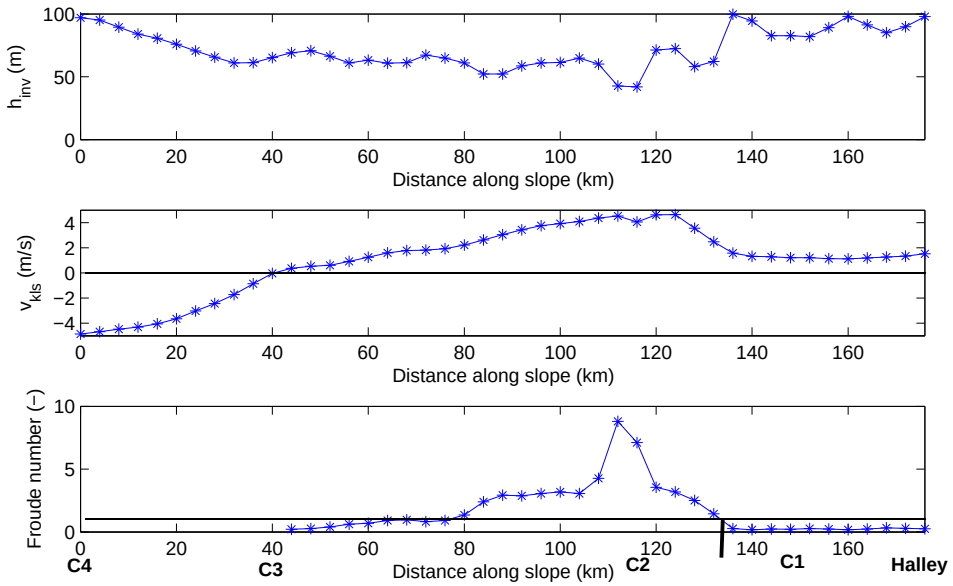

Figure 5.6: Average inversion height (h_{inv}, top panel), average downslope windspeed in the katabatic layer (v_{kls}, middle panel) and average Froude number (bottom panel), averaged over the last 24 hours of the model simulation, along the slope roughly from C4 on the left to Halley on the right for the August 2003 (winter) case study. The locations of Halley and C1-C4 are indicated, and the vertical line on the x-axis indicates the bottom of the slope.

the right. The advection force dominates the budget in such a strong way that the residual force is nearly identical to the advection force. The magnitude of the advection force increases strongly (becoming more negative) towards C2, at the steepest part of the slope. Before it reaches the bottom of the slope, the advection force decreases to nearly zero. The buoyancy force and the divergence force also decrease to nearly zero just after reaching the bottom of the slope. The Coriolis force does not change significantly. Both F_h and $F_{\Delta\theta}$ become more significant near the bottom of the slope, and both are acting to decelerate the flow, something also noted by Renfrew (2004). It is striking that the advection force starts to strongly decrease about 15 km before reaching the bottom of the slope, while the other forces are adjusted further down. The location of this decrease in the advection force is quite stable over time.

Figure 5.6 shows the average height of the katabatic layer, the average downslope wind component and the Froude number along the slope. The Froude number is a dimensionless number defined by (for our case):

$$Fr = -\frac{v_{kls}^2}{(g\Delta\theta/\theta_0)h_{inv}} \tag{5.4}$$

(Renfrew, 2004) The Froude number can be used to determine whether the flow is 'shooting' (when Fr $>$ 1) or 'tranquil' (when Fr $<$ 1), as discussed before.

Figure 5.6 shows the mean Froude number along the slope (only shown where the flow is downslope, starting from near C3). The flow is shooting at the higher parts of the slope (between C4 and C3), but here the flow is upslope. At C3, the flow is tranquil but further down the slope starts to increase to shooting flow, reaching a maximum near C2. Near the bottom of the slope the flow rapidly decreases to tranquil flow and remains like that over the ice shelf. Heinemann (1999) also found the Froude number to be shooting in the katabatic flow. Renfrew (2004) calculated the Froude number for the idealized model simulation, and found the flow to be shooting at C2 and C3. At C4 and Halley, the flow is tranquil, but at C1 he finds a clear transition from shooting to tranquil flow. In our case the flow is tranquil at C1 for the entire model simulation. The transition from shooting to tranquil flow takes place before the flow reaches C1, and this location is pretty constant throughout the model simulation. Yu *et al.* (2005) studied katabatic jumps in Coats Land from idealised non-hydrostatic model simulations with the RAMS model. They found an abrupt change from shooting to tranquil flow near the foot of the slope, accompanied by a sudden decrease of the downslope windspeed and an increase in the height of the katabatic layer, which are all characteristics of a katabatic jump. Figure 5.6 also shows the mean height of the katabatic layer and the average downslope windspeed in the katabatic layer along the slope. The downslope wind component is negative at the highest part of the slope (near C4), indicating the upslope winds here. The flow starts to be downslope at C3, and increases in strength until reaching a maximum around C2, at the steepest part of the slope. It then decreases (though not as rapidly as found by Yu *et al.* (2005)) until it reaches a constant value over the slope. The height of the katabatic layer over that part of the slope showing downslope winds is quite constant until it reaches the foot of the slope and the height increases from 60 to 100 m. These results are quite similar to those found by Yu *et al.* (2005), though we do not find upslope winds at the bottom of the slope, and the katabatic jump is not quite as strong.

5.2.2 Results for the summer case study

Figure 5.7 is similar to figure 5.2, but for the February 2002 (summer) case. The general momentum budget has not changed very much, but the standard deviation is much higher. Both the wind speeds and temperatures show a clear diurnal cycle during this summer case study, and this reflects in the forces of the momentum budget, explaining the large standard deviations. At C2, all forces are very similar to those in the winter case study, but the advection term in the summer case has decreased compared to the winter case. At C1, the summertime momentum budget shows variable forces that can be both negative and positive, just like in the wintertime momentum budget. At C4, the upslope winds (see figure 3.59) appear to be forced by the Coriolis force.

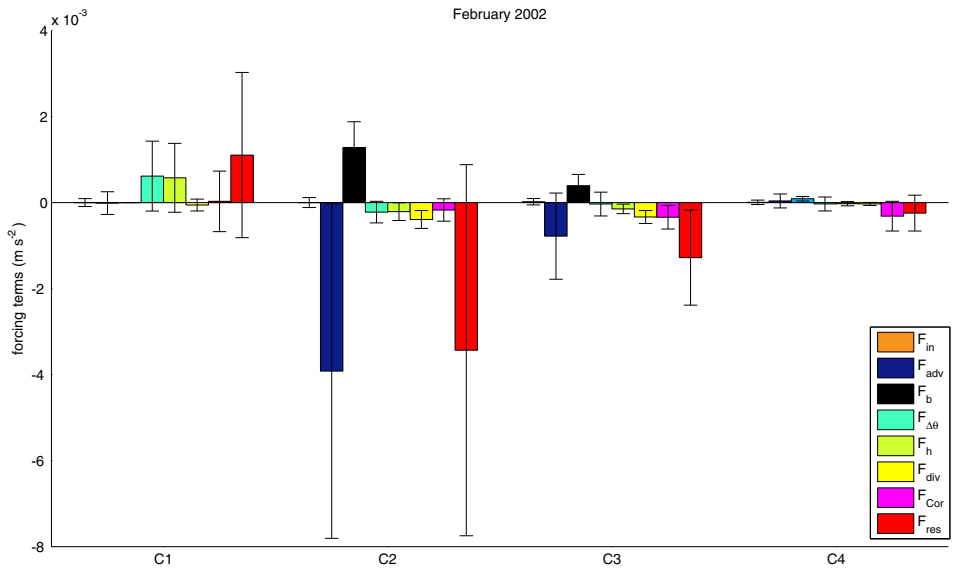

Figure 5.7: Average forcing terms (with error bars indicating the standard deviation)in the downslope momentum equation for the February 2002 case: F_{int} is the inertia term (storage of mean momentum), F_{adv} is the advection term, F_b is the buoyancy force, $F_{\Delta\theta}$ is the force due to the gradient in the potential-temperature deficit, F_h is the force due to the gradient in the katabatic-layer height, F_{div} is the momentum flux divergence force, F_{Cor} is the Coriolis force and F_{res} is the residual.

To have a closer look at the diurnal variation of the different terms of the summertime momentum budget, figure 5.8 shows the forcing terms over time for C1-C4. The downslope momentum budget is a two-layer framework that averages over a katabatic layer up to the height of h_{inv} which is chosen as the height where the temperature gradient falls below 0.027 K/m (for the summer case). During daytime in summer, the temperature gradient can be lower than 0.027 K/m even at the surface. In this event, a katabatic layer is not defined and this explains the missing values in figure 5.8. Figure 5.8 shows that there is a diurnal cycle at nearly all locations, but most noticeable at C2 and C3. The buoyancy force is strongest during the early morning, and weakest in the late afternoon. At C1 the buoyancy force is very small (nearly zero). At C2, all terms of the budget are larger than at the other locations, and all terms show a clear diurnal cycle. The budget at C3 is similar to that at C2, though weaker. At both C2 and C3, the advection dominates the momentum budget, and is balanced only partly by the buoyancy force. At C4, there is a clear diurnal signal, but weaker again, and here the budget is dominated by the Coriolis force which is only partly balanced by the buoyancy force.

Figure 5.9 shows the average forcing terms in a cross-section over the slope ranging roughly from C4 on the left to Halley on the right. As in the winter case

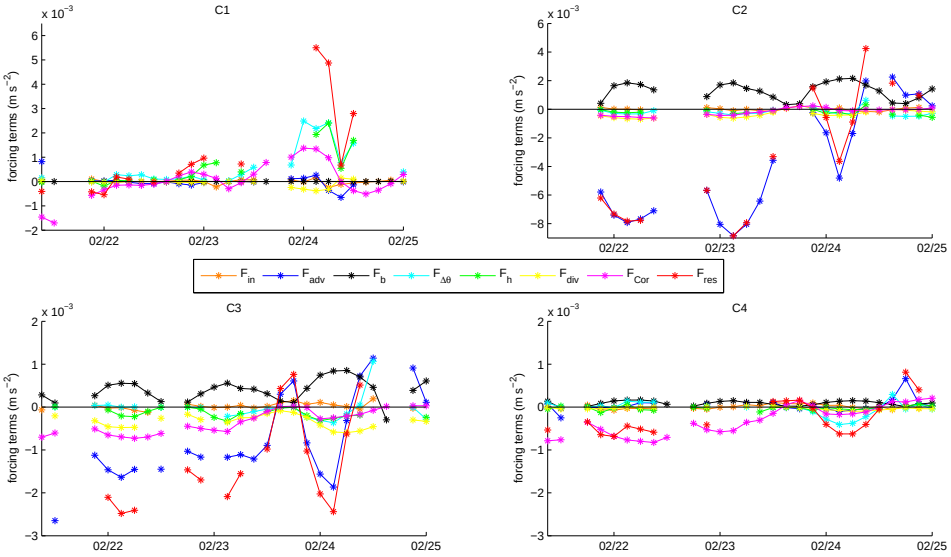

Figure 5.8: The forcing terms in the downslope momentum equation for the February 2002 case, for C1, C2, C3 and C4, showing 3-hour averages for 21-25 February 2002: F_{int} is the inertia term (storage of mean momentum), F_{adv} is the advection term, F_b is the buoyancy force, $F_{\Delta\theta}$ is the force due to the gradient in the potential-temperature deficit, F_h is the force due to the gradient in the katabatic-layer height, F_{div} is the momentum flux divergence force, F_{Cor} is the Coriolis force and F_{res} is the residual. Note that the scale is different at each location.

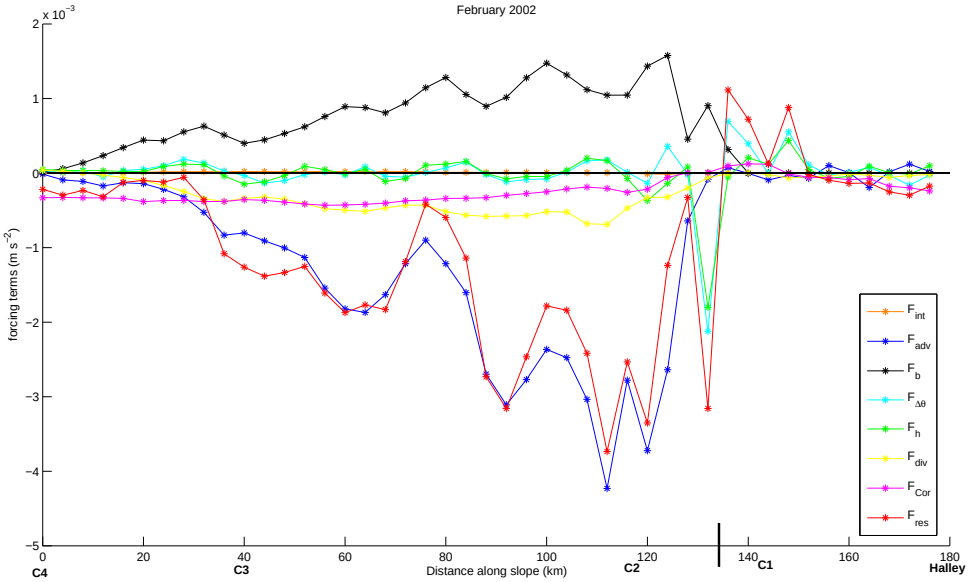

Figure 5.9: Average forcing terms along the slope for the February 2002 (summer) case study: F_{int} is the inertia term (storage of mean momentum), F_{adv} is the advection term, F_b is the buoyancy force, $F_{\Delta\theta}$ is the force due to the gradient in the potential-temperature deficit, F_h is the force due to the gradient in the katabatic-layer height, F_{div} is the momentum flux divergence force, F_{Cor} is the Coriolis force and F_{res} is the residual. The locations of Halley and C1-C4 are indicated, and the vertical line on the x-axis indicates the bottom of the slope.

(figure 5.5), the advection force increases towards C2, at the steepest part of the slope, but is much smaller here. The advection force decreases before it reaches the bottom of the slope. At the bottom of the slope, both F_h and $F_{\Delta\theta}$ become quite large and they dominate the budget here. They are both directed in the upslope direction, thus opposing the katabatic flow. Over the ice shelf, all forces are very small.

Figure 5.10 is similar to figure 5.3, but for the summer case study. All variables in figure 5.10 show a clear diurnal signal at all locations. The katabatic layer is deepest during the night. At C2 and C3, the katabatic layer height during the night is similar to the katabatic layer height found in the winter case (see figure 5.3). At C1, C4 and Halley, the katabatic layer height is more variable and can be quite deep - up to 200 m. The potential temperature difference is largest in the morning, between 2-5 K, which is a bit larger than for the winter case. During the afternoon, $\Delta\theta$ is around 0 K and sometimes even negative. v_{kl} and u_{kl} both show stronger wind speeds during the night. The downslope velocity (v_{kl}) is usually strongest at C2, except towards the end of the model simulation where C3 shows the strongest wind speeds. The wind speeds during the night are of similar strength compared to the winter case study. w_{kl} is very small at C1, C4 and Halley, but at C2 we see stronger negative values (again down to about -0.15 to -0.2 m/s). C3 also shows relatively strong (negative) vertical wind speeds in the katabatic layer, more so than in the winter case. These sinking motions indicate an acceleration of the flow at C2 and C3, related to the katabatic flow.

Figure 5.11 is similar to figure 5.6, but for the February 2002 case. One would expect that a katabatic jump could form more easily during the winter, when constant katabatic flows cause cold air to pile up at the bottom of the slope. During summer, the katabatic flows are strongest during the night and perhaps this shorter time span does not allow for such a cold pool to build up. However, figure 5.11 shows very similar results compared to the winter case study. The katabatic flow in this case extends over nearly the entire slope (except at the top of the slope near C4). The winds are strongest at the steepest part of the slope, at C2. A little further downstream, the winds start to decrease until reaching a constant low windspeed over the ice shelf. Near the foot of the slope, the Froude number indicates a transition from shooting to tranquil flow, accompanied by a sharp increase in the height of the katabatic layer from 68 to 115 m. These results are remarkably similar to the winter case results shown in figure 5.6. This suggests that katabatic jumps are a common feature in katabatic flows, even during the summer months. This is found by Gallée and Pettre (1998) as well. They find cold katabatic air piling up during model simulations of summer case studies at Adélie Land.

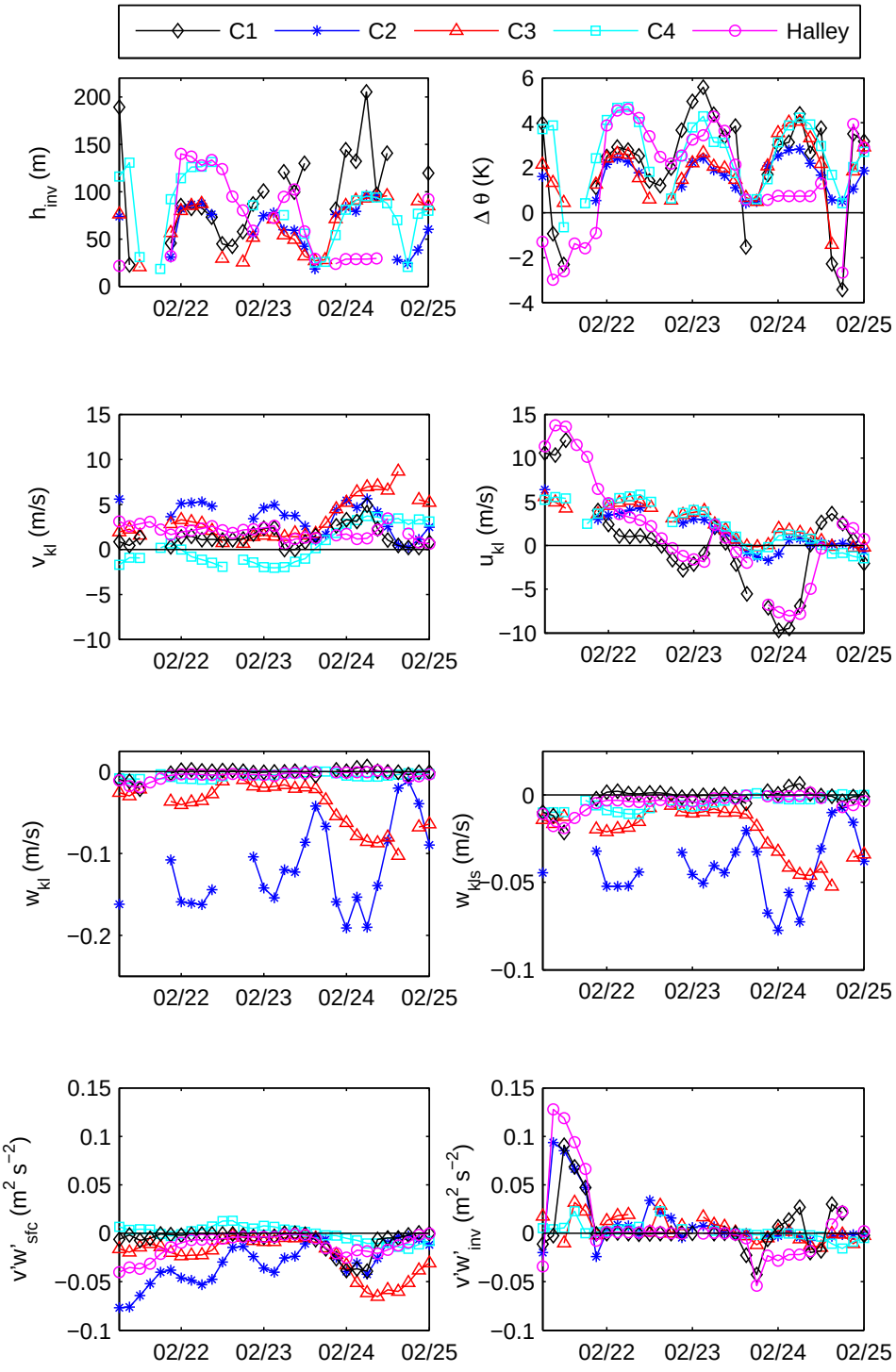

Figure 5.10: Variables used in the calculation of the summer case (21-25 February 2002) downslope momentum budget: the katabatic layer height (h_{inv}), the potential temperature difference between the katabatic layer and the upper layer ($\Delta\theta$), katabatic-layer means of v (v_{kl}: downslope velocity), u (u_{kl}: cross-slope velocity), w (w_{kl}: vertical velocity and w_{kls}: slope-relative vertical velocity), and surface and inversion height fluxes ($v'w'_{sfc}$ and $v'w'_{inv}$) for C1-C4 and Halley. These are all 3-hour means ending at the plotted time.

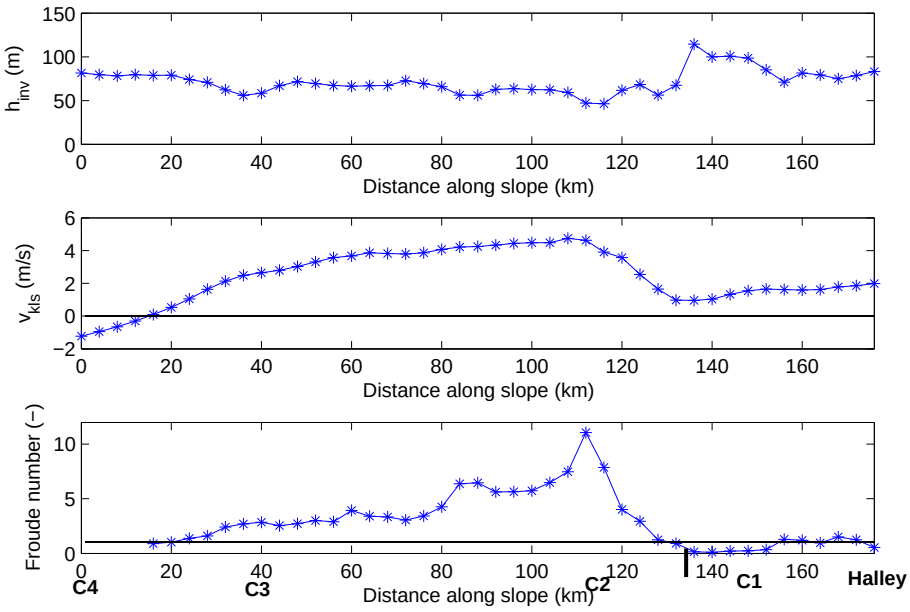

Figure 5.11: Average inversion height (h_{inv}, top panel), average downslope windspeed in the katabatic layer (v_{kls}, middle panel) and average Froude number (bottom panel) for the February 2002 case, averaged between 21-24 February, along the slope roughly from C4 on the left to Halley on the right for the August 2003 (winter) case study. The locations of Halley and C1-C4 are indicated, and the vertical line on the x-axis indicates the bottom of the slope.

5.3 Momentum budget - conservation of momentum

The two-layer method is a very useful tool over sloping terrain, but it is clearly a simplification and quantitative results depend on the way in which the katabatic layer is defined. Therefore we will introduce a complementary way of looking at the momentum budget, by using the equation for the conservation of momentum as described in Stull (1988):

$$\frac{\partial \overline{U_i}}{\partial t} = -\overline{U_j}\frac{\partial \overline{U_i}}{\partial x_j} - \delta_{i3}g + f_c\epsilon_{ij3}\overline{U_j} - \frac{1}{\overline{\rho}}\frac{\partial \overline{P}}{\partial x_i} + \frac{\nu\partial^2\overline{U_i}}{\partial x_j^2} - \frac{\partial\overline{(u_i'u_j')}}{\partial x_j} \tag{5.5}$$

The left hand side represents the storage of mean momentum (inertia). The terms on the right hand side describe the advection of mean momentum by the mean wind (first term), the gravity force in the vertical direction (second term), the Coriolis effect (third term), the mean pressure-gradient force (fourth term), the influence of viscous stress on the mean motions (fifth term) and the divergence of turbulent momentum flux (or the influence of Reynolds' stress on the mean motions, sixth term).

Again, we use model variables averaged over three hours. The momentum budget is calculated on the third model level, at 45 m above the surface. This is the lowest level possible, as two lower model levels are required to calculate the viscous stress term. The results of the two-layer momentum budget showed a katabatic-layer height of 50-100 m for the August 2003 case (see figure 5.3) and 70-150 m for the February 2002 case (during the night, during the day the height can not always be determined but is usually around 25-50 m, see figure 5.10). This means that the height at which we calculate the momentum budget is practically always within the katabatic layer. All model variables are interpolated so they are on the same model level, as some variables are located on half model levels (still terrain-following, but located halfway between the regular model levels). The residual term is taken as the sum of all terms. The kinematic viscosity (ν) is substituted by μ/ρ, where μ is the viscosity calculated using Sutherlands's law:

$$\mu = \mu_0 \left(\frac{0.555T_0 + C}{0.555T + C}\right)\left(\frac{T}{T_0}\right)^{3/2} \tag{5.6}$$

For air, the reference viscosity (μ_0) equals 18.27 10^{-6} Pa s, the reference temperature (T_0) equals 291.15 K and Sutherland's constant equals 120 K. We use the surface and boundary layer stress variable (τ) from the model output to calculate the divergence of turbulent momentum flux, using equation 5.3 and similarly for τ_x:

$$\overline{(u'w')} = -\frac{1}{\rho}\tau_x \tag{5.7}$$

(Stull, 1988)

When we split the equation into the three grid-relative wind components (u, v and w, where u is approximately in the cross-slope direction and v in the downslope direction) and apply the substitutions discussed above, we find the following equations:

$$\frac{\partial \overline{u}}{\partial t} = -(\overline{u}\frac{\partial \overline{u}}{\partial x} + \overline{v}\frac{\partial \overline{u}}{\partial y} + \overline{w}\frac{\partial \overline{u}}{\partial z}) + f_c\overline{v} - \frac{1}{\overline{\rho}}\frac{\partial \overline{p}}{\partial x} + \frac{\overline{\mu}}{\overline{\rho}}\left(\frac{\partial^2 \overline{u}}{\partial x^2} + \frac{\partial^2 \overline{u}}{\partial y^2} + \frac{\partial^2 \overline{u}}{\partial z^2}\right) - \frac{1}{\overline{\rho}}\frac{\partial \overline{\tau_x}}{\partial z} \tag{5.8a}$$

$$\frac{\partial \overline{v}}{\partial t} = -(\overline{u}\frac{\partial \overline{v}}{\partial x} + \overline{v}\frac{\partial \overline{v}}{\partial y} + \overline{w}\frac{\partial \overline{v}}{\partial z}) - f_c\overline{u} - \frac{1}{\overline{\rho}}\frac{\partial \overline{p}}{\partial y} + \frac{\overline{\mu}}{\overline{\rho}}\left(\frac{\partial^2 \overline{v}}{\partial x^2} + \frac{\partial^2 \overline{v}}{\partial y^2} + \frac{\partial^2 \overline{v}}{\partial z^2}\right) - \frac{1}{\overline{\rho}}\frac{\partial \overline{\tau_y}}{\partial z} \tag{5.8b}$$

$$\frac{\partial \overline{w}}{\partial t} = -(\overline{u}\frac{\partial \overline{w}}{\partial x} + \overline{v}\frac{\partial \overline{w}}{\partial y} + \overline{w}\frac{\partial \overline{w}}{\partial z}) - g - \frac{1}{\overline{\rho}}\frac{\partial \overline{p}}{\partial z} + \frac{\overline{\mu}}{\overline{\rho}}\left(\frac{\partial^2 \overline{w}}{\partial x^2} + \frac{\partial^2 \overline{w}}{\partial y^2} + \frac{\partial^2 \overline{w}}{\partial z^2}\right) \tag{5.8c}$$

We use finite forward differences ($\Delta a_n = a_{n+1} - a_n$, where a can be any variable) and interpolate a_{n+1} to be at the same height above sea level as a_n. This is necessary as our domain is sloping downwards in the x-direction. Without interpolating to the same height above sea level, we would introduce errors, especially in the pressure-gradient force which would be governed by the difference in height between two grid points and therefore be nearly constant.

5.3.1 Results for the winter case study

Figure 5.12 shows the result for the v component (equation 5.8b, roughly downslope). At C1 and C3, the budget is dominated by the pressure-gradient force which is balanced by the Coriolis force (geostrophic balance). At C2, the terms of the momentum budget are relatively large. The pressure force is still balanced by the Coriolis force, but the advection force, divergence force and Coriolis force also play a significant role. At C4, the Coriolis force is balanced by the advection force and there is no geostrophic balance. The advection force shows a large standard deviation, ranging from positive to negative values. This is partly an artifact of the way in which the budget is calculated. We use forward differences in the downslope direction, with interpolation to ensure that the same height above sea level is used (which is essential for the pressure force). However, even with a slope of typically 5%, this means that between two grid points (with a resolution of 4 km) the height difference (above the slope) is about 200 m. This could be either just within the katabatic layer, or it could be outside. When the slope is less steep, this will not be as significant, but especially for C2 (located at the steepest part of the slope), this means that the advection force is unreliable. However, the other forcing terms are not affected by this.

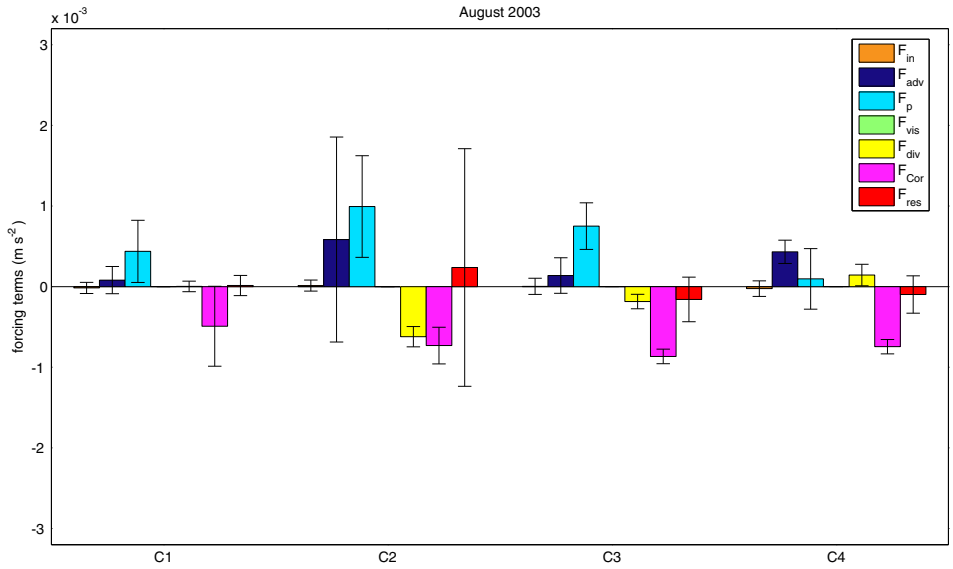

Figure 5.12: Average forcing terms (with error bars indicating the standard deviation) in the y direction (roughly downslope) for the August 2003 (winter) case study, calculated using the equation for the conservation of momentum: F_{in} is the inertia term (the storage of mean momentum), F_{adv} is the advection term, F_p is the pressure-gradient force, F_{vis} is viscous stress term, F_{div} is the momentum flux divergence force, F_{Cor} is the Coriolis force and F_{res} is the residual term.

It is interesting to compare figure 5.12 to figure 5.2 (the momentum balance from the two-layer method for the same case study), though one has to be careful as the two-layer method is directed downslope while the conservation of momentum method is directed horizontally. The Coriolis force and the momentum flux divergence force are similar. The advection force using the conservation of momentum framework is much smaller compared to the advection force in the two-layer framework. The pressure force in the conservation of momentum framework includes both the synoptic pressure gradient and the buoyancy forced pressure gradient, while the synoptic pressure gradient in the two-layer framework ends up in the residual term. If the two frameworks were acting in the same direction, this would enable an estimate of the synoptic force by comparing the buoyancy force (from the two-layer method) and the pressure gradient force (from the conservation of momentum method). In this case, this comparison indicates that the katabatic flow is partly synoptically forced at C3 and less so at C2, but as the two methods are acting in different directions, this comparison is not entirely valid.

Figure 5.13 shows the average forcing terms in a cross-section over the slope ranging roughly from C4 on the left to Halley on the right. From about 35 km down the slope, the flow is in geostrophical balance though the momentum flux divergence also plays a significant role. At the highest part of the slope,

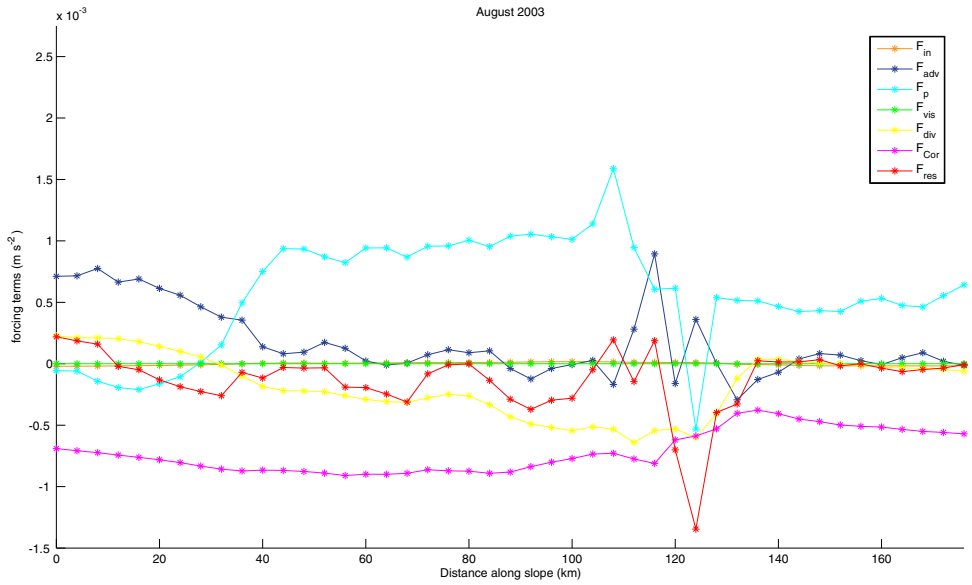

Figure 5.13: Average forcing terms along the slope for the August 2003 (winter) case study, using the equation for the conservation of momentum: F_{in} is the inertia term (storage of mean momentum), F_{adv} is the advection term, F_p is the pressure-gradient force, F_{vis} is viscous stress term, F_{div} is the momentum flux divergence force, F_{Cor} is the Coriolis force and F_{res} is the residual term.

the pressure gradient is acting in the upslope direction, which could explain the upslope winds at C4 in the model (see figure 3.9) Figure 3.24 showed that the mean sea level pressure field is opposed to the katabatic forcing over the slope, so it must be the buoyancy component of the pressure gradient force that dominates here. The pressure-gradient force acts in the downslope direction lower down, except at the bottom of the slope (110-135 km down the slope), where the pressure-gradient force decreases to negative (upslope) values before reaching a more constant (positive) value over the ice shelf. Over the ice shelf, the pressure force loses its buoyancy component in the absence of a slope and is purely synoptically forced. The pressure force over the ice shelf is about 0.5x10^{-3} m s^{-2}, which is about 2-3 times less compared to the pressure force over the slope. If the synoptic pressure force is constant over the slope, this means that the synoptic forcing and the buoyancy forcing are of equal importance over a large part of the slope, while the buoyancy force dominates the synoptic pressure force over the steepest part of the slope near C2. The advection force shows large changes near the bottom of the slope, and the momentum flux divergence force changes to nearly zero over the ice shelf. Over the ice shelf, the budget is in geostrophical balance again, dominated by the Coriolis and the pressure-gradient force, while all other forces are very small. Yu *et al.* (2005) also found a reversal of the pressure-gradient force and an increase in the advection force near the

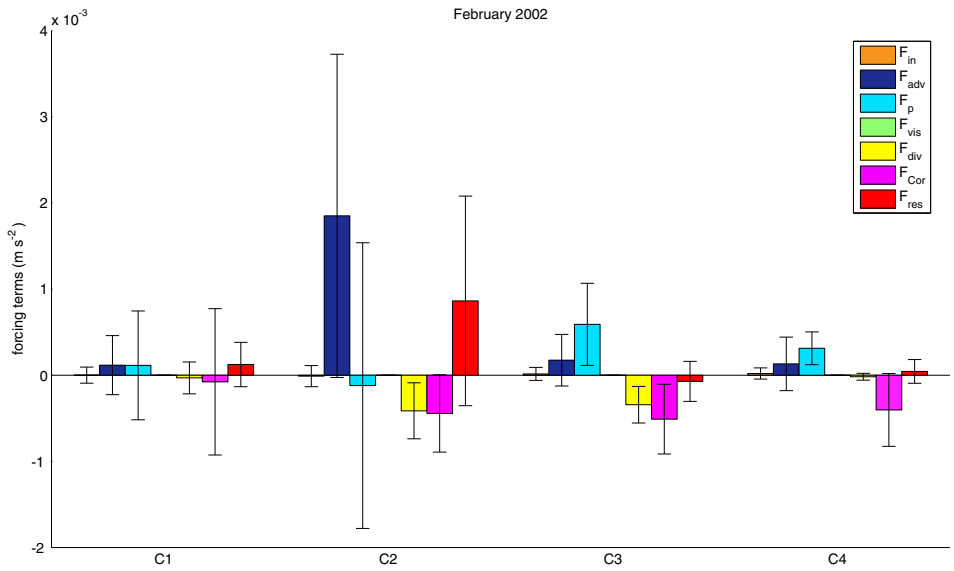

Figure 5.14: Average forcing terms (with error bars indicating the standard deviation) in the y direction (roughly downslope) for the February 2002 (summer) case study, calculated using the equation for the conservation of momentum: F_{in} is the inertia term (storage of mean momentum), F_{adv} is the advection term, F_p is the pressure-gradient force, F_{vis} is viscous stress term, F_{div} is the momentum flux divergence force, F_{Cor} is the Coriolis force and F_{res} is the residual term.

katabatic jump (at the foot of the slope) and these are characteristic features of the katabatic jump.

5.3.2 Results for the summer case study

Figure 5.14 is similar to figure 5.12 but for the February 2002 (summer) case study. In general, the momentum budget is quite similar to that of the winter case study, except for the larger standard deviation in the summer case. Nearly all the averaged terms have the same sign, but the standard deviation is larger and often ranges from positive to negative values. This is related to the diurnal variation in the forcing terms, as discussed before. At C2, the pressure gradient force has a large standard deviation ranging from strongly negative to positive values, while the advection force (though also showing a large standard deviation) is always positive (directed downslope). Figure 3.59 showed downslope winds for the entire simulation. This indicates that when the pressure force is directed upslope, it is the advection force that drives the downslope wind at this location. C4 shows upslope winds (see figure 3.59), which appears to be driven by the Coriolis force. Figure 5.15 shows time series for all the terms for each location. The diurnal variation is not as obvious here as it was in figure 5.8 but can still be found at all locations. C1, C3 and C4 are in geostrophical balance - the pressure force is balanced by the Coriolis force. At C2 this is true for part of the model

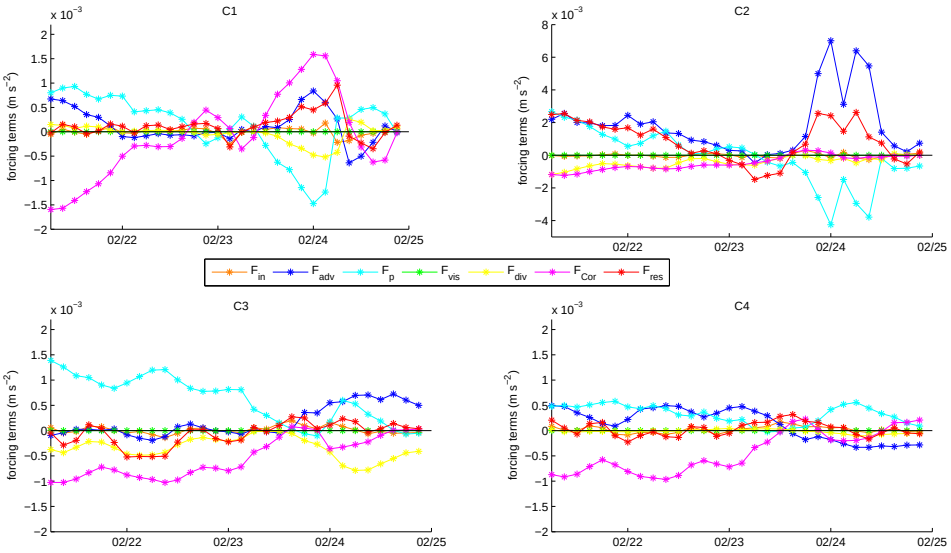

Figure 5.15: The forcing terms in the downslope momentum equation for the February 2002 case, calculated using the equation for the conservation of momentum, for C1, C2, C3 and C4, showing 3-hour averages for 21-25 February 2002. F_{in} is the inertia term (storage of mean momentum), F_{adv} is the advection term, F_p is the pressure-gradient force, F_{vis} is viscous stress term, F_{div} is the momentum flux divergence force, F_{Cor} is the Coriolis force and F_{res} is the residual term. Note that the scale is different for C2 compared to the other locations.

run, but during the last 1.5 days it is the advection force which is partly balanced by the pressure force. This is where the advection force drives the downslope wind while the pressure gradient force is directed upslope. At all locations, the pressure force decreases over time, even becoming negative (upslope forcing) at Halley and C2 on the third day, before increasing again. Figure 3.59 showed alternating upslope and downslope winds at C3 (for the model). At C3 the flow is in geostrophical balance and it appears that these changes in wind direction are caused by the diurnal cycle of the flux divergence force.

Comparing figures 5.7 and 5.8 to figures 5.14 and 5.15, we find that the Coriolis force and the momentum flux divergence force are similar. The buoyancy force does not show the decrease over time that the pressure force shows, indicating that it is the synoptic pressure force that decreases over time, but again a direct comparison is not possible due to the different directions in which the frameworks act.

Figure 5.16 is similar to figure 5.13 but for the February 2002 case, showing the average forcing terms over the slope. The Coriolis force is weaker compared to the August 2003 case, while the advection force and the momentum flux divergence force are stronger. At the foot of the slope, the pressure-gradient force strongly decreases to negative values while the advection force peaks. This is related to the katabatic jump at the foot of the slope, as discussed previously.

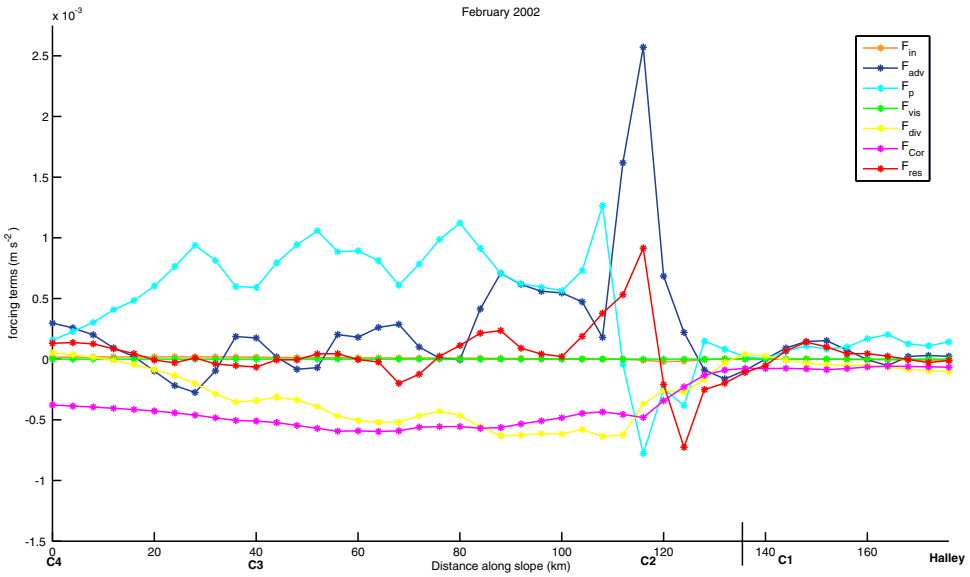

Figure 5.16: Average forcing terms along the slope for the February 2002 (summer) case study, using the equation for the conservation of momentum: F_{in} is the inertia term (storage of mean momentum), F_{adv} is the advection term, F_p is the pressure-gradient force, F_{vis} is viscous stress term, F_{div} is the momentum flux divergence force, F_{Cor} is the Coriolis force and F_{res} is the residual term. The locations of Halley and C1-C4 are indicated, and the vertical line on the x-axis indicates the bottom of the slope.

Just like in the winter case, the momentum flux divergence force changes to nearly zero over the ice shelf. The pressure force over the ice shelf is very small, indicating that the synoptic forcing is weak in this case. Assuming the same (small) synoptic pressure force over the slope, the flow in this case looks more like a 'pure' katabatic flow (forced by buoyancy) than the winter case study.

5.4 Conclusions and discussion

We presented two different methods to calculate the momentum budget of the katabatic flow. The first one uses a two-layer framework consisting of a katabatic layer with a quiescent layer on top. This method is very suitable over sloping terrain and allows us to calculate those terms that are important for the katabatic wind situation. This method is sensitive to the definition of the height of the katabatic layer (and thus the height over which the variables are averaged) is defined; in our case by setting a threshold value for the vertical temperature gradient. However, sensitivity analysis using different values for the vertical potential temperature gradient threshold reveals that the momentum budget is quite robust and at least qualitatively gives similar results when using different potential temperature gradient thresholds. In summer, the vertical temperature threshold is sometimes reached at the surface, and thus there is no katabatic layer and the momentum budget can not be calculated. The main drawback of this method is the large simplification by assuming a continuously stratified flow with two layers of constant density. Using the conservation of momentum method does not have these issues, but here the difficulty is the sloping terrain. Also, in this method the buoyancy force is not directly calculated (instead it is included in the pressure force). The temperature gradient is only included in the viscosity term, which is mostly negligibly small.

The first method (the two-layer framework) shows that the buoyancy force and the advection force are the dominating forces in the budget at C2, though the advection force is only partly balanced by the buoyancy force. At most locations, the buoyancy force is balanced by the flux divergence force and the Coriolis force, but the large (and negative, i.e. upslope) advection force causes the residual force to be very large. This residual force can include several contributions; for example any synoptic forcing and errors in the calculating of the other terms. In general, the average budget remains the same in summer and winter, though in summer the standard deviation of each term is much larger due to the diurnal cycle. In summer, the terms of the momentum budget at C2, C3 and C4 show clear diurnal variation. The forces are strongest at C2 and weakest at C4. At C2 and C3, the buoyancy force dominates the budget, balanced by the advection force. At C4, the Coriolis force dominates the budget. The katabatic layer height in winter is about 50-100 m, and $\Delta\theta$ is around 2 K at most locations. In

summer during the night the katabatic layer height is between 70-125 m while $\Delta\theta$ is mostly between 2-4 K. At the foot of the slope, the flow changes from shooting to tranquil, accompanied by an increase in the katabatic layer height and a decrease in the downslope windspeed. These are typical characteristics of a katabatic jump caused by the piling up of cold air at the foot of the slope. Rising motions are observed in this area, indicating the deceleration of the flow when it reaches the ice shelf. This explains why the katabatic flow does not reach C1, let alone Halley. This situation is remarkably similar for the winter and summer case.

The second method showed the same general result: the average budget is quite similar during winter and summer, but the standard deviation of each term is much larger in summer. At most locations, the budget is in geostrophical balance. Near the foot of the slope, the pressure-gradient force reverses while the advection force increases. This is another characteristic of a katabatic jump: the pool of cold air at the bottom of the slope causes an upslope pressure-gradient which slows the katabatic flow down. Again, this phenomenon is found both in the winter and in the summer case study.

Comparing the results from two different frameworks could provide more insight into the forcing of the katabatic flow. The two-layer framework assumes no synoptic forcing, so the synoptic forcing ends up in the residual term. The buoyancy force is calculated in this budget. The conservation of momentum method has a pressure force which includes both the synoptic pressure force and the buoyancy forced pressure force. This means that by comparing the buoyancy force from the two-layer method to the pressure force from the conservation of momentum method we can obtain more insight into which pressure force (synoptic or buoyancy) drives the katabatic flow. This method shows that over most of the slope, the pressure force is about twice as large as the buoyancy force, indicating that the synoptic pressure force and the buoyancy force are equally important in forcing the katabatic flow. At the steepest part of the slope, the buoyancy force dominates over the synoptic pressure force. However, as the two frameworks are acting in different directions (the two-layer framework is in the downslope direction while the conservation of momentum method acts in the horizontal direction), this comparison is not entirely valid.

Another way to gain insight into the different pressure gradient forces is by looking at the pressure force (from the conservation of momentum method) over the ice shelf. The pressure force loses the buoyancy component over the ice shelf (in the absence of a slope) and this means that the pressure force over the ice shelf only consists of the synoptic pressure force. If we assume that the synoptic forcing over the slope and over the ice shelf is similar, we can estimate the buoyancy component over the slope. This analysis shows that the August 2003 winter case study has more synoptic forcing than the February 2002 summer

case study. For the August 2003 case the pressure force over the slope is about twice as large as over the ice shelf, indicating that the synoptic pressure force and the buoyancy force are approximately equally important in forcing the katabatic flow. In the February 2002 case the synoptic pressure force is smaller, and the buoyancy force is the dominating force behind the katabatic flow.

These results confirm the findings of previous studies (Parish *et al.* (1993a); Parish and Cassano (2001, 2003b); Renfrew and Anderson (2002); Heinemann and Klein (2002); van den Broeke *et al.* (2002); van den Broeke and van Lipzig (2003); Bintanja (2000)) concluding that the synoptic or large-scale pressure-gradient force influences the katabatic flow considerably.

Chapter 6

Conclusions

This thesis aimed to investigate model simulations (using the Unified Model version 6.1) of katabatic flow in Coats Land, Antarctica, using observations from the Coatsland AWS network and three-dimensional wind profiles measured by a Doppler Sodar to verify model results. The boundary layer settings of the model were examined in detail, and a momentum budget analysis of the model results provided more insight into the dynamics of the katabatic flow. In this chapter, the findings will be summarized and discussed, followed by suggestions for future work.

6.1 Model results and boundary layer parameterisation

6.1.1 Model results

In all three case studies, the large scale synoptic situation was reasonably well represented by the model. The model performed better for the summer case than it did for either of the two winter cases. The diurnal cycle for the summer case was well captured, though the magnitude of the diurnal variation is underestimated. The model showed the development of a cold pool at the bottom of the slope, which blocks the katabatic flow from continuing over the ice shelf and thus prevents it from reaching Halley, an observed feature of the climatology of Coats Land (King, 1993; Renfrew and Anderson, 2002).

The model underestimated wind speeds at the surface and the katabatic layer in the model was too deep. The boundary layer over Antarctica is often very stable. Stable boundary layers are difficult to model as they are very complex and stable boundary layer parameterisations are often tuned to perform reasonably at mid-latitudes (Viterbo *et al.*, 1999), which means that the SBL parameterisations commonly used are unlikely to be accurate over the Polar regions (King *et al.*, 2001). Stable boundary layers over Antarctica can also be very shallow (at Halley

often as shallow as 50 m (King, 1990)), which causes problems in models with a coarse vertical resolution. Therefore a thorough investigation of the boundary layer parameterisation of the UM was conducted to investigate the sensitivity of the model results to the vertical resolution, the boundary-layer scheme, the stability function and the roughness length.

6.1.2 Vertical resolution

Increasing the vertical resolution from 38 to 76 vertical levels improved the model results. For the August 2003 case, the temperatures at Halley in the model run with 76 vertical levels are up to 8 degrees higher than in the model run with 38 vertical levels, which is an improvement as the model showed a large underestimation of the temperature (probably due to a decoupled boundary layer) at Halley. Using 76 levels does not solve this issue completely as the temperature at Halley is still underestimated. Wind speeds are stronger at all locations when using 76 vertical levels, which is also an improvement, especially at Halley where the wind speed at the surface was largely underestimated by the run with 38 vertical levels (again related to the decoupled boundary layer). Redistributing the vertical levels so that the vertical resolution is doubled in the lowest 500 m (while keeping the same number of vertical levels, i.e. with a lower resolution higher up in the atmosphere) did not significantly improve the model simulation. The differences between this run and the run with the default distribution of vertical levels were very small, with differences in the surface temperature of maximum 2 degrees, and differences in wind speed of maximum 0.5 m/s. This shows that 76 vertical levels are sufficient, and that the problems with the overly deep katabatic layer and the underestimation of wind speeds at the surface are not related to the vertical resolution.

6.1.3 Boundary-layer scheme

The model results were sensitive to the choice of boundary-layer scheme. Changing the boundary layer scheme from the default Richardson number-based scheme to the equilibrium Stable Boundary Layer (EqSBL) scheme resulted in increased variability in all variables, which compared better to observations. The representation of the range of the diurnal cycle in the February 2002 was improved when using the EqSBL scheme. The EqSBL surface temperatures are up to 5 degrees colder during the night compared to the run using the default Richardson number-based scheme, which compares very well with observations. At times the results from the EqSBL run match the observations remarkably well, but at other times the chaotic behaviour of this boundary layer scheme does not match the observations at all. For example, the EqSBL run showed strong vertical motions over the slope, with strong upward motions near C2 compensated with strong

downward motions higher up the slope, and wind directions which sometimes changed by 180 degrees in two bordering grid points. It is hard to judge whether the EqSBL scheme shows 'random' chaotic behaviour that happens to match the observations at certain times (by coincidence), or whether the EqSBL scheme actually improves the behaviour of the model and is capable of simulating certain quick changes seen in the observations. In a newer version of the UM (version 6.3), it is not possible to use the EqSBL scheme anymore. It was decided that the increased complexity of the EqSBL scheme when compared to the much simpler Richardson number based scheme did not give enough benefit.

6.1.4 Stability function

The model was less sensitive to the choice of stability function than to the choice of boundary-layer scheme. A sharper stability function allows less mixing with increasing stability. Four functions with increasing sharpness were tested: the default long-tailed stability function (equation 4.3), the SHARPEST function (equation 4.4), a blend between the Louis (equation 4.5) and the SHARPEST function, and a newly developed revised version of the Beljaars and Holtslag (1991) stability function (using a = 5, b = 2/3, c = 7 and d = 2 in equations 4.9 and 4.10 at the surface, and equation 4.24 for the boundary layer). Results from model simulations with the different stability functions showed broadly the same pattern, though the temperatures decreased and the wind speed increased with the sharpness of the stability functions, i.e. when less mixing is allowed. The difference between the surface temperatures from the run with the least sharp stability function (the long-tailed stability function) and the run with the sharpest stability function (the revised Beljaars and Holtslag (1991) function) is up to about 4 degrees at most locations and slightly higher for Halley. This is true for both the winter case study and the summer case study, though for the summer case studies the differences are occasionally higher, with in the most extreme example a difference of 15 degrees for an occasion where the long-tailed stability function strongly overestimated the temperatures at Halley. The diurnal cycle in temperature in the February 2002 case was best represented by the new (and sharpest) stability function, which showed the lowest temperatures during the night. The height of the maximum wind speed is not influenced by using different stability functions, but the strength of this wind peak does increase by about 1 m/s when using a sharper stability function than the long-tailed stability function.

6.1.5 Roughness length

Decreasing the roughness length over the ice sheet and the ice shelf did not make a significant impact on the model results. As expected, the wind speeds near

the surface increased when the roughness length was decreased but the changes were very small. The difference in surface wind speed between the run with the highest roughness length (3.0×10^{-4} m, the default value in the model) and the run with the lowest roughness length (5.0×10^{-5} m) is only 0.35 m/s which is negligible. This shows that the model results are not very sensitive to the chosen roughness length.

6.1.6 Conclusions

Unfortunately, none of the different model runs discussed above makes a significant impact on the height of the katabatic layer which is still too deep; nor the height of the katabatic jet maximum which is too high; nor the wind speed at the surface which is still underestimated in all the model runs. This suggests that the model formulation of the stable boundary layer needs further improvement especially over sloping terrain. However, this could require investigating other aspects of the model besides the boundary layer scheme and the stability functions. Stable boundary layer modelling is for example also sensitive to the coupling between the atmosphere and the land surface (Steeneveld *et al.*, 2006) and to the radiation parameterisation (Ha and Mahrt, 2003).

6.2 The dynamics of katabatic flow

Two different methods to calculate the momentum budget of the katabatic flow were presented. The first used a two-layer framework (also used in Renfrew (2004), based on the framework set out by Mahrt (1982)) consisting of a katabatic layer with a quiescent layer on top. This method is suitable over sloping terrain and allowed us to calculate those terms that are important for the katabatic wind situation. This framework assumes no synoptic forcing, so the synoptic forcing ends up in the residual term. The main drawback of this method is that it is an over simplification to assume a continuously stratified flow with two layers of constant density. The second method used the conservation of momentum. This method is arguably less suitable over sloping terrain and it does not calculate the buoyancy force explicitly, but it does include a pressure-gradient force which includes both the synoptic pressure-gradient force and the buoyancy forced pressure gradient. Combining both methods reveals to what extent the katabatic flow is forced by buoyancy ('pure' katabatic flow) and to which extent by the synoptic pressure-gradient force.

The two-layer framework showed similar results for the summer and winter case, though in summer all terms show a diurnal variation. The forces were strongest at the steepest part of the slope, where the buoyancy force and the advection force were the dominating forces. At the foot of the slope, the flow changed from shooting to tranquil, accompanied by an increase in the katabatic

layer height and a decrease in the downslope windspeed. These are typical characteristics of a katabatic jump caused by the piling up of cold air at the foot of the slope (Pettré and André, 1991; Yu *et al.*, 2005). Rising motions were observed in this area, indicating the deceleration of the flow when it reached the ice shelf. This explains why the katabatic flow does not reach C1, let alone Halley.

The conservation of momentum method showed a geostrophic balance at most locations. Near the foot of the slope, the pressure-gradient force reversed while the advection force increased. This is another characteristic of a katabatic jump: the pool of cold air at the bottom of the slope causes an upslope pressure-gradient which slows the katabatic flow down.

The background synoptic forcing can be estimated by the pressure-gradient force over the ice shelf, where the buoyancy component is lost in the absence of a slope. The August 2003 (winter) case study showed more synoptic forcing than the February 2002 (summer) case. For both cases, the (downslope) pressure-gradient force was about twice as large as the buoyancy force over most of the slope, indicating that the synoptic pressure-gradient force and the buoyancy force are equally important in forcing the katabatic flow. At the steepest part of the slope, the buoyancy force dominated over the synoptic pressure-gradient force.

These results confirm the findings of previous studies (Parish *et al.* (1993a); Parish and Cassano (2001, 2003b); Renfrew and Anderson (2002); Heinemann and Klein (2002); van den Broeke *et al.* (2002); van den Broeke and van Lipzig (2003); Bintanja (2000)) concluding that the synoptic or large-scale pressure-gradient force influences the katabatic flow considerably.

6.3 Future work

In this thesis, we improved the orography over the model domain by using the high-resolution Radarsat Antarctic Mapping Project (RAMP) Digital Elevation Model (DEM) dataset instead of the default UM orography. As shown in figure 2.6, there are still large differences between this improved orography and the traverse measured by Peel (1976) which is believed to be more accurate. As a consequence, the location of the AWS's had to be adjusted in the model domain. This is most problematic for C4, as it is now located near the top of the slope where it is relatively flat, and also quite close to the edge of the model domain. Enlarging the model domain and finding a more appropriate location for C4 could partly solve this issue. Ideally, the model would be run with an orography like the one in Peel's traverse, but this is rather difficult to implement as this is just a single traverse.

This thesis has shown that the Unified Model has fundamental problems in simulating the shallow katabatic flow in Antarctica. The sensitivity of the model

results to the vertical resolution, the boundary layer scheme, the stability functions and the roughness length has been examined. None of the experiments resulted in a shallower katabatic layer, and though the maximum wind speed in the katabatic jet increased in some experiments (the run using the EqSBL boundary-layer scheme (on average, but with a very large standard deviation) and all runs using a sharper stability function), the wind at the surface was still underestimated in all simulations. Future work should focus on different ways to try to solve this issue, not only by investigating the boundary layer parameterisation, but also by looking at other aspects of the model's parameterisation, for example the coupling between the atmosphere and the land surface and the radiation parameterisation.

An interesting direction for model improvements is an approach based on the mixing length-scale as discussed in Grisogono and Belušić (2008), who found that only when the shear effect is used explicitly within the stable boundary layer, the mesoscale model was able to reproduce shallow but sharp katabatic flows. The UM does not use a mixing-scale length directly, so it was not possible to use this approach in this thesis. However, the results in Grisogono and Belušić (2008) are promising for future work of modelling katabatic flow in Antarctica.

Concerning the dynamics of the katabatic flow, it would be interesting to use the approach by van den Broeke *et al.* (2002) and van den Broeke and van Lipzig (2003) to calculate the momentum budget. This method calculates the katabatic pressure gradient force (resulting from a negative temperature perturbation over sloping terrain), the large-scale pressure gradient force (driving motion in the Ekman layer over flat terrain) and the pressure gradient due to horizontal changes in the vertically integrated temperature perturbation of the air near the surface relative to the undisturbed background temperature (the force driving sea breeze and snow breeze circulations over flat terrain) separately. This is an improvement over the methods used in this thesis, as it would enable a direct comparison between these contributions to the katabatic flow.

References

Adams, N. *Identifying the characteristics of strong southerly wind events at Casey station in East Antarctica using a numerical weather prediction system*. Monthly Weather Review, 133(12), 3548–3561, 2005.

Adolphs, U. and G. Wendler. *A pilot-study on the interactions between katabatic winds and polynyas at the Adelie coast, Eastern Antarctica*. Antarctic Science, 7(3), 307–314, 1995.

Anderson, P. S. *A method for rescaling humidity sensors at temperatures well below freezing*. Journal of Atmospheric and Oceanic Technology, 11(5), 1388–1391, 1994.

Anderson, P. S. *Ice-shelf microtopography observed using satellite thermal imagery*. Journal of Glaciology, 51(175), 528–538, 2005.

Anderson, P. S., R. S. Ladkin, and I. A. Renfrew. *An autonomous Doppler sodar wind profiling system*. Journal of Atmospheric and Oceanic Technology, 22(9), 1309–1325, 2005.

Argentini, S., G. Mastrantonio, A. Viola, P. Pettre, and G. Dargaud. *Sodar performance and preliminary results after one year of measurements at Adelie Land coast, East Antarctica*. Boundary-Layer Meteorology, 81(1), 75–103, 1996.

Arya, S. P. *Introduction to micrometeorology*. Academic, San Diego, California, 1988.

Ball, F. K. *The theory of strong katabatic winds*. Australian Journal of Physics, 9, 373–386, 1956.

Ball, F. K. *The katabatic winds of Adelie Land and George-V land*. Tellus, 9(2), 200–208, 1957.

Ball, F. K. *Winds on the ice slopes of Antarctica*. In *Symposium on Antarctic Meteorology*, 9–16. Pergamon Press, Melbourne, Australia, 1959.

Beare, R. J., M. K. MacVean, A. A. M. Holtslag, J. Cuxart, I. Esau, J.-C. Golaz, M. A. Jimenez, M. Khairoutdinov, B. Kosovic, D. Lewellen, T. S. Lund, J. K. Lunquist, A. McCabe, A. F. Moene, Y. Noh, S. Raasch, and P. Sullivan. *An intercomparison of large-eddy simulations of the stable boundary layer*. Boundary-Layer Meteorology, 118(2), 247–272, 2006.

Beljaars, A. C. M. and A. A. M. Holtslag. *Flux parameterization over land surfaces for atmospheric models*. Journal of Applied Meteorology, 30(3), 327–341, 1991.

Bintanja, R. *Mesoscale meteorological conditions in Dronning Maud Land, Antarctica, during summer: the momentum budget of the boundary layer*. Antarctic Science, 12(2), 229–242, 2000.

Bintanja, R. *Modelling snowdrift sublimation and its effect on the moisture budget of the atmospheric boundary layer*. Tellus A, 53(2), 215–232, 2001.

van den Broeke, M., C. Reijmer, and R. van de Wal. *Surface radiation balance in Antarctica as measured with automatic weather stations*. Journal of Geophysical Research-Atmospheres, 109(D9), 2004.

van den Broeke, M., D. Van As, C. Reijmer, and R. Van De Wal. *Sensible heat exchange at the Antarctic snow surface: A study with automatic weather stations*. International Journal of Climatology, 25(8), 1081–1101, 2005.

van den Broeke, M. R. and N. P. M. van Lipzig. *Factors controlling the near-surface wind field in Antarctica*. Monthly Weather Review, 131(4), 733–743, 2003.

van den Broeke, M. R., N. P. M. van Lipzig, and E. van Meijgaard. *Momentum budget of the East Antarctic atmospheric boundary layer: results of a regional climate model*. Journal of the Atmospheric Sciences, 59(21), 3117–3129, 2002.

Bromwich, D. H. *An extraordinary katabatic wind regime at Terra Nova Bay, Antarctica*. Monthly Weather Review, 117(3), 688–695, 1989.

Bromwich, D. H. *Estimates of Antarctic precipitation*. Nature, 343(6259), 627–629, 1990.

Bromwich, D. H., J. F. Carrasco, Z. Liu, and R. Y. Tzeng. *Hemispheric atmospheric variations and oceanographic impacts associated with katabatic surges across the Ross Ice Shelf, Antarctica*. Journal of Geophysical Research-Atmospheres, 98(D7), 13,045–13,062, 1993.

Bromwich, D. H., J. F. Carrasco, and C. R. Stearns. *Satellite-observations of katabatic-wind propagation for great distances across the ross ice shelf*. Monthly Weather Review, 120(9), 1940–1949, 1992.

Bromwich, D. H., J. J. Cassano, T. Klein, G. Heinemann, K. M. Hines, K. Steffen, and J. E. Box. *Mesoscale modeling of katabatic winds over Greenland with the Polar MM5*. Monthly Weather Review, 129(9), 2290–2309, 2001.

Bromwich, D. H. and D. D. Kurtz. *Katabatic wind forcing of the terra-nova bay polynya*. Journal of Geophysical Research-Oceans, 89(NC3), 3561–3572, 1984.

Bromwich, D. H. and Z. Liu. *An observational study of the katabatic wind confluence zone near Siple Coast, West Antarctica*. Monthly Weather Review, 124(3), 462–477, 1996.

Brown, A. R., R. J. Beare, J. M. Edwards, A. P. Lock, S. J. Keogh, S. F. Milton, and D. N. Walters. *Upgrades to the boundary-layer scheme in the Met Office Numerical Weather Prediction model*. Boundary-Layer Meteorology, 128(1), 117–132, 2008.

Brown, A. R., A. C. M. Beljaars, H. Hersbach, A. Hollingsworth, M. Miller, and D. Vasiljevic. *Wind turning across the marine atmospheric boundary layer*. Quarterly Journal of the Royal Meteorological Society, 131(607), 1233–1250, 2005.

de Bruin, H. A. R. *Atmosphere-Land Interactions*. Meteorology and Air Quality Group, Wageningen University, 2005.

Cassano, J. J., T. R. Parish, and J. C. King. *Evaluation of turbulent surface flux parameterizations for the stable surface layer over Halley, Antarctica*. Monthly Weather Review, 129(1), 26–46, 2001.

Connolley, W. M. *The Antarctic temperature inversion*. International Journal of Climatology, 16(12), 1333–1342, 1996.

Cullather, R. I., D. H. Bromwich, and R. W. Grumbine. *Validation of operational numerical analyses in Antarctic latitudes*. Journal of Geophysical Research, 102(D12), 13,761–13,784, 1997.

Cullen, M. J. P. *The unified forecast/climate model*. Meteorological Magazine, 122, 81–94, 1993.

Cuxart, J., A. A. M. Holtslag, R. J. Beare, E. Bazile, A. Beljaars, A. Cheng, L. Conangla, M. Ek, F. Freedman, R. Hamdi, A. Kerstein, H. Kitagawa, G. Lenderink, D. Lewellen, J. Mailhot, T. Mauritsen, V. Perov, G. Schayes, G.-J. Steeneveld, G. Svensson, P. Taylor, W. Weng, S. Wunsch, and K.-M. Xu. *Single-column model intercomparison for a stably stratified atmospheric boundary layer*. Boundary-Layer Meteorology, 118(2), 273–303, 2006.

Davies, T., M. J. P. Cullen, A. J. Malcalm, M. H. Mawson, A. Staniforth, A. A. White, and N. Wood. *A new dynamical core for the Met Office's global and regional modelling of the atmosphere*. Quarterly Journal of the Royal Meteorological Society, 131(608), 1759–1782, 2005.

Davolio, S. and A. Buzzi. *Mechanisms of Antarctic katabatic currents near Terra Nova Bay*. Tellus Series a-Dynamic Meteorology and Oceanography, 54(2), 187–204, 2002.

Derbyshire, S. H. *Recommendations for UM parameterization of stable boundary layers*. Cardington Technical Note, 38, 1997.

Duynkerke, P. G. *Radiation fog: A comparison of model simulation with detailed observations*. Monthly Weather Review, 119(2), 324–341, 1990.

Essery, R., M. Best, and P. Cox. *Moses 2.2 technical documentation*. 2001.

Gallée, H. and P. Pettre. *Dynamical constraints on katabatic wind cessation in Adelie Land, Antarctica*. Journal of the Atmospheric Sciences, 55(10), 1755–1770, 1998.

Gallée, H., P. Pettre, and G. Schayes. *Sudden cessation of katabatic winds in Adelie Land, Antarctica*. Journal of Applied Meteorology, 35(7), 1142–1152, 1996.

Gallée, H. and G. Schayes. *Dynamic aspects of katabatic wind evolution in the Antarctic coastal zone*. Boundary-Layer Meteorology, 59(1-2), 141–161, 1992.

Giovinetto, M. B., D. H. Bromwich, and G. Wendler. *Atmospheric net transport of water vapor and latent heat across 70° S*. Journal of Geophysical Research, 97(D1), 917–930, 1992.

Gosink, J. *Measurements of katabatic winds between Dome C and Dumont d'Urville*. Pure and Applied Geophysics, 120(3), 503–526, 1982.

Gregory, D. and P. R. Rowntree. *A mass flux scheme with representation of cloud ensemble characteristics and stability-dependent closure*. Monthly Weather Review, 118(7), 1483Ű1506, 1990.

Gregory, D. and P. R. Rowntree. *Convection scheme*. Unified Model Documentation Paper 27, version 3.0, 1999.

Grisogono, D. and D. Belušić. *Improving mixing length-scale for stable boundary layers*. Quarterly Journal of the Royal Meteorological Society, 134(637), 2185Ű2192, 2008.

Ha, K.-J. and L. Mahrt. *Radiative and turbulent fluxes in the nocturnal boundary layer*. Tellus, 55(4), 317–327, 2003.

Haiden, T. *On the pressure field in the slope wind layer*. Journal of the atmospheric sciences, 60(13), 1632–1635, 2003.

Heinemann, G. *Idealized simulations of the Antarctic katabatic wind system with a three-dimensional mesoscale model*. Journal of Geophysical Research-Atmospheres, 102(D12), 13,825–13,834, 1997.

Heinemann, G. *The KABEG'97 field experiment: An aircraft-based study of katabatic wind dynamics over the Greenland ice sheet*. Boundary-Layer Meteorology, 93(1), 75–116, 1999.

Heinemann, G. *Aircraft-based measurements of turbulence structures in the katabatic flow over Greenland*. Boundary-Layer Meteorology, 103(1), 49–81, 2002.

Heinemann, G. *Local similarity properties of the continuously turbulent stable boundary layer over Greenland*. Boundary-Layer Meteorology, 112(2), 283–305, 2004.

Heinemann, G. and T. Klein. *Modelling and observations of the katabatic flow dynamics over Greenland*. Tellus A, 54(5), 542–554, 2002.

Hines, K. M., R. W. Grumbine, D. H. Bromwich, and R. I. Cullather. *Surface energy balance of the NCEP MRF and NCEP-NCAR reanalysis in Antarctic latitudes during FROST*. Weather and Forecasting, 14(6), 851–866, 1999.

Holtslag, A. A. M. *Modeling of atmospheric boundary layers.*. In Holtslag, A. A. M. and P. G. Duynkerke, eds., *Clear and Cloudy Boundary Layers*, 85–110. Royal Netherlands Academy of Arts and Sciences, 1998.

Holtslag, A. A. M. and B. A. Boville. *Local versus nonlocal boundary-layer diffusion in a global climate model*. Journal of Climate, 6(10), 1825–1842, 1993.

Holtslag, A. A. M. and H. A. R. De Bruin. *Applied modeling of the nighttime surface energy balance over land*. Journal of Applied Meteorology, 27(6), 689–704, 1988.

Holtslag, B. *Preface: GEWEX Atmospheric Boundary-Layer Study (GABLS) on stable boundary layers*. Boundary-Layer Meteorology, 118(2), 243–246, 2006.

Ingram, W. J., S. Woodward, and J. Edwards. *Radiation*. Unified Model Documentation Paper 23, version 4.0, 2004.

Ishikawa, N., Y. Kodama, and G. Wendler. *Meteorological features in Adelie Land during the Austral summer season*. Pure and Applied Geophysics, 132(3), 439–455, 1990.

Kara, A. B., A. Tribble, and P. R. Ruscher. *Effects of roughness length on the FSU one-dimensional atmospheric boundary layer model forecasts*. Atmósfera, 11, 239–256, 1998.

King, J. C. *Low-level wind profiles at an Antarctic coastal station*. Antarctic Science, 1(2), 169–178, 1989.

King, J. C. *Some measurements of turbulence over an Antarctic ice shelf*. Quarterly Journal of the Royal Meteorological Society, 116(492), 379–400, 1990.

King, J. C. *Control of near-surface winds over an Antarctic ice shelf*. Journal of Geophysical Research-Atmospheres, 98(D7), 12,949–12,953, 1993.

King, J. C. and P. S. Anderson. *Heat and water vapour fluxes and scalar roughness lengths over an Antarctic ice shelf*. Boundary Layer Meteorology, 69(1-2), 101Ű121, 1994.

King, J. C., W. M. Connolley, and S. H. Derbyshire. *Sensitivity of modelled Antarctic climate to surface and boundary-layer flux parameterizations*. Quarterly Journal of the Royal Meteorological Society, 127(573), 779–794, 2001.

King, J. C. and J. Turner. *Antarctic Meteorology and Climatology*. Cambridge Atmospheric and Space Science Series. Cambridge University Press, Cambridge, 1997.

King, J. C., M. J. Varley, and T. A. Lachlan-Cope. *Using satellite thermal infrared imagery to study boundary layer structure in an Antarctic katabatic wind region*. International Journal of Remote Sensing, 19(17), 3335–3348, 1998.

Klein, T., G. Heinemann, D. H. Bromwich, J. J. Cassano, and K. M. Hines. *Mesoscale modeling of katabatic winds over Greenland and comparisons with AWS and aircraft data*. Meteorology and Atmospheric Physics, 78(1-2), 115–132, 2001.

Kouznetsov, R. D. *The summertime ABL structure over an Antarctic oasis with a vertical Doppler sodar*. Meteorologische Zeitschrift, 18(2), 163–167, 2009.

van Lipzig, N. P. M., J. Turner, S. R. Colwell, and M. R. van den Broeke. *The near-surface wind field over the Antarctic continent*. International Journal of Climatology, 24(15), 1973–1982, 2004.

Liu, Z. and D. H. Bromwich. *Dynamics of the katabatic wind confluence zone near Siple Coast, West Antarctica*. Journal of Applied Meteorology, 36(2), 97–118, 1997.

Lock, A. P. *The parameterization of turbulent fluxes in the boundary layer*. Unified Model Documentation Paper 24, Section 3, 2007.

Lock, A. P., A. R. Brown, M. R. Bush, G. M. Martin, and R. N. B. Smith. *A new boundary layer mixing scheme. Part I: Scheme description and single-column model tests*. Monthly Weather Review, 128(9), 3187–3199, 2000.

Louis, J. F. *A parametric model of vertical eddy fluxes in the atmosphere*. Boundary Layer Meteorology, 17(2), 187–202, 1979.

Mahrt, L. *Momentum balance of gravity flows*. Journal of the Atmospheric Sciences, 39(12), 2701–2711, 1982.

Mahrt, L. *Grid-averaged surface fluxes*. Monthly Weather Review, 115(8), 1550–1560, 1987.

Mahrt, L., J. Sun, W. Blumen, T. Delany, and S. Oncley. *Nocturnal boundary-layer regimes*. Boundary-Layer Meteorology, 88(2), 255–278, 1998.

Mather, K. B. *The pattern of surface wind flow in Antarctica*. Pure and Applied Geophysics, 75(1), 332–354, 1969.

Meesters, A., N. J. Bink, E. A. C. Henneken, H. F. Vugts, and F. Cannemeijer. *Katabatic wind profiles over the Greenland ice sheet: Observation and modelling*. Boundary-Layer Meteorology, 85(3), 475–496, 1997.

van Meijgaard, E. and A. P. van Ulden. *A first-order mixing-condensation scheme for nocturnal stratocumulus*. Atmospheric Research, 45(4), 253–273, 1998.

Naithani, J. and H. N. Dutta. *Acoustic sounder measurements of the planetary boundary layer at Maitri, Antarctica*. Boundary-Layer Meteorology, 76(1-2), 199–207, 1995.

Nakagawa, K. and H. Shimoodori. *The relationship between the thermal belt on the Soya Coast and the surface inversion layer over Syowa station*. Proceedings of the NIPR Symposium on Polar Meteorology and Glaciology, 8(2), 53–65, 1994.

Parish, T. R. *The katabatic winds of Cape Denison and Port Martin*. Polar Record, 20, 525–532, 1981.

Parish, T. R. *Surface air-flow over East Antarctica*. Monthly Weather Review, 110(2), 84–90, 1982.

Parish, T. R. *Surface winds over the Antarctic continent - a review*. Reviews of Geophysics, 26(1), 169–180, 1988.

Parish, T. R. and D. H. Bromwich. *The surface windfield over the Antarctic ice sheets*. Nature, 328(6125), 51–54, 1987.

Parish, T. R. and D. H. Bromwich. *Instrumented aircraft observations of the katabatic wind regime near Terra Nova Bay*. Monthly Weather Review, 117(7), 1570–1585, 1989.

Parish, T. R. and D. H. Bromwich. *A case study of Antarctic katabatic wind interaction with large-scale forcing*. Monthly Weather Review, 126(1), 199–209, 1998.

Parish, T. R. and D. H. Bromwich. *Reexamination of the near-surface airflow over the Antarctic continent and implications on atmospheric circulations at high southern latitudes*. Monthly Weather Review, 135(5), 1961–1973, 2007.

Parish, T. R., D. H. Bromwich, and R. Y. Tzeng. *On the role of the Antarctic continent in forcing large-scale circulations in the high southern latitudes*. Journal of the Atmospheric Sciences, 51(24), 3566–3579, 1994.

Parish, T. R. and J. J. Cassano. *Forcing of the wintertime Antarctic boundary layer winds from the NCEP/NCAR global reanalysis*. Journal of Applied Meteorology, 40(4), 810–821, 2001.

Parish, T. R. and J. J. Cassano. *Diagnosis of the katabatic wind influence on the wintertime Antarctic surface wind field from numerical simulations*. Monthly Weather Review, 131(6), 1128–1139, 2003a.

Parish, T. R. and J. J. Cassano. *The role of katabatic winds on the Antarctic surface wind regime*. Monthly Weather Review, 131(2), 317–333, 2003b.

Parish, T. R., P. Pettre, and G. Wendler. *The influence of large-scale forcing on the katabatic wind regime at Adelie Land, Antarctica*. Meteorology and Atmospheric Physics, 51(3-4), 165–176, 1993a.

Parish, T. R., P. Pettre, and G. Wendler. *A numerical study of the diurnal-variation of the Adelie Land katabatic wind regime*. Journal of Geophysical Research-Atmospheres, 98(D7), 12,933–12,947, 1993b.

Parish, T. R., Y. C. Wang, and D. H. Bromwich. *Forcing of the austral autumn surface pressure change over the Antarctic continent*. Journal of the Atmospheric Sciences, 54(11), 1410–1422, 1997.

Paterson, C. *Harnessing the power of the windiest continent*. Australian Antarctic Magazine, 1, 40–41, 2001.

Paterson, C. *Blizzard winds now harnessed at Mawson*. Australian Antarctic Magazine, 5, 34–35, 2003.

Peel, D. A. *Snow accumulation, conductance and temperature inland from Halley Bay*. British Antarctic Survey Bulletin, 43, 1–13, 1976.

Pettré, P. and J. C. André. *Surface-pressure change through Loewe phenomena and katabatic flow jumps - study of 2 cases in Adelie Land, Antarctica*. Journal of the Atmospheric Sciences, 48(4), 557–571, 1991.

Pettré, P. and S. Argentini. *On the vertical velocity sodar measurement in the region of Dumont d'Urville, East Antarctica*. Geophysical Research Letters, 28(5), 783–786, 2001.

Pettré, P., R. Renaud, M. Déqué, S. Planton, and J. C. André. *Study of the influence of katabatic flows on the Antarctic circulation using GCM simulations*. Meteorology and Atmospheric Physics, 43(1-4), 187–195, 1990.

Renfrew, I. A. *The dynamics of idealized katabatic flow over a moderate slope and ice shelf*. Quarterly Journal of the Royal Meteorological Society, 130(598), 1023–1045, 2004.

Renfrew, I. A. and P. S. Anderson. *The surface climatology of an ordinary katabatic wind regime in Coats Land, Antarctica*. Tellus Series a-Dynamic Meteorology and Oceanography, 54(5), 463–484, 2002.

Renfrew, I. A. and P. S. Anderson. *Profiles of katabatic flow in summer and winter over Coats Land, Antarctica*. Quarterly Journal of the Royal Meteorological Society, 132(616), 779–802, 2006.

Smith, R. N. B. *A scheme for predicting layer clouds and their water contents in a general circulation model*. Quarterly Journal of the Royal Meteorological Society, 116(492), 435–460, 1990.

Sorbjan, Z., Y. Kodama, and G. Wendler. *Observational study of the atmospheric boundary layer over Antarctica*. Journal of Applied Meteorology, 25(5), 641–651, 1986.

Steeneveld, G. J., A. A. M. Holtslag, C. J. Nappo, B. J. H. van de Wiel, and L. Mahrt. *Exploring the possible role of small-scale terrain drag on stable boundary layers over land*. Journal of Applied Meteorology and Climatology, 47(10), 2518–2530, 2008a.

Steeneveld, G. J., T. Mauritsen, E. I. F. de Bruijn, J. Vilà-Guerau de Arellano, G. Svensson, and A. A. M. Holtslag. *Evaluation of limited-area models for the representation of the diurnal cycle and contrasting nights in CASES-99*. Journal of Applied Meteorology and Climatology, 47(3), 869–887, 2008b.

Steeneveld, G. J., B. J. H. van de Wiel, and A. A. M. Holtslag. *Modeling the evolution of the atmospheric boundary layer coupled to the land surface for three contrasting nights in CASES-99*. Journal of the Atmospheric Sciences, 63(3), 920–935, 2006.

Stull, R. B. *An introduction to boundary layer meteorology*. Atmospheric Sciences Library. Kluwer Academic Publishers, Dordrecht, the Netherlands, 1988.

Valtat, B. *Loewe's phenomenon*. In *Symposium on Antarctic Meteorology*, 67–70. Pergamon, Melbourne, Australia, 1959.

Viterbo, P., A. Beljaars, J. F. Mahfouf, and J. Teixeira. *The representation of soil moisture freezing and its impact on the stable boundary layer*. Quarterly Journal of the Royal Meteorological Society, 125(559), 2401–2426, 1999.

Wendler, G. *Strong gravity flow observed along the slope of Eastern Antarctica. a contribution to I.A.G.O.*. Meteorology and Atmospheric Physics, 43(1-4), 127–135, 1990.

Williams, A. G. *Boundary layer processes option 6a/8a equilibrium stable boundary layer scheme version 2a (eqsbl v.2a)*. Unified Model Documentation Paper 24, 2003.

Wilson, D. R. and S. P. Ballard. *A microphysically based precipitation scheme for the UK Meteorological Office Unified Model*. Quarterly Journal of the Royal Meteorological Society, 125(557), 1607–1636, 1999.

Yu, Y. and Cai. *Structure and dynamics of katabatic flow jumps: Idealised simulations*. Boundary-Layer Meteorology, 118(3), 527–555, 2006.

Yu, Y., X. M. Cai, J. C. King, and I. A. Renfrew. *Numerical simulations of katabatic jumps in Coats Land, Antarctica*. Boundary-Layer Meteorology, 114(2), 413–437, 2005.